

DUNE EROSION DURING STORM SURGES

Deltares Select Series

Volume 3

ISSN 1877-5608

Deltares is a Dutch independent research institute for water, soil and subsurface issues. It was formed in 2008 from a merger of Delft Hydraulics, GeoDelft, the Subsurface and Groundwater unit of TNO and parts of Rijkswaterstaat.

Cover: Beach and dunes at Westenschouwen in The Netherlands; photo by Jaap van Thiel de Vries.

Previously published in this series:

Volume 2. P.M.S. Monteiro and M. Marchand (Eds.), *Catchment2Coast: A Systems Approach to Coupled River-Coastal Ecosystem Science and Management*

Volume 1. F.J. Los, *Eco-Hydrodynamic Modelling of Primary Production in Coastal Waters and Lakes Using BLOOM*

DUNE EROSION DURING STORM SURGES

PROEFSCHRIFT

ter verkrijging van de graad van doctor
aan de Technische Universiteit Delft,
op gezag van de Rector Magnificus prof.dr.ir. J.T. Fokkema,
voorzitter van het College voor Promoties,
in het openbaar te verdedigen op dinsdag 1 september 2009 om 15:00 uur

door

Jacob Simon Marie VAN THIEL DE VRIES
civiel ingenieur
geboren te 's-Hertogenbosch

Dit proefschrift is goedgekeurd door de promotoren:

Prof.dr.ir. M.J.F. Stive

Prof.dr.ir. A.J.H.M. Reniers

copromotor:

Dr.ir. J. van de Graaff

Samenstelling promotiecommissie:

Rector Magnificus	voorzitter
Prof.dr.ir. M.J.F. Stive	Technische Universiteit Delft, promotor
Prof.dr.ir. A.J.H.M. Reniers	University of Miami (Verenigde Staten), promotor
Dr.ir. J. van de Graaff	Technische Universiteit Delft, copromotor
Prof.dr. R.A. Holman	Oregon State University (Verenigde Staten)
Prof.dr.ir. L.C. van Rijn	Universiteit Utrecht
Prof.dr.ir. J.A. Roelvink	UNESCO-IHE Institute for Water Education
Dr. B.G. Ruessink	Universiteit Utrecht

The research has been funded by the Dr.Ir. Cornelis Lely Foundation and the Delft Cluster II joint research program.

Copyright © 2009 by J.S.M. van Thiel de Vries and IOS Press

All rights reserved. No part of this book may be reproduced, stored in a retrieval system, or transmitted, in any form or by any means, without prior written permission from the publisher.

ISBN: 978-1-60750-041-4

Library of Congress Control Number: 2009932267

Publisher

IOS Press BV

Nieuwe Hemweg 6B

1013 BG Amsterdam

Netherlands

fax: +31 20 687 0019

e-mail: order@iospress.nl

LEGAL NOTICE

The publisher is not responsible for the use which might be made of the following information

PRINTED IN THE NETHERLANDS

Duin,

*'k Hou u voor een wonderwerk:
Gij zijt zwak, maar echter sterk;
Schoon uw stoffe niet en kleeft;
En met alle winden zweeft,
Nog zoo moet de oceaen
Voor uw zwakheid stille staan.*

Jacob Cats, (1656), Uit het lange gedicht Hofgedachten.

CONTENTS

Abstract	xi
Samenvatting	xv
Chapter 1 Introduction	1
1.1 Dune erosion -----	1
1.2 Societal importance -----	2
1.3 Process-based modeling of dune erosion-----	3
1.4 Thesis outline -----	4
Chapter 2 Large scale dune erosion tests	7
2.1 Introduction -----	7
2.2 Physical model description and instrument deployment -----	8
2.2.1 Set up of physical model.....	9
2.2.2 Test programme.....	10
2.2.3 Instrument deployment.....	12
2.3 Measured profiles and erosion volumes -----	18
2.3.1 Profiles.....	18
2.3.2 Erosion volumes.....	20
2.4 Detailed test results -----	21
2.4.1 Waves	21
2.4.2 Flow.....	24
2.4.3 Sediment concentrations	26
2.4.4 Sediment transports.....	27
2.5 Effect of the wave period-----	29
2.6 Conclusions-----	32
Chapter 3 Interaction of dune face and swash zone	35
3.1 Introduction -----	35
3.2 High resolution dune face reconstruction from stereo images-----	36
3.2.1 Introduction.....	36
3.2.2 Camera model	38
3.2.3 Camera calibration	39
3.2.4 Image pre-processing	41
3.2.5 Feature matching.....	41
3.2.6 World coordinates from feature matching.....	44
3.2.7 An example reconstruction	44

3.3	Dune face erosion due to wave impacts -----	47
3.3.1	Previous studies on dune face erosion due to wave impacts.....	47
3.3.2	Visual observations during the Deltaflume experiment.....	49
3.3.3	Dune face impact model	51
3.4	Conclusions and discussion -----	57
Chapter 4 Modeling near dune hydrodynamics		59
4.1	Introduction -----	59
4.2	Model description-----	60
4.2.1	Model boundaries	62
4.3	Hydrodynamic simulation for the Deltaflume experiment -----	63
4.4	Hydrodynamic simulations for the La Jolla field experiment -----	67
4.5	Interaction between short wave groups and long waves -----	74
4.6	Conclusions and discussion -----	77
Chapter 5 Modeling near dune sediment suspensions		79
5.1	Introduction -----	79
5.2	Data analysis-----	80
5.3	1DV Sediment suspension model-----	85
5.3.1	1DV Model description.....	86
5.3.2	Simulations	90
5.4	Wave and depth averaged sediment concentration formulation -----	95
5.5	Conclusions and discussion -----	97
5.5.1	Conclusions.....	97
5.5.2	Discussion and recommendations.....	98
Chapter 6 Modeling dune erosion		101
6.1	Introduction -----	101
6.2	Model adaptations and extensions-----	102
6.2.1	Wave energy dissipation formulation	102
6.2.2	Equilibrium sediment concentration formulation	103
6.2.3	Wave shape model	104
6.2.4	Hard structures.....	109
6.3	Model optimization-----	110
6.4	1D Morphodynamic simulations-----	113
6.4.1	Deltaflume experiment.....	113
6.4.1	Dune revetment	128
6.4.2	Calm and moderate conditions	129
6.4.3	1953 storm surge.....	132
6.5	Model sensitivity -----	134
6.5.1	Importance of long waves and short waves	134
6.5.2	Sediment supply from dunes by avalanching	142
6.6	2DH Morphodynamic simulations -----	146
6.6.1	Uniform coast	147
6.6.2	Alongshore variability in dune height	151

6.6.3	Alongshore variability in bathymetry	153
6.6.4	Interaction between a dike and dunes.....	155
6.7	Summary and Conclusions-----	157
Chapter 7	Conclusions and recommendations	159
7.1	Conclusions-----	159
7.2	Recommendations-----	162
References		165
List of symbols		175
Appendix A	Description of the morphodynamic model XBeach	179
Appendix B	Model input files	187
Acknowledgements		197
Curriculum Vitae		199

ABSTRACT

A large scale dune erosion experiment has been conducted in a flume to examine the effect of the wave period on dune erosion and to perform detailed measurements of inner surf water pressure, flow velocities and sediment concentrations. Profile measurements reveal that a 50% increase in the wave period results in 25% larger dune erosion volumes for storm surge conditions that are representative for the Dutch coast. Analysis of the detailed measurements shows that both short wind waves and long waves are important to inner surf hydrodynamics. The mean flows are directed offshore and increase towards the shoreline whereas mean sediment concentrations rise sharply towards the dune face (up to 50 g/l near the bed). The sediment transport is dominated by the mean offshore directed flow and is partly compensated by shoreward sediment transports that take place above the wave trough or are associated with intra wave processes. The effect of the wave period on dune erosion is mainly caused by an $O(60\%)$ increase of the time and depth averaged near dune sediment concentrations whereas the offshore directed mean flows are comparable, yielding a larger offshore directed transport capacity. This increase in transport capacity is only partly compensated by a concurrent increase of the wave related sediment transports (in landward direction).

The interaction of dune face and swash zone is studied in more detail for the large scale dune erosion experiment. First an algorithm is proposed that can make three dimensional reconstructions of the dune face and beach from collected image pairs with two synchronized cameras. Next, available stereo video reconstructions and profile measurements are used to confirm a linear relation according to Fisher et al. (1986) between the average wave impact force on the dune face and the erosion rate. It is found that initially a different and more effective dune erosion mechanism is present in which waves run-up the dune face and steepen it by scouring the face. When the dune face is sufficiently steep waves start to impact it after which the steepening continues until a critical slope is reached and the dune face collapses. Slumping characteristics change over a storm surge and the time interval between successive slumps increases whereas the average volume associated with a slump does hardly change as a surge progresses.

Inner surf zone hydrodynamics have been simulated with a surf beat model for the large scale dune experiment and the field. It is shown that the observed shift in variance towards lower frequencies in the inner surf zone during the experiment is associated with the generation and interaction of long waves with short wave groups. Considering dissipative conditions in the laboratory and field, near shore hydrodynamics can be accurately reproduced with the surf beat model whereas for reflective conditions this is less the case since short (wind) waves are also present near the

shoreline. In shallow water ($H_{rms,lf} \sim h$) long waves contribute to the mean offshore directed flow.

Sediment concentration measurements have been analyzed in more detail and it is found that the mean near dune sediment concentration correlates much better with the maximum wave surface slope than with flow drag. The maximum surface slope is associated with the intensity of wave breaking and if the diffusion of turbulence from the water surface towards the bed is taken into account the correlation with the mean sediment concentrations improves.

The $O(100\%)$ increase in the near-bed sediment concentrations for a larger wave period correlates well with an increase in the intensity of wave breaking whereas the wave averaged turbulence production is comparable for the range of wave periods studied. For this reason it is hypothesized that the near-bed turbulence energy varies over the wave cycle since breaking induced turbulence is generated at the wave front and is injected in the water column over a short period (the bore interval). In addition it is presumed that sediment suspensions respond nonlinearly to the near-bed turbulence intensity and will increase for more intense breaking waves.

The effect of near-bed turbulence on sediment concentrations is examined with a 1DV suspension model. Simulations with constant turbulence energy over the wave cycle are compared with simulations with wave varying turbulence energy. It is found that in cases with a sufficient short duration of the bore interval ($T/T_{bore} > 7$) the wave averaged sediment suspensions are substantially higher (one order of magnitude) when the near-bed turbulence intensity varies over the wave cycle. For larger bore intervals sediment suspensions have the same order of magnitude and the effect of wave breaking induced turbulence on sediment suspensions is expected to be small since this turbulence does not reach the bed. The 1DV model results are aggregated in a wave averaged equilibrium sediment concentration formulation that in addition to flow drag is a function of the bore averaged turbulence intensity.

Obtained insights in dune erosion physics are coupled within a 2DH morphodynamic model XBeach (Roelvink et al., 2007). The model is extended with an adapted wave dissipation model, an equilibrium sediment concentration formulation that depends on the bore averaged turbulence energy and a wave shape model from which the bore interval is estimated. The wave shape model is also utilized to estimate intra wave sediment transports and the dissipation rate in bores that develop after wave breaking.

After optimization the XBeach model is applied to simulate:

1. *The large scale dune erosion experiment described in this thesis.* The model physics over the developing foreshore are favorably compared with detailed measurements during a dune erosion test. In addition the effects of the wave period and spectral shape on dune erosion are correctly simulated. Profile evolution during a small dune breach looks reasonable however the amount of erosion is overestimated at the end of the test.
2. *The effect of a dune revetment on foreshore evolution during a storm surge.* It is found that at this stage the model lacks the right physics to simulate the development of a scour hole and simulated long wave run-up is too small to erode sand above a revetment of medium height.

3. *Profile evolution during moderate and calm wave conditions.* The model tends to erode the beach near the waterline; however the amount of erosion is small.
4. *Impact of the 1953 storm surge on the Delfland coast in The Netherlands.* An erosion volume of $73 \text{ m}^3/\text{m}$ is predicted, which is within the range of estimated erosion volumes ($55 \text{ m}^3/\text{m} - 155 \text{ m}^3/\text{m}$).

In addition, the sensitivity of simulated dune erosion to short waves and long waves is examined. It is found that dune erosion rates during the start of a test are determined by the sediment supply from the dunes rather than by the offshore transport capacity of the near dune hydrodynamics. Considering only short (wind) waves still a reasonable estimation of the amount of dune erosion can be made and the erosion volume is underestimated with about 30%. Wave group generated long waves contribute to the amount of dune erosion (about 30%) and are effective in releasing sand from the dunes.

Dune face erosion is simulated with a simple avalanching algorithm. Robustness of this algorithm is tested for an instable dry bank and for a dune erosion test by performing simulations on various grids. Next, the parameters associated with avalanching are varied showing that the sediment supply from the dunes influences the dune erosion volume during a storm surge.

2DH simulations are conducted with a time varying surge (representative for the Dutch coast) and with directionally spread incoming waves. First a uniform coast is considered and 2DH model results are compared to 1D results showing that dune erosion rates are comparable. Next, a simulation with an alongshore varying dune height and uniform bathymetry is performed. A uniform foreshore develops and sand from areas with higher dunes is transported to cross-shore transects with lower dunes. Simulation results for an alongshore uniform dune height and varying bathymetry (including an offshore bar, an intertidal bar intersected by rips and beach cusps) reveal highly non-uniform flows and sediment concentrations. However, the foreshore develops quite uniform in alongshore direction and dune face retreat varies only slightly along the coastline. Finally, the transition of a (non-erodible) dike that protrudes seaward of a sandy dune system is modeled. In case a longshore flow is present dune erosion volumes are significantly larger downstream of the dike, which is caused by longshore sediment transport gradients related to the presence of the dike.

SAMENVATTING

Een grootschalig duinafslagexperiment is uitgevoerd in een laboratoriumgoot om het effect van de golfperiode op duinafslag te onderzoeken en om gedetailleerde metingen uit te voeren van de waterdruk, stroomsnelheden en sedimentconcentraties in de binnenste brekerzone. Uit de verkregen profielmetingen blijkt dat een toename van 50% in de golfperiode leidt tot ongeveer 25% extra duinafslag voor een representatieve stormopzet voor de Nederlandse kust. Analyse van de gedetailleerde metingen laat zien dat zowel korte (wind) golven als lange golven van belang zijn voor de hydrodynamica in de binnenste brekerzone. De gemiddelde stroming is zeewaarts gericht en neemt toe in de richting van de waterlijn. Ook de sedimentconcentraties nemen scherp toe in de richting van het duinfront (tot 50 gr/l bij de bodem). De sedimenttransporten worden gedomineerd door de gemiddelde zeewaartse stroming en worden deels gecompenseerd met kustwaartse sedimenttransporten die plaatsvinden boven het golfdal of gerelateerd zijn aan intragolfprocessen. Het golfperiode-effect op duinafslag wordt vooral veroorzaakt door een $O(60\%)$ toename van de tijd en diepte gemiddelde sedimentconcentraties terwijl de zeewaartse gemiddelde stromingen vergelijkbaar zijn en dus resulteren in een grotere transportcapaciteit. De toename in de transportcapaciteit wordt slechts gedeeltelijk gecompenseerd door een toename in het landwaarts gerichte golfgerelateerde transport.

De interactie tussen het duinfront en de swash zone is in meer detail onderzocht voor het duinafslagexperiment op grote schaal. Eerst is een algoritme ontwikkeld waarmee uit de verzamelde fotoparen (met twee gesynchroniseerde camera's) drie-dimensionale reconstructies van het duinfront en strand kunnen worden gemaakt. Vervolgens worden de beschikbare stereo video reconstructies en profielmetingen gebruikt om een lineaire relatie tussen de gemiddelde kracht op het duin als gevolg van de golfklappen ertegen en de erosiesnelheid van het duin te bevestigen (Fisher et al., 1986). Het blijkt dat er initieel een ander en efficiënter duinerosiemechanisme is waarbij golven tegen het duinfront oplopen en het uitschuren met een versteiling van het front als gevolg. Wanneer het duinfront voldoende steil geworden is, klappen de golven tegen het duin aan waardoor een verdere versteiling plaats vindt tot het moment dat een kritische helling wordt overschreden en de voorkant van het duin in elkaar zakt. De karakteristieken van het in elkaar zakken van het duinfront veranderen gedurende een storm waarbij het tijdsinterval tussen opeenvolgende ineenstortingen toeneemt maar het gemiddelde volume zand dat afglijdt ongeveer gelijk blijft.

De hydrodynamica in de binnenste brekerzone is gemodelleerd met een surf-beat model voor het duinafslag experiment en voor het veld. Het blijkt dat de verschuiving

in variantie naar de lage frequenties in de binnenste brekerzone, zoals waargenomen tijdens het experiment, gerelateerd is aan de generatie en interactie van lange golven met korte golfgroepen. Voor dissipatieve condities in het laboratorium en in het veld kan de hydrodynamica vlak voor de kust nauwkeurig worden gereproduceerd terwijl dit voor reflecterende condities minder het geval is omdat er bij de waterlijn ook nog korte (wind) golven zijn. In ondiep water ($H_{rms,l} \sim h$) dragen de lange golven bij aan de gemiddelde zeevaartse stroming.

Sedimentconcentratiemetingen zijn in meer detail geanalyseerd en het blijkt dat de sedimentconcentraties in de buurt van het duin beter correleren met de maximale helling van het golfoppervlak dan met de schuifkracht als gevolg van de stroming. De maximale helling van het golfoppervlak wordt in verband gebracht met de intensiteit van golfbreken. En als de diffusie van turbulentie van het wateroppervlak naar de bodem meegenomen wordt, verbetert de correlatie met de gemiddelde sedimentconcentraties.

De $O(100\%)$ toename in de sedimentconcentraties bij de bodem voor een grotere golfperiode correleert goed met een toename in de intensiteit van golfbreken. Echter de golfgemiddelde productie van turbulentie is vergelijkbaar voor de range van golfperiodes die onderzocht is. De hypothese is daarom dat de intensiteit van turbulentie bij de bodem varieert over de golfbeweging omdat de door breken geïnitieerde turbulentie aan de voorkant van een golf ontstaat en geïnjecteerd wordt in de waterkolom over een relatief korte periode (het bore interval). Ook wordt verondersteld dat de sedimentsuspensies niet lineair reageren op de turbulentie bij de bodem en meer dan evenredig groter worden voor intensiever brekende golven.

Het effect van turbulentie bij de bodem op de sedimentconcentraties is verder onderzocht met een 1DV suspensiemodel. Simulaties met een constante turbulentie-energie over de golfcyclus worden vergeleken met simulaties waarbij de turbulentie-energie varieert. Het blijkt dat wanneer de duur van het bore interval voldoende kort is ($T/T_{bore} > 7$) de golfgemiddelde sedimentconcentraties aanzienlijk (een orde) groter zijn in een situatie met variërende turbulentie-energie bij de bodem. Voor grotere bore intervallen zijn de sedimentconcentraties vergelijkbaar en het effect van turbulentie op de sedimentconcentraties is waarschijnlijk klein omdat de door golfbreken gegenereerde turbulentie de bodem niet kan bereiken. De 1DV modelresultaten zijn geaggregeerd in een evenwichts-sedimentconcentratieformulering (golfgemiddeld) die, naast de schuifkracht als gevolg van de stroming, afhangt van de bore gemiddelde turbulentie-energie.

De verbeterde inzichten in de fysica van duinafslag zijn toegevoegd aan het morfodynamische 2DH model XBeach (Roelvink et al., 2007). Het model is uitgebreid met een aangepast golfdissipatiemodel, een evenwichts-sedimentconcentratieformulering die afhangt van de bore gemiddelde turbulentie-energie en een golfvormmodel waarmee het bore interval bepaald kan worden. Ook wordt het golfvormmodel gebruikt om de intragolf sedimenttransporten en de dissipatie in een bore na het breekpunt te schatten.

Na optimalisatie wordt het XBeach model toegepast voor het simuleren van:

1. *De grootschalige duinafslagexperimenten beschreven in dit proefschrift.* De gemodelleerde processen over een zich ontwikkelende vooroever laten zich

redelijk goed vergelijken met gedetailleerde metingen tijdens het experiment. Daarnaast worden de effecten van de golfperiode en een afwijkend golfspectrum op duinafslag juist voorspeld. De profielontwikkeling tijdens de doorbraak van een klein duin wordt redelijk berekend, echter de erosie aan het einde van de test wordt overschat.

2. *Het effect van een duinvoetverdediging op de ontwikkeling van de vooroever.* Het blijkt dat op dit moment de juiste processen in het model ontbreken om de ontwikkeling van een ontgrondingskuil te voorspellen. Ook is de oploop van de lange golven onvoldoende om zand boven een duinvoetverdediging van gemiddelde hoogte te eroderen.
3. *Profielontwikkeling tijdens kalme en gematigde condities.* Het model heeft de neiging om het strand bij de waterlijn te eroderen. Echter de hoeveelheid erosie is klein.
4. *De impact van de stormvloed van 1953 op de Delflandse kust in Nederland.* Het model voorspelt een erosievolume van $73 \text{ m}^3/\text{m}$ wat binnen de range van geschatte afslagvolumes valt ($55 \text{ m}^3/\text{m} - 155 \text{ m}^3/\text{m}$).

Daarnaast is de gevoeligheid van de gesimuleerde duinafslag voor korte golven en lange golven onderzocht. Het blijkt dat de erosiesnelheid tijdens de start van een experiment bepaald wordt door de aanvoer van zand van het duin en niet door de capaciteit van de hydrodynamica voor het duin om zand zeewaarts te transporteren. Wanneer enkel korte (wind-) golven meegenomen worden kan een redelijke schatting van het duinafslagvolume worden gemaakt en het erosievolume wordt onderschat met ongeveer 30%. Golfgroepgegenereerde lange golven dragen bij aan de duinafslag (orde 30%) en zijn effectief in het losmaken van zand van de duinen.

De erosie van het duinfront wordt gemodelleerd met een eenvoudig lawine algoritme. De robuustheid van dit algoritme is onderzocht voor een instabiele droge helling en voor duinafslag condities, door simulaties op verschillende rekenroosters te maken. Daarnaast zijn de aan het lawine algoritme gerelateerde parameters gevarieerd, wat onder andere laat zien dat de aanvoer van zand van het duin het afslagvolume beïnvloedt.

Er zijn 2DH simulaties gemaakt met een tijdsvariërende (voor de Nederlandse kust maatgevende) stormopzet en met inkomende golven uit verschillende richtingen. Eerst zijn 2DH modelresultaten voor een uniforme kust vergeleken met 1D modelresultaten waaruit blijkt dat de mate van duinafslag vergelijkbaar is. Vervolgens is een simulatie met een in langsrichting variërende duinhoogte en een uniforme bathymetrie uitgevoerd. Er ontwikkelt zich een uniforme vooroever en zand uit gebieden met hogere duinen wordt getransporteerd naar gebieden met lagere duinen. Resultaten van een model met een in langsrichting uniforme duinhoogte en een variërende bathymetrie (met een zeewaartse bank, een intergetijde bank doorsneden met muistromen en strandcusps), laten een niet-uniform stromings- en sediment-concentratieveld zien. Echter de vooroever ontwikkelt zich redelijk uniform en de terugschrijving van het duinfront varieert maar weinig in langsrichting. Tot slot is gekeken naar de overgang van een (niet erodeerbare) dijk die zeewaarts uitsteekt voor een zandig duinsysteem. In het geval van een langsstroming is de duinerosie

benedenstrooms van de dijk significant groter, wat veroorzaakt wordt door gradiënten in het langstransport die ontstaan door de aanwezigheid van de dijk.

Chapter 1

INTRODUCTION

1.1 DUNE EROSION

Dune erosion in The Netherlands and more generally along the southwest North Sea coasts takes place during storm surges when the mean water level increases and waves can reach the dune face and impact it (Figure 1.1). Eroded sand from the dunes is transported offshore by a strong undertow and sediment suspensions in proximity of the dunes are high resulting in a large offshore transport capacity. Further seaward the transport capacity of the flow decreases and the sediment starts to settle forming a new coastal profile that is in better equilibrium with the storm surge conditions. The newly developed foreshore is more efficient in dissipating the energy associated with the incoming waves and consequently dune erosion rates decrease as a storm progresses.

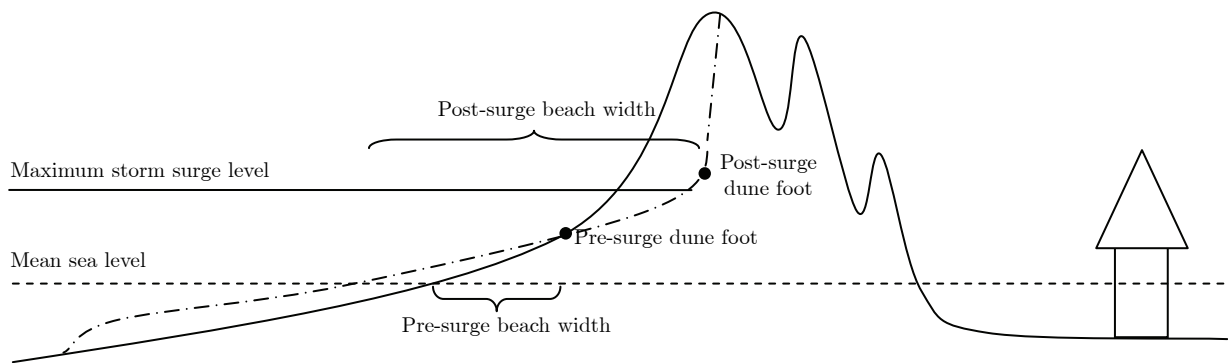


Figure 1.1 Profile evolution during a storm along the Dutch dune coast.

After a storm surge the beach width has become substantially wider (Figure 1.1) and the coastal profile is not in equilibrium with the post-surge hydrodynamic conditions. Waves tide and wind reshape the foreshore and the dunes gain eroded sand back partly. In a situation without longshore sediment transport gradients the dunes recover to pre-storm volume. However, the time scale of dune recovery is considerable larger than that of erosion.

1.2 SOCIETAL IMPORTANCE

The southern North Sea has a relative small water depth and a narrow connection with the Atlantic Ocean (the English Channel). As a result storms from northwestern direction can build up exceptional surges along the southern coast that stretches from Belgium, via The Netherlands and Germany to Denmark. In contrast to the surrounding countries, large parts of The Netherlands are situated below mean sea level and are densely populated. Inundation of the hinterland is prevented at many locations with a narrow system of sea defenses that mainly consist of sandy beaches and dunes.

Depending on the economic value of a region (Law on Water Defenses, 1996) the Dutch government guarantees a safety level against flooding by law, which for the central part of The Netherlands (the provinces of North- and South-Holland) means a storm surge level with a frequency of exceedance of 1/10,000 year should be resisted.

The strength of dunes against normative storm surge conditions is assessed every five years with a guideline that is based on an empirical dune erosion model (Vellinga, 1986; Van Gent et al., 2008). The model is developed from (large scale) flume experiments and computes a post-surge profile, which is a function of the maximum storm surge level, the wave height, the wave period and the grain diameter. Though the model is validated against many experiments it is not generic and is based on a couple of assumptions that not necessarily hold along the Dutch coast or an arbitrary coast in general:

1. The coast is assumed to be uniform in alongshore direction;
2. Non-erodible elements (e.g. revetments, seawalls, groins and dikes) and the interaction of these elements with the sandy dune system are not taken into account;
3. The shape of the post-storm surge profile is independent from the pre-storm profile and is not a function of time;
4. The amount of dune erosion depends on the maximum storm surge level and the shape and duration of the storm surge is only partly taken into account;
5. Shore normal waves without directional spreading are considered.

Most of these assumptions are directly related to the limitations imposed by the use and applied schematization of the physical model in a flume (e.g. the longshore direction cannot be considered in a flume and most experiments were conducted with a constant (maximum storm surge) level to save time and money).

It would require many more experiments and probably new research facilities to further develop an empirical dune erosion model that is applicable at an arbitrary location along the Dutch coast. It seems therefore more appropriate to develop a more generic dune erosion model as first proposed by Steetzel (1993). Such a model is time dependent and predicts the amount of dune erosion from the relevant time averaged physical processes. This thesis can be considered as a follow up of that work. Insights in dune erosion processes are coupled within a physical-based model that takes into account the alongshore direction and predicts dune erosion as function of wave group varying processes.

1.3 PROCESS-BASED MODELING OF DUNE EROSION

In a process-based model the most important physical processes that drive dune erosion are modeled and coupled. The model proposed in this thesis is depth averaged (processes are averaged over the vertical) and solves the physics on the wave group time scale. The model approach is comparable to Reniers et al. (2004a) and is outlined in Figure 1.2.

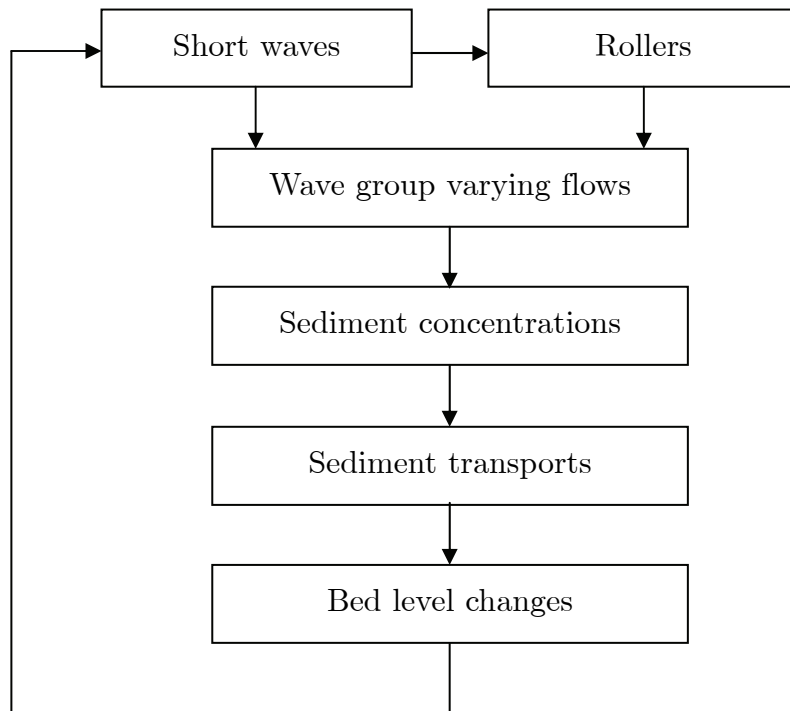


Figure 1.2 Process-based modeling approach for dune erosion.

First the short (wind and swell) wave transformation over the coastal area of interest is computed with a wave action balance (Holthuijsen et al., 1989) that is solved on the wave group time scale. In addition the wave breaking in shallow water, which generates a roller with aerated water at the wave front is taken into account with a roller energy balance (Stive and Dingemans, 1984; Nairn et al., 1990).

The wave forces (varying on the wave group time scale) accelerate or decelerate the flow in the nonlinear shallow water equations (NSWE) accounting for long wave motions called surf beat (Munk, 1949). The wave group varying mass flux associated with the short waves and rollers (Phillips, 1977) is computed and is utilized to obtain Eulerian flow velocities applying the Generalized Lagrangian Mean (GLM) approach (Walstra et al., 2000). As a result the mass flux contributes to the long wave motion and the mean offshore directed flow (undertow) is also taken into account.

Next, computed hydrodynamics and wave transformation are utilized to compute an equilibrium sediment concentration that acts as a source term in an advection diffusion equation for sediment (Galapatti, 1983).

Finally, bed level changes are computed from sediment transport gradients. The new bathymetry affects the wave transformation, currents and sediment transports and as

a consequence a feed-back is introduced in the system that needs to be modeled and results in decreasing dune erosion rates as the storm surge progresses.

In this thesis the model concept of Reniers et al. (2004a) is extended and validated to simulate dune erosion. Use is made of the 2DH XBeach model (Roelvink et al., 2007) that was especially developed to simulate storm (hurricane) impact on a sandy coast. The model includes an elegant avalanching algorithm to simulate the sediment supply from the dunes to the beach.

The emphasis in this thesis is on:

1. Studying the interaction of dune face and swash zone;
2. Examining to what extent near dune hydrodynamics can be associated with long waves;
3. Obtaining more insight in near dune sediment suspensions and how these should be modeled;
4. Integrating new insights in the model and validate it for several situations and conditions.

1.4 THESIS OUTLINE

The research presented in this thesis is focussed on a better understanding of the processes involved in dune erosion. In addition, obtained new insights are coupled in a process-based dune erosion model that takes into account the longshore direction.

First a large-scale flume experiment is discussed that studies the effect of the wave period on dune erosion (Chapter 2). The main focus is on the analysis of detailed measurements of water pressure, flow velocities and sediment concentrations in the inner surf zone where eroded sand from the dunes creates a new foreshore.

In the subsequent three chapters data from the experiment are analyzed to obtain a better understanding of inner surf and swash zone physics that are hypothesized to drive dune erosion. The interaction of dune face and swash zone is studied (Chapter 3) and to this end a stereo video algorithm is proposed that can produce three-dimensional reconstructions of the dune face. The available stereo reconstructions and profile measurements are utilized to examine the episodic slumping of the dune face under wave impacts.

Inner surf and swash zone hydrodynamics are simulated with a surf beat model for storm conditions in the laboratory and the field (Chapter 4). The model simulates the generation and interaction of long waves under wave group forcing and is applied to examine to what extent near dune hydrodynamics can be associated with these long waves.

Measurements of near dune sediment suspensions are analyzed in more detail to develop an equilibrium sediment concentration formulation, which takes into account the effect of wave breaking induced turbulence (Chapter 5). It is hypothesized that

the turbulence energy varies over the wave cycle and the mean sediment concentration is associated with the bore averaged turbulence intensity. The effect of wave varying turbulence over the wave cycle on sediment concentrations is examined with a 1DV suspension model.

Dune erosion and evolution of the foreshore are modeled with the 2DH morphodynamic model XBeach (Chapter 6). Near dune hydrodynamics are computed with the surf beat model and wave breaking induced turbulence is taken into account to simulate sediment suspensions. The interaction of the dune face and the swash zone is modeled with the original avalanching algorithm. The model is optimized to obtain default parameter settings that are applied to simulate:

1. The flume experiment described in Chapter 2 including the effect of the wave period on dune erosion, the effect of the wave spectral shape on dune erosion and the collapse of a small dune in front of a larger dune;
2. The effect of a revetment on dune erosion;
3. Profile evolution during calm and moderate wave conditions;
4. Dune erosion during the 1953 storm surge at the Delfland coast in The Netherlands.

In addition, the effect of respectively long and short waves on dune erosion is investigated and the interaction of dune face and swash zone is further studied by comparing model results for varying avalanching settings.

Finally, simulations including the longshore direction are presented. First, a 2DH simulation with an alongshore uniform bathymetry and topography is compared with 1D model results for a constant and varying storm surge level respectively. Next, three hypothetical cases are studied viz.:

1. An alongshore uniform bathymetry with varying dune height;
2. An alongshore constant dune height and varying bathymetry that contains bars intersected by rips and beach cusps;
3. The transition of a (non-erodible) dike with a sandy dune system.

Chapter 2

LARGE SCALE DUNE EROSION TESTS^I

2.1 INTRODUCTION

In The Netherlands, dune erosion during normative storm conditions is assessed every five years with a guideline based on an empirical dune erosion model that was developed from large scale flume experiments (Vellinga, 1986). Recent analyses of the wave climate along the Dutch coast have revealed that the peak wave period during normative storm conditions is expected to be considerably higher than anticipated in the past (De Ronde et al., 1995; Roskam and Hoekema, 1996). These higher wave periods are not covered by the extensive series of previous flume experiments whereas the results of small-scale physical model tests (Coeveld et al., 2005) showed that a longer wave period could lead to more dune erosion.

The objective of the experiment described in this chapter is to gather quantitative information on the effects of the wave period on dune erosion, as input for new guidelines by the Dutch legislator for the assessment of dune safety. In addition, the aim is to obtain more insight in the cross-shore physical processes important for dune erosion in order to further improve and develop process-based dune erosion models that can be applied to make a more realistic assessment of dune erosion in complex coastal systems.

Six large-scale dune erosion tests were performed in the Deltaflume from November 2005 till March 2006 by simulating wave attack on a coastal cross-shore sandy profile that is considered characteristic for the situation at the Dutch coast. Tests with equal duration, water depth and wave height, but with different wave periods were carried

^I This chapter is based on two articles published in Coastal Engineering:

- Van Gent, M.R.A., Van Thiel de Vries, J.S.M., Coeveld, E.M., De Vroeg, J.H. and Van de Graaff, J., 2008. Large-scale dune erosion tests to study the influence of wave periods. Coastal Engineering, 55(12): 1041-1051.
- Van Thiel de Vries, J.S.M., Van Gent, M.R.A., Walstra, D.J.R. and Reniers, A.J.H.M., 2008. Analysis of dune erosion processes in large-scale flume experiments. Coastal Engineering, 55(12): 1028-1040.

out. Also two tests were conducted in which the spectral wave shape was varied and one test was performed with an initial profile that deviated from the reference profile.

During the experiment the wave transformation over the profile in the flume was measured and various bed profile measurements were obtained during the test period. A mobile frame was deployed in the inner surf area to obtain more insight in near dune hydrodynamics and sediment transports. Stereo video cameras were installed to study inner surf wave transformation and the interaction of dune face and swash zone.

Section 2.2 describes the physical model set-up and deployed instruments. In Section 2.3 the test results are discussed in terms of profile evolution and erosion volumes whereas Section 2.4 analyses the detailed measurements including wave transformation, near dune hydrodynamics, sediment concentrations and sediment transports. The effect of the wave period on dune erosion is studied in more detail in Section 2.5 and the chapter ends with conclusions (Section 2.6). The stereo video data is further discussed in Chapter 3 to study the interaction of dune face and swash zone.

2.2 PHYSICAL MODEL DESCRIPTION AND INSTRUMENT DEPLOYMENT

The physical model was set up in the Deltaflume of Delft Hydraulics and has an effective length, width and height of 225 m, 5 m and 7 m respectively. The wave generator is equipped with Active Reflection Compensation (ARC) to prevent reflected waves to re-reflect into the flume, and 2nd order wave steering including the generation of bound long waves and super harmonics. Irregular waves with a wave height up to 1.9 m can be generated depending on the water depth and the wave period.

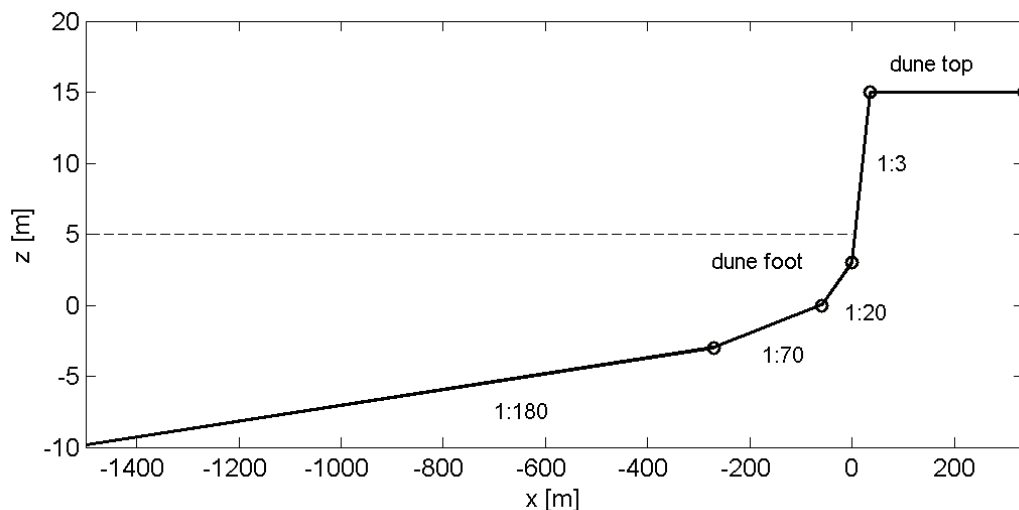


Figure 2.1 Prototype reference bed profile (solid line). The water level $z = 0$ m corresponds to mean sea level and the still water level $z = 5$ m (dashed line) corresponds to the extreme high surge level that is applied during the experiment.

The effect of the wave period on dune erosion was examined for a prototype characteristic cross-shore bed profile as given in Figure 2.1 hereafter named reference pro-

file. This strongly schematized profile contains one dune. No banks and no troughs are present in the foreshore. To translate the prototype situation to a physical model that fits in the flume, use was made of the scaling relations derived by Vellinga (1986).

2.2.1 Set up of physical model

Interpretation of results of small scale and large scale physical model tests in relation to prototype situations requires scale relations. Considering dune erosion during extreme storm surge conditions, deriving these scale relations is not straightforward. Theoretical elaborations are insufficient to obtain a consistent set of scale relations, because the applied theories have a limited validity (*e.g.* linear wave theory is less reliable within the surf zone and important physical processes in dune erosion are not fully understood). In the past, the results of an extensive series of small scale and large scale physical model tests were analyzed (Vellinga, 1986), which resulted in a set of scale relations for dune erosion. Although indications exist (Delft Hydraulics, 1996) that the relations could be improved, no reliable updates of the scale relations can be made without additional experimental data. Hence, the scale relations from Vellinga (1986) were used. Following these relations the desired profile steepness factor (S_1) of the initial profile for a certain depth scale factor (n_d) and sediment fall velocity scale factor (n_w) is determined with:

$$S_1 = \frac{n_l}{n_d} = \left(\frac{n_d}{n_w^2} \right)^{0.28} \quad (2.1)$$

where n_l (-) is the horizontal length scale factor. Ideally an undistorted profile is applied in the model. However, proper modeling of n_w in relation to n_d is difficult, which often results in a steepness factor of $S_1 > 1$. In addition, the limited dimensions of the flume often require an even steeper profile, leading to a second steepness factor S_2 (a total steepness factor S_0 can be estimated from $S_0 = S_1 S_2$). Taking the steepness factor S_1 into account, the dune erosion volumes are thought to be properly simulated at a smaller scale in a wave flume. The erosion area (or volume per linear meter) scale factor (n_A) is:

$$n_A = n_l \cdot n_d = n_d^2 \cdot \left(\frac{n_d}{n_w^2} \right)^{0.28} \quad (2.2)$$

By multiplying the measured dune erosion volume (per linear meter) in the flume with n_A the prototype volume is obtained, which applies for a prototype initial profile that is a factor S_2 steeper than the reference profile (prototype).

The scale, at which the model was set up, was aimed to be as close to prototype as possible to minimize scale effects. A depth scale factor of $n_d = 6$ and a profile steepness factor of $S_0 = 2$ resulted in wave conditions that could be generated by the wave generator and to a profile that fitted in the flume (see Figure 2.2) but was a bit too steep in relation to the reference profile in Figure 2.1. At a water depth of 2.7 m ($\approx 2H_{m0}$) the foreshore was cut off with a 1:25 slope. The diameter of the applied sedi-

ment was $D_{50} = 200 \mu\text{m}$. This diameter is slightly smaller than the desired diameter, which resulted in a value of the factor S_0 that was about 3 to 4% larger.

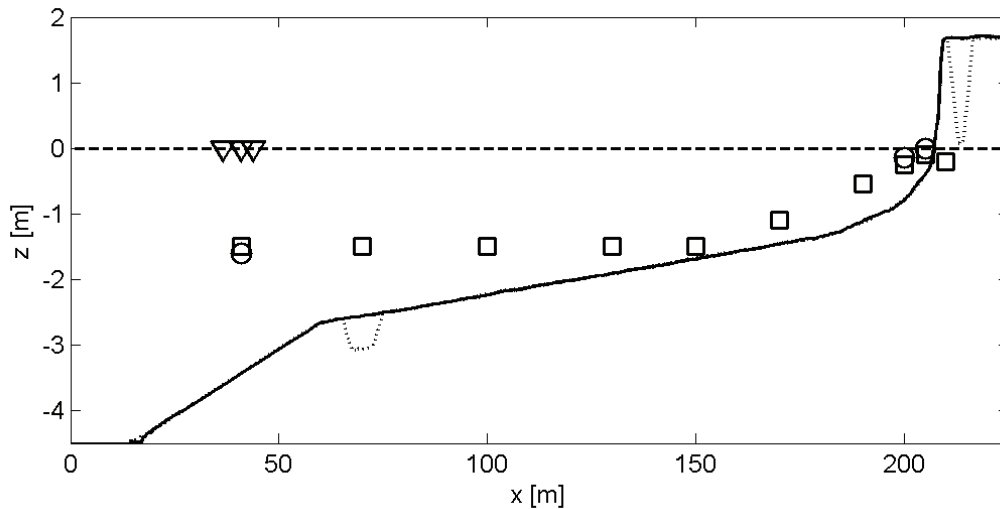


Figure 2.2 Initial profiles and deployed instruments on the flume wall during the Deltaflume experiment. The initial profile for all tests (solid line) except T04 (dotted line). The still water level is shown by the dashed line. The wave board is at the origin of the coordinate system ($x = 0 \text{ m}$); $y = 0 \text{ m}$ is at the middle of the flume and $z = 0 \text{ m}$ coincides with still water level. Devices on the flume wall consist of ten pressure sensors (squares), three electromagnetic current velocity sensors (circles) and three resistance wires (triangles).

2.2.2 Test programme

Six tests were performed in the autumn and winter period of 2005-2006. Table 2.1 shows the test programme with the hydraulic conditions at the wave board. Tests T01, T02 and T03 were set up to provide insight into the effects of the wave period on dune erosion and the wave period was the only parameter that varied in these tests. The wave conditions in tests T01, T02 and T03 correspond to peak wave periods in a prototype situation of $T_p = 12 \text{ s}$, $T_p = 15 \text{ s}$ and $T_p = 18 \text{ s}$ respectively, and to a prototype wave height of $H_{m0} = 9 \text{ m}$. The still water level was fixed at 4.5 m in the flume near the wave board (for all tests) and corresponds to an extremely high storm surge level for the Dutch situation. Tests T01 and T03 were performed twice, which provides insight into the reproducibility of the tests. In test T04 a different initial cross-shore profile was used with wave and surge conditions as in test T03 (see Figure 2.2). In tests T01 to T04 a Pierson-Moskowitz wave spectrum was applied whereas tests DP01 and DP02 were carried out with double-peaked wave spectra (see Figure 2.3) to gain insight into an appropriate measure to characterize the influence of the wave spectral shape on dune erosion.

Table 2.1 Test programme with hydraulic conditions at the wave board.

Test	Interval	H_{m0} [m]	T_p [s]	$T_{m-1,0}$ [s]	SWL [m]	S_p (-)	$S_{m-1,0}$ (-)	Spectrum
T01	A-E	1.50	4.90	4.45	4.50	0.040	0.049	Pierson-Moskowitz
	F	1.50	4.90	4.45	4.50			Pierson-Moskowitz
	G	1.50	7.35	6.68	4.50			Pierson-Moskowitz
	H	0.50	7.35	6.68	4.50			Pierson-Moskowitz
	I	1.40	5.00	4.54	4.50			Pierson-Moskowitz
T02	A-E	1.50	6.12	5.56	4.50	0.026	0.031	Pierson-Moskowitz
T03	A-E	1.50	7.35	6.68	4.50	0.018	0.022	Pierson-Moskowitz
	F	0.80	7.35	6.68	4.50			Pierson-Moskowitz
T04	A-E	1.50	7.35	6.68	4.50	0.018	0.022	Pierson-Moskowitz
DP01	A-E	1.50	6.12	3.91	4.50	0.026	0.063	Double-peaked
	F	0.50	7.35	6.68	4.50			Pierson-Moskowitz
DP02	C-E	1.50	7.35	5.61	4.50	0.018	0.031	Double-peaked

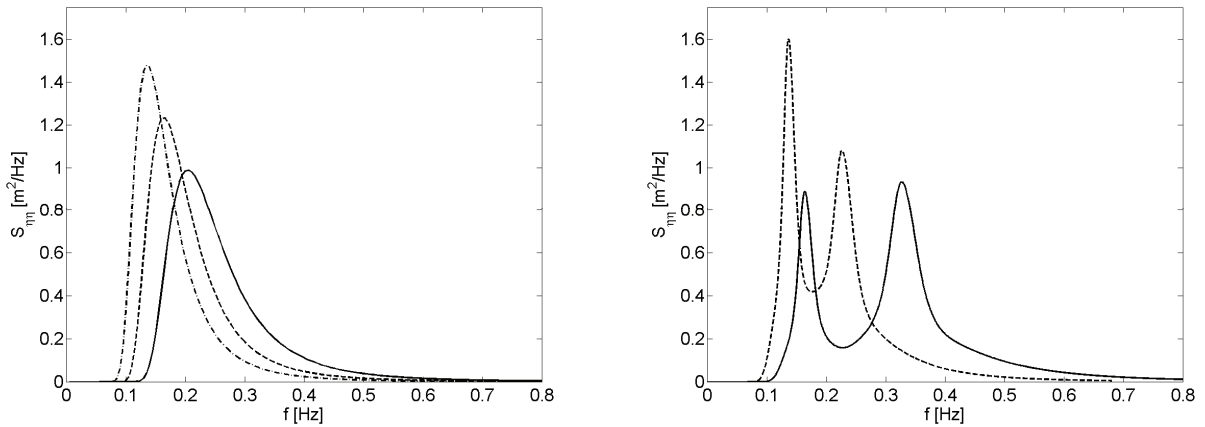


Figure 2.3 Left panel: Applied Pierson-Moskowitz wave variance spectra during test T01 (solid line), T02 (dashed line), T03 (dashed-dotted line) and T04 (dashed-dotted line). Right panel: Applied double-peaked variance spectra during test DP01 (solid line) and DP02 (dashed line).

The total duration of each test was at least 6 hours. With a time scale factor of $n_t = \sqrt[3]{n_d} = 2.4$ a test duration of 6 hours corresponds with a prototype storm duration of almost 15 hours, which was considered sufficiently long to study dune erosion during extreme storm events. For example, for the Dutch practice of verifying the safety level of the dunes a normative storm event is characterized by a prototype storm duration of 5 hours with the water level fixed at the maximum storm surge level. The tests

were temporarily interrupted to carry out bed profile measurements at the following fixed time intervals:

- A. 0 till 6 minutes or 0 till 0.1 hours;
- B. 6 till 18 minutes or 0.1 till 0.3 hours;
- C. 18 till 60 minutes or 0.3 till 1.0 hours;
- D. 60 till 122 minutes or 1.0 till 2.04 hours;
- E. 122 till 360 minutes or 2.04 till 6.0 hours.

The time intervals in the beginning of a test are the shortest, because initially erosion rates are the highest. Similar time intervals were used in earlier research; see e.g. Delft Hydraulics (1984).

Besides the regular intervals A-E, some of the tests have additional intervals (not specifically discussed in this thesis) in which the following was examined:

- *The effect of the wave period on dune erosion;* After completion of the repetition of test T01 the wave conditions of test T03 were generated without repair of the post test dune erosion profile.
- *Equilibrium swash;* Wave conditions were adapted to look at evolution of the beach under accretive swash conditions.
- *Bar evolution;* A bar developed during the tests. Wave conditions were adapted to make detailed measurements of pressure, flow and sediment concentrations over a shoreward moving sand bar.
- *Sheet flow sediment transports* under non-breaking waves.

Finally, during test T04 a sand pit of about 1 m deep was made at $x = 70$ m from the wave board, outside the active dune erosion area (Figure 2.2). The evolution of this sand pit was measured.

2.2.3 Instrument deployment

Bed profile measurements

Bed profile measurements were carried out with a so-called mechanical (amphibious) bed profile follower. The profile follower was equipped with a wheel with a diameter of 0.1 m and a width of 0.05 m, see Figure 2.4. The measurements were carried out before and after each test and between test intervals in three cross-shore transects; one along the longitudinal flume axis and the other two at 1.25 m on both sides of the flume axis.

The figures of bed profile measurements presented in this thesis concern the average of the three cross-shore transects. As a result information about features in cross flume direction, as bed ripples, are lost. Also after the tests the bed was observed to be curved in cross-flume direction between $x = 60$ m and $x = 200$ m from the wave board (Delft Hydraulics, 2006). By simply averaging of the profiles this curvature is

probably only partly taken into account, which may result in erroneous estimated sedimentation or erosion patterns within the cross-shore range of curvatures.



Figure 2.4 Bed profile follower

Instruments deployed on flume wall

Ten pressure sensors (PS) were spaced along the flume wall to measure wave transformation over the foreshore (Figure 2.2 and Table 2.2). A collocated pressure sensor and electromagnetic current velocity sensor (EMF) and three vertical resistance wires (WHM) were installed centered around $x = 41$ m to distinguish between incoming and shoreline reflected waves. Two electromagnetic current velocity sensors were deployed at $x = 200$ m and $x = 205$ m to measure near shore hydrodynamics. All devices on the flume wall were synchronized and sampled with 20 or 25 Hz depending on the specific test. At the beginning of a test the output voltages of the pressure sensors and electromagnetic current velocity sensors were set to zero in still water to obtain information about wave setup and time averaged flow.

Table 2.2 Vertical position in relation to still water level for instruments installed on the flume wall.

	PS01	PS02	PS03	PS04	PS05	PS06	PS07	PS08	PS09	PS10	EMF01	EMF02	EMF03
x [m]	41	70	100	130	150	170	190	200	205	210	41	200	205
z [m]	-1.50	-1.50	-1.10	-1.10	-1.10	-1.10	-0.55	-0.35	-0.20	-0.25	-1.60	-0.15	0.00

Instruments deployed on mobile frame

A frame was fixed to a mobile carriage to measure water pressure and the vertical structure of the flow and sediment concentrations at several cross-shore positions in the flume. Vertical positioning of the mobile frame was realized by telescoping steel pipes controlled by a winch (Figure 2.5). The weight of the frame was guided to the sand bed by a fork shaped steel construction and an instrument pipe was placed between the steel fork legs. All mobile frame devices were deployed on the instrument pipe, which could move vertically independent from the rest of the construction using a second winch. The detailed vertical positioning of the instruments was known in relation to the local bed by lowering the instrument pipe till a small steel plate rested on the bed. If this plate stood on the bed the instrument pipe winch was tightened

again to prevent settling and to keep device elevations constant with respect to $z = 0$ m. The vertical positioning system was not adjusted to bed level changes that are presumed to be minimal within the period of a mobile frame measurement.

Table 2.3 Vertical position in relation to local bed of instruments installed on mobile frame.

z [m]	ST	EMF	OBS	UHCM	ASTM	PS
0.04	ST01					
0.06	ST02	EMF07	OBS02			
0.08	ST03					
0.11	ST04	EMF06	OBS01			
0.14	ST05					
0.19	ST06	EMF05	OBS04	UHCM	ASTM	PS11
0.29	ST07					
0.44	ST08	EMF04	OBS03			
0.64	ST09	EMF10				
0.74		EMF11				
0.94	ST10	EMF09				
1.07		EMF08				

The mobile frame was deployed during tests T01, T03, T04, DP01, DP02 and the repetition of test T01 and T03. Measurements have a typical length of 10 to 20 minutes after which the frame was positioned at another cross-shore location. Wave properties were measured with a pressure sensor and the vertical structure of the flow was obtained with eight electromagnetic current velocity sensors (EMF's) (Table 2.3). The pressure sensor and four EMF's positioned closest to the bed were synchronized with devices on the flume wall and sampled with 20 Hz or 25 Hz depending on the specific test. The upper four EMF's had a 2 Hz sample rate and are only used to estimate the time averaged flow.

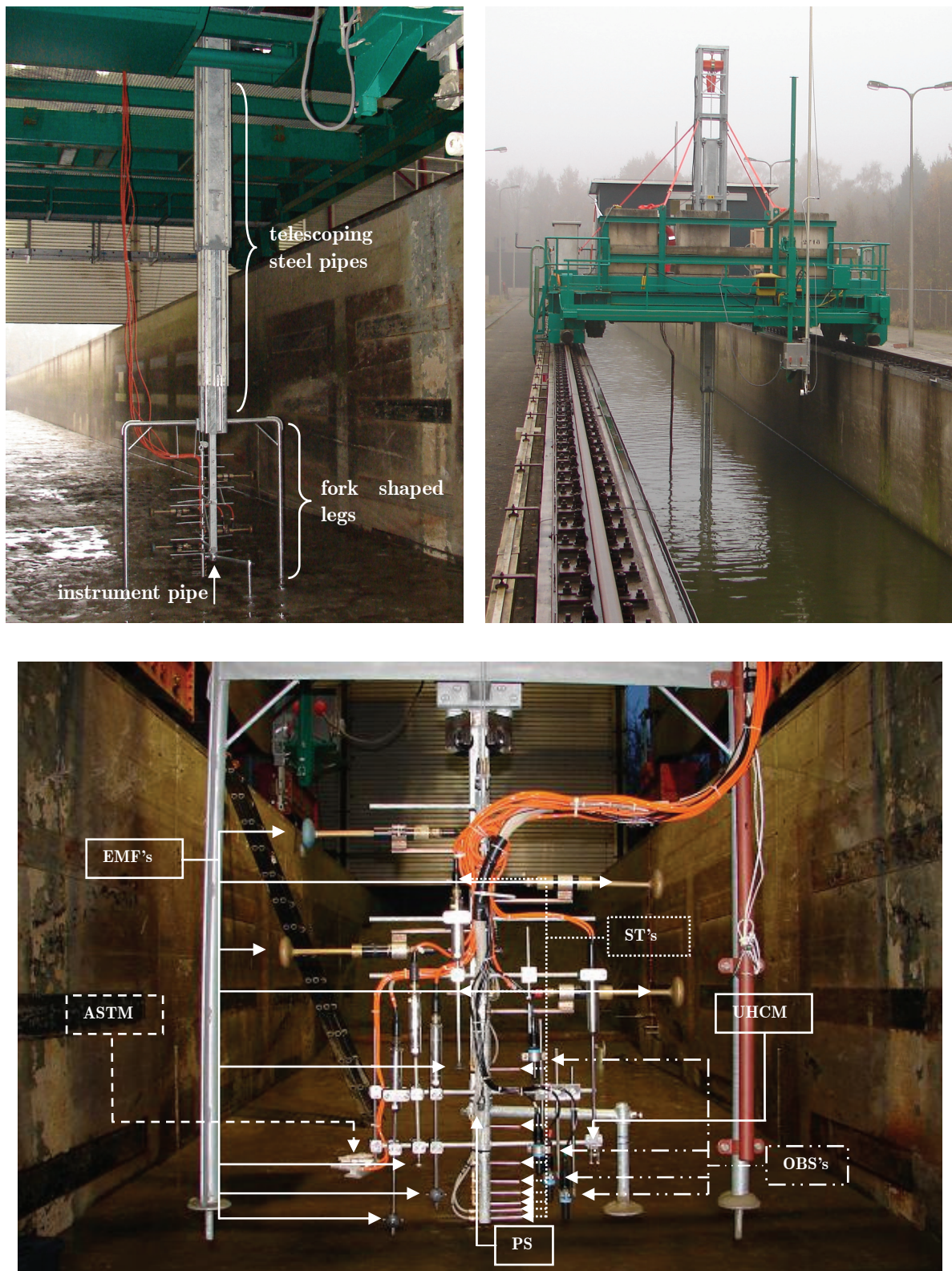


Figure 2.5 Overview mobile frame. Upper left image: The mobile frame in an empty flume. Upper right image: Shallow water frame in action position. Lower image: Close-up of the devices installed on the instrument pipe.

Time averaged sediment concentrations were measured with ten suction tubes (ST's) vertically spaced along the instrument pipe and directed normal to the plane of orbital motions (Bosman et al., 1987). Instantaneous sediment concentrations were measured with four optical backscatter sensors (OBS's), an acoustic sediment transport meter (ASTM) and an ultrasonic high concentration meter (UHCM) (Figure 2.5 and Table 2.3). The OBS's (transmitting an infrared beam) and UHCM (transmitting a 5 MHz signal) were synchronized with devices on the flume wall and had a 20 Hz sample frequency. The ASTM transmits a 4.4 MHz signal (in order to minimize grain size dependency) and samples with 2 Hz. The instantaneous sediment concentration devices were installed at the same vertical elevation from the bed as the EMF's as much as possible (Table 2.3). Instrument configuration of the mobile frame during test T01, T03, DP01 and T04 deviated from that in Table 2.3. More information about instrument configuration during these tests is found in Delft Hydraulics (2006).

Stereo cameras

Two pairs of synchronized video cameras were deployed to obtain stereo video data with the objective of three-dimensional reconstruction of the dune face, inner surf and swash zone surface. Data was collected during test T04 and DP01 and the repetition of tests T01 and T03. Images were collected from video streams with a sample frequency of 2 Hz for tests T01 and T03 and 4 Hz during tests DP01 and T04. The cameras were synchronized using an 11 volt trigger signal and synchronization with in-situ measurements was realized with a small led light visible in camera C2 that illuminated at the start of the in-situ measurements. Collected images were compressed to jpeg-format.

A first camera pair (C1 and C2) was fixed to the roof of the flume's enclosure approximately above the flume centre line (Figure 2.6). Both cameras were pointed in the direction of wave propagation with the aim to resolve bathymetries in an area covering about 12 m in along flume direction and 6 m in cross flume direction. The other camera pair (C3 and C4) was fixed on a crane positioned at the end of the flume (see Figure 2.6) and are respectively 6.7 m and 5.2 m off the flume centre line. The cameras are pointed against the direction of wave propagation and were deployed with the objective to measure wave transformation through the inner surf and swash zone. The area covered by cameras C3 and C4 is larger than that of cameras C1 and C2.

Camera positions and orientation are listed in Table 2.4. The coordinate system originates at the wave board ($x = 0$ m), the flume centre line ($y = 0$ m) and the top of the flume wall ($z = 0$ m). In addition to camera positions 22 Ground Control Points (GCP's) were surveyed; 17 GCP's are bolts on the flume wall and 5 additional GCP's were surveyed in a plane with different vertical elevation. Camera positions and GCP's are utilized to estimate the camera's field of view, tilt, roll and azimuth.

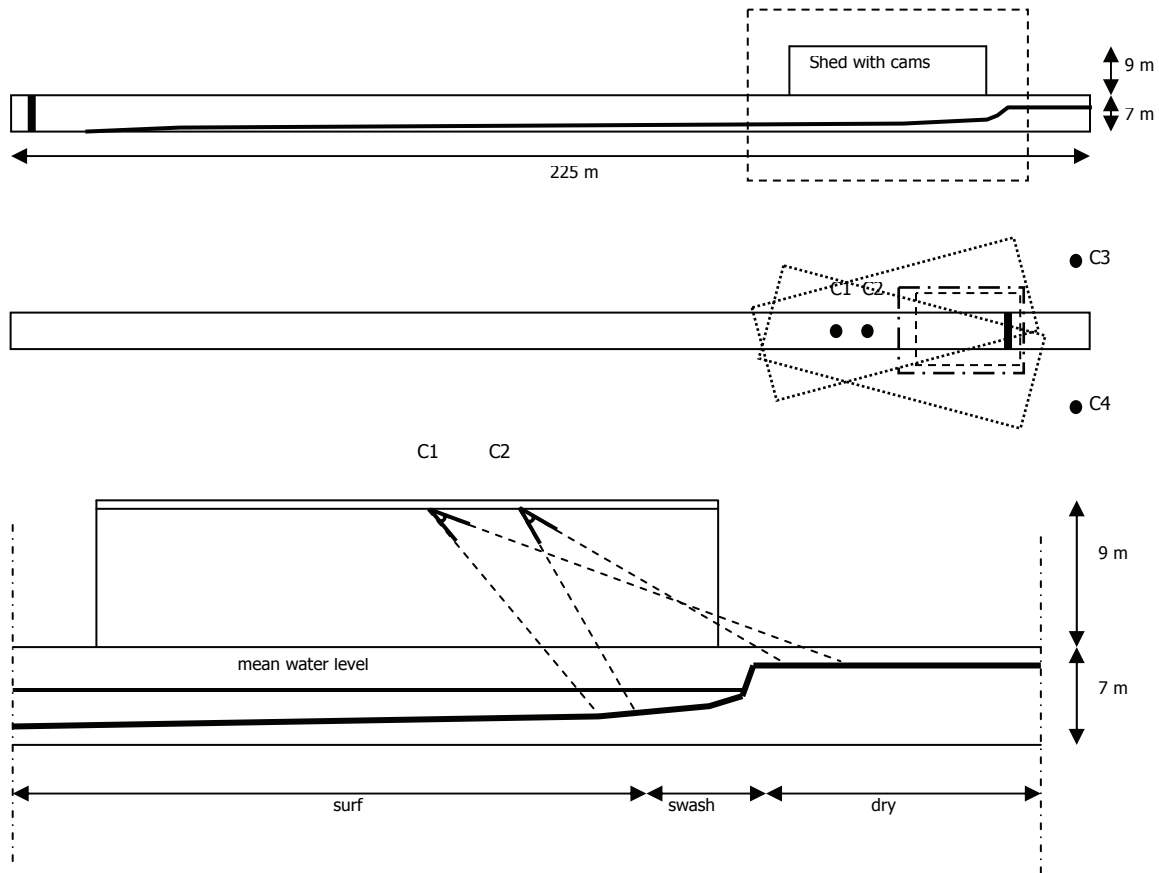


Figure 2.6 Upper panels: Deltaflume layout and camera coverage for C1 (dashed-dotted rectangle), C2 (dashed rectangle), C3 and C4 (dotted rectangles). Lower panel: Camera configuration C1 and C2.

Table 2.4 Camera locations and properties

Camera	x (m)	y (m)	z (m)	Fov ($^{\circ}$)	$Tilt$ ($^{\circ}$)	$Roll$ ($^{\circ}$)	$Azimuth$ ($^{\circ}$)
C1	190.474	0.032	8.331	0.5297	55.06	-87.62	89.49
C2	196.811	0.022	8.312	0.6679	45.98	-90.58	91.40
C3	228.225	6.690	6.500	--	--	--	--
C4	228.198	-5.151	6.459	--	--	--	--

Other measurements

Supplementary to the installed devices described before additional measurements were conducted. These measurements are not analyzed in detail in this thesis and more information on measurement results can be found in Delft Hydraulics (2006):

- *Water temperature*; The water temperature is monitored in each test with a temperature sensor at approximately 180 m from the wave board.
- *Particle size distribution*; Bed sediment samples were taken at 180, 190, 200 and 220 m from the wave board for tests T01, T02, T03 (also during the repe-

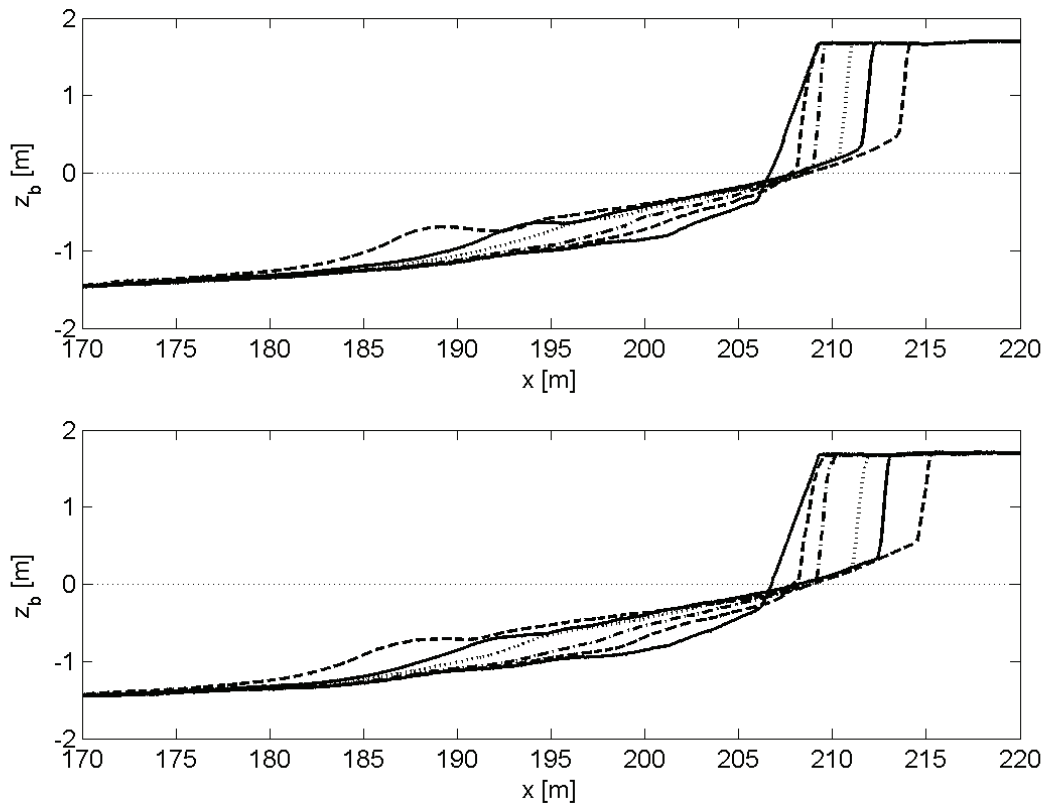
tition of test T01 and T03). The samples were obtained before a test and after 2.04 and 6.0 hours. Obtained sediment samples were utilized to determine particle size distributions by means of sieving.

- *Fall velocities*; Fall velocities were determined for the bed sediment samples that were used to determine the particle size distribution and for the sediment samples captured with the mobile frame suction tube measurements. Settling velocities are obtained using a Visual Accumulation Tube (VAT method) as described in Van Rijn (1993). During the settling measurements the water temperature was measured.

2.3 MEASURED PROFILES AND EROSION VOLUMES

2.3.1 Profiles

The bed profile only shows considerable changes in a relatively small part of the flume between about $x = 170$ m and $x = 220$ m from the wave board. The rest of the profile does hardly change during the tests. The upper two panels of Figure 2.7 show the time-development of the measured cross-shore bed profiles for tests T01 and T03. Since the time intervals increase with a test (see Section 2.2.2) it can be seen that the retreat of the dune face is clearly nonlinear in time.



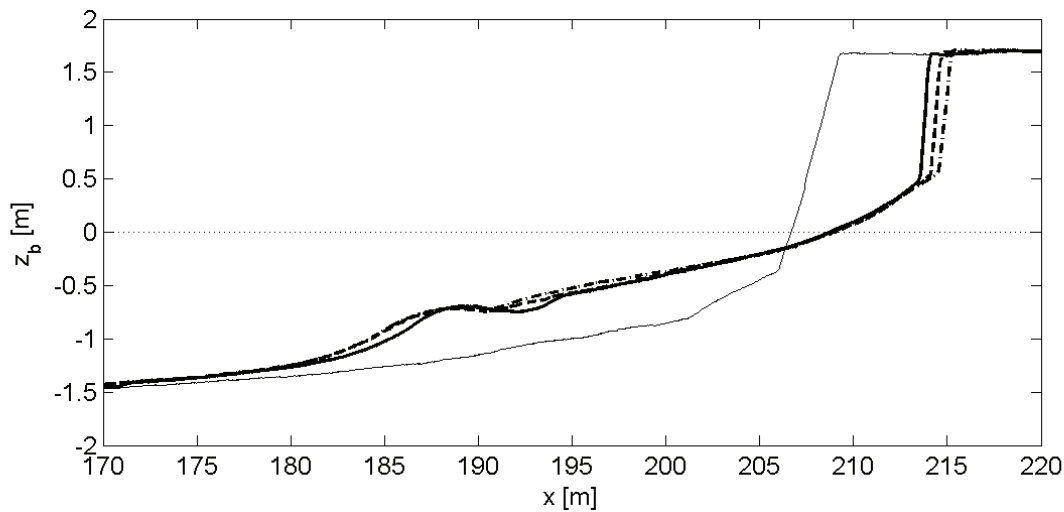


Figure 2.7 Measured near dune bed profiles in test T01 (upper panel) and test T03 (middle panel). Lower panel: Measured profiles after 6 hours for tests T01 (solid line), T02 (dashed line) and T03 (dashed-dotted line). Bed elevations (z_b) are in relation to the still water level in the flume, which is indicated by the dotted line.

Figure 2.7 lower panel compares the bed profile measurements after 6 hours for tests T01, T02 and T03. It shows that the retreat of the dune face is largest in test T03 with the longest wave period and smallest in test T01 with the shortest wave period. The differences in the shape of the bed profile for different wave periods are small, but the change in dune foot location, slope of the profile and the shape of the deposit area for increasing wave periods is consistent. The horizontal position of the dune foot moves more landward for the longest wave periods, while its vertical position hardly changes. The slope of the profiles around the still water level is a bit steeper for the short wave period than for the longer wave period. After 6 hours the seaward edge of the deposit area is located about 1.2 m farther seaward in test T03 compared to test T01.

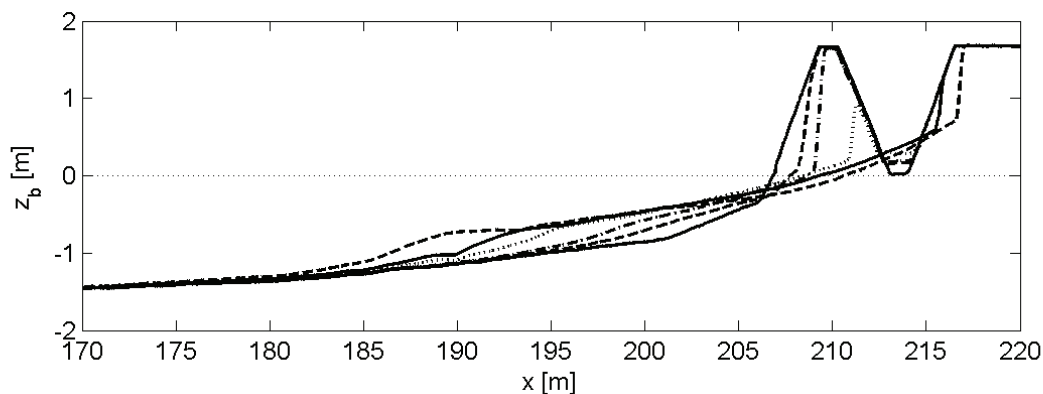


Figure 2.8 Measured profile development during test T04. Bed elevations (z_b) are in relation to the still water level in the flume, which is indicated by the dotted line.

Test T04 had a different initial profile as the other tests and contained a narrow dune in front of the remaining part of the dune profile. The measured bed profiles are shown in Figure 2.8. Since the wave conditions were the same as for test T03, the re-

sults can be compared. The profiles for test T03 and T04 are nearly identical after 6 hours of dune erosion when both profiles are horizontally shifted such that the intersection with the waterline is at the same cross-shore location. This indicates that, the resulting dune erosion profile is to some extent independent of the initial profile if the dune erosion process lasts sufficiently long as was mentioned before by Vellinga (1986).

2.3.2 Erosion volumes

The left panel in Figure 2.9 shows the development of the dune erosion volumes above the still water level (or storm surge level) in test T01, T02 and T03. The dune erosion volume after a certain period of time is based on the difference between the initial profile and the measured profile after that period of time. In the beginning of the tests the erosion rates are substantially larger than at the end of the tests. More and higher waves can attack the dune face at the start of a test, because the water depth in front of the dune face is larger. Repetition of tests T01 and T03 led to differences of less than 2.5% in the total eroded volumes after 1, 2 and 6 hours. The differences after 0.1 and 0.3 hour are only slightly larger and it is concluded that the reproducibility of the tests is good.

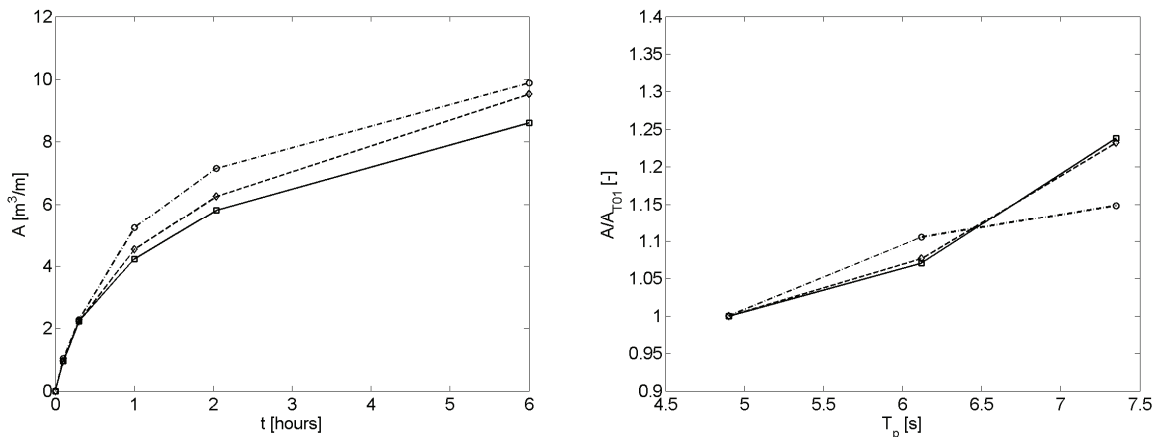


Figure 2.9 Left panel: Erosion volumes above still water level in tests T01 (solid line), T02 (dashed line) and T03 (dashed-dotted line). Right panel: Relative change in erosion volume in tests T02 and T03 compared to test T01 after 1 hour (solid line), 2.04 hours (dashed line) and 6 hours (dashed-dotted line).

The right panel in Figure 2.9 shows the relative change in dune erosion volume of tests T02 and T03 compared to test T01. The increase in volume between the shortest and the mid (25% larger) wave period varies about 7% to 11%, depending on the stage in the tests. The increase in volume between the shortest and the longest (50% larger) wave period varies from about 15% to 25%, depending on the stage in the tests. This is somewhat smaller as the 25% to 35%, observed in small-scale dune erosion tests carried out before (Coeveld et al., 2005). The difference can probably be attributed to the differences in scales (large-scale tests: $n_d = 6$, small-scale tests: $n_d = 30$ and 40). Since the large-scale tests are closer to the prototype situation than the

small-scale tests, the results of the large-scale tests are generally considered to be more reliable to obtain insight in dune erosion volumes for prototype conditions.

Because dune erosion occurs by lumps of sediment that slide down the dune face (see Chapter 3 for more details), the development of dune erosion is somewhat discontinuous in time. The effects of these discontinuities on the relative change in dune erosion volume in time are largest at the beginning of a test. Therefore, the dune erosion volumes after 1 hour, 2 hours and 6 hours test duration provide a better basis to determine the effects of the wave period on the dune erosion volume than those after 0.1 - and 0.3 hour test duration. The increase in dune erosion volume between the shortest wave period and the longest wave period (*i.e.* an increase of 50%) is found to be 25%, 24% and 15% after 1 hour, 2.04 hours and 6 hours test duration respectively.

2.4 DETAILED TEST RESULTS

For brevity this section only discusses measurements from test T01 and T03. In Section 2.5 measurements from test T01 and T03 are compared to examine the effect of the wave period on dune erosion in more detail.

2.4.1 Waves

Near dune pressure sensors were installed in shallow water close to the bed and rarely came out of the water. Time series from pressure sensors spaced along the flume wall and deployed on the mobile frame are translated into water surface elevations using linear wave theory. Wave height transformation over the foreshore of short waves and long waves is obtained from water surface variance in wave frequencies higher and lower than half the deep water peak frequency ($f_{split} = 0.5f_p$) respectively. The wave setup (η_m) is computed from the pressure sensors on the flume wall as the average water surface elevation in relation to still water level.

Wave transformation over the foreshore during test T01 is shown in Figure 2.10, upper left panel. Waves start to break immediately after generation near the wave board (also visual observation) and as a result a section with shoaling waves is not observed in the flume. In landward direction the short wave height decreases whereas the long waves gain slightly more height. Close to the dune face the long wave energy exceeds that of short waves. The spectral mean wave period $T_{m-1,0}$ increases in direction of the shore (Figure 2.10, lower left panel) from 5.4 seconds at $x = 41$ m to 26.8 seconds at $x = 205$ m consistent with a shift of wave variance towards lower frequencies. As a test progresses the foreshore develops and the total wave height near the shore at $x = 205$ m decreases from 0.52 m in interval A to 0.35 m in interval E, a reduction of more than 30%. This is caused by a decline of both the short and long wave height (Figure 2.10, upper right panel). Note that the relative importance of long wave energy near the dune face increases as a test continues (Figure 2.10, upper and lower right panel).

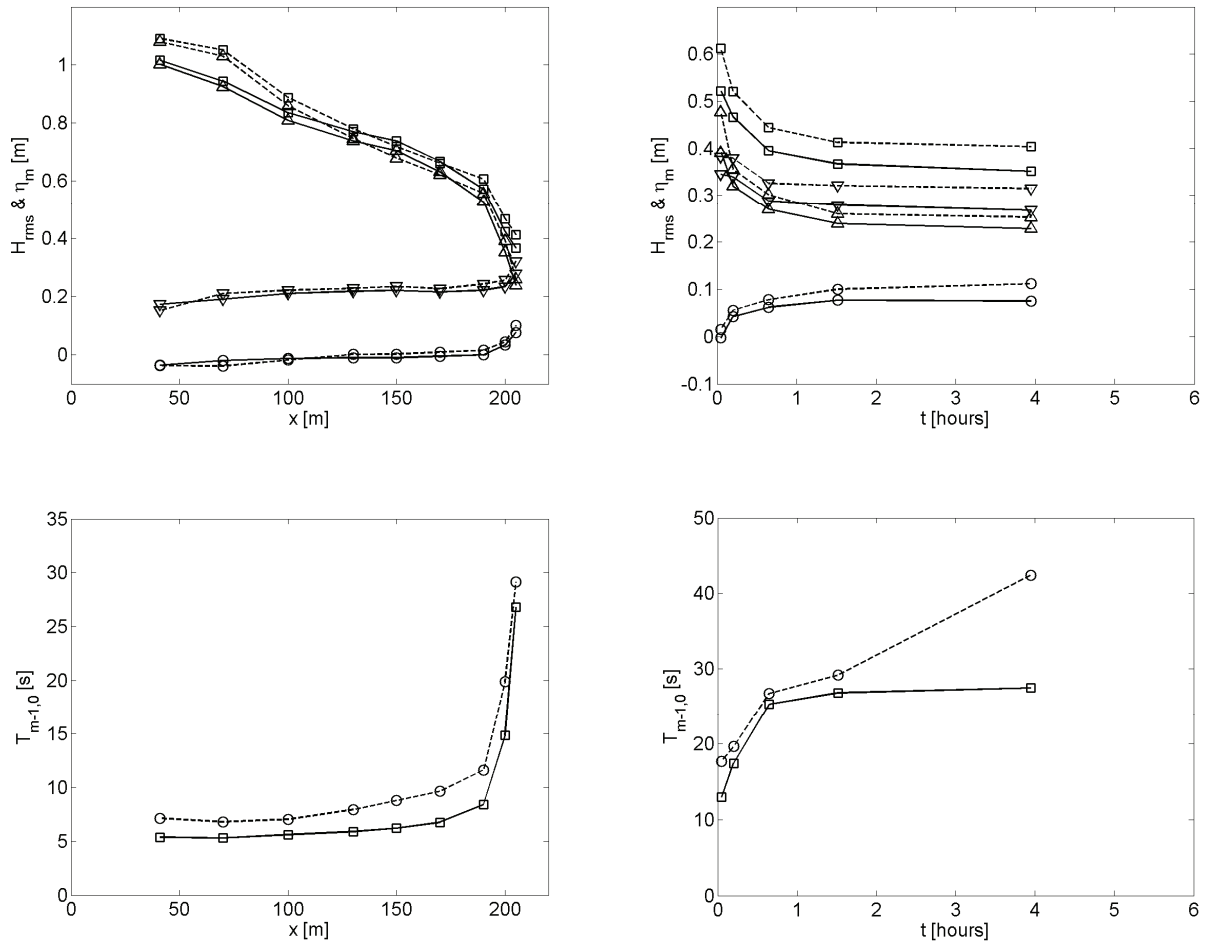


Figure 2.10 Upper left panel: Test averaged transformation of total wave height (squares), short wave height (upward pointing triangles), long wave height (downward pointing triangles) and wave setup (circles) as function of the cross-shore distance for test T01 (solid line) and test T03 (dashed line). Upper right panel: Temporal evolution of wave heights and setup for test T01 (solid line) and test T03 (dashed line) at $x = 205$ m. Lower left panel: Test averaged spectral mean wave period as function of cross-shore distance for test T01 (solid line-squares) and test T03 (dashed line-circles). Lower right panel: Temporal evolution of spectral mean wave period for test T01 (solid line-squares) and test T03 (dashed line-circles) at $x = 205$ m.

Observations during the experiment also revealed that waves reflect near the shoreline. This is illustrated in Figure 2.11 left panel that shows the normalized correlation between horizontal flow velocity and water surface elevation time series for the mobile frame measurements during test T01. Considering progressive waves a correlation close to one is expected whereas for a standing wave pattern the correlation should be close to zero. It is shown that in the near dune area ($x \geq 170$) the correlation between $u(t)$ and $\eta(t)$ decreases rapidly from about 0.75 at $x = 170$ m to 0.15 at $x = 205$ m. A partly standing wave pattern is present in the near dune area.

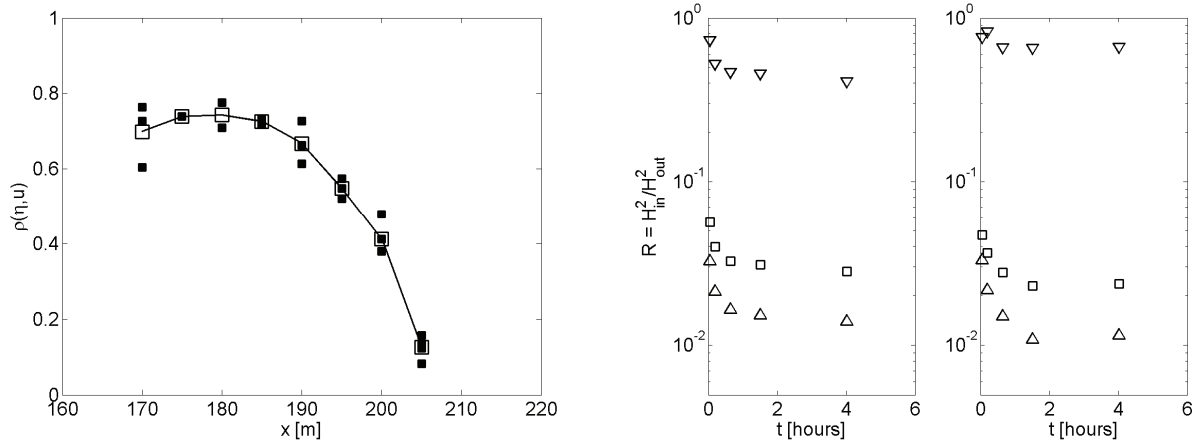


Figure 2.11 Left panel: Correlation ρ between water surface elevation $\eta(t)$ and flow velocity $u(t)$ as function of cross-shore position. Right panel: Wave energy reflection coefficients for all waves (squares), short waves (upward pointing triangles) and long waves (downward pointing triangles) at $x = 41$ m during test T01 (left) and T03 (right).

In order to further examine this partly standing wave pattern the collocated pressure and current velocity sensor at $x = 41$ m are used to decompose the measured water surface elevations in incoming and shoreline reflected short wave heights and long wave heights. A relation presented by Guza et al. (1984) is used for this purpose:

$$\eta_{in} = \frac{\eta c_{out} + Q}{c_{in} + c_{out}} \quad \text{and} \quad \eta_{out} = \frac{\eta c_{out} - Q}{c_{in} + c_{out}} \quad (2.3)$$

where η_{in} and η_{out} are the water surface elevations associated with respectively the incoming and shoreline reflected waves. $Q = uh$ in which u is the depth averaged flow estimated using linear wave theory and h is the water depth. In contrast with Guza the decomposition is performed in Fourier space. Also c_{in} and c_{out} , the wave celerities of the incoming and reflected waves respectively, are computed differently. It is assumed that all frequencies propagate with their free velocity except for the incoming wave frequencies smaller than f_{split} , which are considered as bound long waves that propagate with the wave group velocity c_g , associated with the $T_{m-1,0}$ wave period:

$$c_{in} = \begin{cases} c_{in,1} = \omega / k_w & , f \geq f_{split} \\ c_{in,2} = c_g & , f < f_{split} \end{cases} \quad (2.4)$$

$$c_{out} = \omega / k_w$$

where $\omega = 2\pi f$ and f is the wave frequency. It was found that for the sensor at $x = 41$ m $c_g \approx \sqrt{gh}$.

Short wave reflections are found to be small ($E_{hf,out}/E_{hf,in} < 3\%$) and decrease with progress of a test (Figure 2.11, Right panel). Reflected long wave energy is substantially larger (initially $E_{lf,out}/E_{lf,in} = 75\%$) and decreases to 40% in interval E. Considering all waves, reflected wave energy is less than 5% at $x = 41$ m.

2.4.2 Flow

Mobile frame flow velocity measurements were obtained in the near shore area over the developing foreshore in order to obtain more insight in the time and depth averaged return flow, the time averaged near-bed flow and the importance of short versus long wave orbital motions. Depending on the mobile frame location velocity sensors could be temporally above the water surface. Since electromagnetic current velocity sensors above the water surface drift to a random value, only time series from flow sensors placed below the wave trough are analyzed. The wave trough is defined as $\eta_{tr} = \langle \eta_{min} \rangle$, where η_{min} is the minimum water surface elevation in a zero crossing wave and $\langle \rangle$ means taking a time average. Flow velocity time series obtained below the wave trough may contain spikes due to turbulence and air inclusion, especially in areas with intense wave breaking. Spikes with amplitudes larger than 0.25 m/s and duration smaller than 1.0 s are removed and replaced by linearly interpolated values. In order to measure time averaged flows, flow velocity sensors were calibrated in still water. During test T03 this calibration took place in shallow water, which is not preferable since, due to the proximity of the bottom and water surface, the calibration might result in an artificial offset of the flow devices. It was found that EMF06 had such an offset. As a consequence time averaged flow velocities from EMF06 during test T03 are not included in the analysis.

Time averaged flow velocities, which are of interest to the morphological response of a sandy dune system are considered to be both the near bottom and depth averaged flow velocity. The near bottom flow is related to the shear stress exerted on the bed and in addition to bed load and sediment entrainment. The depth averaged velocity (below the wave trough) is usually related to the advection of suspended sediment in 2DH models. The time averaged near-bed flow velocity is obtained from time series of the flow sensor closest to (approximately 6 cm above) the bed. The depth averaged flow is obtained by vertical integration of measured mean flow velocities below the wave trough (Reniers et al., 2004a):

$$U_m = \int_{z=-h_0}^{z=\eta_{tr}} u_m(z) dz \approx \frac{1}{z_N} \sum_{j=1}^{j=N} (u_{m,j} + u_{m,j-1})(z_j - z_{j-1})/2 \quad (2.5)$$

where U_m is the time and depth averaged flow velocity, h_0 is the still water depth, z_N is the vertical position above the bed of the first sensor below the wave trough, $u_{m,j}$ is the measured time averaged flow velocity from a sensor located at vertical position z_j and $u_{m,j-1}$ and z_{j-1} , correspond to the first flow sensor installed below z_j . At the bed the flow velocity is assumed to be zero.

The near-bed flow velocity exceeds the depth averaged flow velocity within the cross-shore range of mobile frame measurements (Figure 2.12, upper left panel). Both the magnitude of the near-bed and depth averaged velocity increases gradually in shoreward direction to approximately $x = 200$ m and drop drastically at $x = 205$ m. The depth averaged flow velocity at $x = 205$ m should be interpreted with care since the number of flow velocity sensors below the wave trough at this location is usually just one and flow velocity gradients over the vertical might be large. As a test progresses the near-bed and depth averaged flow velocity evolves differently depending on the cross-shore location and evolution (Figure 2.12, upper right panel). Close to the dune

face at $x = 200$ m the time averaged flow velocity decreases 24% between the first and last measurement at this location whereas further seaward at $x = 190$ m the average flow increases with 61%.

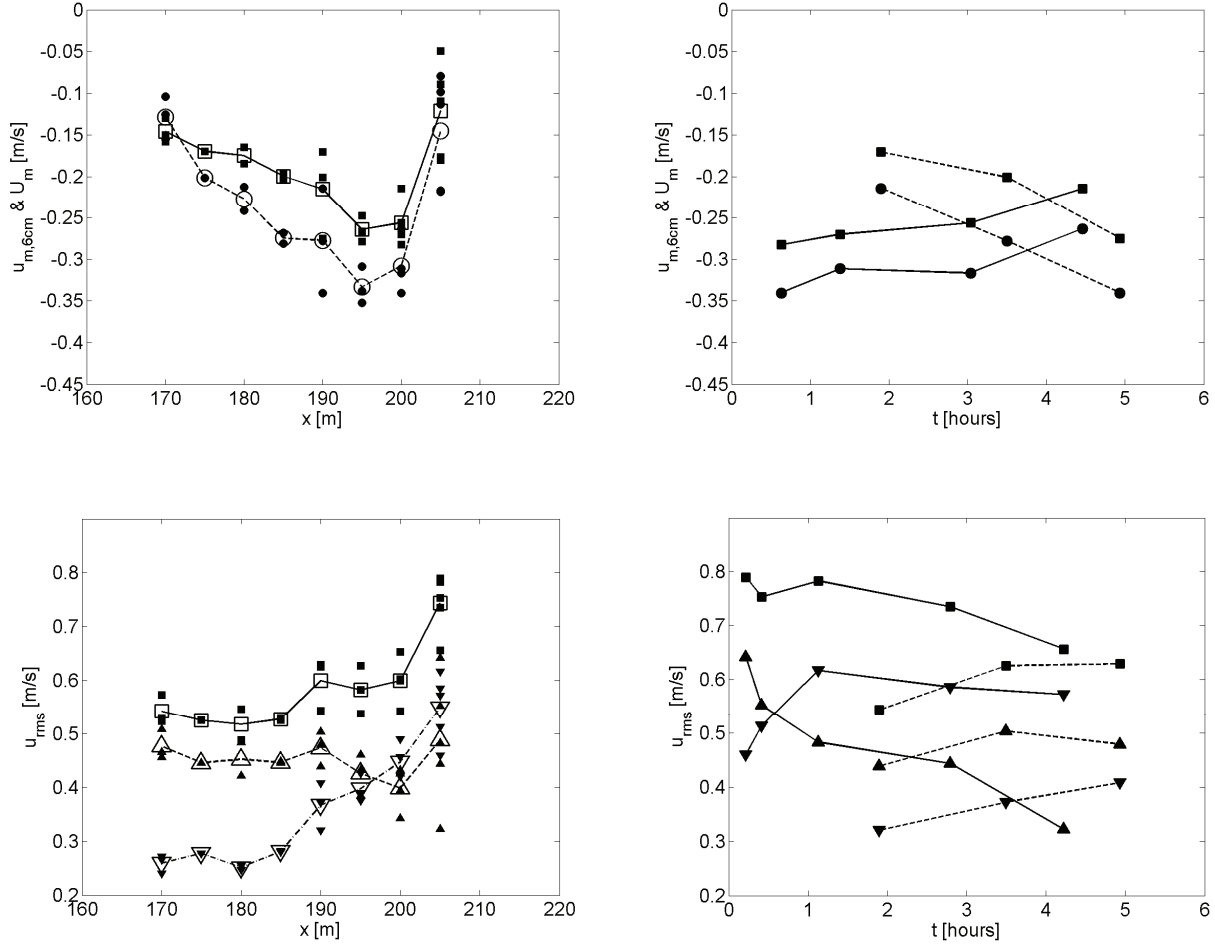


Figure 2.12 Upper left panel: Time and depth averaged flow velocities (squares) and time averaged flow velocity at 6 cm above the bed (circles) for test T01. Open markers are the average of all mobile frame measurements at a location within a test. Upper right panel: Temporal evolution of time and depth averaged flow velocity (squares) and time averaged flow velocity at 6 cm above the bed (circles) at $x = 200$ m (solid lines) and $x = 190$ m (dashed lines) for test T01. Lower left panel: Transformation of the near-bed total orbital flow velocity (squares), short wave orbital velocity (upward pointing triangles) and long wave orbital velocity (downward pointing triangles) over the cross-shore profile for test T01. Open markers are the average of all mobile frame measurements at a location within a test. Lower right panel: Temporal evolution of the near-bed total orbital velocity (squares), short wave orbital velocity (upward pointing triangles) and long wave orbital velocity (downward pointing triangles) at $x = 205$ m (solid lines) and $x = 190$ m (dashed lines) for test T01.

The presence of waves affects suspended sediment concentrations since near-bed orbital motions stir up sediment. In addition phase lags between the wave orbital flow and sediment suspension may directly contribute to the sediment transport. The orbital flow velocity, u_{rms} , is computed as the standard deviation of the near-bed velocity time series obtained at 6 cm above the bed. Similar to the wave height, the orbital

velocity is separated in a short wave and long wave related part. The orbital velocity increases in shoreward direction from about 0.55 m/s at $x = 170$ m to about 0.75 m/s at $x = 205$ m (Figure 2.12, lower left panel). This increase can be attributed to a considerable increase in the long wave orbital velocity (from 0.26 m/s at $x = 170$ m to 0.55 m/s at $x = 205$ m) whereas the short wave orbital velocity remains quite constant with decreasing water depth (0.48 m/s at $x = 170$ m and 0.49 m/s at $x = 205$ m). Close to the shoreline at $x = 205$ m the long wave orbital velocity is of the same order of magnitude as the short wave orbital velocity.

The temporal evolution of the orbital velocity varies with the cross-shore position (Figure 2.12, lower right panel). Close to the dune face at $x = 205$ m the orbital velocity decreases 16% between the first and last measurement at this location. At the start of the test the short wave orbital velocity exceeds that of long waves whereas after one hour the opposite is observed. Further offshore at $x = 190$ m a 17% increase in the orbital velocity is observed and the short wave orbital velocity exceeds that of long waves during the whole test.

2.4.3 Sediment concentrations

Time averaged and instantaneous sediment concentrations have been measured with the mobile frame over the developing foreshore. Time averaged sediment concentrations are obtained with suction tubes and give robust results; also between the wave trough and crest where tubes are regularly above the water surface. Output voltages from the instantaneous sediment concentration devices are calibrated with suction tube measurements. Time averaged voltages from the OBS's and ASTM are correlated to time averaged sediment concentrations obtained with suction tubes at the same height through which a second order polynomial is least square fitted (the correlation coefficients for respectively OBS1, OBS2, OBS3, OBS4 and the ASTM are 0.96, 0.93, 0.90, 0.96 and 0.39). The small correlation coefficient of the ASTM is caused by the limited measurement range of this instrument (up to 10 gr/l). Data from the ASTM is not used in this thesis. A similar procedure is followed for the UHCM except that a first order polynomial is used (correlation coefficient is 0.95). More details about the calibration of the instantaneous sediment concentration devices are found in Delft Hydraulics (2006).

In the ongoing analysis only time series from the OBS's are considered. Sediment concentration time series obtained above the wave trough ($\eta_{tr} = \langle \eta_{min} \rangle$) are eliminated from the analysis since OBS's that are regularly above the water surface give unrealistic peaks in sediment concentrations not corresponding to measurements obtained with OBS's installed below the wave trough.

The near-bed time averaged sediment concentration obtained with the suction tube located closest to (4 cm above) the bed increases with decreasing water depth from a concentrations smaller than 1 gr/l at $x = 180$ m to up to more than 30 gr/l during test T01 and 50 gr/l during test T03 at $x = 205$ m (Figure 2.13, left panel). As a test progresses the sediment concentration close to the dune face ($x = 205$ m and $x = 200$ m) decreases with more than 70% between the first and last measurement at this location whereas further offshore ($x = 190$ m) the sediment concentration increases with 39% (Figure 2.13, right panel). It is found that the standard deviation of instan-

taneous sediment concentration time series is positively related to the time averaged sediment concentration (not shown).

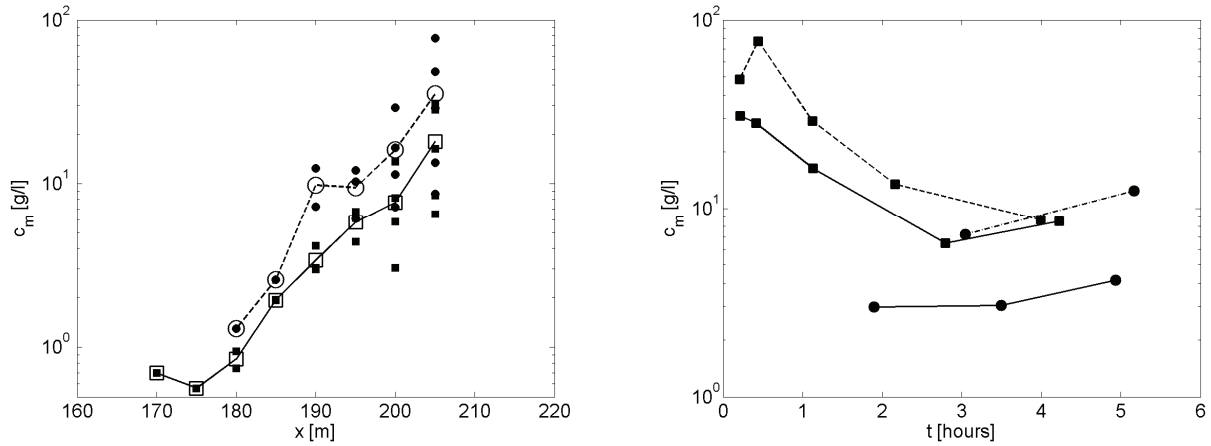


Figure 2.13 Left panel: Time averaged sediment concentration 4 cm above the bed as function of cross-shore distance for test T01 (squares) and test T03 (circles). Open markers are the average of all mobile frame measurements at a location within a test. Right panel: Temporal evolution of sediment concentration for test T01 (solid lines) and test T03 (dashed lines) at $x = 205$ m (squares) and $x = 190$ m (circles).

2.4.4 Sediment transports

In sandy coastal systems the sediment transport is commonly separated in bed load and suspended load (Fredsoe and Deigaard, 1992). Considering dune erosion the suspended load is dominant (Vellinga, 1986). Here, the total time and depth averaged sediment transport over a test interval is estimated from profile evolution whereas the time and depth integrated suspended load is computed from flow and sediment concentration measurements. The bed load cannot be estimated (accurately) from available measurements but is expected to be of minor importance.

The total sediment transports are computed from cross-shore integration of bed level changes starting at the (dry) end of the flume (225 m from the wave board) where the sediment transport is known to be zero:

$$S_x(x) = \int_{x=225}^{x=x} \frac{\partial z}{\partial t} (1-p) dx \quad (2.6)$$

where S_x is the cross-shore sediment transport, $\partial z/\partial t$ is the cross flume averaged bed level change between successive profile measurements and p is porosity. The sediment balance is artificially closed by redistributing the residual transport at the wave paddle uniformly over the sedimentation area. It is noted that a curvature in the cross flume bathymetry was observed after the tests between $x = 60$ and $x = 200$ m (Delft Hydraulics, 2006). The differences in bed level in cross flume direction can be up to 0.1 m. In the present analysis bed level changes from the three transects are simply

averaged, which might result in erroneous computed sediment transports from profile measurements.

Suspended sediment transports obtained from flow and sediment concentration measurements are computed summing three transport components. Two components represent the sediment transport below the wave trough and consist of respectively the time averaged (flow related) and instantaneous (wave related) sediment transport:

$$\begin{aligned} S_{x_1} &= \frac{1}{\rho_s} \int_{z=-h}^{z=\eta_{tr}} c_m u_m dz \\ S_{x_2} &= \frac{1}{\rho_s} \int_{z=-h}^{z=\eta_{tr}} c_f u_f dz \end{aligned} \quad (2.7)$$

where c_m and u_m are the time averaged part and c_f and u_f are the demeaned sediment concentration and flow time series. The third component is an estimation of the sediment transport above the wave trough. Especially close to the dune face, the sediment transport above the wave trough cannot be assumed to be close to zero since the measured sediment concentration is substantial up to the water surface. The sediment transport above the wave trough is estimated by the product of the depth averaged flow and the mean sediment concentration above the wave trough:

$$S_{x_3} = \frac{1}{\rho_s} U_m (h - \eta_{tr}) C_m \quad (2.8)$$

In this expression $U_m(h - \eta_{tr})$ represents the time averaged discharge between wave trough and top obtained from continuity over the vertical and C_m is the depth and time averaged sediment concentration obtained with suction tubes between wave trough and top.

Sediment transports obtained from measured profiles and mobile frame measurements are shown in Figure 2.14, upper left panel. The magnitude of the sediment transport increases towards the dune face where the sediment transport gradient must reverse (erosion). As a test continues the near dune maximum sediment transport decreases with 95% between interval A and E. The temporal transport gradient is largest near the dune face and decays in offshore direction (Figure 2.14 upper panel and lower left panel). The location of the maximum sediment transport, which is the transition of sedimentation and erosion, moves shoreward with dune face retreat. The sediment transport is dominated by the mean offshore directed flow whereas the onshore sediment transport is relatively small (Figure 2.14 lower left panel). In general the suspended sediment transport computed from flow and sediment concentration measurements exceeds the total transport obtained from the profile evolution. This can be explained if an onshore bed load transport is present; however uncertainties in the estimated total load and suspended load might be substantial and prevent any firm conclusions about magnitude and direction of the bed load transport.

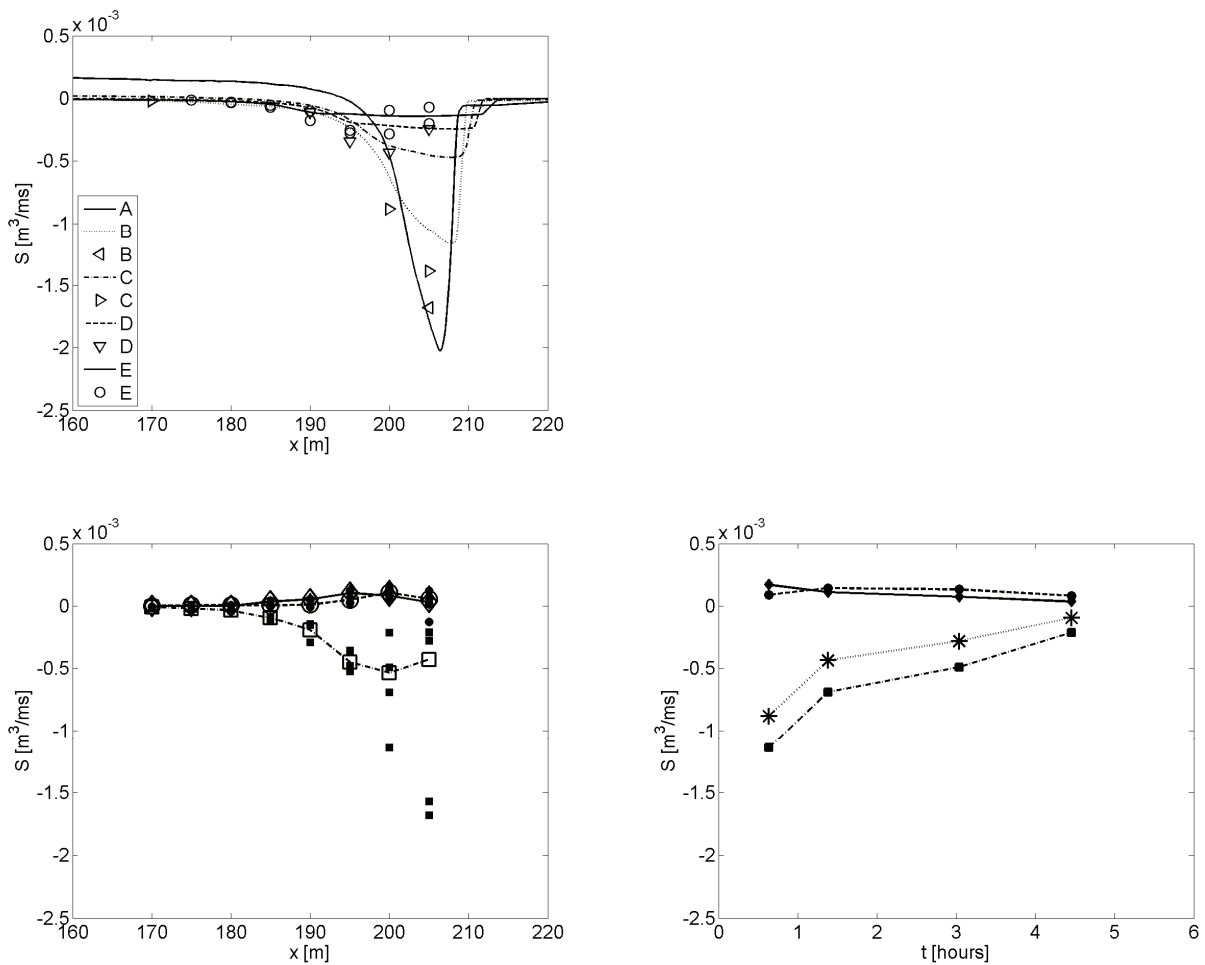


Figure 2.14 Upper panel: Sediment transports from bed level changes (lines) and mobile frame measurements (markers) at different intervals (see legend) as function of cross-shore position for test T01. Lower left panel: Suspended sediment transport obtained from mobile frame measurements split out in flow related sediment transport (dashed-dotted line-squares), wave related sediment transport (dashed line-circles) and sediment transport above the wave trough (solid line-diamonds). Open markers are the average of all mobile frame measurements at a location within a test. Lower right panel: Temporal evolution of flow related sediment transport (dashed-dotted line-squares), wave related sediment transport (dashed line-circles), sediment transport above the wave trough (solid line-diamonds) and the total sediment transport (dotted line-asterisk) at $x = 200$ m.

2.5 EFFECT OF THE WAVE PERIOD

A 50% larger wave period during test T03 results in 24% more dune erosion after two hours and 15% more erosion after six hours (see Section 2.3.2). The objective is to improve the physical understanding of these effects by examining changes in wave transformation, flow, sediment concentration and the resulting transport for conditions with a larger wave period.

Wave transformation over the foreshore changes with an increase of the wave period (Figure 2.10, upper left panel). Waves with larger wave period on average loose less energy over the first 100 m of the flume. Between $x = 120$ m and $x = 160$ m the wave heights is smaller in comparison to test T01 whereas close to the dune face ($x > 190$ m) the wave height is larger again. Since the near shore wave height during test T03 exceeds that of test T01 during the whole test with 10 to 15% (Figure 2.10, upper right panel) it follows that for a larger wave period more energy reaches the dune face. The ratio between short wave and long wave variance remains the same with increasing wave period.

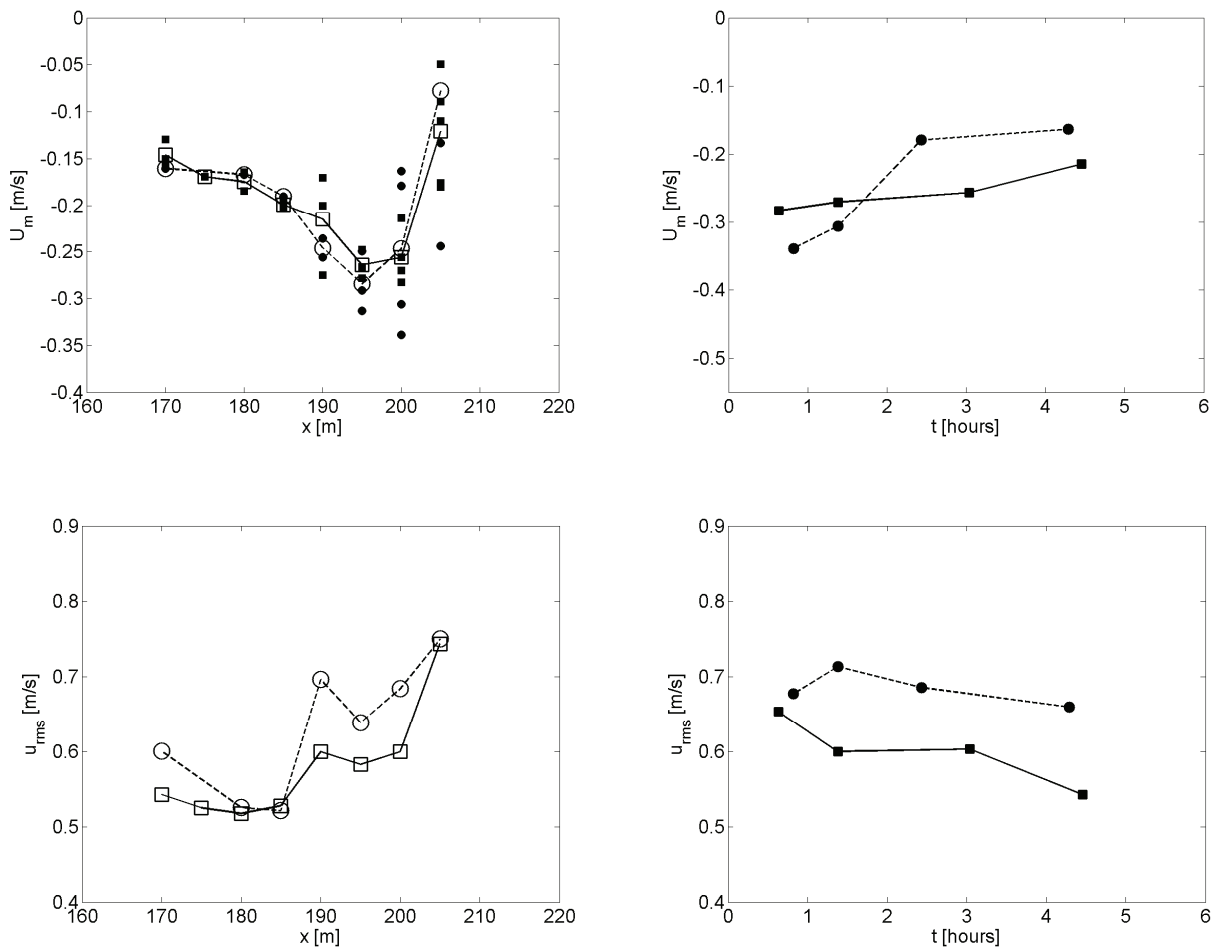


Figure 2.15 Upper left panel: Time and depth averaged flow velocity as function of cross-shore distance for test T01 (solid line-squares) and test T03 (dashed line-circles). Open markers are the average of all mobile frame measurements at a location within a test. Upper right panel: Temporal evolution of time and depth averaged flow velocity for test T01 (solid line-squares) and test T03 (dashed line-circles) at $x = 200$ m. Lower left panel: Total near-bed orbital velocity as function of cross-shore distance for test T01 (solid line-squares) and test T03 (dashed line-circles). Shown markers are the average of all mobile frame measurements at a location within a test. Lower right panel: Temporal evolution of total orbital velocity for test T01 (solid line-squares) and test T03 (dashed line-circles) at $x = 200$ m.

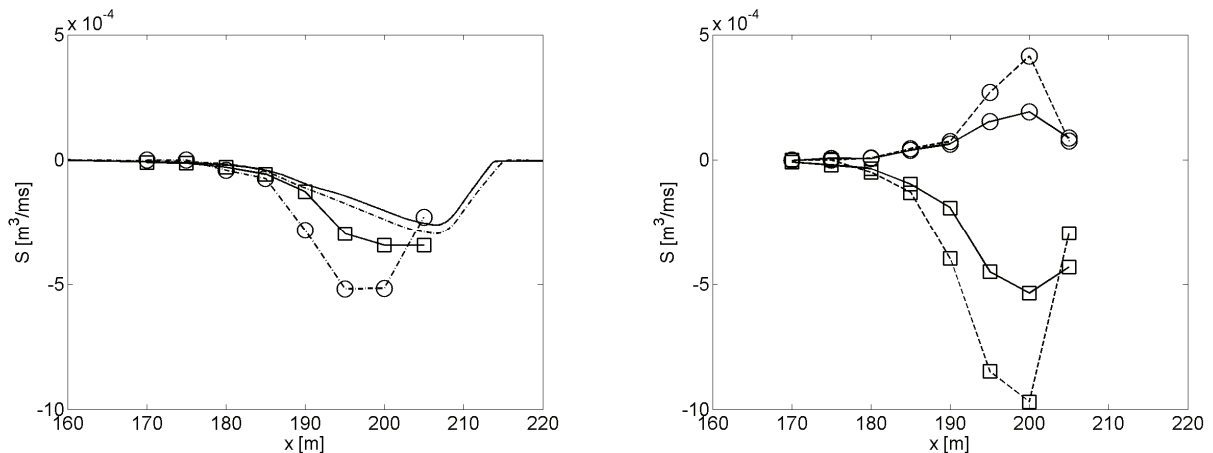
The time and depth averaged flow velocity has the same order of magnitude during test T01 and T03 (Figure 2.15, upper left panel). The evolution of the depth averaged

flow with progress of a test is different (Figure 2.15, upper right panel). Initially the magnitude of the depth averaged flow at $x = 200$ m in test T03 is larger. However, after approximately two hours the return flow during test T01 appears to be stronger. It is remarked that the overall observed larger near dune wave height ($x > 200$ m) during test T03 does not result in a larger return flow. This could be related to the increased setup level (and consequently comparable pressure gradients) close to the shore (see Figure 2.10), however the sparse instrument coverage at these locations prevent any firm conclusions.

The near-bed sediment concentration during test T03 is $O(100\%)$ higher shoreward of $x = 185$ m (Figure 2.13, left panel) and the time and depth averaged sediment concentration increases with $O(60\%)$ in this cross-shore range. Evolution of the sediment concentration with progress of a test is comparable with test T01. The sediment concentration decreases in time close to the dune face whereas further offshore the concentration increases (Figure 2.13, right panel). The sediment concentration during test T03 exceeds that of test T01 during the whole experiment.

Comparison of the test averaged sediment transports based on bed level changes show that the maximum sediment transport during test T03 is about 14% larger after six hours (Figure 2.16, upper left panel). The test averaged sediment transport computed from flow and sediment concentration measurements also shows a larger sediment transport for increasing wave period; however this increase is larger than the 14 % that was obtained for the profile evolution. In addition, the maximum in the sediment transports computed from flow and sediment concentration measurements are located further offshore.

Decomposing the sediment transport from flow and sediment concentration measurements into S_{x1} , S_{x2} and S_{x3} (see Equation 2.7 and 2.8) reveals that the increase in the maximum sediment transport is caused by an increase in the offshore directed flow related sediment transport. This rise is only partly compensated by an increase in the onshore directed wave related transport and transport above the wave trough (Figure 2.16, upper right panel). In addition Figure 2.16, lower panel shows that the additional dune erosion due to a larger wave period occurs mainly at the start of the test whereas after approximately 2 hours sediment transports in test T03 are even smaller than during test T01.



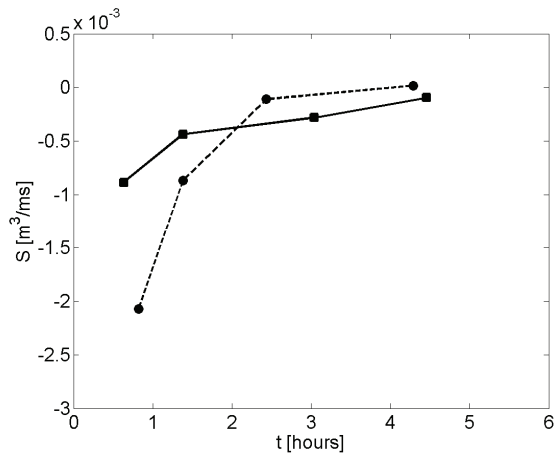


Figure 2.16 Upper left panel: Test averaged sediment transports as function of cross-shore position for test T01 (solid line) and test T03 (dashed-dotted line). Lines with markers are computed from the mobile frame measurements (as the average of all mobile frame measurements at a location within a test) and the remaining lines are computed from bed level changes. Upper right panel: Suspended sediment transport obtained from mobile frame measurements decomposed in the offshore mean flow related sediment transport (squares) and the onshore sediment transport ($S_{x2} + S_{x3}$; circles) for test T01 (solid line) and T03 (dashed line). Lower left panel: Temporal evolution of the suspended sediment transport measured with the mobile frame for test T01 (solid line) and test T03 (dashed line) at $x = 200$ m.

2.6 CONCLUSIONS

Large-scale dune erosion tests were conducted to obtain a better understanding of dune erosion physics and to study the effects of the wave period on dune erosion. It is found that:

- Both long and short waves are important to near dune hydrodynamics. As a test progresses and a new foreshore develops long waves become relatively more important.
- With the progress of a test the amount of wave energy at $x = 205$ m reduces with more than 30% suggesting that less energy reaches the dune face.
- A partly standing wave pattern is observed near the dune face.
- The magnitude of the time and depth averaged flow velocity increases gradually with decreasing water depth to approximately -0.3 m/s. As a test progresses the mean flow velocity magnitude decreases with 25% near the dune face.
- Time averaged sediment concentrations 4 cm above the bed rise sharply towards the dune face from less than 1 g/l in deeper water to more than 50 g/l. With the progress of a test time averaged sediment concentrations near the dune face decrease with more than 70%.

- The maximum sediment transport decrease 95% with progress of a test and the position with the maximum transport shifts shoreward with the retreating dune face. The flow related offshore directed sediment transport below the wave trough is dominant and is only partly compensated by the onshore directed wave related sediment transport and sediment transport above the wave trough.

Dune erosion volumes increase for a larger wave period. For an increase of 50% in the wave period, the dune erosion volume increases with 25%, 24% and 15% after 1, 2 and 6 hours test duration respectively. In addition it is found that with a larger wave period:

- Dune face retreat increases.
- The slope of the cross-shore bed profile around the still water level becomes gentler.
- On average 10 to 15% more wave energy is expected to reach the dune face.
- The time and depth averaged flow velocity remains comparable whereas the near dune orbital flow velocity increases with about 15%.
- The near dune ($x > 185$ m) sediment concentration 4 cm above the bed increases with $O(100\%)$ and the time and depth averaged concentration increases with $O(60\%)$.
- The maximum time averaged sediment transport during test T03 is about 14% larger after 6 hours, which is caused by an increase of the flow related offshore directed sediment transport in the first hours of the test. This increase is only partly compensated by an increase of the wave related sediment transport and the sediment transport above the wave trough.

Chapter 3

INTERACTION OF DUNE FACE AND SWASH ZONE^{II}

3.1 INTRODUCTION

During severe storms the beach is flooded causing that storm waves can reach the dune face and impact it. As a result sand is episodically released from the dunes and falls on the beach where it serves as a sediment source to the coastal profile that has a demand for sand since its shape is adapting to the extreme hydraulic conditions.

The sediment supply from the dunes to the beach is important for a better understanding and modeling of dune erosion. Depending on the dune face erosion rate the wet profile will develop differently (the shape of the profile can change and the time scale of its evolution will be affected). This can best be illustrated by considering a dune face that is protected with a revetment. In this case the sediment supply from the dunes to the beach is forced to be zero and a scour hole develops in front of the dune foot. A new foreshore cannot develop, which results in continuing heavy wave loads on the dune face.

Several approaches are available to describe sediment fluxes from the dune to the swash and inner surf. A first approach is based on the assumption that the capacity of the near dune hydrodynamics to transport sediment offshore is always fulfilled by the dune face (Steetzel, 1993; Steetzel, 1994; Van Rijn, 2009). Sediment transports are computed with a physical based model up to a critical position where the transport is empirically extrapolated over the (remaining) swash and dune face up to a computed run-up level. In this approach dune strength is not relevant and as a result the geotechnical properties of the dune face need not be considered.

^{II} This chapter is based on a manuscript and on a contribution to conference proceedings:

1. Clarke, L.B., Van Thiel de Vries, J.S.M. and Holman, R.A., in preparation. High resolution morphology from stereo video cameras. Planned to be submitted to *Journal of Geophysical Research*.
2. Van Thiel de Vries, J.S.M., Clarke, L.B., Aarninkhof, S.G.J., Coeveld, E.M., Holman, R.A., Palmsten, M.L., Reniers, A.J.H.M., Stive, M.J.F. and Uijttewaai, W.S.J., 2007. Interaction of dune face and swash zone, *Coastal Sediments*, New Orleans, pp. 1975-1987.

Another approach is to directly decouple inner surf and swash zone sediment transports from dune face erosion, which means that the offshore transport capacity of the near dune hydrodynamics is not necessarily fulfilled. It is presumed that the dune face has a certain resistance against erosion that depends on geotechnical properties. A method like this is proposed by Fisher and Overton (1984), Fisher et al., (1986), Overton and Fisher (1988b), Overton et al. (1994b) and Nishi and Kraus (1996), which relate the dune face erosion rate to wave impact forces.

It is expected that morphodynamic models in which the dune face erosion rate does not solely depend on flow based sediment transports but also on (parameterized) geotechnical properties of the dune face (Larson et al., 1989; Larson et al., 2004b; Roelvink et al., 2007) better represent the actual physics in nature. In these models the beach in front of the dune face is allowed to breathe since over short time intervals dune face erosion and offshore sediment transports are not forced to be the same. Considering a longer period of time, the feedback between near dune hydrodynamics, beach evolution and dune face erosion will assure that the time averaged dune face erosion rate and near dune offshore sediment transport are equal.

The objective of this chapter is to further examine the interaction of dune face and swash zone assuming a relation between wave impact and dune face erosion. In order to elaborate the volumes and other properties (e.g frequency and width) associated with the episodically slumping of the dune face use is made of (stereo) video images. Wave impacts on the dune face are estimated from near dune in-situ measurements and profile measurements are utilized to examine the interaction of dune face and swash over multiple slumps.

In Section 3.2 an algorithm is discussed to make high resolution dune face reconstructions from stereo images. The algorithm includes camera calibration, pre-processing of the images, feature matching and the computation of world coordinates from matched pixels in two images. Section 3.3 studies a relation between wave impact and dune face erosion. The relation is derived from literature and visual observations during the experiment. The chapter ends with conclusions and a discussion (Section 3.4).

3.2 HIGH RESOLUTION DUNE FACE RECONSTRUCTION FROM STEREO IMAGES

3.2.1 Introduction

Video imagery has been employed for the past 25 years to obtain more insight in the physical phenomena in the near shore area (Holman and Stanley, 2007) and has been deployed to study the position and evolution of sand bars (Lippmann and Holman, 1989), the shoreline (Plant and Holman, 1997) and the inter-tidal and sub-tidal (Aarninkhof, 2003) beach bathymetry. Video observations have supplementary value in relation to in-situ measurements due to the dense spatial and temporal resolution of an image, which covers a wide range of scales observed in the near shore. In addition, the deployment of a camera system is relatively cheap and in contrast with in-situ measurements video data collection does not affect the system observed (e.g. an

in-situ sensor is likely to influence the local flow field and consequently disturbs the observations of local processes, which might affect the morphodynamic evolution in more extreme cases).

Most near shore camera observations at this stage are based on a single camera system. For quantitative measurements with such a system, imaged features have to be related to a world reference frame, which requires either a scaled object in the field of view or projection of the image onto a surface of known elevation^{III}. In most cases the images are projected on a plane that is known from in-situ measurements (e.g. a beach survey or a tide level).

Considering two cameras with overlapping views this a priori knowledge of the projection surface is not required. By triangulation from both camera centers through an imaged point, the 3D world coordinates of this point can be derived. Obtaining 3D coordinates from (multiple) cameras with overlapping views is sometimes referred to as stereo reconstruction and has found wide application in several research fields, however has been underutilized in near shore research. The few documented cases include estimation of foreshore topography by tracking swash fronts using three towered cameras (Holland and Holman, 1997), the study of near shore bed form geometry using submerged stereo (Doucette et al., 2002) and monitoring of surface waves (Santel et al., 2002).

An automated and robust stereo reconstruction algorithm gives the possibility to make quantitative measurements with a dense spatial and temporal resolution. Complicated environments such as rapidly evolving surfaces (e.g. the dune face during a storm, the beach within the swash zone or the water surface) can be studied in much more detail, which will likely result in a better understanding of the near shore region.

This section describes a pilot version of an automated stereo reconstruction algorithm that is applied to obtain the 3D surface of the dune face from camera pair C1 and C2 deployed during the Deltaflume experiment (see Section 2.2.3). Stereo reconstructions are made in a number of steps that consist of:

- Coordinate transformation from the real world to image coordinates with a camera model (Section 3.2.2 and Section 3.2.3);
- Image pre-processing (Section 3.2.4) including amplification of image contrast and image rectification to improve and speed up feature matching;
- Mapping of pixels in one image to corresponding pixels in an image with overlapping view (Section 3.2.5);
- Triangulation from the camera centers through corresponding pixels to obtain real world coordinates (Section 3.2.6).

The section concludes with an example reconstruction that is compared with in-situ profile measurements (Section 3.2.7).

^{III} For a calibrated camera a (3D) world coordinate can be transformed to a unique (2D) image coordinate; however transformation from the image to world coordinates is an undetermined problem unless an additional geometric constraint on the world coordinate is specified, such as elevation.

3.2.2 Camera model

Charged couple device (CCD) cameras are frequently modeled as finite projective cameras. The transformation of world points to their representation on a camera imaging plane can be expressed as:

$$x = PX \quad (3.1)$$

where $X = [x, y, z, 1]$ is an homogeneous vector of world coordinates, $x = [u, v, w]$ is the homogeneous vector of image coordinates, and P is the projective transformation or camera matrix, which describes the camera and its relation to the world. Homogeneous coordinates allow elegant transformation between the three-dimensional world and two-dimensional camera coordinates with image coordinates specified as horizontal, u/w and vertical, v/w , position in the imaging plane. An introduction to homogeneous coordinates can be found in texts on projective geometry (Hartley and Zisserman, 2003).

The camera matrix, P , is a 3×4 matrix and represents the product of several matrices (see Hartley and Zisserman (2003) Chapter 6):

$$P = KR[I | -\tilde{C}] \quad (3.2)$$

where K is the internal camera calibration matrix, R is the camera rotation or external camera matrix and $\tilde{C} = [x_c, y_c, z_c]$ is the coordinate vector for the camera center (see Figure 3.1 left panel for an overview of the camera model parameters and their meaning).

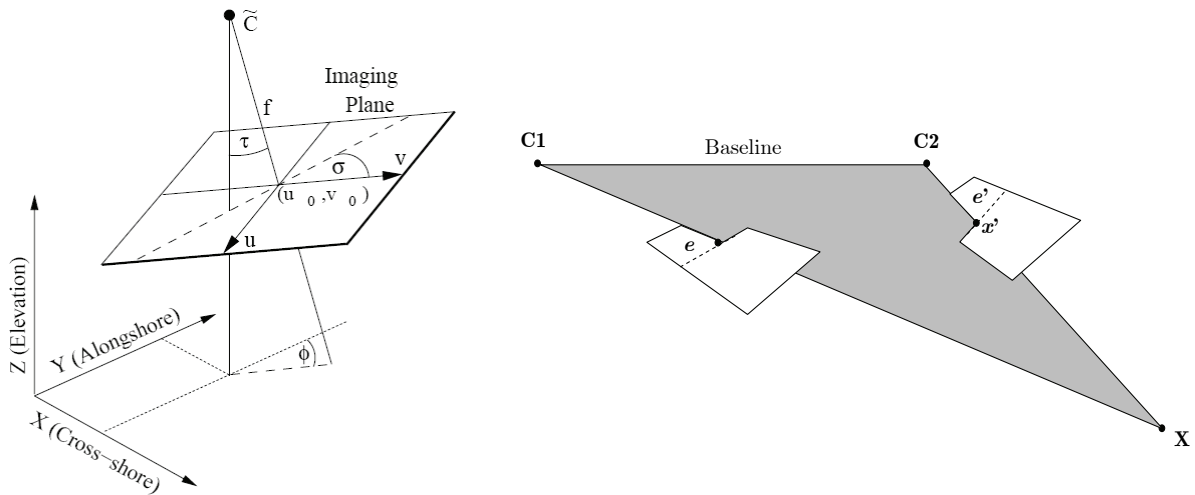


Figure 3.1 Left panel: Camera model parameters: Camera center, \tilde{C} ; focal length, f , so that $\alpha_u = fm_u$ and $\alpha_v = fm_v$, where m_u and m_v are the number of pixels per unit distance in image coordinates; principal point, $[u_0, v_0]$, (intersection of principal axis and imaging plane); azimuth, ϕ ; tilt, τ ; roll σ . Right panel: Searching for a feature match. Any plane intersecting camera centers $C1$ and $C2$ and a world point X is an epipolar plane. Intersection of the epipolar plane and the imaging planes defines epipolar lines, e and e' . X has corresponding image coordinates, x , in view $C1$. The search for the conjugate point, x' , in view $C2$, is limited to the line e' .

The internal camera matrix, K , has the form:

$$K = \begin{bmatrix} \alpha_u & s & u_0 \\ 0 & \alpha_v & v_0 \\ 0 & 0 & 1 \end{bmatrix} \quad (3.3)$$

where α_u and α_v are the focal length in horizontal or vertical pixel dimensions respectively (α_u/α_v is the pixel aspect ratio), s is the skew in CCD axes (generally assumed to be zero), u_0 and v_0 are pixel coordinates for the principal point (Figure 3.1, left panel). The rotation matrix, $R[r_{i,j}]$, $i, j = 1, 2, 3$, is a 3×3 matrix derived from three angles describing the direction of the camera principal axis in the world reference frame; azimuth, ϕ ; tilt, τ ; roll σ (Figure 3.1, left panel) (Wolf, 1983).

$$\begin{aligned} r_{1,1} &= \cos \phi \cos \sigma + \sin \phi \cos \tau \sin \sigma \\ r_{1,2} &= -\cos \sigma \cos \phi + \sin \sigma \cos \tau \sin \phi \\ r_{1,3} &= \sin \phi \cos \tau \\ r_{2,1} &= -\sin \sigma \cos \phi + \cos \sigma \cos \tau \cos \phi \\ r_{2,2} &= \sin \sigma \cos \phi + \cos \sigma \cos \tau \cos \phi \\ r_{2,3} &= \cos \sigma \sin \tau \\ r_{3,1} &= \sin \tau \sin \phi \\ r_{3,2} &= \sin \tau \cos \phi \\ r_{3,3} &= -\cos \tau \end{aligned} \quad (3.4)$$

Calibration of a single camera requires estimation of 10 parameters; 4 internal from K and 6 external from R and \tilde{C} .

3.2.3 Camera calibration

Accurate camera calibration is essential to accurate scene reconstruction within a designated reference frame. There are three components to camera calibration:

- removal of lens distortion;
- internal calibration;
- external calibration.

Lens and internal calibration can be performed independent of camera deployment while external calibration is performed once the camera is installed at the designed position and orientation.

Lens distortion and internal camera calibration

The apparent outward bending of objects and lines toward the image corners is known as barrel distortion and is a consequence of using a lens with a wider than standard field of view. The effect of barrel distortion in an image is routinely removed

in photogrammetry assuming a radial distortion model where the relation between distorted and undistorted points is (Weng et al., 1992):

$$\begin{aligned} u_d &= u_u + k_1 u_u r_u^2 + k_2 u_u r_u^4 \\ v_d &= v_u + k_1 v_u r_u^2 + k_2 v_u r_u^4 \end{aligned} \quad (3.5)$$

where u_d and v_d are distorted horizontal and vertical image coordinates respectively relative to the center of distortion, $[u_0, v_0]$, k_1 and k_2 are scalar parameters with $k_1 < 0$ for barrel distortion and $r_u^2 = u_u^2 + v_u^2$. Lens distortion parameters, k_1 , k_2 , u_0 and v_0 may be estimated independently of internal camera parameters but in the present work these parameters are estimated concurrently using a technique that is easily implemented without specialized calibration equipment. The calibration technique to estimate distortion and intrinsic camera parameters follows Zhang (2000) and uses as input a minimum of two images of a calibration target at random orientation. The calibration target was a printed 15×20 rectangular array of white circles on a black background secured to a rigid board. For each camera being calibrated ten images of the target were captured. Circle center coordinates were determined from the images and used to estimate 2D homographies between target and imaging planes for each image, ignoring the effect of lens distortion. The resulting group of homographies provides constraints on the intrinsic camera parameters (in Equation 3.3) and initial estimates of those parameters are obtained by solution to the eigenvalue problem. External camera parameters describing the relative rotation and translation between target and camera centers are estimated for each of the image views. Still neglecting lens distortion, internal and external parameters are refined using an iterative nonlinear minimization scheme, the result of which is used as the initial guess in a final refinement of all parameters, now including a lens distortion model^{IV}.

External camera calibration

External camera calibration requires several fixed targets or control points with accurately known world coordinates within the view. The location and orientation of the camera within the world reference frame is defined by 6 external camera parameters; the camera center, $C = [x_c, y_c, z_c]$ and 3 rotation angles. The camera centers for the Deltaflume experiment were surveyed (see Section 2.2.3) and consequently $[x_c, y_c, z_c]$ are considered to be known leaving only three unknown parameters. Azimuth, tilt and roll angles for each camera are estimated using ground control points that consisted of 17 bolts on the flume wall and 5 additional markers with different vertical elevation. The camera matrix, P is populated using estimated values for “known” parameters and an initial guess for values of rotation angles. World coordinates for the control points are transformed to image coordinates (Equation 3.1) and compared to the known image coordinates. The geometric error between transformed world and known image coordinates is minimized to solve for camera rotation angles.

^{IV} For the Deltaflume experiments the calibration target images to estimate the intrinsic camera parameters were not obtained at the original observation location in the Deltaflume. As a result estimated external camera parameters are not useful in the further analysis.

3.2.4 Image pre-processing

In collected images during the Deltaflume experiment the distribution of visible distinct features on the water surface, beach and dune face can be sparse, however enhancement of gradients in image intensity using a scale-dependent filter (Deng and Cahill, 1994) amplifies local image variance by a factor of 4-10 allowing more robust correlation of images. Images are then corrected for lens distortion. A list of coordinates defining a rectangular grid spanning the original image is distorted using the calibrated lens distortion model. The distortion-free image is constructed by mapping color from distorted to undistorted pixel locations using bi-linear interpolation. Matching a feature from the enhanced, distortion-corrected image C1, requires a two-dimensional search in the corresponding image from C2. Such a process is slow and poorly constrained because of substantial differences in feature appearance between the views owing to scaling by perspective or rotation by camera orientation. Using the concept of epipolar lines it is possible to simplify the matching process to a one-dimensional search. An epipolar plane is any plane containing the camera baseline (line joining the camera centers) (Figure 3.1 right panel). An epipolar line is the intersection of the imaging plane with an epipolar plane (Hartley and Zisserman, 2003). Consequently, the match to a feature located along an epipolar line in image C1 will be located along the associated epipolar line in image C2. The approximately horizontal baseline of C1 and C2 at the Deltaflume results in approximately horizontal epipolar lines but because of different camera orientations the epipolar lines are generally not aligned between images. Images from C1 and C2 are rectified so that pairs of conjugate epipolar lines become collinear and parallel to the vertical image axes thereby confining the feature search to a single column in the conjugate image. This stereo rectification requires formation of a virtual camera matrix, P' , for each view (Equation 3.2). Virtual cameras have camera center coordinates identical to the original cameras but azimuth, tilt and roll are modified such that the camera principal axes are parallel. Enhanced, distortion-corrected images are re-projected using an homography between the original and virtual imaging planes. The homography H is defined by:

$$H_i = P_i P_i'^+ \quad (3.6)$$

where P_i , $i = 1, 2$ is the original camera matrix and $P_i'^+$ is the pseudo-inverse of the reoriented camera matrix. Images are rectified using $x' = Hx$, where x is a list of homogeneous coordinates for all pixels in the original image and x' is the transformed coordinate in the virtual image plane. Pixel intensity in the red, green and blue color bands are interpolated onto a regular grid within the region of interest on the virtual imaging planes, I and J . Note, that if the focal lengths of the original cameras differ, the resulting scaling difference can be accounted for by assigning identical α_u and α_v (see Equation 3.3) in the formation of P_i' .

3.2.5 Feature matching

Following stereo rectification, pixels in rectified C1 are mapped to corresponding pixels in rectified C2 using normalized cross-correlation as a measure of feature similarity. For a given pixel in C1 the conjugate pixel in C2 will have an identical horizontal

coordinate, u , and disparity in the vertical coordinate, v . For the dune face reconstructions during the Deltaflume experiment, a 9×9 pixel area from rectified C1 centered at coordinate $[u, v]$ is correlated with pixels from rectified C2 centered at $[u, v + D]$, for disparity $D_{min} \leq D \leq D_{max}$:

$$\begin{aligned} \rho(u, v, D) &= s \sum_{i=u-m}^{u+m} \sum_{j=v-n}^{v+n} [I(i, j) - \bar{I}_{u,v}] [J(i, j + D) - \bar{J}_{u,v+D}] \\ s &= \frac{1}{\sqrt{\sigma_I^2 \sigma_J^2}} \\ \sigma_I^2 &= \sum_{i=u-m}^{u+m} \sum_{j=v-n}^{v+n} (I(i, j) - \bar{I}_{u,v})^2 \\ \sigma_J^2 &= \sum_{i=u-m}^{u+m} \sum_{j=v-n}^{v+n} (J(i, j + D) - \bar{J}_{u,v+D})^2 \end{aligned} \tag{3.7}$$

where ρ is the normalized cross correlation coefficient, I and J are rectified grey scale images from C1 and C2 respectively, \bar{I} and \bar{J} are mean image intensities for the correlation window. Numerous algorithms exist for efficient cross correlation computation (for example Lewis (1995) and Sun (2002)). To reduce computation time correlation is performed for a range in disparity, which is defined by computing a maximum and minimum disparity associated with a maximum and minimum expected elevation of the imaged surface.

The three-dimensional array $\rho(u, v, D)$ comprises one vertical slice per pixel column in I . For any given pixel in I there may be numerous correlation maxima corresponding to different disparity values but the true disparity lies along a more or less continuous surface of high correlation splitting the volume. This surface through the correlation volume uniquely defines disparity at every pixel in I .

Many algorithms have been proposed to determine the true disparity surface through a multi-dimensional similarity space. Ambiguity in the similarity between views may arise due to repeated patterns or featureless regions and unique pixel mapping is impossible where part of a view is occluded by an obstructing feature. Design of algorithms performing this task accurately and efficiently remains an active research topic in computer vision.

Since occlusion is not an issue in the images collected for dune face reconstruction a relative simple algorithm is developed based on Sun (2002). The disparity surface is determined by tracing a path across each $D - v$ slice through the volume using a two-stage dynamic programming algorithm. The algorithm goal is to identify a continuous path from left to right across the slice, monotonic in v , which maximizes the path correlation sum. In practice, the algorithm performs a cost minimization requiring a transformation of correlation values: $\rho' = 1 - \rho$. The monotonic requirement reflects the assumption that the imaged surface is smooth and without occlusions.

Tracing a disparity path

A slice through the correlation volume corresponding to fixed u defines a map, ρ' , for all v and a range of disparity. In the first stage of the algorithm, $B(D, v = 1) \equiv \rho'(D, v = 1)$. Progressing from left to right, for $v > 1$:

$$B(D, v) = \rho' + \min[B(D + \Delta D_i, v - 1)], \quad -1 \leq \Delta D_i \leq 1 \quad (3.8)$$

The values $\Delta D(D, v)$ corresponding to the minimum are recorded. In the second stage of the algorithm, starting at the node defined by $\min[B(D, v = n)]$, where n is the last column of nodes in the map, a path is propagated from right to left across the map by linking to nodes defined by $\Delta D(D, v)$. The resulting list of connected nodes defines the disparity path and global minimum of $\sum \rho'$ along any monotonic path across that volume slice.

Correlation of image regions with low variance results in regions of low or uniform correlation through which the disparity path may be spuriously erratic. To improve path finding through these regions the first stage of the algorithm was modified by adding two factors to the calculation of B . The first factor encourages a change in path direction if the sequence of preceding nodes traces a straight line. The second factor discourages linking to preceding nodes having greater disparity, which is justified in the absence of occlusion since disparity must decrease toward the horizon (decreasing v) in the Deltaflume images. The choice of a node from the preceding column is influenced by inflating B by these two factors and Equation 3.8 becomes:

$$B(D, v) = \rho' + \min[B(D + \Delta D_i, v - 1)(1 + F_1 + F_2)], \quad -1 \leq \Delta D_i \leq 1 \quad (3.9)$$

where:

$$F_1 = f_1 p^g \quad \& \quad p(D, v) = \begin{cases} p(D + \Delta D_i, v - 1) + 1, & \text{if } \Delta D_i(D, v) = \Delta D(D + \Delta D_i, v - 1) \\ 0, & \text{if } \Delta D_i(D, v) \neq \Delta D(D + \Delta D_i, v - 1) \end{cases} \quad (3.10)$$

$$F_2 = \begin{cases} f_2, & \text{if } \Delta D_i(D, v) = -1 \\ 0 & \end{cases} \quad (3.11)$$

In Equation 3.9 F_1 and F_2 are related to discouraging a straight path and a path with increasing disparity towards the horizon respectively. The coefficients $f_1 = 0.07$, $g = 1.3$ and $f_2 = 1$ in Equations 3.10 and 3.11 were empirically determined. For the results reported here computed disparity paths are insensitive to variation in parameter values of about 75%.

Disparity surface

A disparity surface, $D(u, v)$ is computed from all slices in the correlation volume. However, because D is computed independently for each slice, changes in D for adjacent slices in regions of low image variance may vary by several pixels, which translate to unrealistic gradients in topography. To further aid tracing of the disparity path through low relief regions of the correlation map the position of the disparity

path from slices where the path is reliably traced is propagated to adjacent slices where the path may be less clearly defined. First, alongshore uniformity is assumed and a disparity path is computed for the accumulated correlation map in u -direction. Next this path is used to mask the middle slice of the correlation volume such that $\rho'(D_i', v) = 2$ where $D_i' > D(v, u_{all}) + k$ or $D_i' < D(v, u_{all}) - k$; $k = 2$. The disparity path traced through the masked middle slice is thereby constrained to lie within k pixels of the path computed for the accumulated correlation map in u -direction. For the other slices a similar procedure is used in which the masked area is determined by the path found in the adjacent slice.

3.2.6 World coordinates from feature matching

Two rays can be projected from the camera centers into the world through a point on each imaging plane related by disparity. The intersection of these rays in the world reference frame defines the world coordinates for the imaged feature. In general, inaccuracies in camera calibration or disparity estimation prevent perfect intersection of the rays and a best estimate solution is necessary. From relations, $x_1 = P_1'X$ and $x_2 = P_2'X$, a system of equations linear in X comprises the relation:

$$AX = 0 \quad (3.12)$$

where

$$A = \begin{bmatrix} u_1 p_1^{3T} - p_1^{1T} \\ v_1 p_1^{3T} - p_1^{2T} \\ u_2 p_2^{3T} - p_2^{1T} \\ u_2 p_2^{3T} - p_2^{2T} \end{bmatrix} \quad (3.13)$$

and p_i^{nT} are rows of P_i' . Least squares solution of Equation 3.12 yields X by computing the singular value decomposition (SVD) of A so that $\text{SVD}(A) = UDV^T$, where U and V^T are unitary matrices, D is a diagonal matrix with entries in decreasing order and X is the last column of V , i.e. $V = [\lambda x, \lambda y, \lambda z, \lambda]$ (Hartley and Zisserman, 2003) p.313. Alternatively, a well-documented non-iterative triangulation method (Hartley and Zisserman, 2003) p.315 provides an optimal solution, but computation time increased considerably without notable improvement in reconstruction accuracy.

3.2.7 An example reconstruction

A three dimensional example reconstruction of the dune face and near shore is obtained from a raw image pair (see Figure 3.2) at the end of test T01. Besides the images, input to the algorithm are the camera geometries including camera orientation, position and focal length (see Section 3.2.2 and 3.2.3).

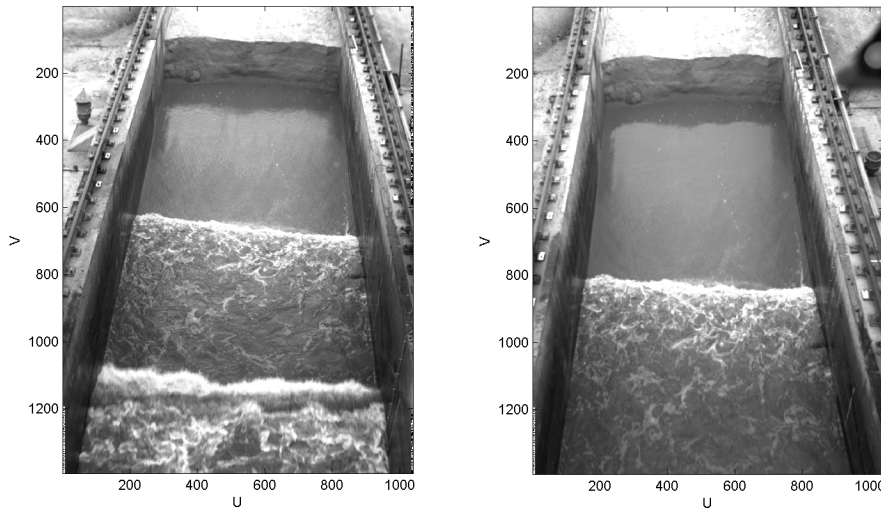


Figure 3.2 Raw image at the end of test T01 for camera C1 (left panel) and camera C2 (right panel)

To compare stereo reconstructions with in-situ measurements and to prevent spurious feature matches the water surface, dry beach and reflection areas are identified using a series of (additional) empirical image processing algorithms prior to the feature matching process. The waterline is detected using the contrast between wave breaking induced foam and the dry beach. Using intensity variance images, large variance areas are identified as wet whereas small variance areas are marked as dry (Figure 3.3 left panel). In addition, the most shoreward bore edge (indicated by the white arrow in the right panel of Figure 3.3) is detected as the continuous line maximizing the sum of variance across the flume. If the resulting bore edge is within a user specified number of pixels from the waterline the bore edge is marked as being the waterline. In this case it is used as a strong feature to generate high confidence coordinates along contour lines on the otherwise poorly featured beach.

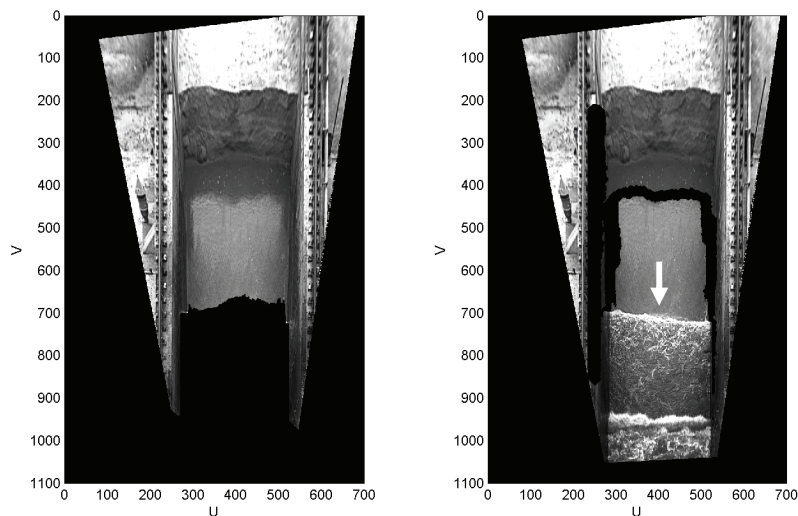


Figure 3.3 Enhanced, undistorted and rectified images (as described in Section 3.2.4) Left panel: Distinguish between water surface and dry beach. Here the water surface is masked. Right panel: Masking of edges reflection area. The white arrow points to the most shoreward bore

In some areas in the flume features appear as reflections on either the water surface or the wet sand surface during shallow swash uprush or downrush. Computed coordinates for reflected features are erroneous compared to the coordinates in the absence of such reflections and for that reason areas in the image containing features that are related to these reflections are identified and excluded from further analysis (Figure 3.3 right panel).

About 100,000 xyz coordinates with a normalized cross correlation ρ larger than 0.65 are computed by the automated stereo algorithm in an area of $15 \times 4 = 60 \text{ m}^2$, which means one xyz coordinate per 6 cm^2 on average. Available xyz coordinates from the reconstruction are interpolated on a regular grid with spacing $1 \text{ cm} \times 1 \text{ cm}$. Since the dune face is nearly vertical, this feature is resolved in the interpolation by first transforming computed xyz to a temporary coordinate system, xyz' , in which the plane xy' represents a best fit through all xyz . The transformed points xyz' are interpolated onto a regular grid in xy' and are then transformed back to the un-rotated reference frame (Figure 3.4).

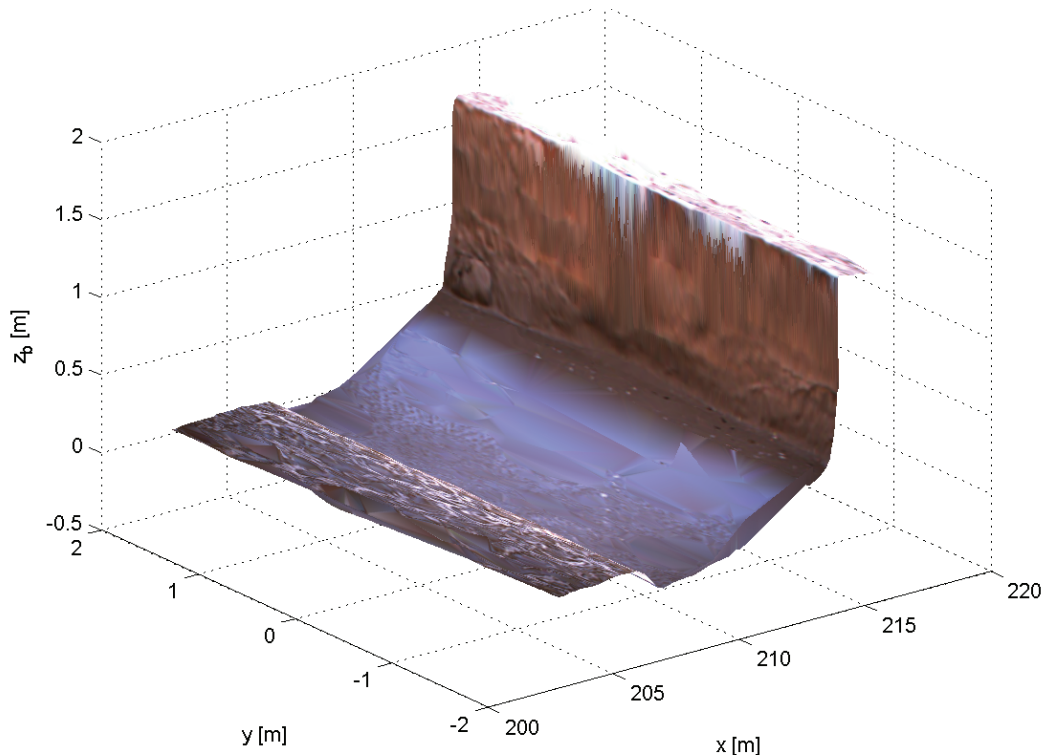


Figure 3.4 Three dimensional reconstruction of near shore area from two images at the end of test T01. Bed level elevations are in relation to the still water level in the flume, which is 4.5 meter above the flume's floor.

For a first verification of the algorithm, dry points from the stereo reconstruction are compared with in-situ profile measurements at the end of interval E in test T01 (Figure 3.5). Stereo and in-situ measurements compare reasonably well for the beach in the swash zone. Also, the transition from the water surface to the dry beach seems reasonably predicted. However, for the dune face the stereo reconstruction strongly deviates from the profile measurements. The differences are due to erroneous measurements of the in-situ profiler in this area since bed level changes over the dune face

are too large to be followed by the profiler. In the middle panel of Figure 3.5 the dune crest position in the in-situ measurements is located more landward, which is probably explained by the small time difference between stereo and in-situ measurements (in-situ and profile measurements cannot be carried out at the same time since the bed profiler blocks the camera views of C1 and C2). It is seen that the dune face in the stereo reconstruction is really steep (even overhanging), which suggests it can collapse any moment. It is most likely that the dune face collapsed after the images for the reconstruction in Figure 3.5 were collected, resulting in a retreat of the dune crest as observed in the profile measurements.

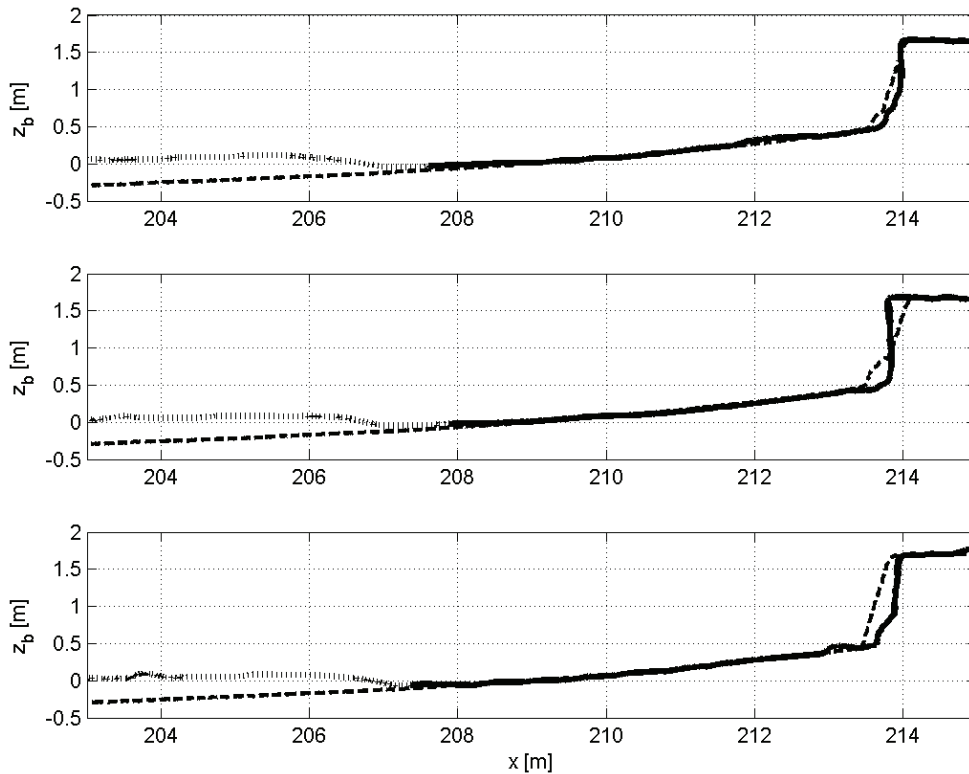


Figure 3.5 Wet coordinates (dotted line) and dry coordinates (solid line) from a stereo reconstruction at the end of test T01 compared with in-situ measured profiles (dashed line) along three transects in the flume. Bed level elevations are in relation to the still water level in the flume, which is 4.5 meter above the flume's floor.

3.3 DUNE FACE EROSION DUE TO WAVE IMPACTS

3.3.1 Previous studies on dune face erosion due to wave impacts

Fisher and Overton (1984) proposed a dune erosion mechanism in which the erosion rate depends on frequency and intensity of the swash. They relate the impact of an individual swash run-up on the dune face to the volume of sand eroded from it. In order to examine this relation experiments were carried out in both the laboratory

and the field. The experiments in the laboratory were conducted in a flume (Overton and Fisher, 1988a) in which bores were generated by releasing water from a head tank with a quick opening gate. In order to mimic different bore sizes several initial head tank levels were used and the dunes were all constructed with the same size sand and about the same moisture content. A linear relation was found between individual wave impacts and the volumes eroded from the dune.

Besides the laboratory experiments Fisher et al. (1986) presented four field experiments conducted at Duck beach in North Carolina. Taking sand from local dunes an artificial dune was constructed on the inter-tidal beach during low water. As the water level rose with the incoming tide the swash reached the dune face and started to impact it, causing erosion. Whereas for the laboratory experiments a clear relation was found between an individual wave impact and the specific eroded volume from the dune, considerable scatter was observed during the field experiment. This scatter was explained by two properties that are different in the field:

1. Swash heights and velocities are noisier in the field.
2. The nature of dune face erosion in the field differs from that in the flume.

It was found that in the field the dune face is not always vertical (critical) and its steepness changes during the experiment. This means that some of the incoming bores hit a vertical wall whereas others meet a recently failed mass of sand that slumped from the dune face. Grouping of the field data reduced scatter and showed a linear relation between average swash impacts on the dune face and the average erosion volume. After grouping, field results are in agreement with the linear relation observed during the laboratory experiment^V.

Additional flume experiments were carried out by Overton et al. (1994a) to examine the effect of the grain size and sediment density on the linear relationship between wave impact force and dune erosion. It was found that grain size and dune density are important parameters in this relation. A smaller grain size and sediment with a higher density were both found to make a dune more resistant against erosion. The effect of sand density on dune erosion varied with the sediment grain size and was found to be more important for a larger grain size. In addition, the effect of the grain size on the resistance against erosion was found to be larger than that of sand density.

Finally, a large scale dune erosion experiment (Overton et al., 1994b; Nishi and Kraus, 1996) confirmed a strong linear relation between the wave impact force and the dune erosion volume.

^V Analyzing both laboratory and field results, the relation between the wave impact force and dune face erosion volume obtained with linear regression are different for the laboratory data than for the field data. This is probably related to the relative different cross-shore position of the instruments deployed to estimate bore impact on the dune face. Also soil properties were likely different in the field.

3.3.2 Visual observations during the Deltaflume experiment

In the Deltaflume experiment (Chapter 2) the process of dune face erosion changes as a test progresses. Initially, the dune foot is below still water level and the slope of the dune face is relatively mild (1:1.5). Many waves reach the dune face and run over it causing flow drag based erosion, which steepens the dune front till it is nearly vertical or even overhanging. At this stage a different erosion mechanism starts in which the dune face episodically retreats under waves impacting it (as suggested by Fisher et al., (1986)). When the dune face collapses, big lumps of sediment fall or slide down the dune face on the beach in front of it. The sand is picked up by inner surf and swash zone bores that transport the sediment further seaward building up a new foreshore. It seems that sand from a slump temporarily obstructs further dune erosion by direct wave attack. The part of the dune face that is still entirely exposed to waves is at that moment more susceptible to erosion than the obstructed part. This process seems to promote uniformity in erosion in cross-flume direction.

The width of a slump in cross-flume direction is mostly smaller than the entire width of the flume, but often exceeds one third of the flume width. The length of a slump in the along-flume direction is about 0.1 to 0.3 m. The volume that is episodically added to the beach by slumping varies (see the time stacks in Figure 3.6 that are generated for images collected with camera C1). However, the temporal evolution of the size of slumps does not seem to vary much in time; at the beginning of a test (after 1 hour) the size seems to be slightly larger than at the end. The time interval between successive slumps is found to be shorter at the beginning of the test than at the end.

As the dune erodes the foreshore starts to develop and waves start to break further offshore. Also the dune foot moves in landward and in upward direction and becomes located above the maximum storm surge level. Waves have to run up the newly formed beach in order to reach the dune face, reducing the intensity and number of impacting waves and hence the erosion rates. This is confirmed by the time stacks in Figure 3.6, which show a reduction in dune face retreat rate with progress of a test. In addition, Figure 3.7 shows that the shoreward directed momentum close to the dune face (expected to be related to the intensity and number of wave impacts) also decays.

It is expected that the dune face will continue to erode as long as incoming waves that run up the beach can reach the dune face and impact it. Considering this it is hypothesized that the rate of dune face retreat should be related to the wave impact frequency. However, a direct relation between wave impact and dune face erosion was not observed. Collapsing of the dune face also occurred after an experiment in the absence of waves. In general, the dune face is overhanging slightly before a slump suggesting the dune face becomes unstable reaching a critical slope. An instantaneous relation between discrete wave impacts and dune face retreat is absent, but a relation between dune face retreat and the accumulated dune face wave impacts between two slumps is examined in the following section.

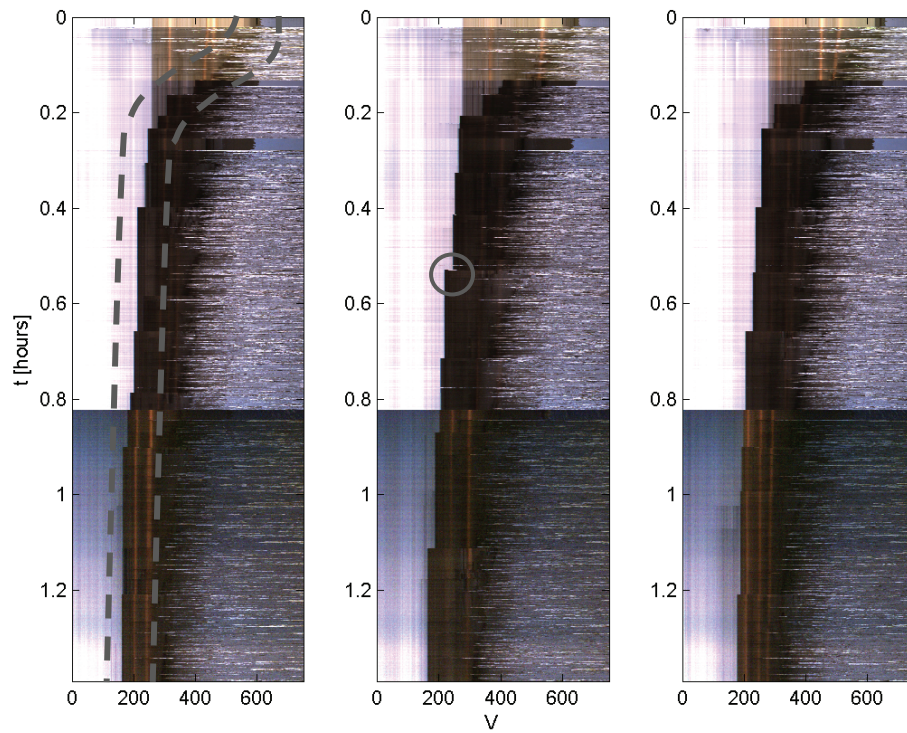


Figure 3.6 Time stacks for three transects in cross tank direction comprising the first four intervals of test DP01. The dune crest (lying between the dashed lines in the left panel) is indicated by the transition from light to dark, where light is the top of the dune. Slumps are indicated by a discontinuity of the dune crest in time (e.g. the circle in the middle time stack).

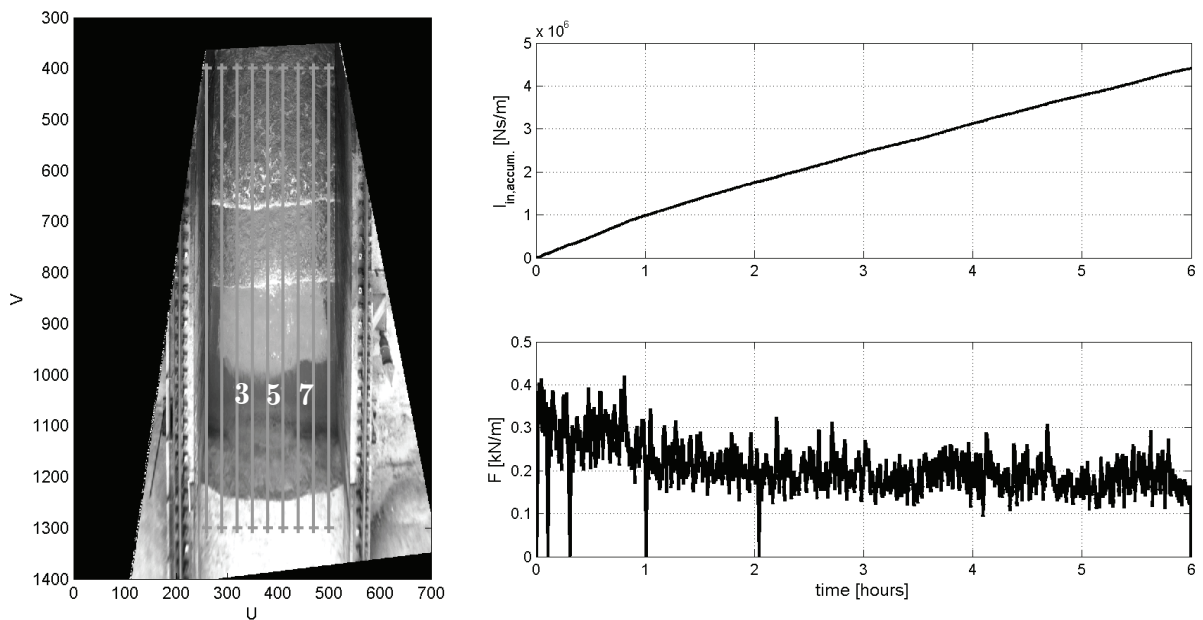


Figure 3.7 Left panel: Rectified image with transects used to generate time stacks. Transect 3,5 and 7 are used in elaborating Figure 3.6. Right panel: Accumulated shoreward directed momentum (upper) and ten minutes averaged gradient of shoreward directed momentum (lower) at the collocated pressure and current velocity sensor at 205 meter from the wave board.

3.3.3 Dune face impact model

In Fisher et al. (1986) and later Overton et al. (1988b) and Nishi and Kraus (1996) a linear relationship is assumed between the change in momentum of waves impacting the dune face (a force F) and the weight of the volume sediment eroded from the dune (ΔW):

$$\Delta W = C_E F \quad (3.14)$$

In this expression C_E is an empirical coefficient to be obtained from data and ΔW is computed from the eroded sediment volume from the dune (ΔV) (Figure 3.8):

$$\Delta W = \Delta V \rho_s (1 - p) g \quad (3.15)$$

where ρ_s is sediment density, p is porosity and g is the gravitational acceleration.

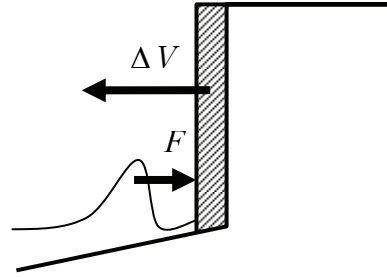


Figure 3.8 Dune face erosion (ΔV) due to wave impacts (F).

To examine whether a relation exists as proposed in Equation 3.14 and to calibrate the coefficient C_E for the Deltaflume experiment requires estimation of dune face erosion volumes (ΔV) and associated wave impacts (F). The change in dune face volume is computed from profile measurements and (stereo) video reconstructions. Profile measurements are conducted between constant tests intervals (see Chapter 2) in which multiple slumps can take place. The (stereo) video reconstructions are utilized to estimate dune face volume changes over a single slump. Wave impacts on the dune face are estimated from near dune in-situ pressure and flow measurements.

Momentum flux due to incoming waves

Wave impact on the dune face can be computed from the near dune momentum flux of incoming waves. During the Deltaflume experiment a collocated pressure and flow velocity sensor at 205 meter from the wave board (this is about 5-15 meter from the dune face) are available to estimate this flux. Using shallow water linear wave theory pressure time series are translated into water surface elevations. The flow velocity time series are de-spiked such that velocity peaks with a minimum amplitude of 0.25 m/s and duration smaller than 1 second are removed. Both pressure and flow velocity time series are used to distinguish between incoming and shoreline reflected waves assuming shallow water (Guza et al., 1984):

$$\eta_{in} = \frac{\eta + u\sqrt{h/g}}{2} \quad \text{and} \quad \eta_{out} = \frac{\eta - u\sqrt{h/g}}{2} \quad (3.16)$$

where η_{in} and η_{out} are the water surface elevation associated with the incoming waves and outgoing waves respectively, η ($= \eta_{in} + \eta_{out}$) is the measured water surface elevation, u is the measured flow velocity, h is water depth and g is the gravitational acceleration.

The incoming wave signal is considered representative for the momentum flux and consists of two contributions, which represent the advection of momentum by the flow (first right hand side term) and a term taking in account the dynamic water pressure (second right hand side term):

$$I(t) = \rho_w u_{in}(t)^2 h_{in}(t) + 0.5 \rho_w g \eta_{in}(t)^2 \quad (3.17)$$

where u_{in} ($= (g/h)^{0.5} \eta_{in}$) and h_{in} ($= h_{mean} + \eta_{in}$) are the flow velocity and the water depth associated with the incoming waves respectively. From this momentum flux the (average) wave impact can be computed integrating over (a number of) wave periods:

$$F = \frac{1}{\Delta T} \int_{t_0}^{t_0 + \Delta T} I(t) dt \quad (3.18)$$

where ΔT is the integration interval, t_0 is the start time of integration and $I(t)$ is the momentum flux due to incoming waves as expressed in equation 3.17.

The incoming momentum at the collocated pressure and flow velocity sensor is absorbed in the swash zone and by the dune face. Since the dune face retreats during the experiment, the distance between the sensors and the dune face will increase and more momentum will be absorbed in the swash zone shoreward of the sensors (the number of incoming waves at the collocated sensors that actually is going to reach the dune face will decrease). To include this effect requires the modeling of intra wave forces that act on the fluid in the swash zone. However, in the further analysis in this chapter the change in momentum decay in the swash zone is not accounted for in the analysis. The dune face erosion is simply associated with the momentum flux at 205 meter from the wave board.

Interaction of dune face and swash zone using profile measurements

The most straightforward way to examine relation 3.14 is by using the profile measurements conducted during the Deltaflume experiment. For successive profile measurements an erosion volume (ΔV) above the maximum storm surge level is computed, which is associated with the average impact force on the dune face.

In Figure 3.9 the dune face erosion rates are compared with the average wave impact force on the dune face. The dune face erosion rate ($\Delta V / \Delta T$) is used instead of the eroded volume (ΔV) since multiple waves impact the dune face before a slump takes place. This means that in fact the erosion volume is associated with the absorbed momentum by the dune face and swash zone over a test interval.

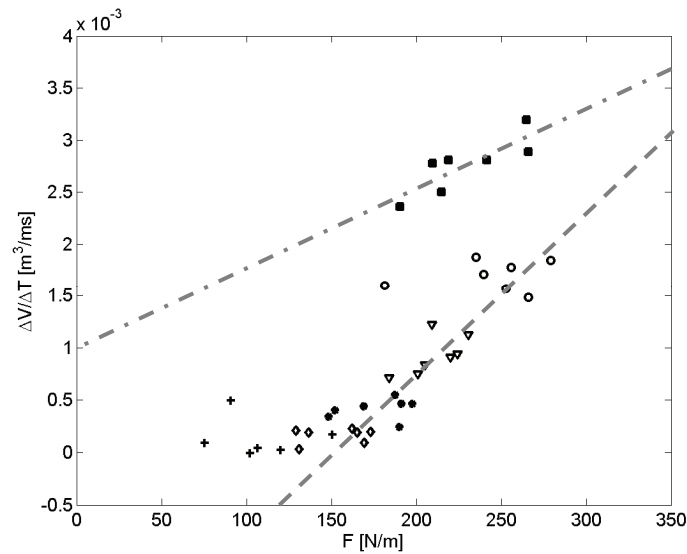


Figure 3.9 Dune face erosion rates from profile measurements as function of the average wave impact force. Solid squares relate to interval A and intervals B-E are represented by circles, downward triangles, stars and diamonds respectively. Intervals after E are indicated with plusses.

Analysis of Figure 3.9 indeed reveals a clear relation between the dune face erosion rate and the wave impact force. Also it seems that the relation is changing during a dune erosion test. Data points associated with the first test interval (solid squares) have a different relation with the average wave impact force (see qualitatively fitted dashed-dotted trend line) than the other markers (see qualitatively fitted dashed trend line). This is in agreement with visual observations (Section 3.3.2), which showed that the erosion mechanism at the start of a test is different. Initially waves are not impacting the dune face but instead they run over it causing flow drag based erosion. As a result the dune face steepens until a transitional slope is reached after which waves start to impact the dune face. Interestingly, the initial erosion mechanism is more efficient relative to erosion by wave impacts (initial dune face erosion rates are largest) and the dune face develops to a shape that is more resistant against erosion.

Dune erosion rates decrease during a test, which corresponds with a decrease in the average wave impact on the dune face (Figure 3.9). Following the trend line (dashed line in Figure 3.9) and thus assuming a linear relation as proposed in Equation 3.14, it seems a threshold in the wave impact force for dune erosion exists (the trend line intersects $\Delta V/\Delta T = 0 \text{ m}^3/\text{ms}$ at F is approximately 120 N/m). However, looking at the data points, the relation between the average wave impact force and the dune face erosion rate tends to become nonlinear for smaller erosion rates. Any firm conclusions about the threshold cannot be made also because the data scatter is large and momentum decay in the swash zone shoreward of $x = 205 \text{ m}$ is not accounted for and may partly mask the relation.

Morphodynamic response dune face from video images

Supplementary to profile measurements also stereo video images can be utilized to make 3D reconstructions of the dune face and to compute the morphodynamic response associated with a slump. In contradiction to the slump averaged analysis from profile measurements stereo images allow investigating individual slump events and in addition also give insight in slump volume, dimensions and the time interval between successive slump events.

Slump events are detected in the available video data using time stacks of nine uniformly spaced transects in cross flume direction (see Figure 3.7, left panel and Figure 3.6). The real world distance between transects is about half a meter, which is close enough to detect most slump events. Since retreat of the dune face does usually not extend over the full width of the flume, slump events are not necessarily visible in all time stacks.

Considering the episodic retreat of the dune face that is non-uniform along the dune crest illustrates the complexity of the near dune system and the difficulty to make an unambiguous analysis of a relation between wave impact and dune face erosion for individual slump events (e.g. what average impact force and time interval should be related to a slump event over one third of the flume width that partly overlaps with the previous slump event?). In the following analysis the interaction of dune face and swash is simplified relating accumulated wave impacts between successive slumps (assumed to be uniform in cross flume direction) to the cross flume integrated volume change of the dune.

The volume change (ΔV) associated with a slump event has to be specified and computed from stereo reconstructions. The most straightforward way to estimate ΔV seems to determine the difference between reconstructed dune and beach morphology immediately before and after a slump event (see Figure 3.10 and Figure 3.11, left panel). The volume change ΔV can be estimated by cross-shore integration of negative bed level changes. However, it is questionable whether with this approach the volume of active sand is obtained that serves as a sediment source to the swash zone. Taking the erosion volume as specified in the left panel of Figure 3.10 will probably be an underestimation since a substantially larger amount of sand is redistributed by the near shore flows in the time interval between successive slumps. From a physical point of view it seems therefore more logical to compute the volume change ΔV from the difference between pre-slump bathymetries for two successive slumps (Figure 3.10 right panel):

1. The volume considered equals the amount of sand that is picked up and transported seaward by the near dune hydrodynamics (this is explained as active sand that serves as a source to the developing foreshore).
2. The porosity of the volume can assumed to be constant and is equal to the porosity of the (initial) dune sand^{VI}. Another option could have been to determine the difference between reconstructions just after a slump event and just

^{VI} Porosity is of relevance to examine relation 3.14 since the weight of sand depends on porosity.

before the next slump event. However, this would provoke discussion about porosity of the released sand, which is expected to be non-uniform.

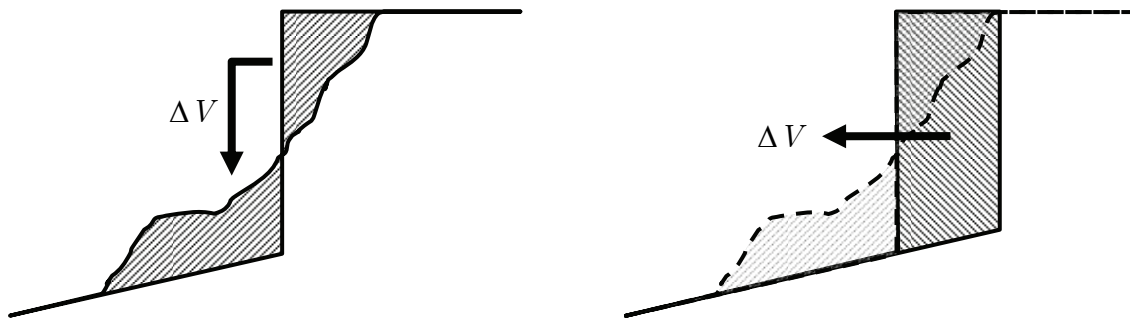


Figure 3.10 Left Panel: Morphodynamic response of the dune face over a slump event and associated volume that seems to be released (shaded area dune). The volume that is deposited on the beach (shaded area on beach) does not necessarily equal the released volume from the dune due to possible differences in porosity. Right panel: Volume change from the difference between pre-slump bathymetries for successive slumps (shaded area between solid lines; the mass equals the mass of the shaded area under the dashed line that has a different porosity).

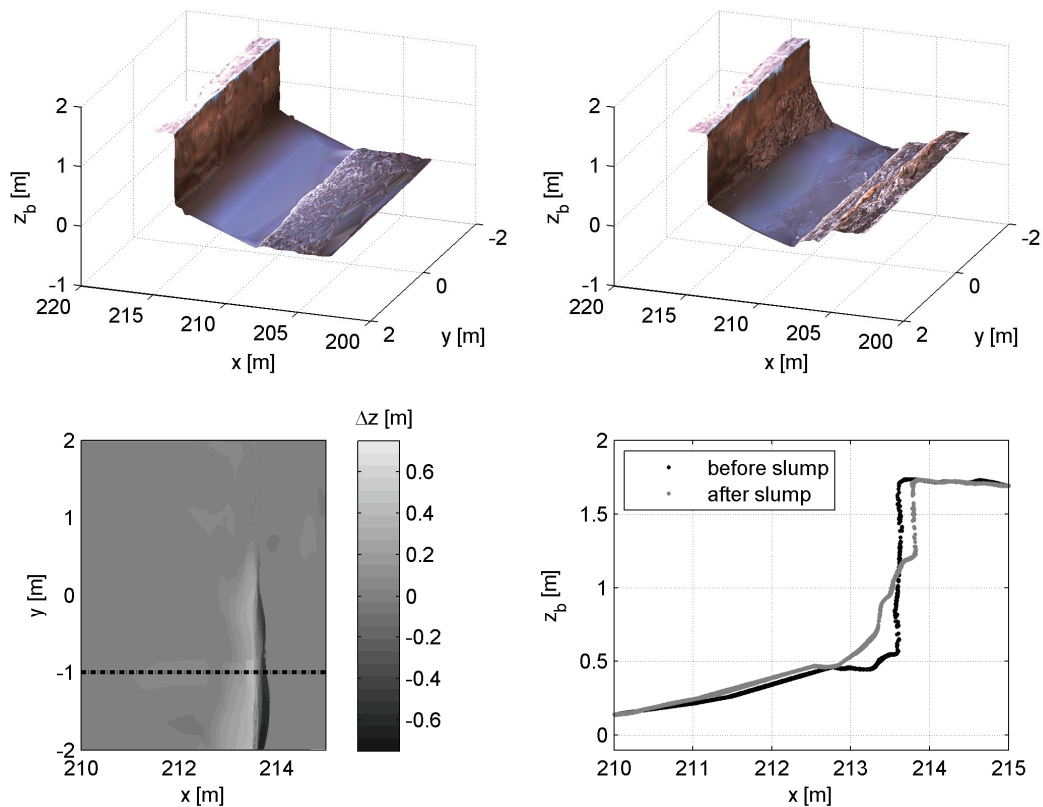


Figure 3.11 Morphodynamic response during a dune face slump. Upper panels: Three dimensional reconstruction of the near shore area just before (left) and after the slump (right). Lower left panel: Morphodynamic response of the dry beach and dune. Lower right panel: Preslump and post slump profiles obtained from interpolated grid data between $Y = -1.05$ m and -0.95 m.

In the time stacks generated from available video image time series only limited data points could be obtained to examine relation 3.14 since the erosion rate $\Delta V/\Delta T$ cannot always be estimated accurately for two reasons:

1. Light conditions during the experiment change and as result the stereo algorithm (see Section 3.2) was not always successful in making a 3D reconstruction of the dune face area.
2. Though several time series of images have been collected, the length of these time series was usually relatively short containing only a few slumps. It was found that several detected slump events cannot be used for analysis since the time interval associated with the first slump cannot be determined (no information is available about the juncture of the preceding slump).

In the time stacks generated from available video data 43 slump events are detected and for 13 slump events the volume change can be estimated with stereo video reconstructions successfully. The time interval associated with a slump event is estimated for 21 data points however only two data points are available for which both volume and time interval can be determined (see solid circles in Figure 3.12). These data points fall within the scatter cloud that is available from the profile measurements but the number of data points is too small to make any conclusion about a possible (linear) relation that might be present in the video data.

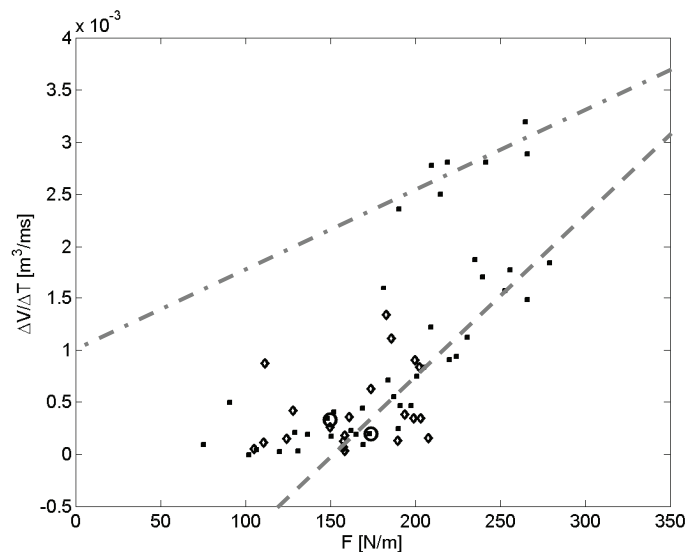


Figure 3.12 Dune face erosion rates from profile measurements and video reconstructions as function of average impact force. Profile measurements are indicated by the small solid squares. Data points from video reconstructions with stereo (two) and retreat areas (nineteen) are visualized by open circles and open diamonds respectively.

In order to increase the number of data points it is examined whether retreat surfaces of the dune crest (see Figure 3.13, left panel) can be related to the volume change associated with a slump event. In Figure 3.13, right panel it is shown that a reasonable linear relation is found ($\rho = 0.75$). Using this relation to generate extra data points results in 19 new points (see open diamonds in Figure 3.12). Most of the extra points coincide reasonable with data points obtained from profile measurements and stereo

reconstruction. However, the scatter in the data is large and most extra points are obtained (at the end of a test) in conditions when dune erosion rates are small. As a result a relation between wave impact and dune face erosion is not obvious from the video measurements.

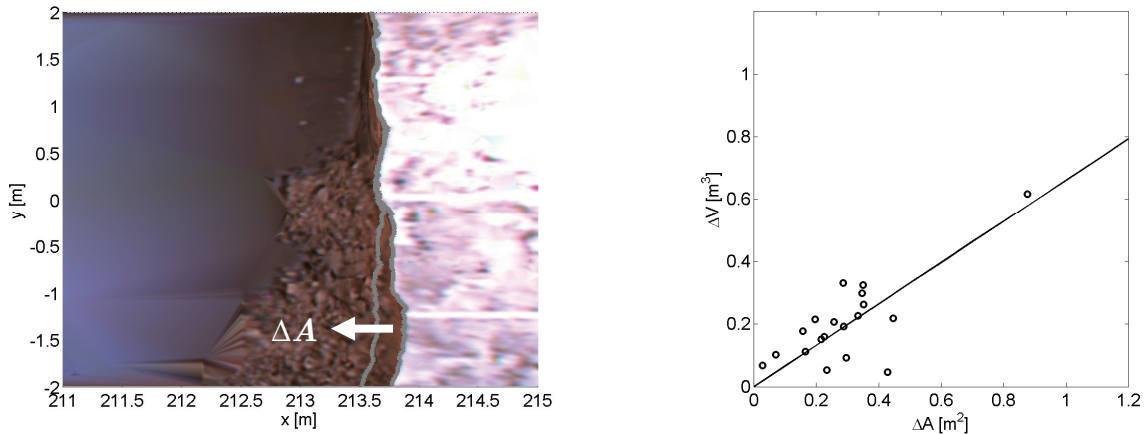


Figure 3.13 Left panel: Top view snap shot of near dune area during Deltaflume test T01 (interval E) just after a slump event. The most left line is the position of the dune crest just before a slump and the line on the right is the post slump dune crest. The area in between the black lines is the retreat area, which is related to the volume change ΔV . Right panel: Volume change (ΔV) as function of retreat area (ΔA). Open circles are data points obtained from (stereo) video images and the black line is a linear regression ($\rho = 0.75$).

3.4 CONCLUSIONS AND DISCUSSION

Collected stereo video data during the experiment are utilized to develop an algorithm that can make three dimensional reconstructions of the dune face and swash zone. Measurements with stereo cameras are relatively new within the near shore research field and give the possibility to make high resolution measurements in time and space without disturbing the monitored system. It is likely that a fast and robust stereo reconstruction algorithm gives the opportunity to reveal and explore new physics that will improve our understanding of the near shore.

Stereo video reconstructions are successfully compared with in-situ profile measurements. In addition, the reconstructions were utilized to examine a linear relation between the wave impact force on the dune face and the dune erosion rate. However, only limited data points could be obtained from the stereo reconstructions since light conditions over the experiment changed and as a result reconstructions with the algorithm were not always successful. Also, the length of the measured video time series was sometimes insufficient long to study the process of interest.

In order to improve the applicability of stereo video measurements for future research it is suggested to improve the algorithm performance by making it faster (reconstruction of a single image pair (1040 x 1392 pixels) takes about 10 minutes on a standard processor) and more robust (such that it can deal with video time series in which lighting conditions change). In addition it would be interesting to apply the algorithm

to measure near shore surface flows and wave transformation (see Clarke et al. (in preparation) and De Vries (2007) for preliminary results).

A linear relation between the wave impact force and the weight of sand eroded from the dunes as proposed by Fisher and Overton (1984) is also found for the large scale dune erosion tests discussed in Chapter 2. At the start of a test this relation is different yielding a larger dune face erosion rate since waves are not impacting the dune face but instead they run over it causing flow drag based erosion. The dune face steepens up to a stage that waves start to impact it causing the episodically slumping of the dune face. Observations reveal that the dune face steepens till a critical slope is reached after which a new slump takes place.

Usually the (cross flume) length of slump is smaller than the flume width and the time interval between successive slumps increases as a test progresses. On a longer time scale the dune face retreats relatively uniform, which is explained by the accumulation of the sand from a slump in front of the dune face, which obstructs further dune erosion by direct wave attack.

Chapter 4

MODELING NEAR DUNE HYDRODYNAMICS^{VII}

4.1 INTRODUCTION

Improving the modeling of dune face slumping (Chapter 3) and inner surf sediment transports associated with foreshore evolution during a storm surge, requires a good understanding of near dune hydrodynamics. During a storm sand is episodically released from the dune face and falls on the beach where it is picked up by waves that transport the sediment further seaward. In Chapter 2 it was observed that in the direction of the dune face a shift in variance towards lower wave frequencies takes place, which was suggested to be related to (wave group) generated long waves. In addition, short wave reflections were found to be minimal (less than 3%) whereas long wave reflections were found to be significant (initially 75% and decreasing to 40% at the end of the 6 hours test duration).

In deep water, short wave energy, and therefore also radiation stresses, vary on the wave group scale. These temporally and spatially fluctuating radiation stresses are compensated by water level gradients that form a bound long wave, which is 180° degrees out of phase with the short wave envelope (Longuet-Higgins and Stewart, 1961). The bound long wave propagates and shoals with the wave group velocity (Battjes et al., 2004) and is released in the surf zone where the groupiness of the short waves disappears due to depth-induced breaking (Figure 4.1). In addition, the presence of wave groups causes the break point, defined as the location with most intensive wave breaking, to vary in time. This moving break point works like a wave paddle generating a free long wave (Symonds et al., 1982). Shoreward from the break point, released long waves propagate with the shallow water wave celerity, which results in a phase shift relative to the short wave envelope (Roelvink and Stive, 1989). As the water depth decreases further, the long-wave fronts become steeper and may eventually break (Van Dongeren et al., 2007). At the shoreline, remaining long waves reflect.

^{VII} This Chapter is based on a paper in conference proceedings: Van Thiel de Vries, J.S.M., Van de Graaff, J., Raubenheimer, B., Reniers, A.J.H.M. and Stive, M.J.F., 2006. Modeling inner surf hydrodynamics during storm surges, 30th International Conference on Coastal Engineering, San Diego, USA, pp. 896-908.

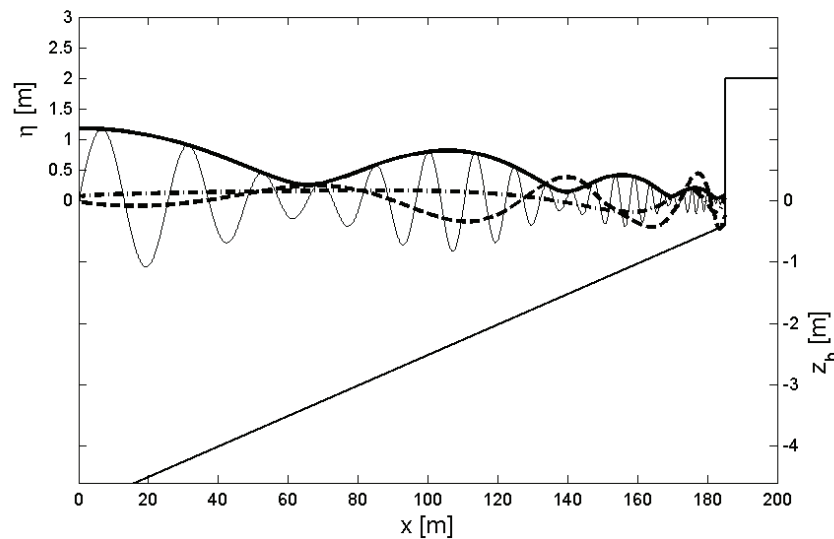


Figure 4.1 Waves normally incident on a sandy dune coast (thin solid line) with the corresponding short wave envelope (thick solid line), incoming bound (and released) long waves (dashed line) and outgoing shoreline-reflected free long waves (dashed-dotted line).

The aim of this chapter is to further examine whether near shore hydrodynamics can be related to wave group generated long waves and to what extent these long waves can be reproduced with a numerical (surf beat) model that solves hydrodynamics on a wave group time scale. It is hypothesized that short waves dissipate most of their energy towards the shoreline due to depth induced breaking whereas wave group generated long waves dissipate less strong and may even increase in height due to shoaling. As a result the long waves are expected to become more important to the hydrodynamics getting closer to the dune face.

In Section 4.2 the surf beat model is described that solves the hydrodynamics associated with the wave group time scale. First, the model is applied to simulate near dune hydrodynamics during the Deltaflume experiment (Section 4.3). In order to test model applicability in prototype conditions, field measurements containing both dissipative and reflective conditions are modeled (Section 4.4). Finally, the importance of the interaction between short waves and long waves is further studied by considering simulations with only free long waves and simulations with only short wave groups (Section 4.5). The chapter ends with conclusions and a discussion (Section 4.6).

4.2 MODEL DESCRIPTION

The Delft 3D surfbeat model solves nearshore hydrodynamics on the wave group time scale (Reniers et al., 2004a). The model is depth averaged and simulations presented in this chapter do not include the longshore direction. The numerical scheme was modified to switch between a momentum conservative scheme in flow expansions and an energy conservative scheme in flow contractions to simulate the rapidly varying

flows in hydraulic jumps and bores in the inner surf and swash zones (Stelling and Duinmeijer, 2003).

The hydrodynamics are solved using the nonlinear shallow water equations for continuity and conservation of momentum (NSWE):

$$\begin{aligned} \frac{\partial \eta}{\partial t} + \frac{\partial(hu^L)}{\partial x} &= 0 \\ \frac{\partial u^L}{\partial t} + u^L \frac{\partial u^L}{\partial x} &= -\frac{F_x}{\rho_w h} - g \frac{\partial \eta}{\partial x} + \nu_t \frac{\partial^2 u^L}{\partial x^2} - \frac{\tau_{bx}}{\rho_w h} \end{aligned} \quad (4.1)$$

where η is the water surface elevation, h is the water depth, u^L is the Generalized Lagrangian Mean (GLM) flow velocity, g is gravitational acceleration, t is time, and x the cross-shore position (positive onshore). The terms on the right hand side of the second equation (conservation of momentum) represent the wave and roller computed spatial radiation stress gradients F_x , forces due to water level gradients, a momentum diffusion term in which ν_t is the turbulent eddy viscosity related to wave breaking (Battjes, 1975), and bottom friction respectively.

The radiation stresses are computed with linear wave theory from wave energy (E_w) and roller energy (E_r) balances given by (Reniers et al., 2004a):

$$\begin{aligned} \frac{\partial E_w}{\partial t} + \frac{\partial E_w c_g}{\partial x} &= -D \\ \frac{\partial E_r}{\partial t} + \frac{\partial 2E_r c_w}{\partial x} &= D - D_r \end{aligned} \quad (4.2)$$

where c_g represents the wave group velocity, c_w is the phase velocity, and D and D_r represent dissipation of short wave energy (due to depth-induced breaking) and dissipation of roller energy, respectively.

Dissipation due to depth-induced breaking is computed by (Roelvink, 1993):

$$D_w = \frac{2\alpha E_w}{T_{m-1,0}} \left[1 - \exp \left[\left(-\frac{E_w}{\gamma^2 E_{ref}} \right)^{\frac{n}{2}} \right] \right] \quad \text{where } E_{ref} = \frac{1}{8} \rho_w g h_{bd}^2 \quad (4.3)$$

In these equations α is a coefficient $O(1)$, γ accounts for wave-height saturation, n relates the dissipation to the randomness of the incoming waves, and ρ_w is water density. The term h_{bd} is a water depth weighted over about one wavelength seaward from the cross-shore position of interest (Roelvink et al., 1995). Dissipation of roller energy is modeled with a constant β ($\beta = O(0.1)$) (Reniers and Battjes, 1997):

$$D_r = \frac{2g \sin(\beta) E_r}{c_w} \quad (4.4)$$

Finally, computed Lagrangian flow velocity is corrected for the short wave Stokes drift to obtain the Eulerian velocity (Walstra et al., 2000):

$$u^E = u^L - u^S \quad (4.5)$$

where u^L is the GLM velocity, u^E is the Eulerian velocity, and u^S is the Stokes drift computed from (Phillips, 1977):

$$u^S = \frac{(E_w + 2E_r)}{\rho_w h c_w} \quad (4.6)$$

4.2.1 Model boundaries

The two lateral boundaries are modeled as frictionless, impermeable walls. At the sea-floor, which is assumed fixed in time, a shear stress due to the combined effect of waves and currents is computed (Soulsby et al., 1993). Pressure is assumed to be zero at the water surface. An absorbing-generating boundary condition is applied at the seaward model boundary (Van Dongeren and Svendsen, 1997), which allows outgoing waves to leave the model domain with minimum reflection while incoming long waves can still be specified.

To calculate the incoming long wave time series, the measured water surface elevation and velocity time series are low-pass filtered with a high frequency cut-off computed from a characteristic wave period ($T_{m-1,0}$): $f_{split} = 0.5/T_{m-1,0}$. The low-passed time series are then used to separate incoming and reflected waves (Guza et al., 1984):

$$\eta_{in} = \frac{\eta\sqrt{gh} + Q}{c_g + \sqrt{gh}} \quad \text{and} \quad \eta_{out} = \frac{\eta\sqrt{gh} - Q}{c_g + \sqrt{gh}} \quad (4.7)$$

where η_{in} and η_{out} are the water surface elevation time series associated with the incoming and reflected long waves respectively, and Q is a discharge expressed as $Q = uh$. The incoming long waves are assumed to be bound and propagate with the wave group velocity, while the outgoing waves are assumed to be free and propagate with the shallow water wave velocity. In reality, however, it is expected that both free and bound incoming long waves are present, which introduces small errors in Equation 4.7. Incoming bound long waves that do not correspond to the wave group forcing are released (at the model boundary), so within the model domain, incoming long waves can be free or bound depending on the phase coupling between simulated short wave energy and water surface elevation.

Finally, the high frequency incident wave components from the measured variance spectrum at the model boundary are utilized to construct a short wave envelope, which is related to the short wave energy as:

$$E_w(t) = \frac{1}{2} \rho_w g A(t)^2 \quad (4.8)$$

where A is the short wave envelope that is obtained by taking the absolute value of the Hilbert transform of the water surface elevations. The resulting wave energy time series vary on the wave group time scale and are input to the short wave energy balance. The roller energy is set to zero at the offshore model boundary.

4.3 HYDRODYNAMIC SIMULATION FOR THE DELTAFLUME EXPERIMENT

To obtain more insight in the near dune hydrodynamics and associated shift in variance towards lower frequencies in this area, surf beat simulations are conducted for the last hour of test T01. Model performance is evaluated with measurements obtained from devices installed on the flume wall (see Chapter 2), which consist of ten pressure sensors and three electromagnetic current velocity sensors. The computational model starts at 41 m from the wave board and the input time series of incoming bound long waves and short wave energy are obtained from the collocated pressure and flow velocity measurements at this location. The still water level is set at 4.5 m above the flume's floor and the applied (non-erodible) profile is the measured profile after 6.0 hours of waves (end of interval E).

Time averaged model results are compared in Figure 4.2. The simulated wave transformation (Figure 4.2, second panel) compares reasonably well with measurements. However, the simulated short wave height is underestimated between $x = 41$ m and $x = 100$ m whereas the long wave variance is slightly overestimated in this area. In the inner surf zone, which is mainly studied in this section, the model tends to slightly underestimate the long wave height.

The correlation between the short wave envelope and long wave water surface elevations is negative at the offshore model boundary and increases towards the dune face in both measurements and simulations (Figure 4.2, third panel from top), which is in line with earlier observations (Abdelrahman and Thornton, 1987; Roelvink and Stive, 1989). Though model results and measurements show the same trend, the simulated correlation between long waves and short wave groups is underestimated over the main part of the profile whereas closer to the dune face the simulated correlation is too high.

The negative correlation offshore is explained by long waves that are bound to the short wave groups. However, also free long waves are present that suppress the negative correlation. These free long waves can be associated with reflections at the shoreline and by incoming free long waves that are not picked up by the short wave group forcing since short waves are (partly) breaking at/before the offshore model boundary. In shoreward direction the fraction of breaking short waves increases and the wave group forcing partly disappears. As a result bound long waves are released and now propagate faster than the short wave groups, resulting in an increase of the correlation coefficient towards the dune face. Close to the dune face both measurements and simulations reveal a positive correlation indicating that the highest short waves travel on top of the long wave crests.

The magnitude of the time and depth averaged (Eulerian) flow velocity increases over the foreshore in both the measurements and simulations (Figure 4.2, fourth panel from top). However, the simulated mean flow is underestimated on the foreshore whereas close to the dune face simulated mean flow exceeds the measurements. Note that the measured mean flow at $x = 205$ m should be interpreted with care due to the sparse number of flow measurements over depth at this location (see Section 2.4.2 for more details).

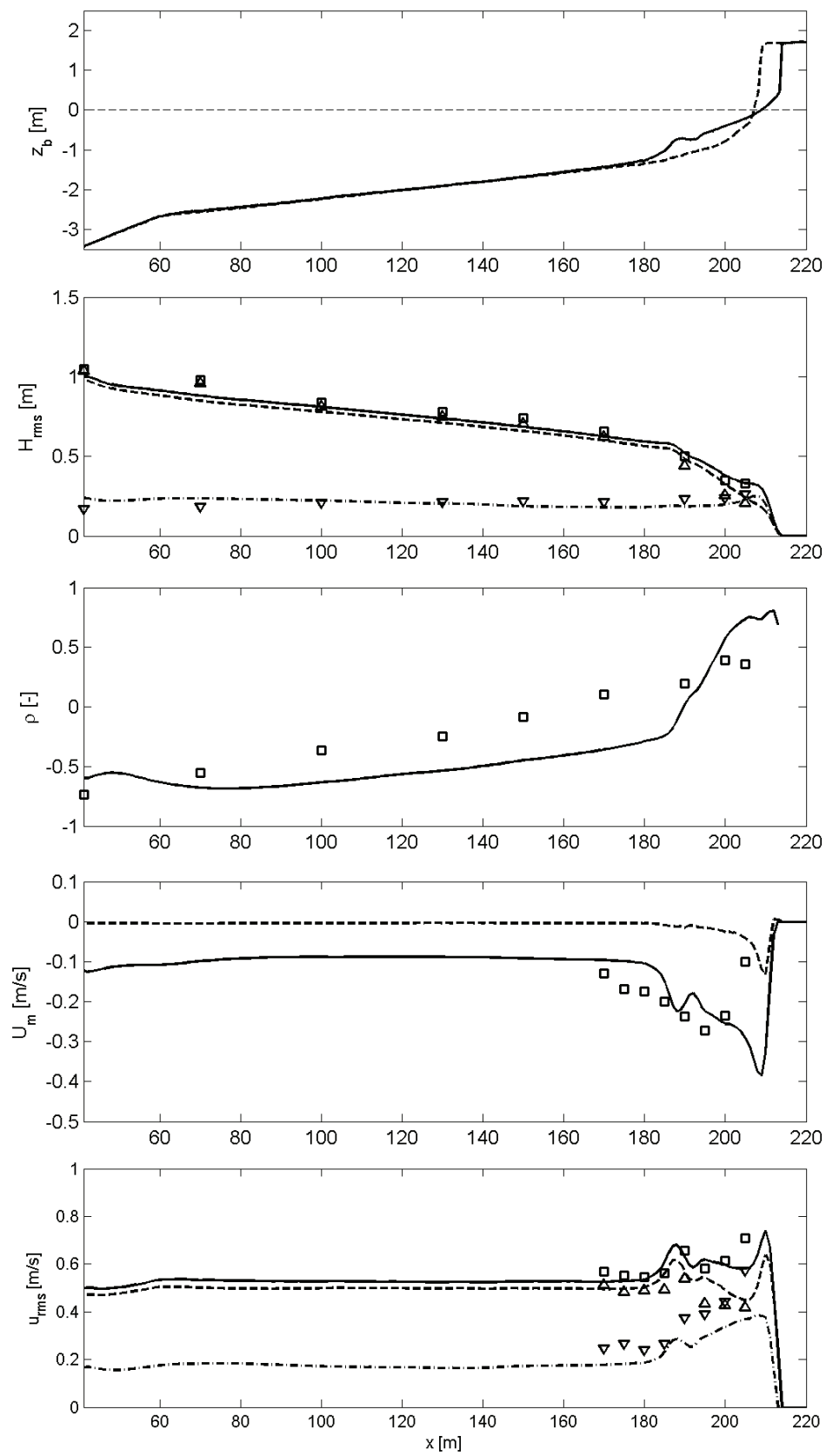


Figure 4.2 Upper panel: Applied profile during the simulation (thick solid line) and initial profile for test T01 (dashed line). The still water level in the flume is indicated by the dashed line. Second panel: Simulated wave transformation for the total wave height (solid line), the short wave height (dashed line) and the long wave height (dashed-dotted line) compared with the measured total wave height (squares), short wave height (upward triangles) and long wave height (downward triangles) over the last hour of interval E. Third panel: Simulated (solid line) and measured (squares) correlation between the short wave envelope and long wave water surface elevation. Fourth panel: Simulated Eulerian (solid line) and Lagrangian (dashed line) mean flow compared with the measured time and depth averaged flow (squares). Lower panel: Simulated orbital flow velocity for all waves (solid line), short waves (dashed line) and long waves (dashed-dotted line) compared with the measured total orbital flow (squares), short wave orbital flow (upward triangles) and long wave orbital flow (downward triangles).

Adding the Stokes drift velocity (related to the short wave and roller mass flux) to the Eulerian flow velocity gives the Lagrangian mean flow (see Equation 4.5), which is intuitively expected to be zero in a depth averaged model. However, a time and depth averaged offshore directed flow velocity is still present in the inner surf zone that can be explained by the presence of long waves. In shallow water, the depth under the long wave crest is larger than under the trough, which considering continuity may lead to on average larger offshore than onshore flow velocities. In addition, the long wave nonlinearity is expected to increase towards the shoreline. As a result the time interval associated with the long wave crest becomes relatively shorter in relation to the trough suppressing the mean offshore flow velocity. Continuity over a long wave cycle is guaranteed when:

$$\int_0^{t_c} hu^L dt = \int_{t_c}^{T_{long}} hu^L dt \quad (4.9)$$

where t_c is the time interval associated with shoreward flow velocities and T_{long} is the long wave period. The left hand side of Equation 4.9 corresponds to the integrated volume flux over the wave crest and should equal the integrated volume flux over the trough (right hand side Equation 4.9). Given the fact that h is larger (smaller) during the onshore (offshore) motion of a long wave, a time averaged offshore flow velocity results. The differences in integration intervals associated with wave nonlinearity for the onshore and offshore motion respectively probably suppress the mean offshore flow velocity.

Measured and simulated short wave orbital flow velocities are more or less constant in the cross-shore direction (Figure 4.2, lower panel) whereas long wave orbital flows increase towards the dune face over the developing foreshore. The simulated short wave orbital flow is slightly overestimated in the inner surf zone whereas the long wave orbital flow is underestimated. The total orbital flow velocity compares well with the measurements.

In the following, presented model results for test T01 are analyzed in more detail. First, simulated long wave water surface elevations are utilized to construct variance spectra that are compared with measured wave spectra in the Deltaflume (see Figure 4.3). At the offshore model boundary most of the measured variance is in the short wave frequencies and the simulated variance with the surf beat model is small but

compares reasonable with the measured wave variance below the split frequency ($f_{split} = 0.096$ Hz). In shoreward direction the measured (short wave) variance decreases, which is mainly explained by wave breaking. In addition, the variance below the split frequency (slightly) increases towards the shoreline and at 205 m from the wave board wave variance below the split frequency is larger than the variance above the split frequency.

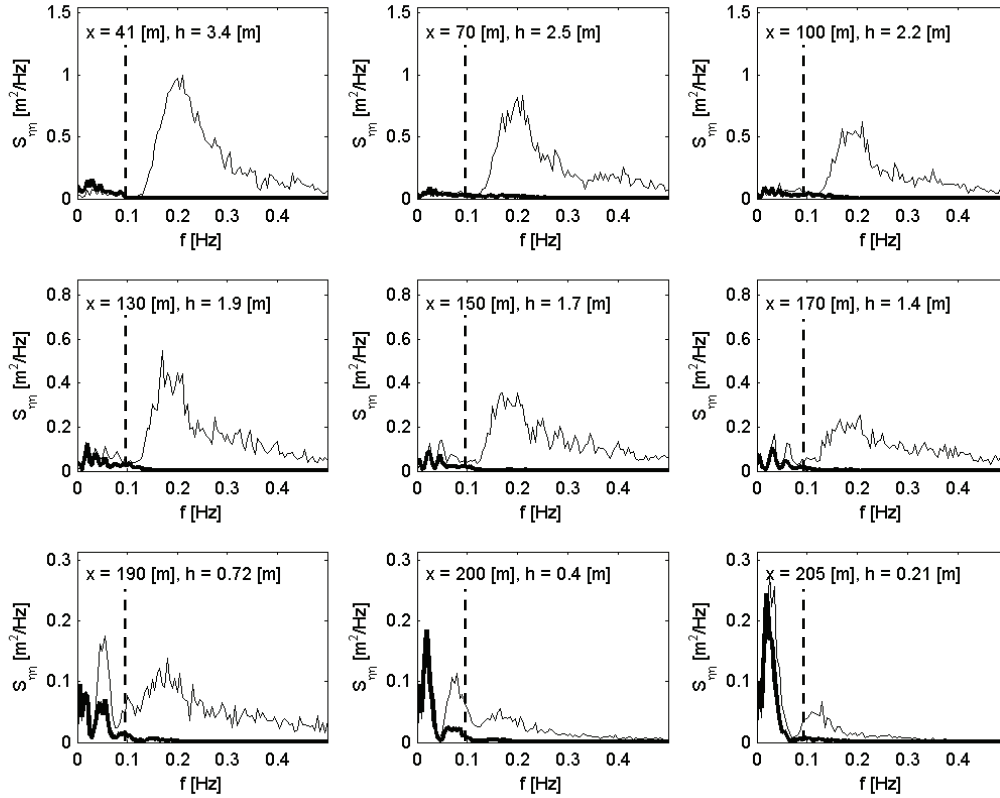


Figure 4.3 simulated (long) wave spectra with the surf beat model (thick solid line) compared with measured wave spectra including both long and short wave variance (thin solid line) for various cross-shore positions in the flume as indicated in the upper left corner of each panel. The split frequency is indicated by the dashed line.

The relative importance of the long wave variance increases in shoreward direction and at 205 m from the wave board it dominates the total variance. The model simulations reproduce the long wave variance and typically explain about 80 % of the measured variance below the split frequency. In addition, towards the shoreline the importance of simulated long wave variance further increases (see also the second panel of Figure 4.2) in relation to that of short waves, which suggests that mainly wave group generated long waves reach the dune face and erode it. It is remarked though that over the foreshore (shoreward of $x = 180$ m) short waves are dominant in generating the mean offshore directed flow (Figure 4.2, fourth panel), which is crucial for transporting eroded sand from the dune face further offshore (see Chapter 2, but also the results presented in Chapter 6). In addition, (mainly) short waves are breaking in the inner surf zone and are expected to generate a lot of turbulence that affects the sediment suspensions (see Chapter 5).

Finally, measured water surface elevations and flow velocities are compared with simulation results in Figure 4.4. At the offshore model boundary simulated water surface elevations generally have a depression in areas where the measured (mainly short wave) variance is high, indicating that simulated incoming long waves are (partly) bound. In the inner surf zone the correlation between measured and simulated time series improves. The measured flow time series close to the dune face are sensitive to noise, which might (partly) mask the agreement between measured and simulated flow time series.

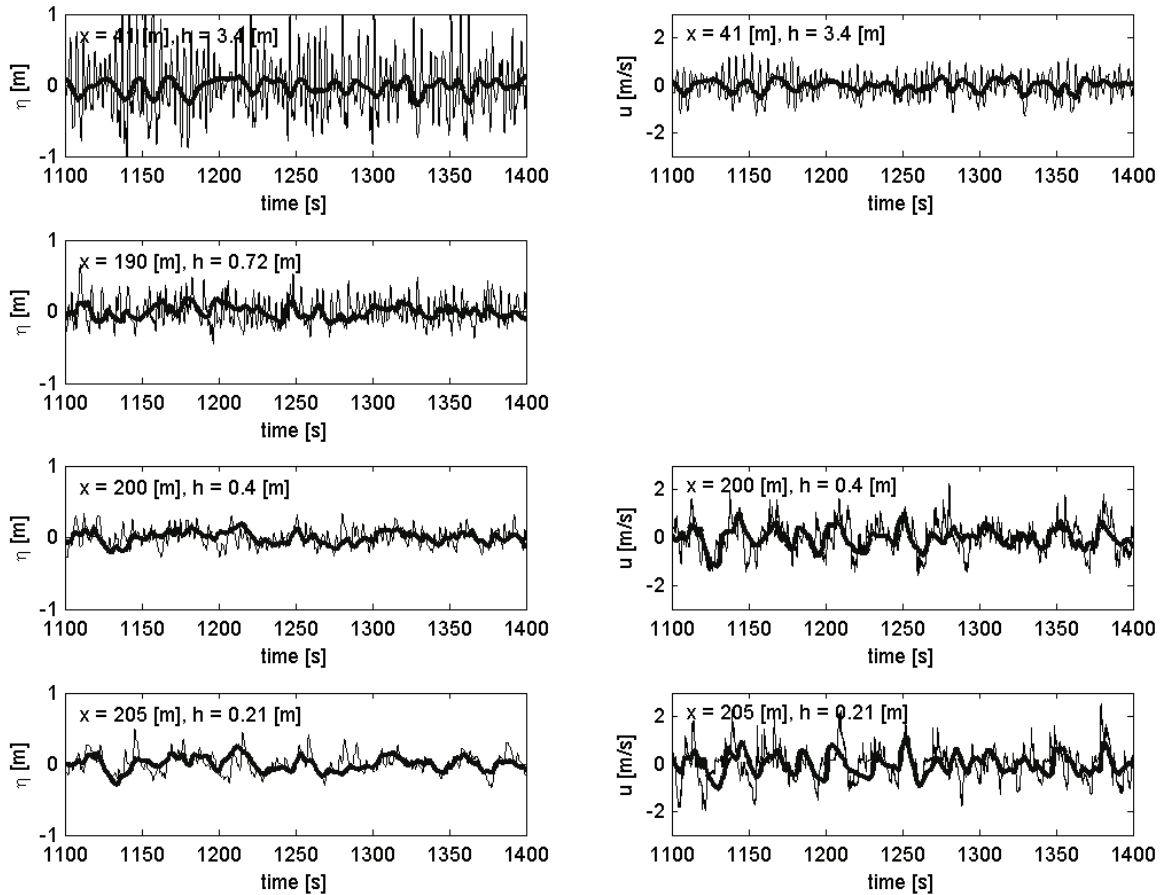


Figure 4.4 Simulated (thick lines) and measured (thin lines) water surface elevations (left panels) and flow velocities (right panels) as function of time at various cross-shore positions and water depths in the Deltaflume.

4.4 HYDRODYNAMIC SIMULATIONS FOR THE LA JOLLA FIELD EXPERIMENT

In the previous section it was shown that the shift in variance towards lower frequencies during the Deltaflume experiment can be explained by wave group generated long waves. In order to examine the importance of long waves to inner surf hydrodynamics in prototype conditions, this section compares surf beat model results with field measurements for both reflective and dissipative wave conditions. The field experiment considered was focused on measuring inner surf and swash zone hydrody-

namics and was conducted on a mildly sloped (about 0.02), fine grained (mean diameter about 0.2 mm) beach near La Jolla (California, USA) during September and October 2000 (Raubenheimer, 2002).

Eight buried pressure sensors and acoustic Doppler velocity meters (ADV) located 5 and 20 cm above the bed were deployed on a cross-shore transect (Figure 4.5). Data were sampled at 16 Hz for 3072 second (51.2 minute) bursts starting every hour. The position of the instruments relative to the surf and swash zones varied with the tide, which had a vertical range of about two meters. Measured wave angles at the most seaward sensor were within ten degrees of normal incidence.

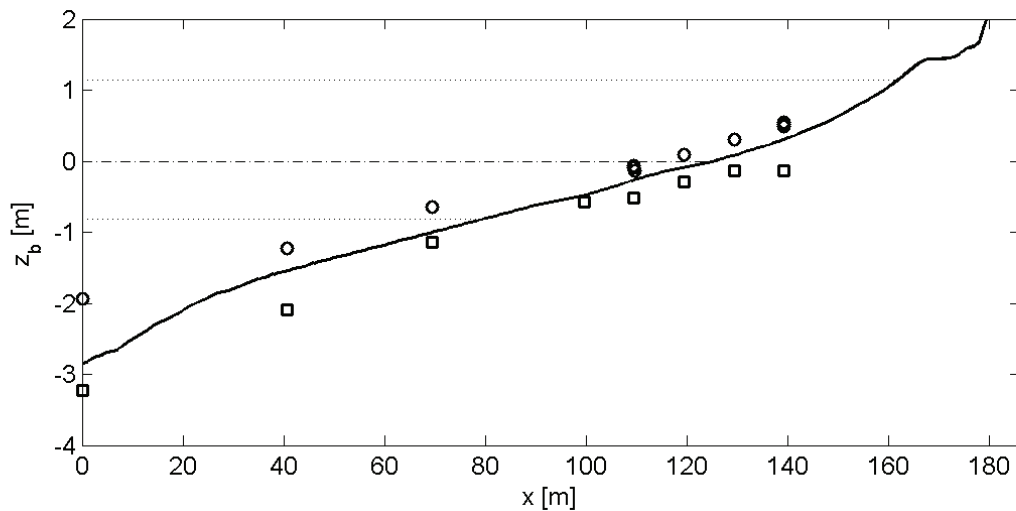


Figure 4.5 Cross-shore beach profile (solid line) and instruments deployed during the field experiment. Squares are buried pressure sensors and circles correspond to acoustic Doppler velocity meters (ADV). The mean water level is given by the dashed line and the tidal range is indicated by the dotted lines.

The beach and foreshore profiles were measured several times during the experiment with a differential global positioning system (GPS). In water depths greater than 50 cm, a sonar altimeter was used to measure the distance from the GPS to the seafloor. Using triangular interpolation, the bathymetric data was used to construct eleven profiles along the cross-shore transect.

Dissipative simulation

In this subsection the dissipative conditions observed on September 29th 2000 are simulated. The computational model starts at a water depth of 3.2 m and the measured wave height (H_{m0}) and characteristic wave period ($T_{m-1,0}$) at this location are 1.05 m and 8.73 s respectively. Imposed bound long waves and wave energy time series are obtained from the collocated ADV and buried pressure sensor measurements, available at the offshore model boundary. In the conditions considered here, the Iribarren number was approximately 0.3, which indicates spilling breakers and thus dissipative conditions (Battjes, 1974).

Simulated and measured sea-surface elevation variance spectra agree well for frequencies below the split frequency (Figure 4.6). The measured distribution of variance

spectra shifts toward lower frequencies with decreasing water depth. Low frequency energy (below the split frequency) dominates the measured and modeled spectra in the inner surf zone. The simulated water surface variance in frequencies larger than the split frequency could be owing to nonlinear interactions between long waves or to the presence of wave groups with envelope frequencies larger than the split frequency.

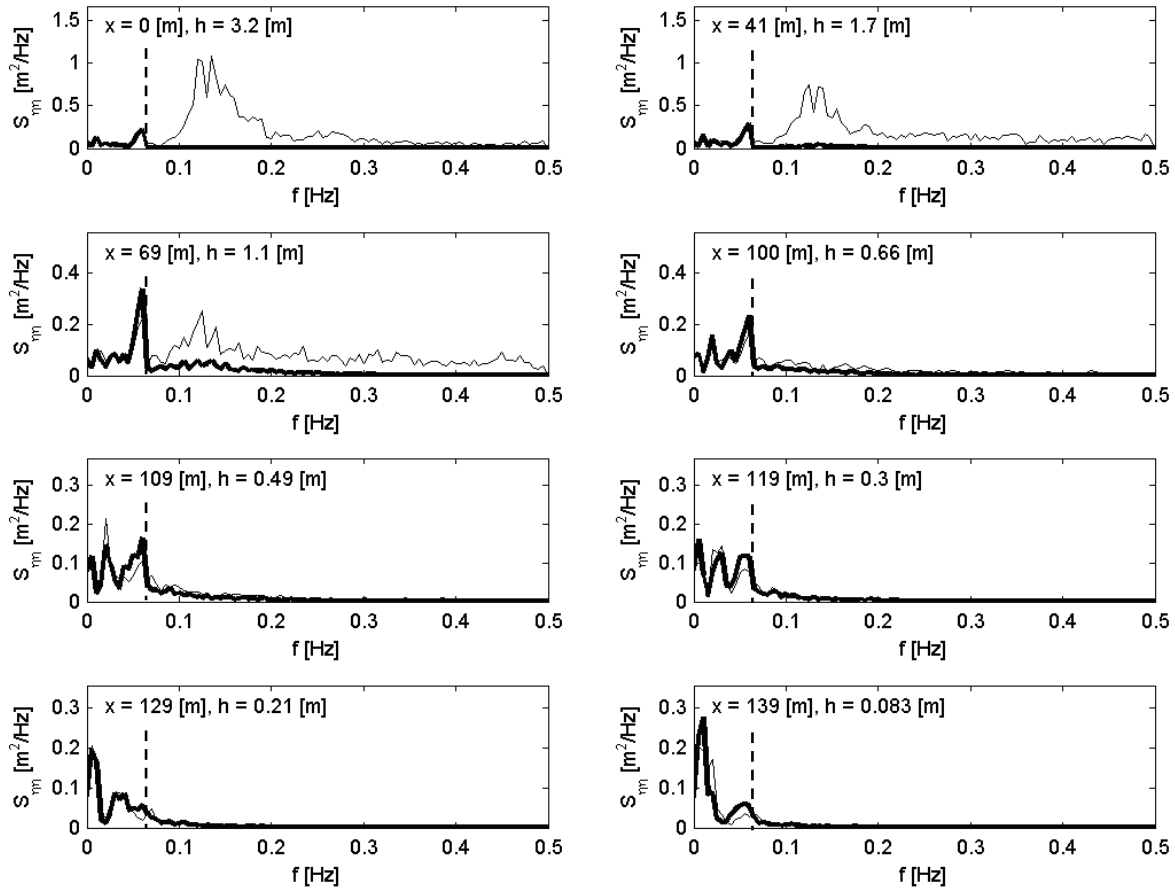


Figure 4.6 Measured (thin solid line) and simulated (thick solid line) variance spectra at different cross-shore positions and water depths as indicated in the upper left corner of each panel. The split frequency is indicated by the dashed line.

For water depths smaller than 0.7 m, measured and simulated water surface elevation time series are well correlated (Figure 4.7). Steep wave fronts are observed in both measurements and simulations and indicate that long waves may break in shallow water, as suggested by Van Dongeren et al. (2007). Measured and simulated flow velocity time series also compare well in the inner surf and swash zones (Figure 4.8). Strong accelerations and decelerations are observed in both measurements and simulations again indicating depth induced breaking of the long waves. At $x = 109$ m and $x = 139$ m multiple flow measurements over depth were carried out (see Figure 4.5). These flow time series mainly overlap (see Figure 4.8) and suggest that the instantaneous flow gradients are relatively small over depth.

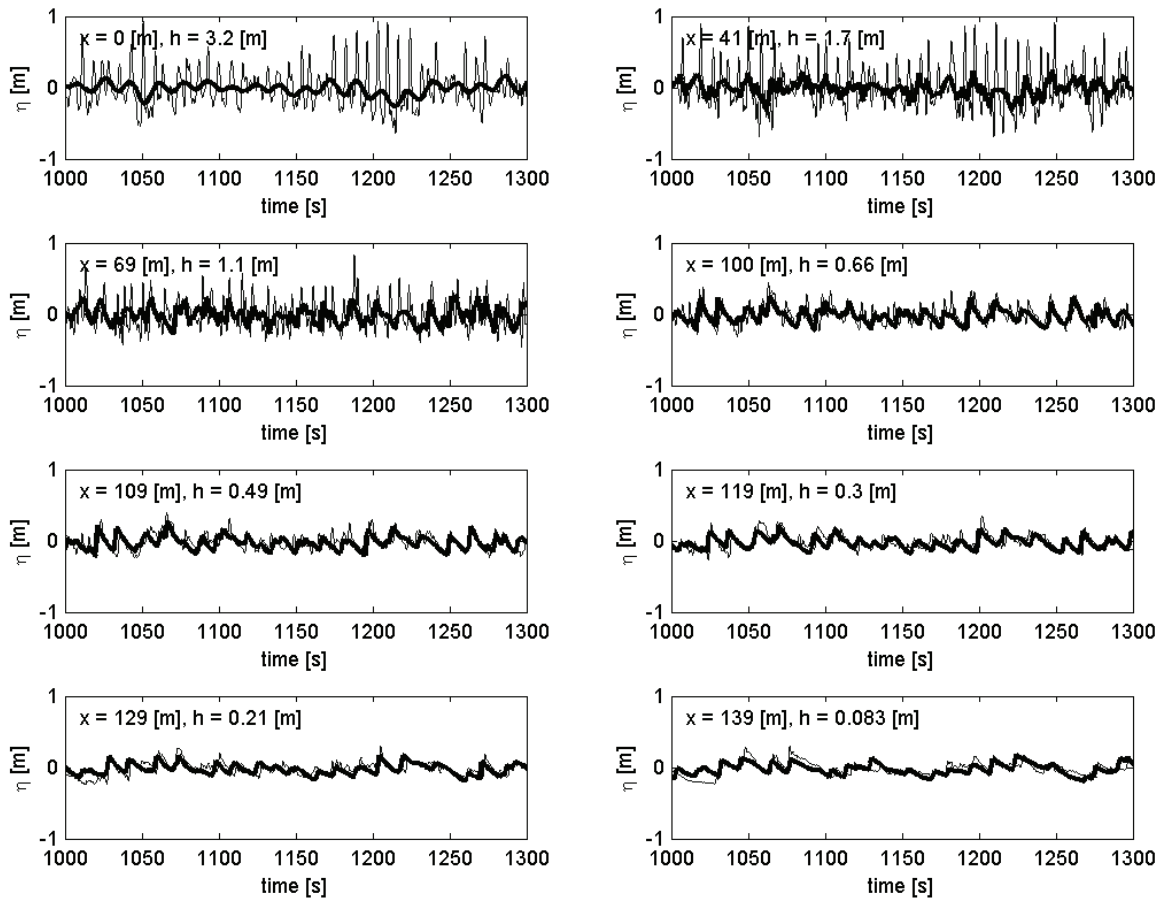


Figure 4.7 Measured (thin solid line) and simulated (thick solid line) water surface elevations at different cross-shore positions and water depths as indicated in the upper left corner of each panel.

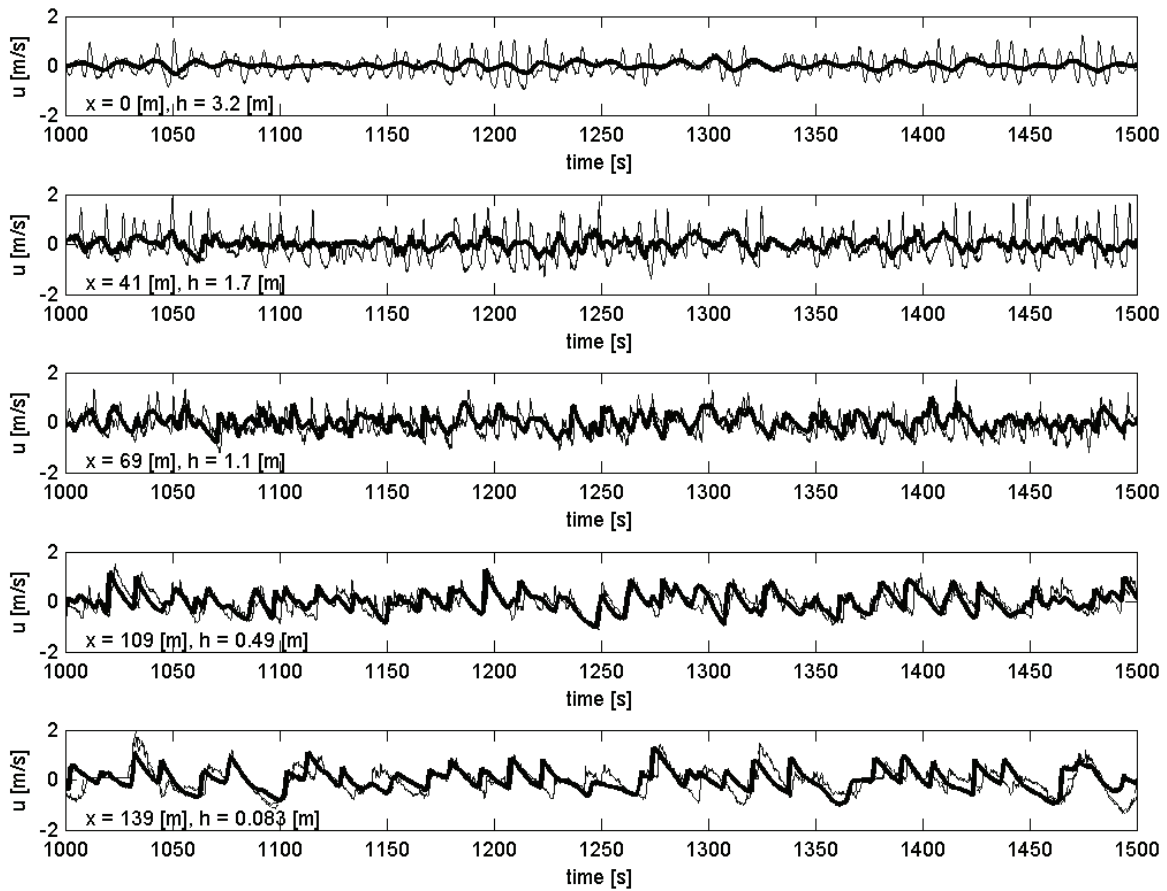


Figure 4.8 Measured (thin solid line, thin dashed line, thin dashed-dotted line) and simulated (thick solid line) flow velocities at different cross-shore positions and water depths as indicated in the lower left corner of each panel (at $x = 109$ m and $x = 139$ m multiple measurements at different vertical elevations are obtained, which coincide and cannot be distinguished from each other).

Reflective simulation

In this subsection the reflective conditions observed on September 27th 2000 are simulated. The computational model starts at a water depth of 3.8 m and the measured wave height (H_{m0}) and characteristic wave period ($T_{m-1,0}$) at this location are 0.41 m and 18.7 s respectively. Imposed bound long waves and wave energy time series are obtained from the collocated ADV and buried pressure sensor measurements, available at the offshore model boundary. In the simulation considered, the Iribarren number was approximately 1.4, which indicates reflective conditions (Battjes, 1974).

Similar to the dissipative conditions the measured spectra for the reflective conditions (Figure 4.9) show a shift in the variance distribution towards lower frequencies with decreasing water depth and simulated and measured sea surface variance compare well below the split frequency. However, at the most shoreward location in a water depth of 0.69 m still most of the measured sea surface variance is associated with short waves whereas in the dissipative simulation almost all variance at a comparable water depth (0.66 m, see Figure 4.6) is associated with long waves. As a result, for reflective conditions the surf beat model can only partly reproduce the measured vari-

ance in the inner surf zone. In addition short waves are expected to be important to both inner surf and swash zone hydrodynamics.

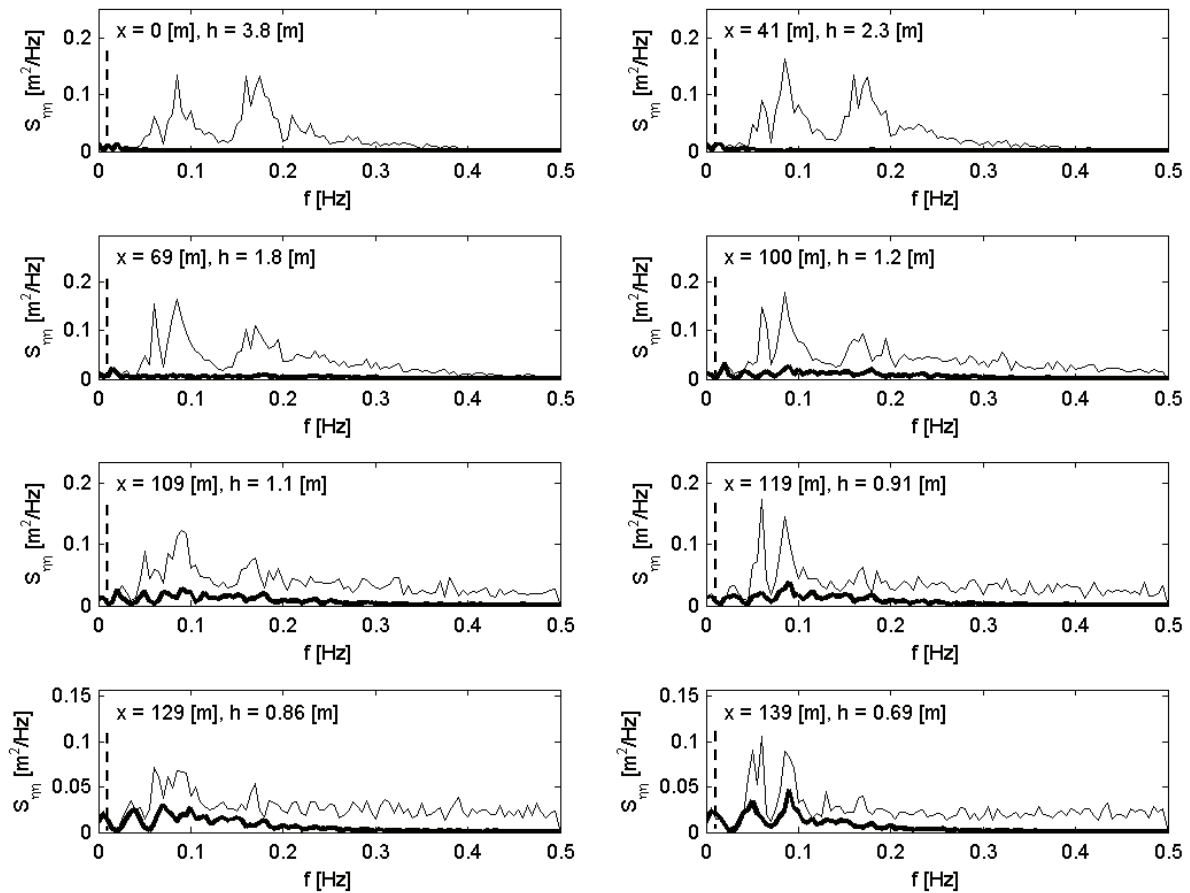


Figure 4.9 Measured (thin solid line) and simulated (thick solid line) variance spectra at different cross-shore positions and water depths as indicated in the upper left corner of each panel. The split frequency is indicated by the dashed line.

Comparing simulated sea surface elevations (Figure 4.10) and flow velocity time series (Figure 4.11) with measurements reveals that the agreement between measurements and simulations is less good than for the dissipative case. Although simulated time series to some extent correlate with the measurements it is clearly observed that still significant (short wave) variance is present, which is not solved for by the model.

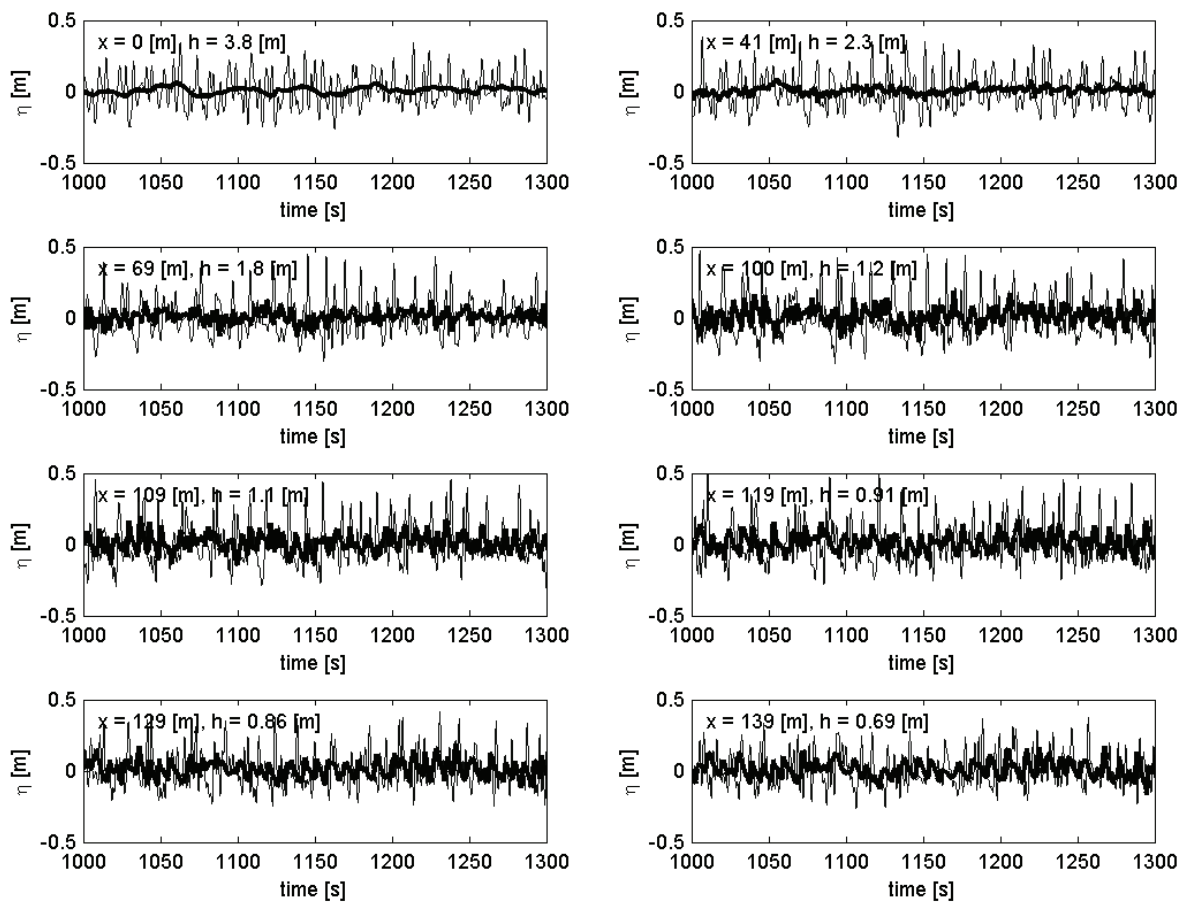


Figure 4.10 Measured (thin solid line) and simulated (thick solid line) water surface elevations at different cross-shore positions and water depths as indicated in the upper left corner of each panel.

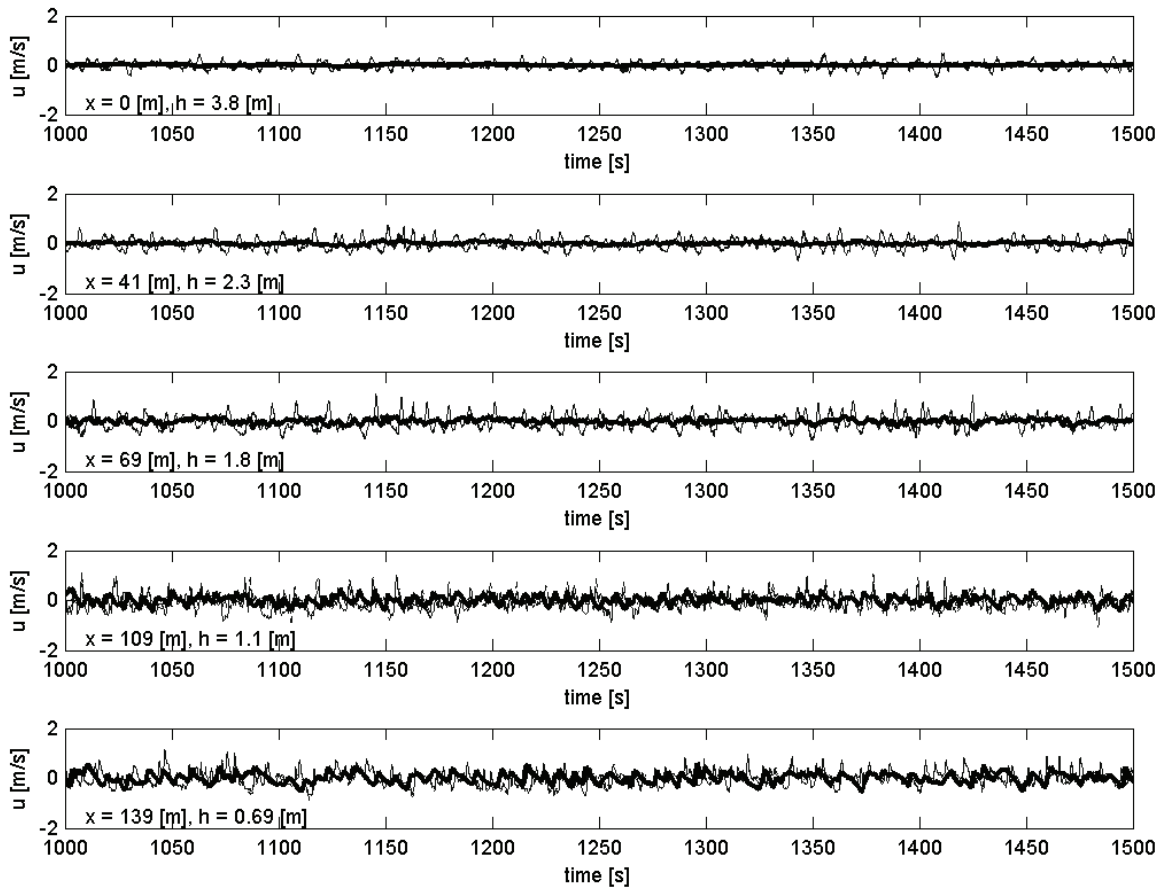


Figure 4.11 Measured (thin solid line, thin dashed line, thin dashed-dotted line) and simulated (thick solid line) flow velocities at different cross-shore positions and water depths as indicated in the lower left corner of each panel (at $x = 109$ m and $x = 139$ m multiple measurements at different vertical elevations are obtained, which coincide and cannot be distinguished from each other).

4.5 INTERACTION BETWEEN SHORT WAVE GROUPS AND LONG WAVES

To obtain more insight in the processes dominating near shore hydrodynamics, simulations for dissipative, reflective and dune erosion cases are conducted with the model driven by:

1. All wave components: nonlinear interactions can occur between long waves and short waves (results of these simulations were analyzed in detail in the previous sections).
2. Only long wave components: free long waves propagate from deep to shallow water. Nonlinear interactions occur only between pairs of long waves, without any interaction with short waves.
3. Only short wave components: near shore hydrodynamics result from wave group generated long waves that are released in the shoreward direction and that may interact with the short waves.

Considering the dune erosion case first, the predicted and measured variance spectra compare well for frequencies below the split frequency when the model is driven with either all wave components or short wave components only (Figure 4.12). The model overestimates the measured variance if only the long wave components are input. The measured and simulated water surface elevation time series are well correlated in 0.21 m water depth. However, when only the short wave components are input to the model, a small erroneous phase shift is visible between measurements and simulations.

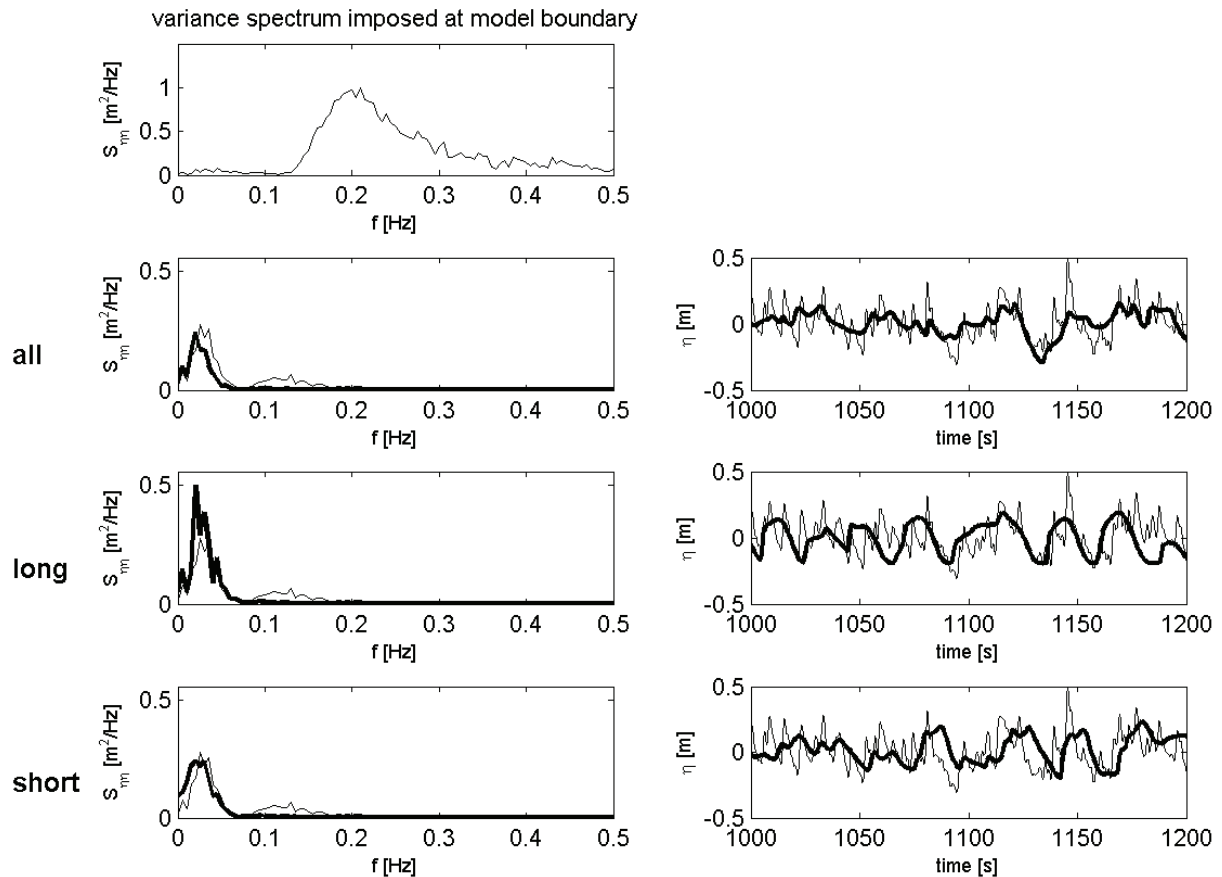


Figure 4.12 Measured (thin lines) and simulated (thick lines) variance spectra (left panels) and water surface elevation fluctuations (right panels) at 0.21 m water depth for the dune erosion case. The variance spectrum imposed at the model boundary is shown as a reference (upper plot). Results are shown for imposing all wave components (correlation ρ between measured and simulated water surface elevations is 0.50), only long wave components ($\rho = 0.24$) and only short wave components ($\rho = 0.19$).

For the dissipative condition near La Jolla, the simulated and measured variance spectra are similar at frequencies below the split frequency, when all wave components or only the long wave components are prescribed (Figure 4.13). Model-data agreement is significantly worse when only the short wave components are input at the seaward model boundary and for this case the inner surf variance (at a water depth $h = 0.49$ m) is only partly solved for by the model. A possible explanation can be found in the relative location of the offshore model boundary, which is in the surf zone where (short) waves are breaking and the groupiness of the waves has already

partly disappeared. It is remarked though that the best model-data agreement occurs when all wave components are input to the model (compare also the correlation between measured and simulated water surface elevations in Figure 4.13 for a model driven by all wave components ($\rho = 0.44$) and only the long wave ($\rho = 0.34$) components).

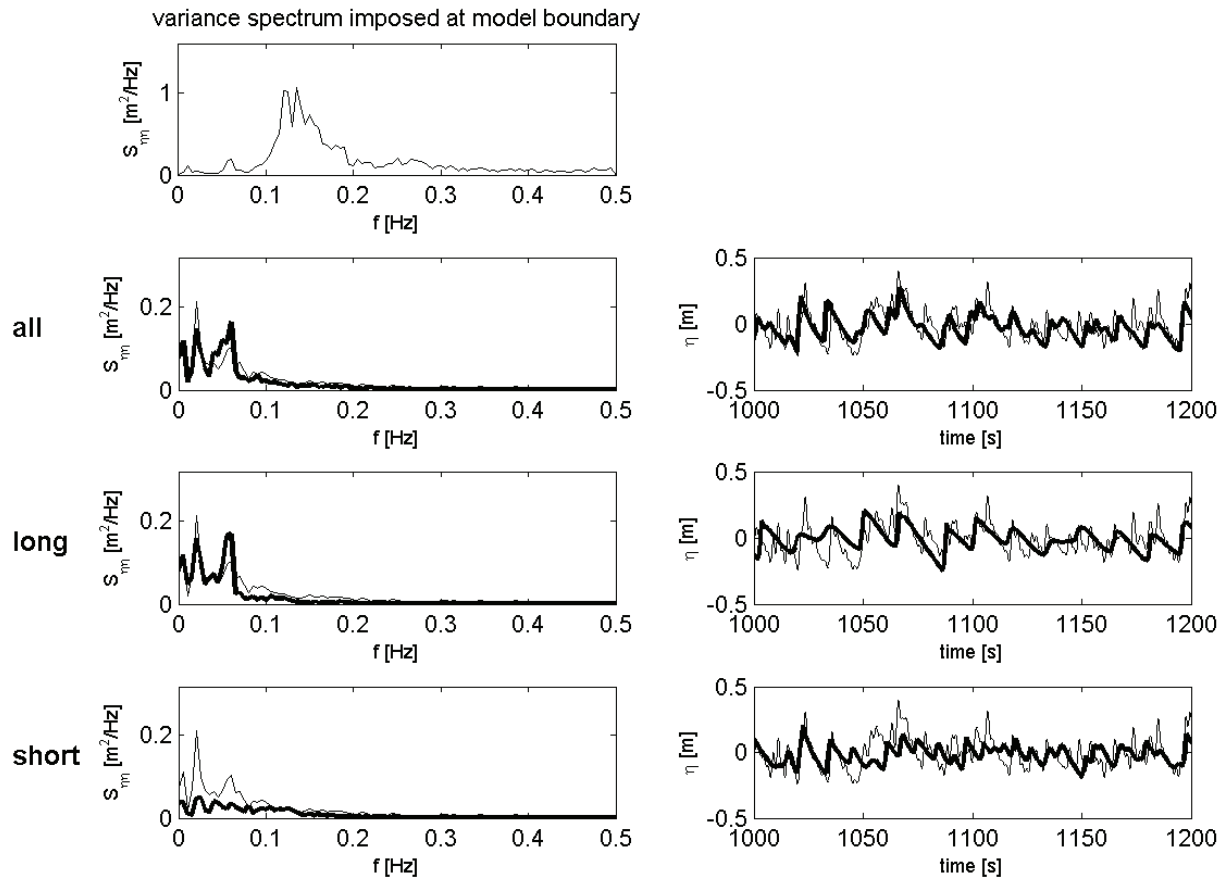


Figure 4.13 Measured (thin lines) and simulated (thick lines) variance spectra (left panels) and water surface elevation fluctuations (right panels) at 0.49 m water depth for the dissipative case. The variance spectrum imposed at the model boundary is shown as a reference (upper plot). Results are shown for imposing all wave components ($\rho = 0.44$), only long wave components ($\rho = 0.34$) and only short wave components ($\rho = 0.21$).

Considering the reflective conditions, the measured wave variance in 0.69 m water depth is partly solved when the model is driven with either all wave components or only the short wave components (Figure 4.14). Model-data agreement worsens when the model is driven with only the long wave components and the interaction between short and long waves clearly affects the simulation results. For all input conditions, the correlation between measured and simulated water surface elevation time series is worse for the reflective case than for the dissipative case.

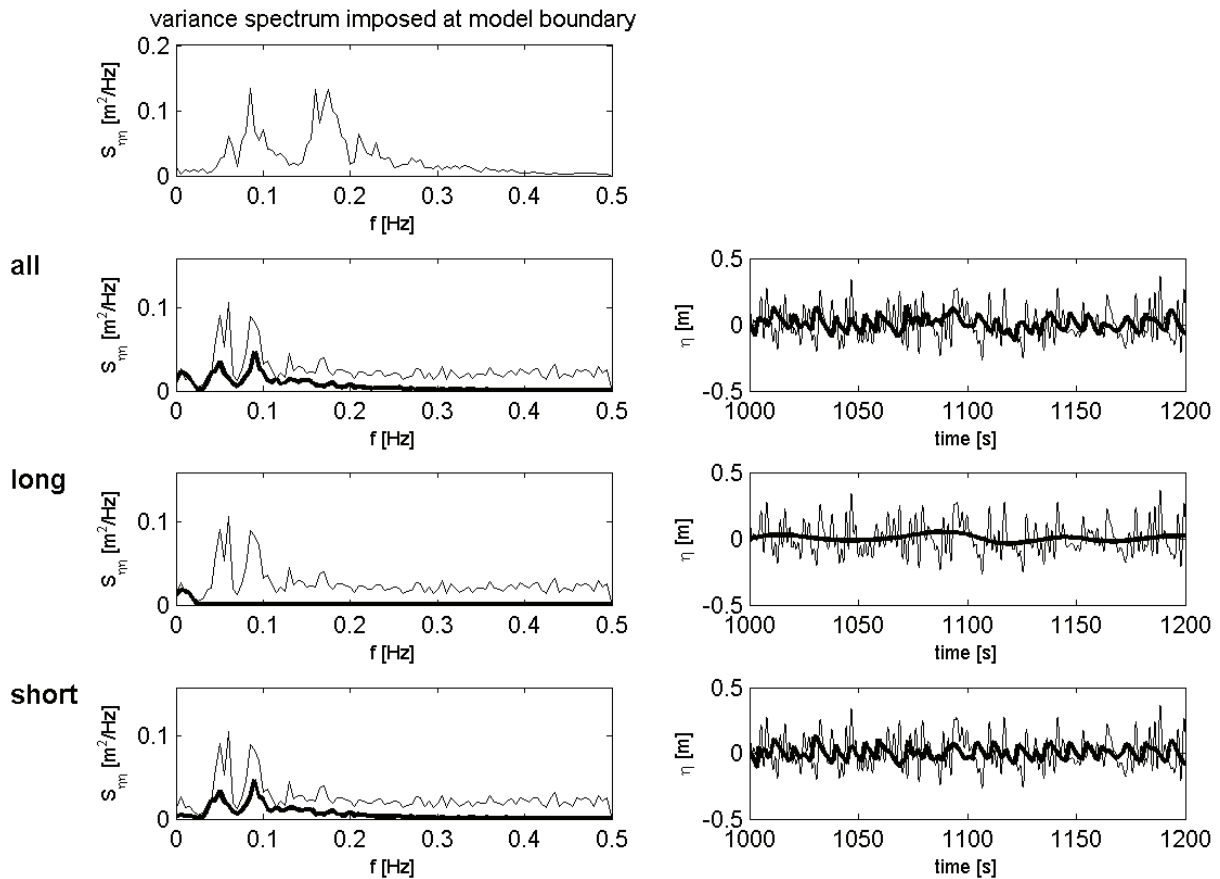


Figure 4.14 Measured (thin lines) and simulated (thick lines) variance spectra (left panels) and water surface elevation fluctuations (right panels) at 0.69 m water depth for the reflective case. The variance spectrum imposed at the model boundary is shown as a reference (upper plot). Results are shown for imposing all wave components ($\rho = 0.07$), only long wave components ($\rho = 0.12$) and only short wave components ($\rho = 0.03$).

4.6 CONCLUSIONS AND DISCUSSION

Near shore hydrodynamics are accurately simulated with the surf beat model for dissipative conditions in the field and for a large scale dune erosion test in the laboratory. It is concluded that the shift in variance towards lower frequencies in the direction of the dune face as observed in the Deltaflume experiment is explained by wave group generated long waves. In addition the long waves contribute to the mean offshore directed flow that transports eroded dune sand further seaward to build up a new foreshore. The contribution is relatively small in relation to the undertow associated with the short wave and roller mass flux, but increases towards the shoreline.

In addition it is found that:

- For reflective conditions, a relative small part of the measured near shore variance is associated with wave group generated long waves.

- Imposing all wave components (prescribing a slowly varying water surface elevation signal to the nonlinear shallow water equations and a wave group varying energy signal to the wave energy balance) results in the best model performance.
- A model driven with only short wave components results in accurate hydrodynamic predictions for the dune erosion test.
- A model driven by only long waves, results in good predictions of the near shore hydrodynamics for the dissipative case. However, this is probably related to the position of the model boundary, which is in the surf zone where the short wave groupiness has already partly disappeared due to depth induced breaking.

It is unclear whether the near shore dominance of long waves is mainly related to depth-induced breaking of short waves, or to the nonlinear transfer of energy from short to long waves. The best model-data agreement occurs when the model is driven with all wave components, and thus when nonlinear interactions are included in the simulations. However, imposing only long wave components at the model boundary gives reasonable predictions of near shore variance for both the dissipative and dune erosion conditions, suggesting that nonlinear interactions have little effect on the near shore hydrodynamics. In addition, for both the dissipative and dune erosion studies, the offshore model boundary is within the surf zone, onshore of the region in which significant interactions are expected. As a result the long waves may have already partly been released owing to depth-induced short wave breaking.

Chapter 5

MODELING NEAR DUNE SEDIMENT SUSPENSIONS^{VIII}

5.1 INTRODUCTION

In Chapter 2 it is found that the inner surf seaward transport is mainly driven by the time averaged flow velocity and sediment concentration that both increase towards the shoreline. Especially the mean sediment concentration rises sharply towards the dune face (up to 50 gr/l near the bed). Also it is observed that for a larger wave period more dune erosion takes place leading to an increase of the offshore directed time averaged sediment transport. This increase is mainly caused by higher sediment concentrations ($O(100\%)$ near the bed and $O(60\%)$ when averaged over the water depth), whereas the offshore directed flows are comparable.

The aim of this chapter is to further analyze the high sediment concentrations in the near dune area in order to develop an improved sediment concentration model that can be applied in process-based dune erosion models (as discussed in Chapter 6). In addition the focus is on a better understanding and modeling of the higher sediment concentrations associated with a 50% increase of the wave period.

In Section 5.2 collected mobile frame measurements during the Deltaflume experiment (Chapter 2) are analyzed in more detail to obtain insight in the physical mechanisms that cause the sharp rise in sediment concentration towards the dune face. It is hypothesized that these high sediment concentrations are explained by wave breaking induced turbulence that is injected in the water column at the bore front and reaches the bed as a pulse. The hypothesis is further examined (Section 5.3) ap-

^{VIII} This chapter is based on an article published in Coastal Engineering and a manuscript that is planned to be submitted to Coastal Engineering:

1. Van Thiel de Vries, J.S.M., Van Gent, M.R.A., Walstra, D.J.R. and Reniers, A.J.H.M., 2008. Analysis of dune erosion processes in large-scale flume experiments. Coastal Engineering, 55(12): 1028-1040.
2. Van Thiel de Vries, J.S.M. and Reniers, A.J.H.M., 2009. Modeling inner surf sediment concentrations during storm surges. Manuscript for Coastal Engineering, in preparation.

plying an intra wave 1DV sediment suspension model to assess the difference in sediment response for wave constant near-bed turbulence and wave varying near-bed turbulence (pulse approach). The 1DV model results are translated to a wave and depth averaged equilibrium sediment concentration formulation (Section 5.4) that in addition to flow drag also depends on the bore-averaged near-bed turbulence energy. The chapter ends with conclusions and discussion (Section 5.5).

5.2 DATA ANALYSIS

Sediment suspensions are usually explained by the flow drag exerted on the bed and in addition most sediment concentration models relate the amount of suspension to the near-bed (orbital) flows to a certain (e.g. the third) power (Bailard, 1981; Van Rijn, 1984; Nielsen, 1992). However, for the mobile frame measurements conducted during the Deltaflume experiment (see Chapter 2), the measured time and depth averaged sediment concentration poorly correlates with both the total near-bed flow velocity and the near-bed orbital flow velocity (see Figure 5.1). Therefore, it is likely that for this data set also other physical processes are important to sediment suspension.

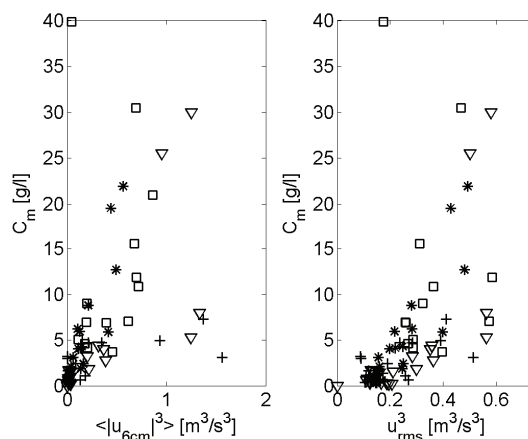


Figure 5.1 Time and depth averaged sediment concentration compared with near-bed total flow velocity (correlation $\rho=0.48$; left panel) and near-bed orbital flow velocity ($\rho=0.56$; right panel) for test T01 (asterisk), T03 (squares), T04 (pluses) and DP01 (triangles). The time and depth averaged sediment concentration is obtained by vertical integration of suction tube measurements below mean water depth using a same procedure as proposed in Equation 2.5 and assuming the sediment concentration at the bed equals the sediment concentration observed in the lowest suction tube.

The sediment concentration measurements are mainly obtained in the inner surf zone where predominantly breaking saw tooth shaped waves are present. In addition to flow drag these pitched forward bores may contribute to the sediment suspension in two ways:

1. Steep wave fronts under saw tooth shaped waves imply larger spatial pressure gradients and thereby increase the forces on the bed material possibly causing additional sediment suspension (Madsen, 1974). In literature this mechanism is

also discussed as the effect of acceleration skewness (Nielsen, 1992; Drake and Calantoni, 2001; Hoefel and Elgar, 2003) where it is assumed that the spatial flow gradients are relatively small in relation to temporal flow gradients and the flow is driven by pressure gradients.

2. Fronts of bores are unstable. As a result turbulence is generated that propagates from the water surface (surface roller) into the water column. Depending on the intensity and type of wave breaking, turbulent vortexes might be able to reach the bed and stir up sediment (Roelvink and Stive, 1989; Steetzel, 1993; Puleo et al., 2000; Reniers et al., 2004a). Also increased turbulence intensity over water depth causes extra mixing, which results in a higher time averaged sediment concentration (Van Rijn, 1993).

In the present data set it is not possible to distinguish between these two processes since they both occur at the front of a wave. As a consequence, in the following the combined effect of the pressure gradient and wave breaking generated turbulence on near dune sediment concentration is examined. It is assumed that the spatial steepness of the wave front ($\partial\eta/\partial x$) is (also) related to the intensity of wave breaking, which seems not unlikely from a physical point of view (Longuet-Higgins and Turner, 1974; Deigaard, 1993)

In the analysis a characteristic wave for each mobile frame measurement is derived. Next, the shape of this wave is related to the time and depth averaged sediment concentration in that measurement. Water surface elevation time series are divided into zero crossing waves after which the waves are rescaled, weighted and summed as follows:

$$\eta_r(x) = \left(\sum_{i=1}^{i=n_{waves}} \left(\frac{H_{z,i}^2}{\sum_{i=1}^{i=n_{waves}} H_{z,i}^2} \frac{\eta(t_{1,i}:t_{2,i})}{L_{z,i}} \right) \right) L_{z,m} \quad (5.1)$$

where $\eta_r(x)$ is the characteristic wave surface elevation in space and n_{waves} is the number of zero down crossing waves in a time series. $H_{z,i} = \eta_{max,i} - \eta_{min,i}$ where $\eta_{max,i}$ and $\eta_{min,i}$ are respectively the maximum and minimum water surface elevation within a specific zero down crossing wave surface elevation signal $\eta(t_{1,i}:t_{2,i})$, where $t_{1,i}$ and $t_{2,i}$ are the times of the two consecutive zero down crossings. $L_{z,i}$ is the wavelength of a zero crossing wave and $L_{z,m}$ is the weighted zero crossing wavelength over a measurement. The wavelengths and the conversion from time to cross-shore coordinate position is obtained assuming the wave celerity is constant over a zero crossing wave: $L_{z,i} = c_{w,i} T_{z,i}$ and $x(t_{1,i}:t_{2,i}) = t(t_{1,i}:t_{2,i}) c_{w,i}$ where $c_{w,i} = w_i/k_{w,i}$ in which w_i is the radian frequency and $k_{w,i}$ is the wave number associated with a zero crossing wave. A similar procedure is applied on the flow velocity time series by replacing $\eta(t_1:t_2)$ by $u(t_1:t_2)$ and $H_{z,i}$ by $U_{z,i} = u_{max,i} - u_{min,i}$ where $u_{max,i}$ and $u_{min,i}$ are respectively the maximum and minimum flow velocity within a specific zero crossing wave.

The water surface elevations associated with the characteristic waves in test T01 are plotted in Figure 5.2 for two locations. It is observed that the characteristic wave shape evolves from a mainly Stokes slightly pitched forward shaped wave at $x = 170$

m towards a strongly pitched forward shaped wave with a steep wave front at $x = 200$ m.

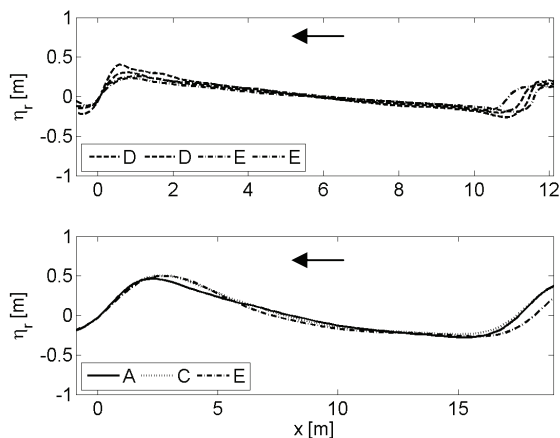


Figure 5.2 Rescaled water surface elevations associated with a characteristic wave shape for test T01 at $x = 200$ m (upper panel) and $x = 170$ m (lower panel). Legends indicate the interval in which a mobile frame measurement was obtained. Within a test interval multiple measurements can be conducted at the same location. The arrows indicate the propagation direction of the waves (from right to left).

In order to examine the effect of a changing wave shape on the near dune sediment concentration, the maximum surface slope $\partial\eta/\partial x$ in the characteristic wave shape is related to the corresponding time and depth averaged sediment concentration for each mobile frame measurement (Figure 5.3, left panel). Available measurements from test T01, T03, DP01 and T04, having different boundary conditions (T_p , spectral shape, and initial profile) are included. Apparently, the near dune sediment concentration correlates much better with the maximum wave surface slope than with flow drag (compare Figure 5.1 with left panel Figure 5.3), from which it can be concluded that spatial pressure gradient and/or wave breaking generated turbulence are likely to be important to the sediment suspension in front of the dune face.

Next, the depth averaged sediment concentration is related to the near-bed pressure gradient and a measure for the near-bed turbulence energy, which could give additional insight in whether high near dune sediment suspensions are principally related to an effect of the pressure gradient or the wave breaking induced turbulence.

The dynamic pressure under a wave decays with the distance from the water surface. The intensity of decay depends on the wave number and is more rapid for shorter waves than for longer waves. In the inner surf zone steep wave fronts are present that contain phase coupled higher (shorter) harmonics, which cause the pressure gradient to decay over depth. The maximum near-bed pressure gradient is estimated from near-bed pressure time series that are obtained applying the relation:

$$p_{bed}(x) = \eta_r(x) \frac{1}{\cosh k_w h} \quad (5.2)$$

where p_{bed} is the wave related near-bed pressure in meters water. The transformation is performed in Fourier space assuming all harmonics propagate with shallow water

wave celerity, which results in an expression for the wave number that reads $k_w = \omega/(gh)^{0.5}$.

Wave breaking induced turbulence at the water surface has to be transported towards the bed in order to affect the up-stirring of sediment. Roelvink and Stive (1989) used an exponential decay model with the mixing length proportional to H_{rms} to estimate the time averaged turbulence energy at the bed from turbulence at the water surface:

$$k_b = \frac{k}{\exp(h/H_{rms})-1} \quad (5.3)$$

where k_b is turbulence variance at the bed and k is the time averaged turbulence variance at the water surface.

Correlating the maximum near-bed pressure gradient $(\partial p_{bed}/\partial x)_{max}$ with the depth averaged sediment concentration slightly improves the correlation to $\rho = 0.77$ (Figure 5.3, middle panel). However, applying the turbulence decay model as an additional multiplication factor to $(\partial \eta/\partial x)_{max}$, the correlation with the sediment concentration improves more to $\rho = 0.84$ (Figure 5.3, right panel). Also the relation intersects the origin of the coordinate system, which means that in deeper water, $((\partial \eta/\partial x)_{max} \neq 0)$, the effect of the maximum surface slope on the sediment concentration vanishes since potential turbulence at the water surface does not reach the bed.

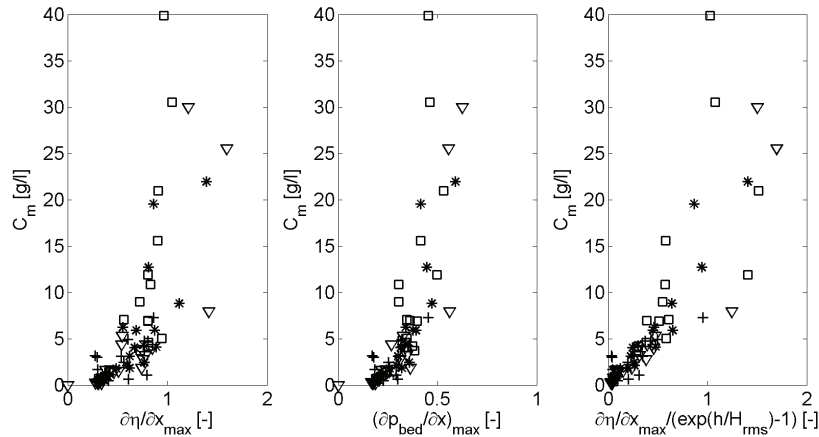


Figure 5.3 Time and depth averaged sediment concentration compared with the maximum wave surface slope (left panel; correlation $\rho=0.72$), the near-bed pressure gradient (middle panel; $\rho=0.77$) and the maximum wave surface slope multiplied with an additional factor representing turbulence energy decay over depth (right panel; $\rho=0.84$) for test T01 (asterisk), T03 (squares), T04 (pluses) and DP01 (triangles).

Considering higher sediment concentrations ($C_m > 10$ g/l) both the relation with the maximum near-bed pressure gradient and the measure for near-bed turbulence energy become more scattered. Data points in this range are relatively few and are obtained nearby the dune face ($x = 200$ m or $x = 205$ m) at the start of an experiment (interval B and C). It is unclear what causes the scatter, however dune face erosion rates in the initial phase of a test are large and irregular due to the episodically slumping of the dune face (see Chapter 3), which might affect the sediment concentration close to

the dune face and thereby masks a relation with the local near-bed pressure gradient or wave breaking generated turbulence.

It is often assumed that under the assumption of $u\partial u/\partial x \ll \partial u/\partial t$ the local flow acceleration can be used as a proxy for the pressure gradient. However, relating the time averaged sediment concentration in the inner surf with the maximum flow acceleration shows considerably more scatter compared to the relation with the maximum wave surface slope (compare results in Figure 5.4, left panels). It is found that the local flow acceleration accounts only for a part of the pressure gradient (Figure 5.4, right panel). This is especially true close to the dune face where the waves are highly nonlinear and spatially inhomogeneous.

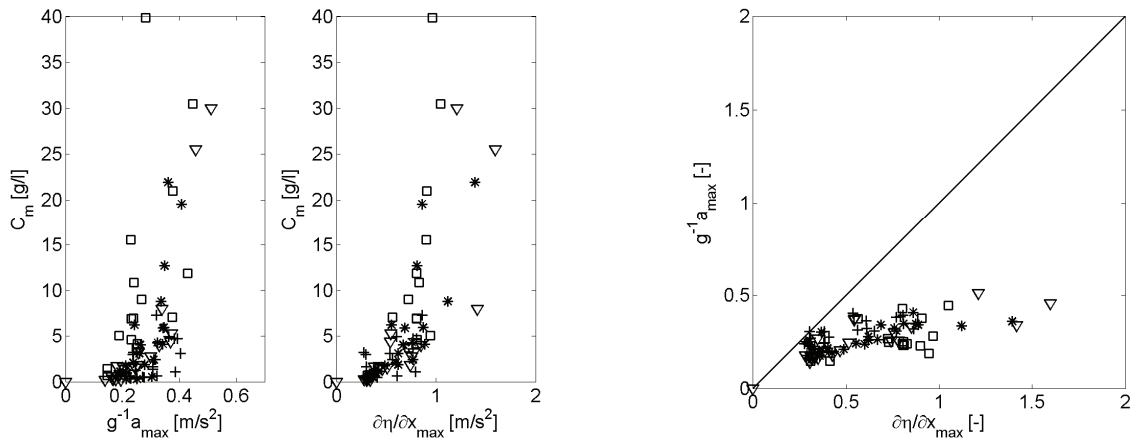


Figure 5.4 Left panel: Time and depth averaged sediment concentration compared with the maximum flow acceleration a_{max} under the characteristic wave (correlation $\rho=0.56$) and the maximum spatial steepness of this characteristic wave ($\rho=0.72$) for test T01 (asterisk), T03 (squares), T04 (pluses) and DP01 (triangles). Right panel: Comparison of the maximum flow acceleration with the maximum wave surface slope for test T01 (asterisk), T03 (squares), T04 (pluses) and DP01 (triangles).

Effect of the wave period

The mobile frame measurements revealed that with increasing wave period the depth and time averaged flows remain more or less the same whereas the time averaged sediment concentrations increase with $O(100\%)$ near the bed and with $O(60\%)$ when averaged over depth. As the high sediment concentrations in the near dune area have just been related to the spatial steepness of the wave front it seems logical to examine whether this steepness also clarifies the increase of the time averaged sediment concentration with a larger wave period.

Indeed it is found that for the larger wave period test (T03) the steepness of the wave front was on average larger (Figure 5.5, left panel). Comparison with Figure 2.13 reveals that the increase in the near-bed time averaged sediment concentration as function of the cross-shore position correlates reasonably well with the increase in wave steepness observed in Figure 5.5. It is hypothesized that steeper maximum surface slopes during test T03 indicate more intensive wave breaking, which causes that more turbulence is injected into the water column at the bore front and reaches the bed, increasing the suspension of sediment.

The latter is further examined by use of the pressure sensors spaced along the flume wall. A 4th order spline is fitted through the energy flux Ec_g , where E is the measured wave energy (obtained from pressure measurements) and c_g is the wave group velocity associated with the $T_{m-1,0}$ wave period at the wave board computed from linear wave theory. Dissipation due to wave breaking is estimated as $D = \partial Ec_g / \partial x$ from which the time averaged turbulence variance k is computed as $(D/\rho_w)^{2/3}$ following (Battjes, 1975) (Figure 5.5, right panel). It is shown that the test averaged energy dissipation due to wave breaking shoreward of $x = 170$ m is comparable for both tests. Considering that the number of waves in test T03 is smaller, since waves in test T03 have a larger wave period, means that the amount of dissipation in a single bore has to be larger on average in test T03. This seems to be in line with the hypothesis that steeper maximum surface slopes during test T03 indicate a different, more intensive, type of wave breaking.

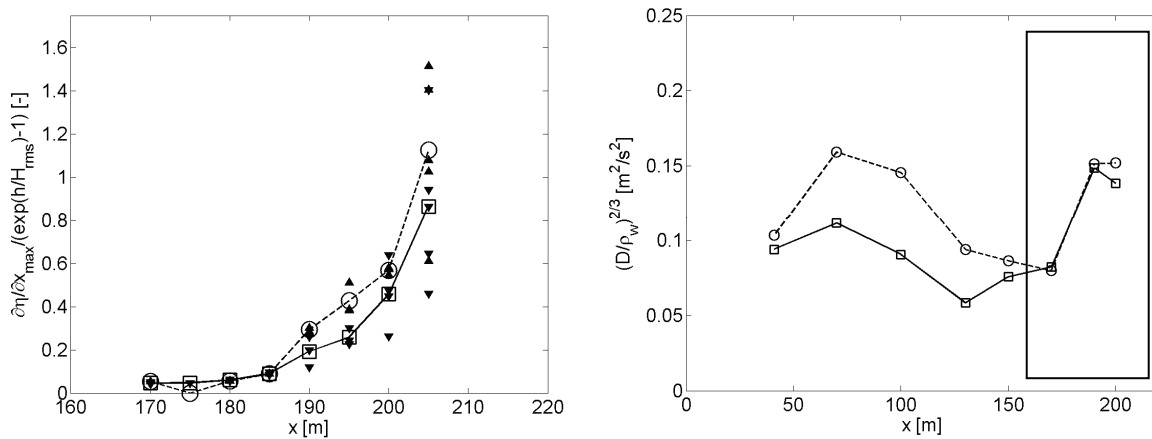


Figure 5.5 Left panel: Maximum wave steepness multiplied with an additional factor representing turbulence energy decay over depth as function of cross-shore position for test T01 (solid line) and test T03 (dashed line). Open markers are the average of all mobile frame measurements at a location within a test. Right panel: Test averaged turbulence energy at the water surface as function of cross-shore position for test T01 (solid line-squares) and test T03 (dashed line-circles). The black box corresponds to the cross-shore range plotted in the left panel.

5.3 1DV SEDIMENT SUSPENSION MODEL

Data analysis in Section 5.2 revealed that near dune sediment concentrations are not likely to be correctly reproduced with velocity based sediment concentration formulations. The inner surf mobile frame measurements showed a relatively poor correlation ($\rho = 0.48$) between the near-bed flow velocity and the time and depth averaged sediment concentration. In addition it was shown that the maximum wave surface slope correlates significant better ($\rho = 0.72$) with the time and depth averaged sediment concentration. The maximum surface slope is a substitute for the pressure gradient but can also be a measure for the intensity of wave breaking (Longuet-Higgins and Turner, 1974; Deigaard, 1993).

With available measurements from the Deltaflume it is not possible to conclude whether the pressure gradient or wave breaking induced turbulence explains the relative good correlation between the maximum wave surface slope and the sediment concentration. However, multiplying the maximum wave surface slope with an exponential decay model for turbulence (Roelvink and Stive, 1989) to estimate a measure for the near-bed turbulence intensity improves the correlation with the sediment concentration ($\rho = 0.84$). For that reason, in the rest of this chapter, the good correlation between the maximum wave surface slope and the sediment concentration is related to wave breaking induced turbulence instead of the pressure gradient.

Analysis of the effect of the wave period on the sediment concentration showed that the higher sediment concentration for a larger wave period test can be associated with a larger maximum surface slope (indicating more intense wave breaking). In addition, it was found that the wave averaged turbulence production near the dune face is comparable within the range of wave periods studied, which suggests the dissipation rate for larger wave periods is higher. Considering this, it is hypothesized that wave breaking induced turbulence is injected in the water column over a short (the bore) interval, which results in a wave varying intensity of near-bed turbulence with high peak values under the bore front. In addition, the sediment suspension is expected to respond nonlinearly to the turbulence intensity and as a result it is expected that the sediment concentration will be higher on average compared to a situation with constant turbulence intensity over the wave cycle.

In the following section the effect of wave varying near-bed turbulence on the sediment concentration is further examined with an intra wave 1DV sediment suspension model. Simulations with constant turbulence intensity over the wave cycle are compared to simulations with varying turbulence intensity to examine the second part of the hypothesis that the sediment concentration shows a nonlinear response to the near-bed turbulence intensity.

5.3.1 1DV Model description

In the proposed model, the sediment concentration can vary with time and vertical elevation and is described by the concentration balance equation:

$$\frac{\partial c}{\partial t} + w_s \frac{\partial c}{\partial z} + \frac{\partial}{\partial z} \left(D_v \frac{\partial c}{\partial z} \right) + \frac{\partial cu}{\partial x} = 0 \quad (5.4)$$

where c is the sediment concentration, t is time, w_s is the sediment fall velocity and z is the vertical elevation (zero at the bed and positive upward). D_v represents diffusion of sediment in the vertical and x is the cross-shore position (positive onshore)

At the interface between water and air (at the edge of the upper computational cell) it is presumed that the vertical sediment flux is zero. As a result, the sediment concentration in the upper cell is described by:

$$\frac{\partial c}{\partial t} - w_s \frac{c}{\delta z} + \frac{1}{\delta z} \left(D_v \frac{\partial c}{\partial z} \right) + \frac{\partial cu}{\partial x} = 0 \quad (5.5)$$

The sediment concentration near the bed (in the lowest computational cell) is computed differently for underload and overload. In a overload situation no upward sediment flux from the bed is present and the change in the near-bed sediment concentration is computed from local settling and mixing:

$$\frac{\partial c}{\partial t} + w_s \frac{\partial c}{\partial z} - \frac{1}{\delta z} \left(D_v \frac{\partial c}{\partial z} \right) + \frac{\partial cu}{\partial x} = 0 \quad (5.6)$$

Considering underload the near-bed hydrodynamics (flow and turbulence) indeed stir up sediment at the bed resulting in an increase of the near-bed sediment suspension. The entrainment of sediment is computed with an equilibrium sediment concentration formulation as proposed by Van Rijn (2007) that is adapted (see below) and multiplied with a calibration factor. Distinguishing between overload and underload follows by simply taking the maximum of sediment stirring and the equilibrium between local mixing and settling:

$$c_0 = \max(c, \gamma_{cbed} c_{stir}) \quad (5.7)$$

where c_0 is the imposed sediment concentration in the lowest computational cell, c is the sediment concentration computed from Equation 5.6 and γ_{cbed} is a calibration factor. The sediment concentration c_{stir} is related to up-stirring and is computed from the suspended related part of the equilibrium sediment concentration formulation of Van Rijn (2007):

$$c_{stir} = \frac{A_{ss}}{h} \left(\sqrt{(u + \gamma_{wave} u_{bed,2})^2} - u_{cr} \right)^{2.4} \quad (5.8)$$

In this expression h is the water depth u is the wave averaged flow, $u_{bed,2}$ is the near-bed wave orbital flow velocity^{IX} including the effect of turbulence (see below) and γ_{wave} is a calibration coefficient set to 1.0^X. The suspended load coefficient A_{ss} is computed as:

$$A_{ss} = \frac{0.012 D_{50} \rho_s D_*^{-0.6}}{((s-1)gD_{50})^{1.2}} \quad (5.9)$$

where ρ_s is the sediment mass density, D_{50} is the median grain diameter; s is the relative density (ρ_s/ρ_w) and D_* is the dimensionless particle size. The critical flow velocity u_{cr} in Equation 5.8 is described as $u_{cr} = \alpha u_{cr,c} + (1-\alpha)u_{cr,w}$ in which $u_{cr,c}$ is the critical flow velocity for steady flows based on Shields and $u_{cr,w}$ is the critical flow velocity for waves based on Komar and Miller (1975). The weighting coefficient α equals $u/(u+u_{bed,2})$.

In the proposed model the up-stirring of near-bed sediment is computed from only the suspended related part of the Van Rijn formulation. Also the formulation is extended to include the near-bed turbulence intensity. Following Reniers et al. (2004a),

^{IX} The wave orbital flow includes both short waves and long waves.

^X This means that time averaged flow and wave related flow have the same efficiency in stirring-up sand, which seems appropriate for intra wave simulations.

the near-bed wave breaking induced turbulence is included in the model via the near-bed wave orbital flow assuming the effectiveness of turbulence to stir up sediment is related to that of short waves:

$$u_{bed,2} = \sqrt{u_{bed}^2 + \gamma_{turb} k_b} \quad (5.10)$$

where γ_{turb} is a calibration factor set to 1.0 and k_b is the near-bed turbulence intensity. In addition to the near-bed turbulence contribution in picking up sand from the bed, the turbulent eddy viscosity is also related to sediment diffusion and thereby affects the shape of simulated concentration profile. The computation of the turbulence intensity and the estimation of the turbulent eddy viscosity are further discussed below.

Near-bed turbulence

The near-bed turbulence intensity can vary with time and is computed from turbulence production at the water surface due to wave breaking. The wave averaged turbulence intensity at the water surface is associated with the dissipation of roller energy as (Battjes, 1975):

$$\overline{k_s} = (D_r / \rho_w)^{2/3} \quad (5.11)$$

in which $\overline{k_s}$ is the wave averaged turbulence energy at the water surface and ρ_w is the mass density of water. D_r is the dissipation of roller energy computed from the work done by shear between roller and wave (Deigaard and Fredsøe, 1989; Stive and De Vriend, 1994):

$$D_r = \frac{2g \sin \beta E_r}{c_w} \quad (5.12)$$

where g is the acceleration of gravity, β is the wave front slope, c_w is the wave celerity and E_r is roller energy. The roller energy is estimated assuming all waves are breaking in the inner surf zone (which agrees with visual observations during the measurements discussed in Section 2.2) and following Svendsen (1984):

$$E_r = \frac{\rho_w A_r c_w}{2T} \quad (5.13)$$

where A_r is the roller volume computed as $0.9H_{rms}^2$ and T is the wave period of a characteristic wave (see Equation 5.1 and its explanation).

In the simulations with constant turbulence over the wave cycle the turbulence energy at the water surface equals the wave averaged turbulence energy in Equation 5.11 whereas in the model approach with wave varying turbulence intensity at the water surface it is presumed that the wave integrated turbulence is produced over the bore interval:

$$\text{Wave averaged turbulence: } k_s(t) = \overline{k_s} \quad (5.14)$$

$$\text{Wave varying turbulence: } k_s(t) = \begin{cases} k_s(t) = 0 & T_{bore} < t < T \\ k_s(t) = S_f(t) \bar{k}_s \frac{T}{T_{bore}} & t < T_{bore} \end{cases} \quad (5.15)$$

In expression 5.15, S_f is a shape function to smooth discontinuities^{XI} and T_{bore} is the time interval associated with passing of the bore front that is estimated as:

$$T_{bore} = \gamma_{T_{bore}} (t_{\eta, \max} - t_{\eta, \min}) \quad (5.16)$$

where $\gamma_{T_{bore}}$ is a calibration coefficient set to 1.0 and $t_{\eta, \max}$ and $t_{\eta, \min}$ are respectively the times related to the maximum and minimum water surface elevation within a wave.

The near-bed turbulence energy is obtained applying an exponential turbulence decay model (Roelvink and Stive, 1989). This means that spilling breakers are considered and it is assumed that the time scale of turbulence is substantially smaller than that of waves.

$$k_b(t) = \frac{k_s(t)}{\exp(h/L_{mix}) - 1} \quad (5.17)$$

In which the mixing length L_{mix} is expressed as the thickness of the surface roller near the water surface and depends on the roller volume A_r :

$$L_{mix} = \sqrt{A_r} = 0.95 H_{rms} \quad (5.18)$$

Diffusion coefficient

The diffusion coefficient is related to the turbulent eddy viscosity that is estimated from the vertical distribution of turbulence energy over depth:

$$D_v(z, t) = \nu_{v, back} + \gamma_{viscv} \nu_v(z, t) = \nu_{v, back} + \gamma_{viscv} L_{mix} \sqrt{k(z, t)} \quad (5.19)$$

where $\nu_{v, back}$ is a background viscosity set to 10^{-2} m²/s, L_{mix} is computed with Equation 5.18, γ_{viscv} is a calibration parameter set at 0.1 following Reniers et al., (2004b)^{XII} and $k(z, t)$ is expressed as:

$$k(z, t) = \frac{k_s(t)}{\exp((h-z)/L_{mix}) - 1} \quad (5.20)$$

^{XI} The shape function is expressed as $S_f(t) = A \cos(\pi t/T_{bore} - 0.5\pi)$ where t varies between zero and T_{bore} . A is an amplitude that assures the wave integrated turbulence equals $\bar{k}_s T$.

^{XII} In this paper the depth averaged turbulent eddy viscosity due to breaking waves is optimized to simulate undertow profiles. The authors find a calibration coefficient of 0.1. The eddy viscosity is not automatically a substitute for the sediment diffusion coefficient as is assumed here but research showed this not an unlikely assumption (see Van Rijn, (1993) page 7.53-7.55).

This expression converges to the near-bed turbulence intensity $k_b(t)$ described in Equation 5.17 for $z = 0$ m.

5.3.2 Simulations

Model simulations are performed for 86 mobile frame measurements conducted during test DP01, T04 and the repetition of test T01 and T03 (see Chapter 2 for more details). The measurements are mainly obtained in the inner surf that is defined as the region after the main breakpoint where (almost) all waves are breaking. In the tests considered the wave period, spectral shape and initial profile were varied. In this section the measurements of water pressure, mean sediment concentration over depth and mean flow velocity over depth are utilized to force the model and compare with model results.

Each simulation is associated with a mobile frame measurement and the wave varying sediment entrainment near the bed (Equation 5.8) is computed from the near-bed time averaged flow, orbital flow velocity and turbulence energy, which are estimated from the measurements. The time and depth averaged flow is constant over the wave cycle and is computed as described in Equation 2.5. The near-bed orbital flow and turbulence intensity, that both vary over the wave cycle, are obtained from the characteristic wave shape (Equation 5.1). The near-bed turbulence energy is computed from the characteristic wave shape applying Equation 5.11-5.18 and the near-bed orbital flow is computed from the characteristic water surface elevation as:

$$u_{bed}(t) = \eta_r(t) \frac{\omega}{\sinh(k_w h)} \quad (5.21)$$

where $u_{bed}(t)$ is the near-bed flow cycle, $\eta_r(t)$ is the time series of the characteristic wave surface ($\eta_r(t) = \eta_r(x)/c$) and ω is the angular frequency.

Sediment concentrations (as described in Equation 5.4) are solved for numerically with an upwind explicit numerical scheme on a staggered grid. In order to build up a sediment concentration vertical and reach stationary conditions each simulation is performed for ten wave cycles simply repeating the imposed near-bed equilibrium sediment concentration time series for a wave cycle. The model is solved for ten layers over depth (the vertical resolution varies for each simulation and depends on the water depth) and a time step of 0.001 seconds. The time step has to be this small due to the high, diffusion driven vertical sediment transports. The sediment fall velocity is constant in all simulations and is set at 0.022 m/s corresponding to a median grain diameter of 200 μm and a water temperature of 10°C.

Model optimization

The 1DV model has one remaining free parameter γ_{cbed} that is optimized for each mobile frame measurement to get a best fit between the time averaged simulation result and the measured sediment concentration vertical. The following equation is minimized:

$$e = \sum_{i=1}^{i=10} (c_{m,s}(z) - c_{m,m}(z))^2 \quad (5.22)$$

where e is the error that is minimized, i represents the i th suction tube, $c_{m,s}$ is the mean simulated sediment concentration and $c_{m,m}$ is the mean measured sediment concentration.

Optimizing the model for wave varying turbulence and wave constant turbulence respectively results in different values for γ_{cbed} . For the model with wave varying turbulence the standard deviation (σ) of γ_{cbed} is 1.23 and the mean value (μ) is 1.34 whereas in the model with constant turbulence over the wave cycle $\sigma = 2.85$ and $\mu = 2.54$. This means that the wave constant turbulence approach tends to predict smaller sediment suspension than the wave varying turbulence approach.

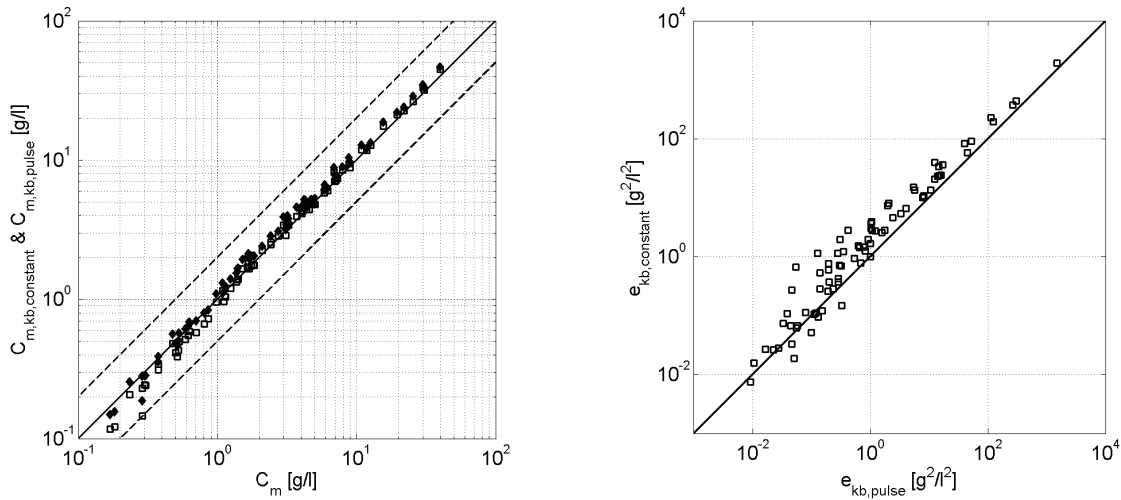


Figure 5.6 Left panel: Optimized model results for the wave varying turbulence model (open squares; $c_{m, kb, pulse}$) and the wave constant turbulence model (filled diamonds; $c_{m, kb, constant}$) compared with the measured time and depth averaged sediment concentrations (that are estimated by vertical integration of the suction tube measurements following a comparable approach as in Equation 2.5). The solid line corresponds to a perfect match between simulations and measurements whereas simulation results between the dashed lines are within a factor two with the measurements. Right panel: Comparison of the computed errors with Equation 5.22 for the wave varying ($e_{kb, pulse}$) and wave constant ($e_{kb, constant}$) turbulence model approach. Model errors are the same for both models along the solid line.

Time and depth averaged simulation results are favorably compared with measured time and depth averaged sediment concentrations in Figure 5.6 left panel. The correlation coefficient ρ for both the wave varying and wave constant turbulence model is 0.95. However, if the errors obtained with Equation 5.22 are compared (Figure 5.6, right panel) it is shown that the discrepancy between measurements and simulations is structurally larger for the wave constant turbulence approach, which is explained by on average too steep sediment concentration verticals (see e.g. Figure 5.9 as an example). This is found to be especially the case for higher sediment concentrations where the effect of near-bed turbulence on sediment suspensions is larger and the variation of turbulence over the wave cycle increases.

Considering smaller time and depth averaged sediment concentrations the wave constant turbulence model tends to give better results (Figure 5.6, right panel). These simulations are related to measurements obtained in relatively deeper water in which wave breaking is likely to be less intense and the resulting near-bed turbulence is expected to be of subordinate importance for the up-stirring of sediment.

In the rest of this paragraph differences in simulated sediment response for wave varying turbulence and wave constant turbulence are further examined by feeding the optimized γ_{cbed} values for the wave varying turbulence model in the model with wave constant turbulence intensity. It is remarked that this exercise can also be carried out in reverse order and it was found that the differences in response are equal (not shown here).

Intra wave model results

Intra wave model results are discussed for a mobile frame measurement obtained during test T03 at $x = 195$ m from the wave board in about 0.6 m water depth. The simulation results presented in Figure 5.7 show that more sediment ends up higher in the vertical for the wave varying turbulence model and as a result the wave and depth averaged sediment concentration is higher. In addition sediment settling in the wave varying turbulence approach is faster. This is observed in the lower panel of Figure 5.7, which shows that after the maximum sediment concentration in a wave cycle is reached, the concentration drops more rapidly in relation to the model with wave constant turbulence. The increased settling in the wave varying turbulence model is explained by the relative small sediment diffusion coefficient over the remaining part of the wave cycle after the bore front has passed (no turbulence is present over this part of the wave cycle). Finally the results in Figure 5.7 reveal that initially the sediment concentration vertical builds up with each wave cycle. For this specific case stationary conditions are reached in approximately six wave cycles after which the wave averaged sediment concentration remains constant. It is found that the number of wave cycles necessary to reach stationary conditions varies for each test and is larger for smaller time and depth averaged sediment concentrations.

The suspension mechanism is different for both model approaches as can be seen in Figure 5.8 that compares near-bed hydrodynamics with the near-bed response in sediment suspensions. In the wave varying turbulence approach sediment is brought in suspension over the bore front, which is associated with the peak in turbulent flow velocities whereas in the wave constant turbulence model sand is stirred up at the end of the wave cycle when offshore flow velocity is maximal.

Considering a model that does not include the time averaged flow (not shown) it was found that in both model approaches sediment is brought in suspension over the bore front. In the wave constant turbulence model this is explained by skewed near-bed orbital flow velocities. It seems that depending on the intensity of the offshore directed time averaged flow sediment is stirred up at a different phase of the wave cycle, which could reverse the direction of the wave related sediment transport.

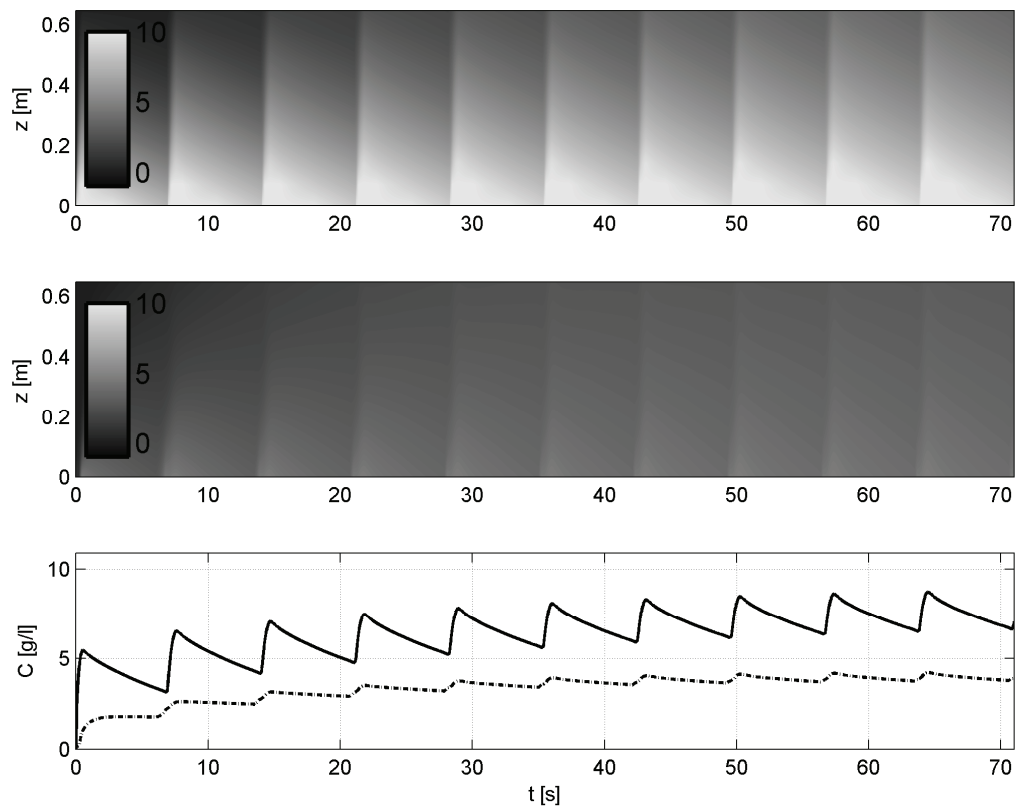


Figure 5.7 Intra wave model results for test T03 at $x = 195$ m in a water depth of about 0.6 m. Upper panel: Simulated intra wave sediment concentration [g/l] for wave varying turbulence as function of time and vertical position. Middle panel: Simulated intra wave sediment concentration [g/l] for wave constant turbulence as function of time and vertical position. Lower panel: Depth averaged sediment concentration as function of time for wave varying turbulence (solid line) and constant turbulence (dashed-dotted line).

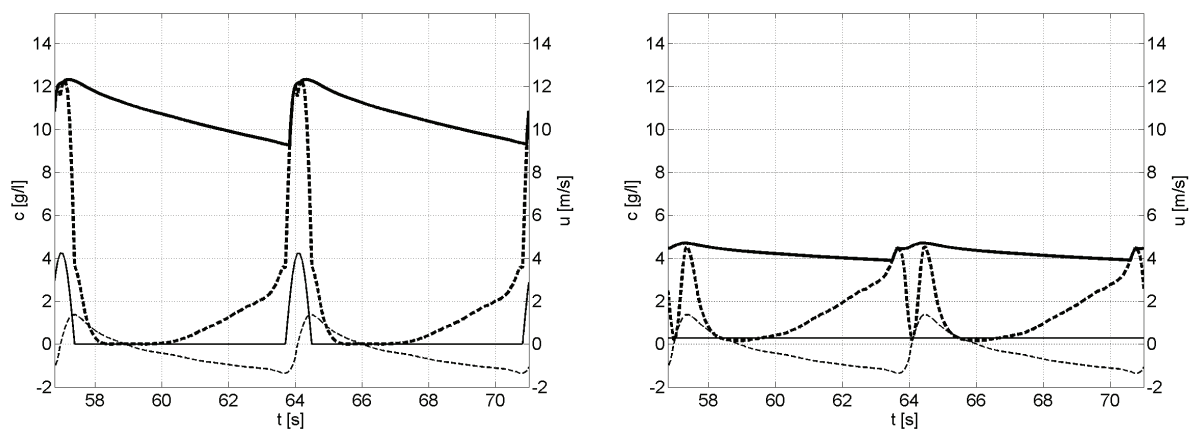


Figure 5.8 Near-bed sediment concentrations (thick solid line), near-bed sediment up-stirring (as described in Equation 5.8; thick dashed line), flows due to near-bed turbulence ($\sqrt{k_b}$; solid line) and near-bed flows (dashed line) as function of time for wave varying turbulence (left panel) and wave constant turbulence (right panel). The model results correspond to a mobile frame measurement during test T03 at $x = 195$ m in a water depth of about 0.6 m.

Finally, Figure 5.9 shows that the steepness of the simulated concentration vertical is substantially larger in the wave constant turbulence model as in the wave varying turbulence model. It seems this is mainly related to the different approach in computing the sediment diffusion coefficient. Considering wave varying turbulence sediment diffusion is small after bore front passing, which causes faster sediment settling (as already observed in Figure 5.7, lower panel) and larger vertical gradients in the sediment concentration (the upward diffusive transport of sediment is small since the mixing is small).

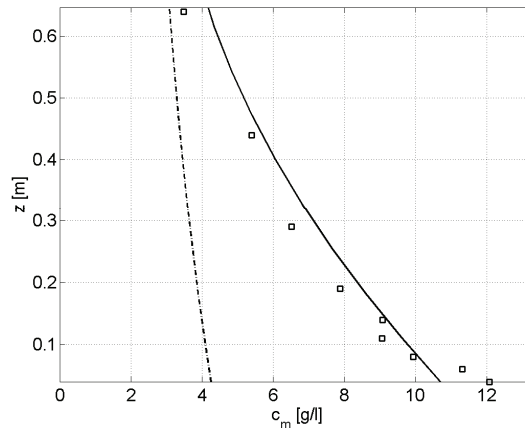


Figure 5.9 Simulated time averaged sediment concentrations for wave varying turbulence (solid line) and wave constant turbulence (dashed line) compared with measured time averaged sediment concentrations (squares) during test T03 at $x = 195$ m in a water depth of about 0.6 m.

All model results

Time and depth averaged simulation results for all 86 mobile frame measurements are further analyzed in Figure 5.10 that compares the ratio of simulated sediment concentrations with both model approaches as function of T/T_{bore} (that is used as a measure for the intensity of wave breaking). The simulation results can be split out in two parts. Considering $T/T_{bore} < 7$ the ratio of near-bed sediment concentrations is close to one, which suggests that both models show a comparable response near the bed (see also Figure 5.10 right panel). However, the ratio of the depth averaged sediment concentrations is smaller than one; and the highest sediment concentrations are simulated with a wave constant turbulence model. The mean of the measured sediment concentrations is 0.95 g/l and the results are associated with conditions in which wave breaking is less intense and the bore interval is still relatively large. But probably more important is that the water depth in these simulations is still substantial and as a result wave breaking induced turbulence hardly reaches the bed. Sediment concentrations for the wave constant turbulence model are higher since sediment settling in the wave varying turbulence approach is faster on average.

Simulation results for $T/T_{bore} > 7$ show a totally different response and the highest sediment concentrations are obtained with the wave varying turbulence model. The mean of the measured sediment concentrations is 8.8 g/l and the results are associated with conditions in which wave breaking induced turbulence is injected in the

water column over the bore interval, and reaches the bed as a pulse leading to extra sediment stirring and consequently higher time averaged sediment concentrations.

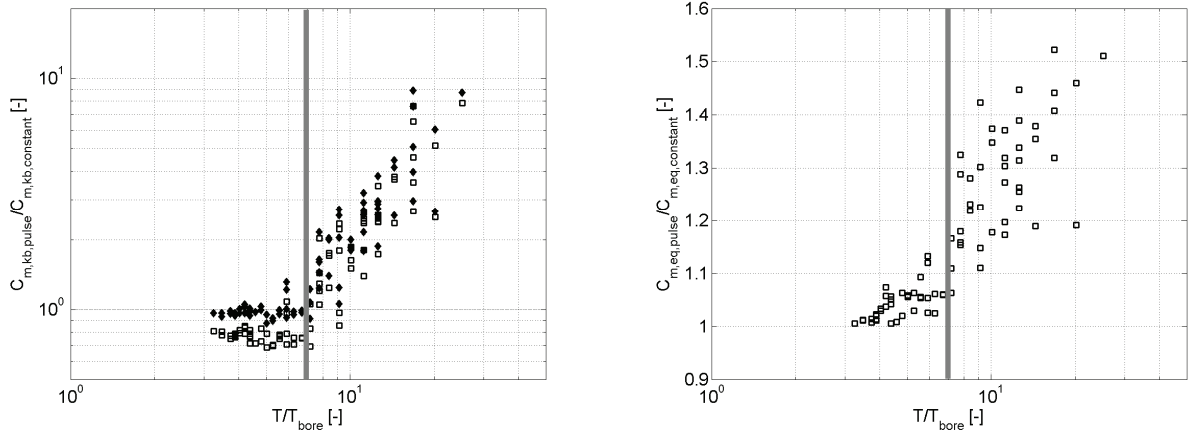


Figure 5.10 Left panel: The ratio of simulated sediment concentrations with respectively wave varying turbulence ($C_{m,kb,pulse}$) and wave constant turbulence ($C_{m,kb,constant}$) as function of T/T_{bore} . Filled diamonds concern time averaged near-bed sediment concentrations and open squares are related to the time and depth averaged sediment concentrations. Right panel: The ratio of simulated sediment up-stirring (with Equation 5.8) for respectively wave varying turbulence and wave constant turbulence as function of T/T_{bore} .

5.4 WAVE AND DEPTH AVERAGED SEDIMENT CONCENTRATION FORMULATION

The 1DV simulation results revealed that wave breaking induced turbulence that is injected in the water over the bore front and reaches the bed as a pulse can indeed lead to considerable higher sediment suspensions in relation to a model with constant near-bed turbulence. The difference response is a function of the water depth and T/T_{bore} . The latter can be explained as a multiplication factor for the wave averaged turbulence energy to obtain a measure for the bore-averaged turbulence energy.

In this section, the velocity based equilibrium sediment concentration formulation of Van Rijn (2007) is extended with wave breaking induced near-bed turbulence. As in the previous section two model approaches are proposed in which the sediment concentration is related to the wave averaged turbulence energy and the bore-averaged turbulence energy respectively. The proposed model is depth and wave averaged. In addition the bed load related part of the Van Rijn expression is also included and extended with near-bed turbulence:

$$c_{eq} = \frac{A_{sb}}{h} \left(\sqrt{\gamma_{flow} u^2 + \gamma_{wave} u_{rms,2}^2} - u_{cr} \right)^{1.5} + \frac{A_{ss}}{h} \left(\sqrt{\gamma_{flow} u^2 + \gamma_{wave} u_{rms,2}^2} - u_{cr} \right)^{2.4} \quad (5.23)$$

where A_{sb} is a bed load coefficient

$$A_{sb} = \frac{0.015h\rho_s(D_{50}/h)^{1.2}}{((s-1)gD_{50})^{0.75}} \quad (5.24)$$

The effect of wave breaking induced turbulence is again included via the short wave orbital flow ($u_{rms,2} = (u_{rms}^2 + \gamma_{turb}k_b)^{0.5}$) and the near-bed turbulence intensity depends on the model approach:

$$\text{Wave averaged near-bed turbulence energy: } k_b = \frac{\overline{k_s}}{\exp(h/L_{mix}) - 1} \quad (5.25)$$

$$\text{Bore-averaged near-bed turbulence energy: } k_b = \frac{\overline{k_s} T/T_{bore}}{\exp(h/L_{mix}) - 1} \quad (5.26)$$

Model optimization

The proposed sediment concentration formulation (Equation 5.23) has three free parameters γ_{flow} , γ_{wave} and γ_{turb} that need to be set in order to make simulations. Van Rijn, (2007) proposes $\gamma_{flow} = 1$ and $\gamma_{wave} = 0.64$ for irregular waves and $\gamma_{wave} = 2.56$ for regular waves^{XIII}. Here $\gamma_{wave} = 0.64$ is used since random waves are considered. The mobile frame measurements are utilized to optimize γ_{turb} by minimizing:

$$e = \sum_{i=1}^{i=86} (\log(c_{eq}) - \log(C_m))^2 \quad (5.27)$$

Where e is the minimized error, i represents the i th mobile frame measurement, c_{eq} is the simulated equilibrium sediment concentration and C_m is the measured time and depth averaged sediment concentration. In the optimization the logarithm of the sediment concentration is taken in order to force a reasonable fit for the small- and large concentrations (sediment concentrations vary between 0.2 g/l and 40 g/l).

The prediction capability for both model approaches is compared in Figure 5.11 and looks considerable better for the bore-averaged turbulence model as for the wave averaged turbulence model. The optimal value of γ_{turb} in the bore-averaged turbulence model is 1.45 and γ_{turb} is 12.4 in the wave constant turbulence model demonstrating that the bore-averaged turbulence model is far more efficient in producing large sediment suspensions.

The results in Figure 5.11 suggest that for the analyzed measurements the hypothesis that wave breaking induced turbulence reaches the bed as a pulse is physically more likely in relation to a situation with wave constant near-bed turbulence. However, in the performed analysis it is presumed that high sediment concentrations near the dune face are related to the near-bed wave breaking induced turbulence and that oth-

^{XIII} In expression 5.23 the near-bed orbital flow velocity is used instead of the near-bed peak orbital flow velocity that is proposed by Van Rijn. Also the time averaged flow and orbital flow are summed differently. As a result the calibration coefficients mentioned by Van Rijn had to be translated to the adapted model and are different. However, they are consistent with the calibration factors proposed by Van Rijn.

er possible mechanisms that may scale with the bore interval (i.e. the pressure gradient or boundary layer thickness) are of minor importance. The latter has not been verified in this chapter.

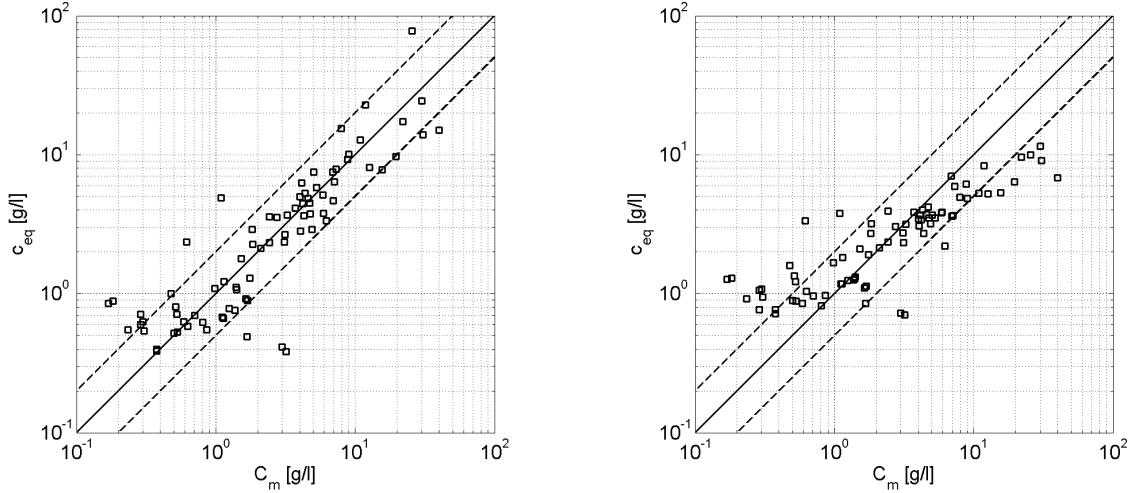


Figure 5.11 Left panel: Suction tube measurements compared with the optimized simulation results for the equilibrium sediment concentration based on the bore-averaged turbulence. The found value for $\gamma_{turb} = 1.45$ and the correlation coefficient ρ is 0.87 taking first the logarithm of the sediment concentrations. The solid line corresponds to a perfect match between simulations and measurements whereas simulation results between the dashed lines are within a factor two with the measurements. Right panel: Suction tube measurements compared with the optimized simulation results for the equilibrium sediment concentration based on the wave averaged turbulence. The found value for $\gamma_{turb} = 12.4$ and the correlation coefficient ρ is 0.83 taking first the logarithm of the sediment concentrations.

5.5 CONCLUSIONS AND DISCUSSION

5.5.1 Conclusions

Detailed analysis of the measured time and depth averaged sediment concentrations reveals that these correlate much better with the maximum wave surface slope than with flow drag. This slope is associated with both the pressure gradient and wave breaking induced turbulence at the water surface. Relating the near-bed pressure gradient and a measure for the near-bed turbulence intensity to the depth averaged sediment concentration both improve the correlation. However, the highest correlation is found between the depth averaged sediment concentration and the near-bed turbulence intensity. The pressure gradient was found to be only partly coupled to flow acceleration suggesting the latter should not always be used as a proxy for the first, especially in the near dune area with highly nonlinear waves.

The increase in dune erosion with a larger wave period is mainly caused by a rise in the time averaged sediment concentration. This higher sediment concentration is ex-

plained by steeper maximum wave surface slope, which is coupled to a larger pressure gradient and an increase in the wave breaking generated turbulence. It is found that the average wave energy dissipation due to breaking is comparable for tests with different wave periods. However this energy is dissipated by fewer waves for a larger wave period, resulting in more intensive wave breaking and steeper wave fronts.

Intra wave simulations with a 1DV suspension model reveal that the sediment response to turbulence is nonlinear. Inner surf simulations with varying near-bed turbulence energy, in which wave breaking induced turbulence is injected in the water column over the bore interval and reaches the bed as a pulse, result in substantially higher sediment concentrations compared to a situation with wave constant near-bed turbulence energy. The higher sediment concentrations in the wave varying turbulence model are caused by extra up-stirring and vertical mixing of sediment over the bore front and are associated with high intensity turbulence flows over this interval. In a model with constant turbulence energy over the wave cycle sediment is mostly stirred up at the end of the wave cycle when offshore flow velocities are maximal. It was found that sediment settling in a wave varying turbulence approach is larger on average, which is explained by the small sediment mixing rate over the remaining part of the wave cycle after the bore front has passed.

Intra wave simulation results with the 1DV suspension model were utilized to extend the wave and depth averaged equilibrium concentration formulation of Van Rijn (2007) with wave breaking induced turbulence. Optimizing the free model parameters for the Deltaflume measurements showed that an equilibrium concentration formulation based on the bore-averaged turbulence energy has a larger predicting capability than a formulation that is based on the wave averaged turbulence energy.

5.5.2 Discussion and recommendations

Data analysis

The data analysis presented in this chapter considers only the time averaged sediment concentration measured with suction tubes in order to examine the processes that may cause the high sediment suspensions observed in the near dune area. Since the studied processes (pressure gradient and wave breaking induced turbulence) act on the (intra) wave time scale, available sediment concentration time series (from OBS's, UHCM and ASTM (see Chapter 2) could give additional insight in the considered suspension mechanisms.

To separate the effects of the pressure gradient and the wave breaking induced turbulence on sediment suspensions would probably require an additional experiment. Tests with both breaking and non-breaking saw tooth shaped waves should be conducted and in addition to (intra wave) sediment concentration measurements, the flows associated with turbulence and the near-bed pressure should be measured.

Intuitively another approach to study the effect of turbulence on sediment suspensions would be to analyze the measured sediment concentration verticals. Getting closer to the shore it is expected that turbulence is better mixed over depth and consequently gradients in concentrations over the vertical might be smaller. However,

taking into account the proposed mechanism in which wave breaking induced turbulence is injected in the water column over the bore interval an opposite effect is expected. Towards the shore the bore interval decreases and the maximum near-bed turbulence intensity (Figure 5.5, left panel) is expected to increase. As a result a lot of sand is brought in suspension over a short period and settles again relatively fast after the bore front has passed. The simulations in Section 5.3 reveal that due to this effect (wave varying turbulence) the steepness of the sediment concentration vertical decreases (compare simulated concentration verticals for a wave varying and a wave constant turbulence approach in Figure 5.9). Finally, it is remarked that the entrainment of sediment also affects the steepness of the sediment concentration vertical. Considering strong up-stirring at the bed in the absence of (extra) mixing (e.g. due to effect of a pressure gradient), the concentration gradients over the vertical are expected to be larger (less steep concentration profile).

Intra wave 1DV suspension model

An intra wave 1DV suspension model has been applied to obtain qualitative insight in the effect of wave varying near-bed turbulence on sediment suspensions compared to a situation with constant near-bed turbulence. In order to make a more fundamental (quantitative) study of the effect of turbulence on sediment suspensions it is possibly required to set up new experiments (see above) and to develop a more detailed suspension model. Especially the approach in modeling turbulence energy and related viscosity is rather simple and it might be useful to reconsider and/or further examine the following assumptions:

- In the simulations a background viscosity of 10^{-2} m²/s is applied and it was found that especially for the model with wave varying turbulence this background viscosity influences the steepness of the simulated concentration verticals.
- The duration of the bore interval is considered to be a constant over the water depth. Applying a more complex turbulence model that takes into account the advection and diffusion of turbulence (e.g. k - ϵ model) would probably result in a different temporal and spatial distribution of turbulence and viscosity, which will influence the evolution of the simulated sediment suspensions over depth.
- It is presumed that turbulence at the water surface is transported towards the bed by diffusion. However, considering the plunging breakers in the Deltaflume tests at the seaward edge of the developing fore-shore (visual observation), the advection of turbulence is expected to be far more important than diffusion. It is likely that at this location the proposed model underestimates the near-bed turbulence energy. A turbulence model that considers both spilling and plunging waves is expected to give better results.
- Wave varying turbulence may cause a temporal shift in the moments that sediment is entrained in the water column (see Figure 5.8), which will likely influence the magnitude and/or direction of the wave related sediment transport. In order to analyze the effect of near-bed turbulence on the wave related sediment transport a more sophisticated turbulence model can possibly more accu-

rately predict the wave intervals over which turbulence reaches the bed and sand is entrained in the water column.

The 1DV simulations are conducted with a characteristic wave shape, which is based on both short waves and long waves (it is difficult to distinguish between short and long waves in the inner surf since the variance is in (partly) overlapping frequency ranges). However, looking at the short wave and long wave height transformation during the Deltaflume tests (see e.g. Figure 2.10 upper left panel) mainly short waves are breaking and consequently are expected to be most important for the extra sediment stirring in the inner surf. It is remarked though that close to the dune face long waves can break (Van Dongeren et al., 2007) and consequently also may contribute to sediment stirring. Finally, the fronts of breaking short waves in the inner surf tend to merge with long wave fronts (Sénéchal et al., 2001), which may lead to locally more intensive breaking waves. The possibly merging of short wave bore fronts with long wave fronts is implicitly included in the analysis presented in this chapter (since the characteristic wave shape is based on the total water surface elevation time series including both long and short waves).

Chapter 6

MODELING DUNE EROSION

6.1 INTRODUCTION

In the previous chapters the physics of dune erosion have been analyzed in detail. During a storm surge the beach is flooded and storm waves impact the dune face causing episodically sand release from the dunes and falling onto the beach. The average dune erosion rate is related to (an estimate of) the average force exerted on the dune face (Chapter 3) as was previously suggested by Fisher et al. (1986). The stability of the dune front is related to its slope.

Eroded dune face sand on the beach acts as a sediment source for the coastal profile and is picked up by long waves (see Chapter 2 and 4) that transport the sediment through the swash into the inner surf. In the inner surf zone a strong undertow is present and the sediment concentration is high. The inner surf sediment concentration correlates well with the wave maximum surface slope that is presumed to be related to the intensity of wave breaking (Chapter 5). It is hypothesized that breaking induced turbulence is injected in the water column over the bore interval. As a result the near-bed turbulence intensity varies over the wave cycle, which causes additional up stirring of sediment and explains the high sediment concentrations.

Further offshore, in deeper water, the sediment starts to settle and a new profile develops that is closer to equilibrium with the extreme hydrodynamic conditions. The new profile introduces a feedback in the system and affects wave transformation, inner surf hydrodynamics and sediment transports. As a result dune erosion rates will decrease as a storm progresses.

The aim of this chapter is to implement obtained insights in dune erosion physics (Chapter 2-5) in a process-based dune erosion model and to explore the prediction capability of the model in various situations.

Section 6.2 describes the extensions of the applied morphodynamic model XBeach (Roelvink et al., 2007). The model includes the surf beat model described in Chapter 4 in order to accurately reproduce near dune hydrodynamics and is extended with a new equilibrium sediment concentration formulation (see Chapter 5). A (short) wave

shape model is proposed to simulate the nonlinearity of waves, which affects the turbulence intensity, the intra wave sediment transport and the roller energy dissipation.

The extended model is optimized in Section 6.3 and the obtained parameter setting is applied to conduct several simulations (Section 6.4) including the Deltaflume experiment described in Chapter 2, the effect of a dune foot revetment, calm and moderate conditions and the 1953 storm surge in The Netherlands.

In Section 6.5 model sensitivity to short and long waves is examined. Also the interaction of the dune face and swash zone is studied in more detail. Section 6.6 presents simulations that take into account the longshore direction. Four situations are considered including an alongshore uniform coast, a coast with a longshore varying dune height, a coast with a longshore varying bathymetry and a coast where a (non-erodible) dike interacts with a sandy dune system. The chapter ends with a summary and conclusions (Section 6.7).

6.2 MODEL ADAPTATIONS AND EXTENSIONS

Simulation results presented in this chapter are obtained with the morphodynamic model XBeach (Roelvink et al., 2007). In contrast to other dune erosion models (Vellinga, 1986; Larson et al., 1989; Steetzel, 1993; Larson et al., 2004a) XBeach solves the physical processes on the wave group time scale and includes the longshore direction. This section describes some model adaptations and extensions that are (partly) based on new insights in dune erosion physics as described in Chapters 2-5. A detailed overview of the model formulations is given in Appendix A.

6.2.1 Wave energy dissipation formulation

The dissipation D of wave group varying energy is computed as the product of two components (Roelvink, 1993):

$$D = P_b D_b \quad (6.1)$$

where P_b is the probability that a wave with energy $E (= 1/8 \rho_w g H_{rms}^2)$ is breaking in a given water depth and D_b is the expected dissipation rate in a breaking wave given its energy. The probability of wave breaking and the expected dissipation rate are expressed as:

$$P_b = 1 - \exp\left(-\left(\frac{H_{rms}}{\gamma h}\right)^n\right) \quad (6.2)$$

$$D_b = 2\alpha f_m E$$

In which γ , n and α are calibration coefficients, and f_m is the mean intrinsic wave frequency assuming a narrow banded spectrum.

The dissipation rate D_b is obtained from the analogy with a bore (Le Méhauté, 1962) and the assumption that the penetration depth of wave breaking induced turbulence is in the order of the wave height (Stive and Dingemans, 1984). However, considering Janssen and Battjes (2007) this last assumption may lead to (unacceptable) singularities near the shoreline since the computed wave energy dissipation is insufficient to counteract the effect of shoaling.

Considering the incorrect shoreline singularities and the expectation that near shore wave energy will likely influence computed dune erosion volumes, the dissipation formulation of Roelvink is slightly adapted by applying the original energy dissipation formulation that follows from bore analogy:

$$D_b = \frac{\alpha}{4} \rho_w g f_m \frac{H_{rms}^3}{h} \quad (6.3)$$

Equation 6.3 can easily be substituted in Equation 6.1 since a non-stationary wave propagation model is considered in which the probability of breaking of an individual wave is examined^{XIV}. The resulting expression for wave dissipation applied in this chapter reads:

$$D = P_b D_b = \left(1 - \exp \left(- \left(\frac{H_{rms}}{\gamma h} \right)^n \right) \right) \frac{\alpha}{4} \rho_w g f_m \frac{H_{rms}^3}{h} \quad (6.4)$$

6.2.2 Equilibrium sediment concentration formulation

The equilibrium sediment concentration is computed with the formulation presented in Chapter 5 and takes into account the bore averaged turbulence energy:

$$c_{eq} = \frac{A_{sb}}{h} \left(\sqrt{(u^E)^2 + 0.64u_{rms,2}^2} - u_{cr} \right)^{1.5} + \frac{A_{ss}}{h} \left(\sqrt{(u^E)^2 + 0.64u_{rms,2}^2} - u_{cr} \right)^{2.4} \quad (6.5)$$

where A_{sb} and A_{ss} are respectively a bed load coefficient and a suspended load coefficient:

$$A_{sb} = \frac{0.015h\rho_s(D_{50}/h)^{1.2}}{((s-1)gD_{50})^{0.75}} \quad (6.6)$$

$$A_{ss} = \frac{0.012D_{50}\rho_s D_*^{-0.6}}{((s-1)gD_{50})^{1.2}} \quad (6.7)$$

where ρ_s is the mass density of sand, D_{50} is the median grain diameter, s is the relative density (ρ_s/ρ_w) and D_* is a dimensionless particle size. The effect of near-bed wave breaking induced turbulence is included via the short wave orbital flow ($u_{rms,2} = (u_{rms}^2 + 1.45k_b)^{0.5}$; where the coefficient 1.45 was estimated in Section 5.4) and is expressed as:

^{XIV} Implementing Equation 6.3 in a stationary wave propagation model is usually more complex since not an individual but a distribution of wave heights is considered.

$$k_b = \frac{\overline{k_s} T_m / T_{bore}}{\exp(h / L_{mix}) - 1} \quad (6.8)$$

in which T_m is the mean intrinsic wave period, T_{bore} is the (short wave) duration of the bore interval and $\overline{k_s}$ is the wave averaged turbulence energy at the water surface computed from the roller energy dissipation and following (Battjes, 1975):

$$\overline{k_s} = (D_r / \rho_w)^{2/3} \quad (6.9)$$

The mixing length L_{mix} in Equation 6.8 is expressed as the thickness of the surface roller near the water surface and depends on the roller volume A_r (Svendsen, 1984):

$$L_{mix} = \sqrt{A_r} = \sqrt{\frac{2E_r T_m}{\rho_w c_w}} \quad (6.10)$$

6.2.3 Wave shape model

The morphodynamic model considered is (short) wave averaged and resolves hydrodynamics associated with the wave group time scale. As a result the short wave shape is not solved for and the bore interval T_{bore} that is required to compute the equilibrium sediment concentration (in Equation 6.5) cannot easily be determined.

In order to estimate T_{bore} the parameterized wave shape model as proposed by Rienecker and Fenton, (1981) is utilized and extended. In this model the short wave shape is described by the weighted sum of eight sine and cosine functions:

$$u_{bed} = \sum_{i=1}^{i=8} w A_i \cos(i\omega t) + (1-w) A_i \sin(i\omega t) \quad (6.11)$$

where u_{bed} is the near-bed short wave flow velocity, i refers to the i th harmonic, ω is the angular wave frequency, A_i is the amplitude of a specific harmonic and w is a weighting function affecting the wave shape. The amplitudes $A_{1:8}$ are computed from stream function theory and vary with the dimensionless wave height $H_0 = H_{rms}/h$ and dimensionless wave period, $T_0 = T_m(g/h)^{0.5}$.

The bore interval T_{bore} is directly related to the wave shape and hence requires that the weighting function w is determined. For w equals one a skewed (Stokes) wave is obtained with high peaks and flat troughs whereas w equals zero results in an asymmetric (saw tooth) wave with steep wave fronts. It is hypothesized that the weighting w can be expressed as a function of wave skewness and asymmetry. The wave skewness of near-bed flow velocities is computed as:

$$S_k = \frac{\overline{u_{bed}^3}}{\sigma_{u_{bed}}^3} \quad (6.12)$$

and the wave asymmetry, A_s can be computed with the same expression replacing u_{bed} by its Hilbert transform.

Wave skewness and asymmetry can be utilized to obtain a measure for the total non-linearity $B = (A_s^2 + S_k^2)^{0.5}$ and a phase $\phi = \tan^{-1}(A_s/S_k)$. The latter gives insight in the relative skewness or asymmetry of a wave and is expected to be directly related

to the weighting, w . The total nonlinearity B is independent of this weighting and depends on the ratio of the amplitudes obtained with stream function theory as proposed by Rienecker and Fenton (1981).

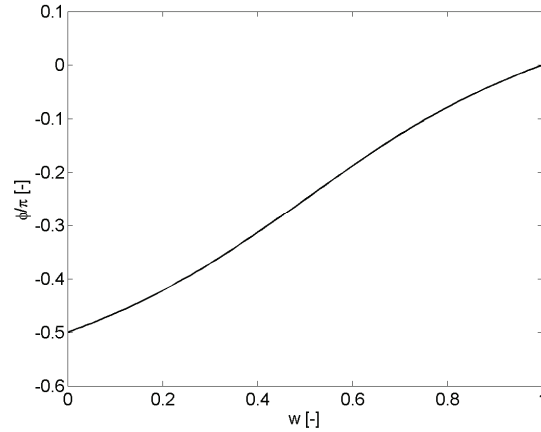


Figure 6.1 Phase ϕ as function of the weighting w for a wide range of wave heights, wave periods and water depths.

The relation between the phase ϕ and the weighting w is studied in more detail by varying w between zero and one in small steps and computing the amplitudes $A_{1:8}$ with Rienecker and Fenton for a range of wave heights, wave periods and water depths. Combining obtained amplitudes for different values of w , near-bed flow velocity time series can be constructed with Equation 6.11. For each time series the wave skewness and asymmetry are calculated from which the phase ϕ is estimated and plotted as function of the weighting w (Figure 6.1). It is found that a unique relation between w and ϕ exists for any combination of wave height, wave period and water depth that is described by:

$$w = 0.2719 \ln \left(\left| \frac{\phi - 1.8642}{0.2933 - \phi} \right| \right) + 0.5 \quad (6.13)$$

Comparison with measurements

In the following it is further examined whether the measured bore intervals during the Deltaflume experiment can be reproduced with the extended Rienecker and Fenton model. Use is made of the mobile frame measurements described in Chapter 2, from which characteristic wave surface elevations are obtained (see Equation 5.1).

Input to the wave shape model is the wave height, wave period, wave skewness and wave asymmetry. The wave height $H_{z,m}$ ($= \eta_{r,max} - \eta_{r,min}$) and wave period $T_{z,m}$ ($= L_{z,m}/c_w$) are computed from the characteristic wave surface elevation. In combination with the known water depth the dimensionless wave height H_θ and wave period T_θ are defined and the amplitudes $A_{1:8}$ can be computed with stream function theory. Since the weighting w cannot directly be obtained from the measurements, the wave skewness and asymmetry are estimated from the characteristic near-bed flow time series

(see Equation 5.1 and following text for more details) and are utilized to compute ϕ , which is related to the weighting w via Equation 6.13.

Simulation results with the extended wave shape model are compared in Figure 6.2. A reasonable correlation is observed between simulated and measured near-bed wave skewness and wave asymmetry. However, the modeled wave skewness is overestimated as is the asymmetry for increasing nonlinearity. This means that the predicted wave nonlinearity is too large on average, which might be explained by free harmonics that are present in the measured time series and damp the total nonlinearity. Also in the measurements waves will eventually break, which is not accounted for in the wave shape model. Measured and simulated phases are identical (Figure 6.2) since they are explicitly coupled by the weighting w (Equation 6.13). The simulated bore intervals compare well with the measurements but are slightly underestimated for highly asymmetric waves (The wave fronts are slightly too steep and as a result predicted bore intervals are too short).

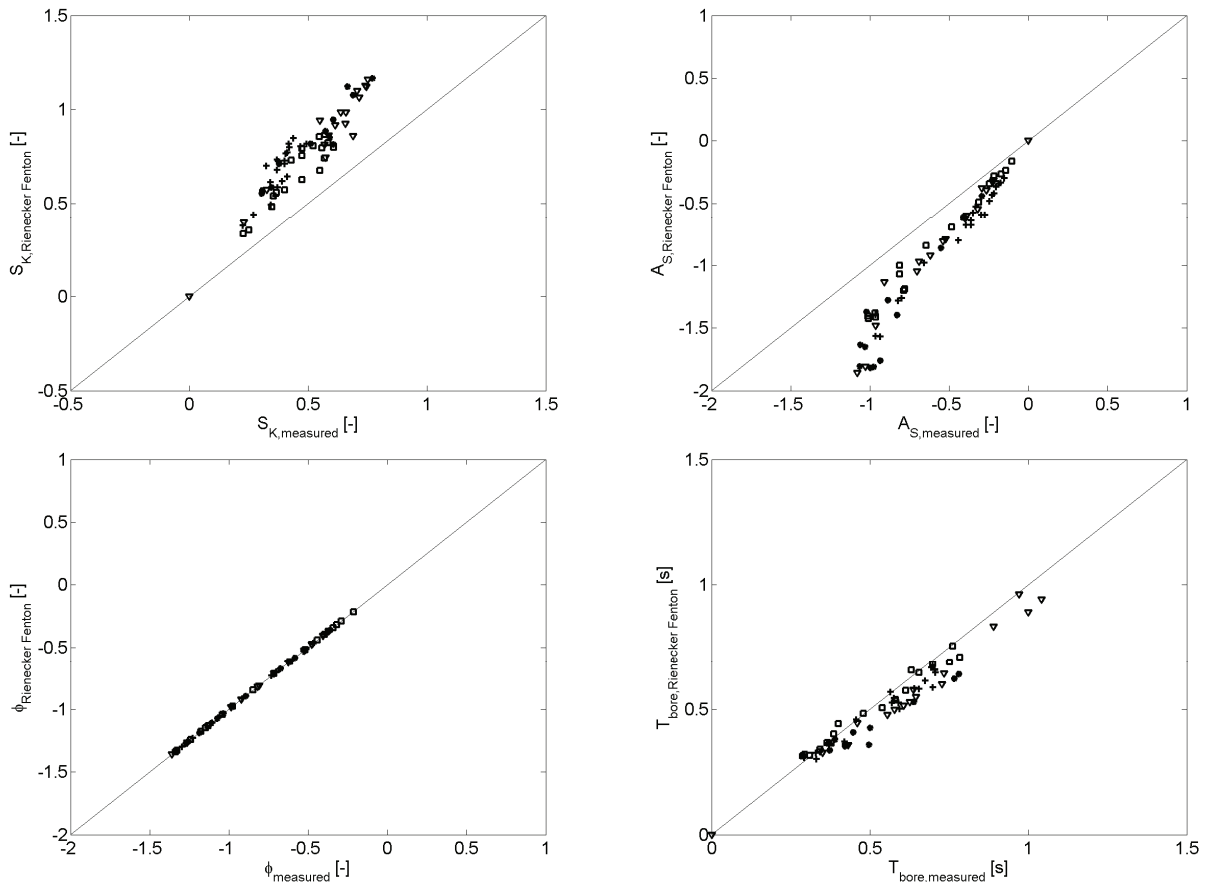


Figure 6.2 Upper left panel: Simulated wave skewness compared with measured wave skewness for test T01 (asterisk), T03 (squares), T04 (pluses) and DP01 (triangles). Upper right panel: Simulated wave asymmetry compared with measured wave asymmetry. Lower left panel: Simulated phase compared with measured phase. Lower right panel: Simulated bore interval compared with measured bore interval. The bore interval is estimated as $T_{bore} = H_{rms} / (\partial\eta / \partial x_{max} c_w)$.

Finally, Figure 6.3 favorably compares the characteristic near-bed orbital flow obtained from measurements with the simulated near-bed orbital flow for a Stokes type

wave in a water depth of approximately 1.5 m and a saw tooth shaped wave in about 0.3 m of water depth.

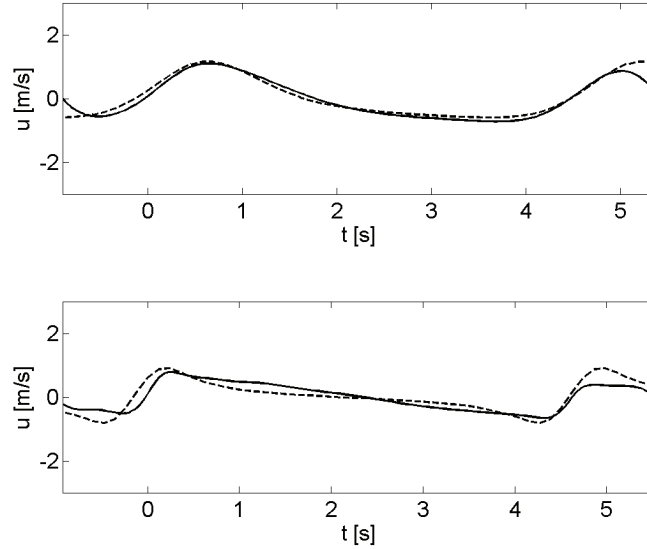


Figure 6.3 Simulated near-bed flow velocity with wave shape model (dashed line) compared with characteristic near-bed flow velocity obtained from the measurements (solid line) at a water depth of 1.46 m (upper panel) and a water depth of 0.28 m (lower panel) .

Implementation in XBeach

It is shown that the extended Rienecker Fenton model can reasonably predict the bore interval T_{bore} if the phase ϕ is known. In order to estimate ϕ within the XBeach model use is made of a parameterization (Ruessink and Van Rijn, manuscript in preparation) for the wave skewness and wave asymmetry as function of the Ursell number ($U_r = 0.75ak_w / (k_w h)^3$ where $a = 0.5H_{m0}$). The parameterization was optimized by applying a nonlinear least square fit procedure to more than 30.000 observations:

$$S_k = \frac{0.79}{1 + \exp\left(\frac{-0.61 - \log U_r}{-0.35}\right)} \cos\left(-\frac{\pi}{2} + \frac{\pi}{2} \tanh\left(0.64 / U_r^{0.60}\right)\right) \quad (6.14)$$

$$A_s = \frac{0.79}{1 + \exp\left(\frac{-0.61 - \log U_r}{-0.35}\right)} \sin\left(-\frac{\pi}{2} + \frac{\pi}{2} \tanh\left(0.64 / U_r^{0.60}\right)\right) \quad (6.15)$$

Computing the phase ϕ from this parameterization and applying it to the wave shape model, the bore interval is simulated and can be compared with the measured bore interval (see Figure 6.4). It is concluded that the bore interval is reasonably reproduced obtaining the phase from the parameterization even though the underestimation of the bore intervals is a little larger in relation to the case where the phase is obtained from the characteristic wave shape (see Figure 6.2 lower right panel).

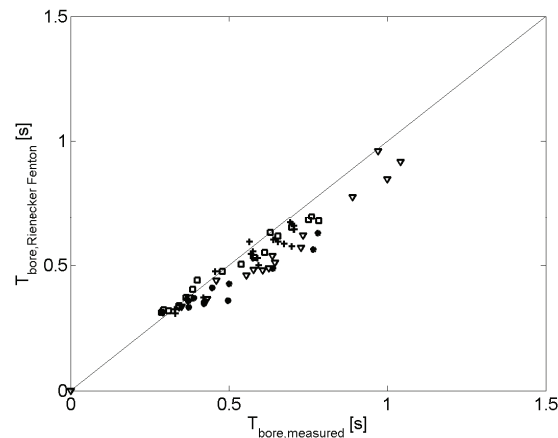


Figure 6.4 Simulated bore interval based upon the parameterized phase as proposed by Ruesink and Van Rijn compared with the bore interval obtained from measurements for test T01 (asterisk), T03 (squares), T04 (pluses) and DP01 (triangles).

Additional applications

Roller dissipation

Including the short wave shape in the XBeach model also gives the possibility to update computed roller energy dissipation. This dissipation is related to the short wave surface slope β (see Equation A.18), which can now be obtained from the parameterization. In the simulations discussed in this chapter, roller energy dissipation is computed using the mean surface slope over the wave front.

Wave related sediment transport

It is well established that the nonlinearity of waves affects the sediment transport (Ribberink and Chen, 1993; Janssen et al., 1998). A Stokes wave has higher onshore than offshore flow velocities and as a result it is expected that more sediment is stirred up under the wave crest (Bowen, 1980; Roelvink and Stive, 1989). Considering a fully saw tooth shaped wave the maximum onshore and offshore flow velocity are equal. However, several mechanisms, including turbulence production (Puleo et al., (2000) but also this thesis Chapter 5) and the pressure gradient (Madsen, 1974; Nielsen, 1992; Drake and Calantoni, 2001; Hoefel and Elgar, 2003), have been suggested to cause additional sediment stirring over the wave front. Depending on the phase shift between intra wave sediment suspensions and the orbital flow velocity the nonlinearity of waves may cause onshore sediment transport^{XV}.

Simulated skewness and asymmetry are utilized to estimate a wave averaged (onshore) sediment advection velocity due to the presence of nonlinear waves. This velocity is added up to the Eulerian flow velocity in order to solve for the advection and diffusion of sediment (see Equation A.28). The sediment advection velocity associated with wave skewness is estimated as:

^{XV} Considering fine sediments, nonlinear waves may also cause offshore sediment transports (Ribberink and Chen, 1993).

$$u_{A,1} = \alpha_u \frac{\int_0^T u(t)^2 u(t) dt}{\int_0^T u(t)^2 dt} = \alpha_u S_k u_{rms} \quad (6.16)$$

where $u_{A,1}$ is the sediment advection velocity due to wave skewness, α_u is a coefficient related to the phase shift between the intra wave sediment concentration and flow. The sediment concentration is presumed to be proportional to u^2 . The wave asymmetry related sediment advection velocity is estimated as:

$$u_{A,2} = \alpha_u \frac{\int_0^T (a(t)/\omega)^2 u(t) dt}{\int_0^T (a(t)/\omega)^2 dt} \quad (6.17)$$

where $u_{A,2}$ is the sediment advection velocity due to wave asymmetry and $a(t)$ is the intra wave flow acceleration. The intra wave sediment concentration is presumed to be proportional to $(a(t)/\omega)^2$, which corresponds to Nielsen's (1992) approach to include flow accelerations in the skin friction Shields parameter for turbulent boundary layers (which is assumed to be proportional to the sediment concentration).

Equation 6.17 is further simplified replacing $u(t)$ by $\omega^{-1}a(t + \phi)$ where ϕ is a phase shift set to zero for convenience (instead of $\pi/2$, which would be more appropriate):

$$u_{A,2} = \alpha_u \frac{\int_0^T (a(t)/\omega)^2 \omega^{-1}a(t + \phi) dt}{\int_0^T (a(t)/\omega)^2 dt} \approx \alpha_u' \frac{1}{\omega} \frac{\int_0^T a(t)^2 a(t) dt}{\int_0^T a(t)^2 dt} = -\alpha_u' A_s u_{rms} \quad (6.18)$$

in which α_u' takes into account the phase shift between flow and sediment suspension. It is remarked that the value of α_u' is expected to be different from α_u since in the elaboration of 6.18 an arbitrary phase shift of $\pi/2$ was introduced (asymmetry related sediment suspensions and orbital flows are presumed to be in phase). In the simulations presented in this chapter α_u' and α_u are presumed to be equal.

6.2.4 Hard structures

Hard layers are included in the XBeach model by specifying the initial thickness of the sediment layer on top of it as input to the model. In each time step computed bed elevation changes are utilized to update the remaining sediment layer thickness (dz_{remain}). In case the remaining sand thickness becomes sufficiently small bed level changes are limited by suppressing the source term in the advection diffusion equation for sediment (see Equation A.28):

$$S = \min \left(S_{\max}, \frac{h(c_{eq} - C)}{T_s} \right) \quad (6.19)$$

where

$$S_{\max} = (1 - p) \frac{dz_{remain}}{dt} \quad (6.20)$$

in which p is the porosity of the sand bed and dt is the numerical time step in the computation. Bed level changes due to avalanching are also limited by the thickness of the sediment layer on top of the hard structure.

6.3 MODEL OPTIMIZATION

The model as described in Appendix A and Section 6.2 has several input parameters that need to be set in order to perform simulations. Most of these parameters are associated with physical processes and appropriate values are available from literature. However, for a few remaining parameters that directly influence the morphodynamic evolution objective settings are less obvious. Two of these parameters ($m_{cr,wet}$ and A_{max}) are related to the applied avalanching algorithm in the model, which solves for the sediment release from the dunes by slumping. Two other parameters are related to undertow computation (h_{min}) and the onshore sediment transport due to nonlinear waves (α_u). A detailed description of the parameters is found in Table 6.1.

Table 6.1 Overview used parameters and the applied range in model optimization

Parameter	Description	$T_{morf} = 10$	$T_{morf} = 1$
h_{min} [m]	Threshold water depth considered in computing undertow (the near shore undertow is estimated over a water depth equal or larger than h_{min}).	[0.1 0.2]	[0.2]
$m_{cr,wet}$ [-]	Critical slope for avalanching in wet points	[0.1 0.15 0.30]	[0.1 0.15]
A_{max} [m ³ /ms]	Maximum erosion rate due to avalanching	[0.003 0.005 0.1]	[0.003 0.004 0.006]
α_u [-]	Calibration factor related to phase shift between intra wave sediment suspensions and orbital flows	[0.1 0.2 0.3]	[0.075 0.1 0.15]

In this section the four parameters are optimized exploring a 4-dimensional parameter space defined in Table 6.1. In order to save computational time and to get a first estimate of the model optimum, 54 simulations with a morphological factor of ten are performed first. Next 18 simulations with a morphological factor of one are conducted in the neighbourhood of the optimum found from the first series of simulations.

Simulations are conducted for test T01, T03 and T04 of the Deltaflume experiment to obtain optimal model prediction capability for different regimes. All simulations are performed on a regular grid with $dx = 1$ m and input to the model are time series of short wave varying energy (low pass filtered on the wave group time scale) and incoming (bound) long waves. The time series are constructed from pressure and flow measurements at $x = 41$ m from the wave board. Settings for the wave energy dissipation model (parameter values for test T03 and T04 are equal) are found in Table 6.2 on page 120 and other setting are listed in the input file that is found in Appendix B.

Model performance is quantified with an error term that is expressed as:

$$err = \sqrt{\sum_{I=1}^5 \sum_{x=160}^{x=220} (z_{m,I}(x) - z_{s,I}(x))^2} \quad (6.21)$$

where $z_{m,I}$ is the measured profile after interval I , $z_{s,I}$ is the simulated profile after interval I and x is the cross-shore position. The error is computed over a cross-shore range of 60 m between $x = 160$ m and $x = 220$ m in which most of the morphodynamic activity is observed.

Simulation results for a morphodynamic factor of ten are shown in Figure 6.5. It is observed that computed errors for test T01, T02 and T03 correlate reasonably well (see lower panel) suggesting that parameter sensitivity has the same trend in the tests considered. However, error differences between test T01, T02 and T03 vary with the parameter set, which points out that parameter sensitivity is different for the tests considered. Hence, the model response is nonlinear for the parameters that are optimized.

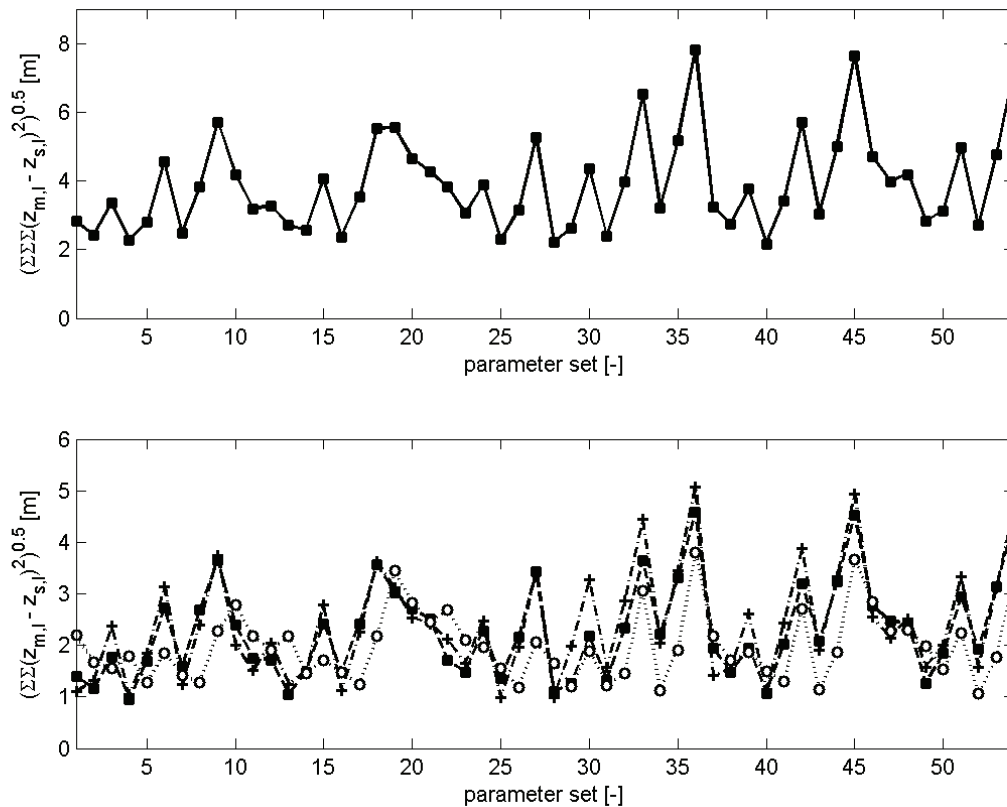


Figure 6.5 Optimization results for a morphodynamic factor of ten. Upper panel: Accumulated errors for test T01, T03 and T04 for various parameter combinations (for each parameter set the error is based on 915 points yielding a mean difference with the measured profile of about 6.6 cm for the smallest errors). Lower panel: Individual errors for test T01 (dashed line with filled squares), T03 (dashed-dotted line with plusses) and T04 (dotted line with open circles) for various parameter combinations.

Several model optima (minima) are observed in Figure 6.5 (upper panel) and it seems that several parameter combinations can lead to satisfying results. In order to select a model optimum for the detailed simulations with a morphological factor of one, only

three minima are considered in which the errors are comparable for test T01, T03 and T04 (see Figure 6.5, lower panel):

	h_{min} [m]	$m_{cr,wet}$ [-]	A_{max} [m ³ /ms]	α_u [-]
Optimum 25	0.1	0.30	0.010	0.1
Optimum 28	0.2	0.10	0.003	0.1
Optimum 40	0.2	0.15	0.005	0.1

Optima 28 and 40 are in close proximity for the four parameters and are used to define the parameter space for the simulations with a morphological factor of one (see Table 6.1). Simulation results for these computations (Figure 6.6) show that fluctuations in computed errors are relatively small for the parameter combinations investigated (upper panel). Splitting out the errors to each individual test (lower panel) it is seen that computed errors for test T01 and T03 correlate well whereas errors for test T04 do not. It is concluded that it is not possible to minimize the errors for the studied conditions with the present parameters, which suggests that some processes are missing or erroneously implemented in the model.

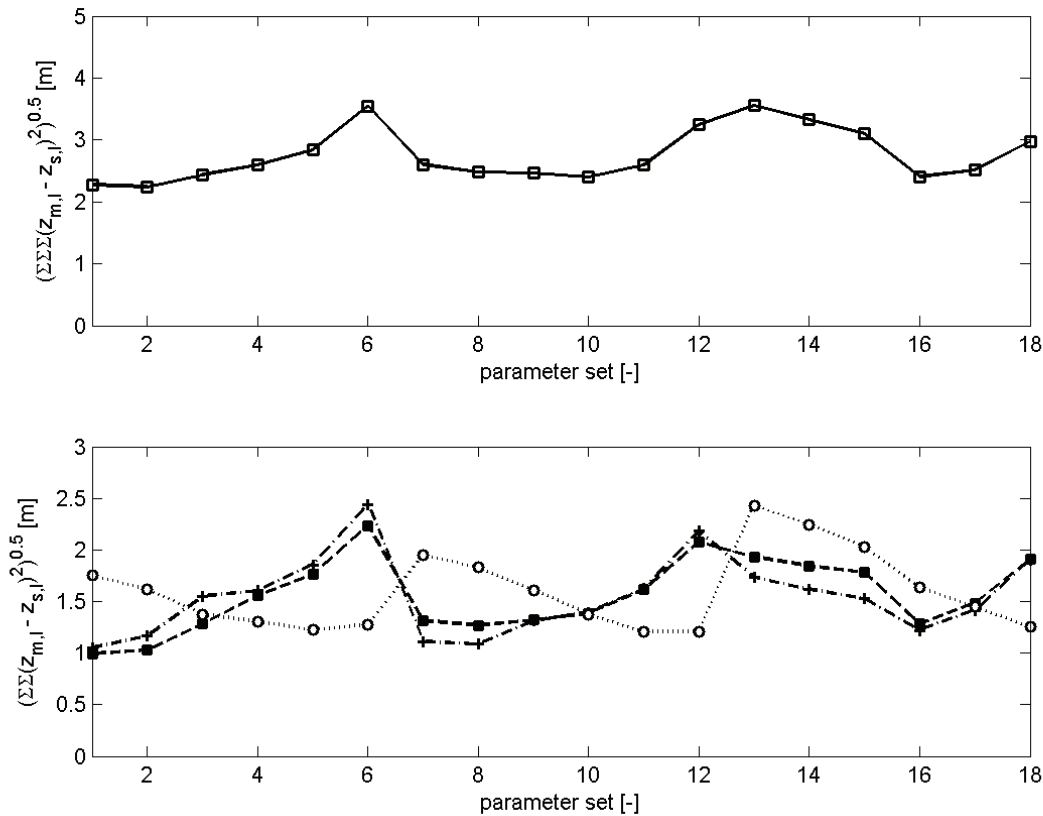


Figure 6.6 Optimization results for a morphodynamic factor of one. Upper panel: Accumulated errors for test T01, T03 and T04 for various parameter combinations. Lower panel: Individual errors for test T01 (dashed line with filled squares), T03 (dashed-dotted line with plusses) and T04 (dotted line with open circles) for various parameter combinations.

The parameter settings applied in the simulations conducted in this chapter are based on the minimum total error in the simulations with a morphological factor of one (optimum number two), which corresponds to an undertow threshold water depth (h_{min})

of 0.2 m, a critical slope for avalanching in wet points ($m_{cr,wet}$) of 0.1, a maximum dune face erosion rate (A_{max}) of 0.003 m³/ms and a calibration factor for the onshore sediment transport due to nonlinear waves (α_u) of 0.1:

	h_{min} [m]	$m_{cr,wet}$ [-]	A_{max} [m ³ /ms]	α_u [-]
Optimum 2	0.2	0.10	0.003	0.1

Note that the found optimum is based on the same parameter settings as optimum 28 in the simulations with a morphological factor of ten. The total errors for the simulations are also comparable.

6.4 1D MORPHODYNAMIC SIMULATIONS

6.4.1 Deltaflume experiment

Detailed comparison for test T01

The aim of this subsection is to make a detailed comparison between simulated physics over an evolving bathymetry and the measurements obtained during the Deltaflume experiment. For brevity this comparison is performed only for test T01 (this test corresponds best to the Dutch normative conditions). The simulation is carried out with settings as discussed in Section 6.3.

Wave height transformation and wave setup (Figure 6.7 upper left panel) are favourably reproduced with the model. The long wave height is slightly underestimated whereas the wave setup is slightly overestimated. The correlation between measured short wave variance and long wave water surface elevations (Figure 6.7 upper right panel) corresponds reasonably well with the measurements. Towards the shoreline this correlation increases (Abdelrahman and Thornton, 1987; Roelvink and Stive, 1989) meaning the highest short waves travel on top of long waves likely, which likely causes that more short wave energy gets closer to the dune face.

Short wave skewness and asymmetry are reasonably predicted with the extended Rienecker Fenton model (Figure 6.7 lower left panel). However, in the inner surf zone both wave skewness and asymmetry are overestimated. Possible explanations are wave breaking, which limits the steepness and height of waves and the presence of free harmonics in the flume. Both these effects are not included in the wave shape model but indeed are present in the flume test (see Section 6.2.3). From simulated skewness and asymmetry it follows that the total nonlinearity of a short wave is overestimated close to the dune face (Figure 6.7 lower right panel). The phase β is favourably simulated with the model but is underestimated further offshore.

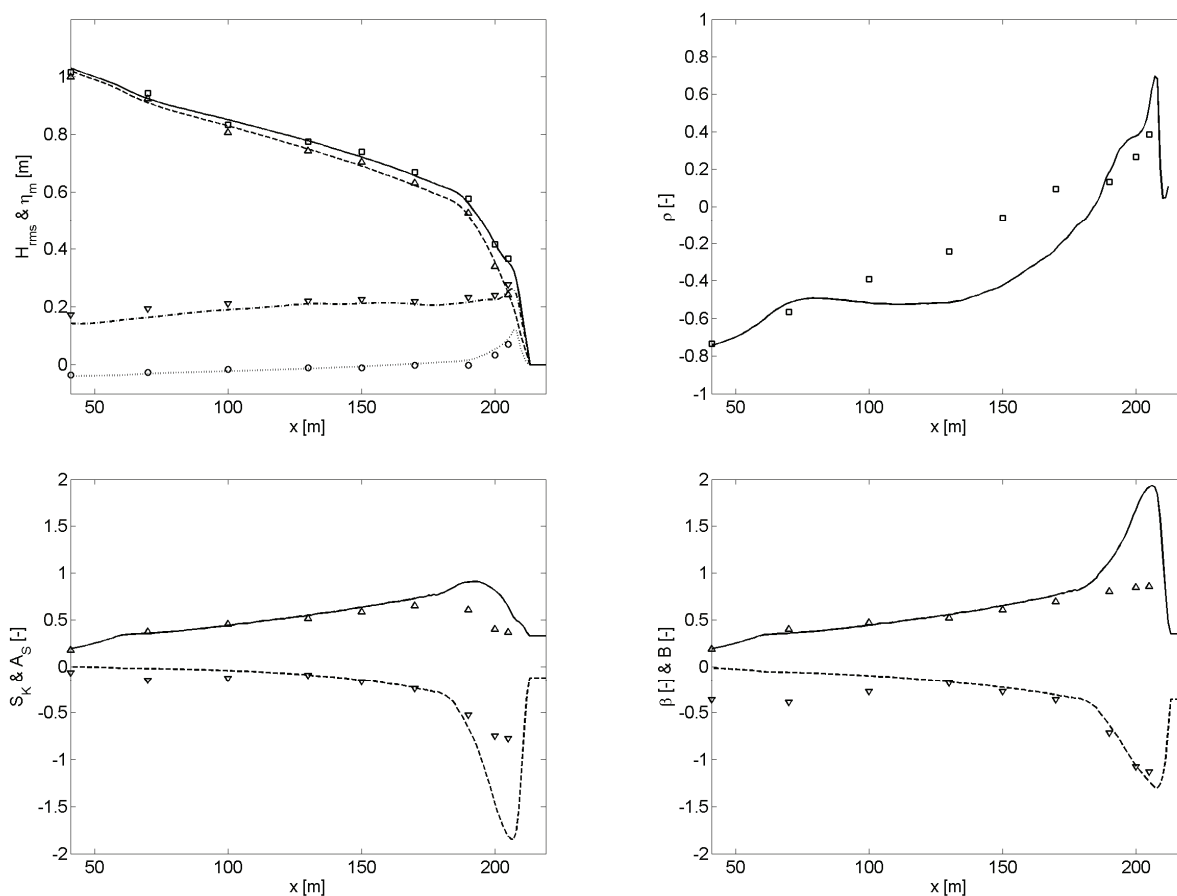


Figure 6.7 Upper left panel: Simulated wave setup (dotted line) and transformation of the total (solid line), short (dashed line) and long (dashed-dotted line) wave height compared with measurements of the wave setup (circles) and the total (squares), short (upward triangles) and long (downward triangles) wave height. Upper right panel: Simulated correlation ρ between the short wave variance and long wave water surface elevations (solid line) compared with the measured correlation (squares) as function of cross-shore position. Lower left panel: Simulated wave skewness S_K (solid line) and asymmetry A_S (dashed line) compared with measured^{XVI} skewness (upward triangles) and asymmetry (downward triangles) as function of cross-shore position. Lower right panel: Simulated wave nonlinearity B (solid line) and phase β (dashed line) compared with measured nonlinearity (upward triangles) and phase (downward triangles) as function of cross-shore position.

The simulated test and depth averaged flow velocity shows the same trend as in the measurements and increases towards the shoreline (Figure 6.8 left panel). However, in the simulation the cross-shore range with a high offshore mean flow is smaller and extends less far seaward than in the measurements. This is possibly explained by differences in profile development (see Figure 6.11) or inaccurate measurements. In addition, another explanation may be found in the incorrect modeling of the roller energy dissipation. Simulations (not shown) with a smaller roller dissipation rate revealed

^{XVI} The skewness and asymmetry are obtained from the near bed flow velocity time series, which are estimated from the measured pressure time series using linear wave theory (in Fourier space). Applying Equation 6.16 and 6.18; the measured time averaged sediment advection velocity associated with nonlinear waves is computed.

that roller energy in the inner surf increases, leading to higher return flow over a broader cross-shore range.

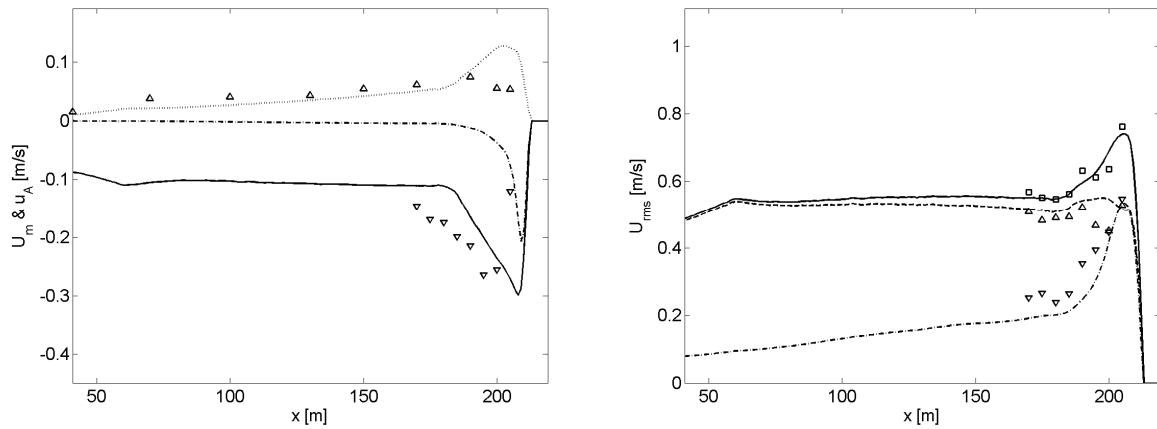


Figure 6.8 Left panel: Simulated test and depth averaged flow U_m due to short and long waves (solid line) and long waves only (dashed line) as function of the cross-shore position. The dotted line corresponds to the wave averaged sediment advection velocity u_A due to nonlinear short waves. Markers correspond to measured undertow flow velocities due to short and long waves (downward triangles) and the sediment advection velocity due to nonlinear waves^{XVI} (upward triangles). Right panel: Transformation of the simulated total (solid line), short (dashed line) and long (dashed-dotted line) wave orbital flow compared with the measured total (squares), short (upward triangles) and long (downward triangles) wave orbital flow as function of cross-shore position.

Long waves contribute to the time and depth averaged flow close to the shoreline. The contribution of long waves to the mean flow is explained by on average larger water depths during the interval associated with shoreward flow velocities in relation to the interval with offshore flow velocities. Considering continuity and a uniform vertical structure of the long wave flow this means a time and depth averaged offshore directed flow should be present (see also Chapter 4).

Nonlinear waves may cause onshore sediment transport presuming non-uniform sediment stirring over the wave cycle and a positive correlation between sediment suspension and the intra wave flow (see Section 6.2.3). In order to include the wave averaged effect of nonlinear waves on the sediment transport a mean flow u_A is computed, which is added to the mean (Eulerian) flow U_m (see relation A.28 and Equations 6.16 and 6.18). The simulated time averaged flow associated with nonlinear waves shows a comparable evolution as in the measurements^{XVI} but is overestimated especially closer to the dune face. Near the shoreline the wave skewness related sediment transport vanishes (see Figure 6.7, lower left panel) since waves develop towards fully saw tooth shaped bores that have negligible skewness.

The orbital flow velocity (Figure 6.8 right panel) is favourably predicted by the model. The short wave orbital flow velocity is slightly overestimated whereas the long wave orbital flow is underestimated. The underestimation of the simulated long wave orbital flow corresponds well to the slight underestimation of the observed long wave water surface variance.

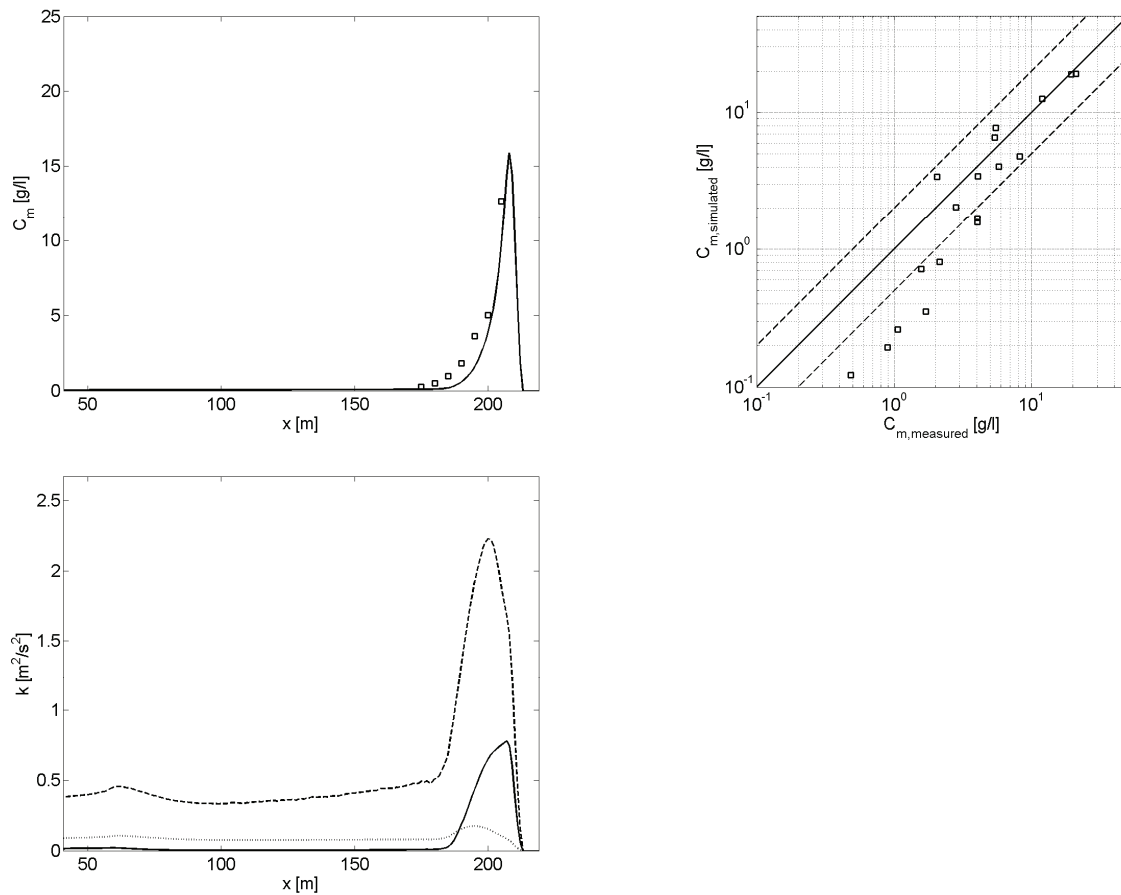


Figure 6.9 Upper left panel: Simulated test and depth averaged sediment concentration (solid line) compared with the sediment concentrations obtained from suction tubes (squares). Upper right panel: Scatter plot of simulated time and depth averaged sediment concentrations compared with vertically integrated suction tube measurements. The solid line corresponds to a perfect match between measurements and simulations whereas simulation results between the dashed lines are within a factor two with the measurements. Lower left panel: Simulated wave averaged turbulence energy (dotted line), bore averaged turbulence energy (dashed line) and near-bed bore averaged turbulence energy (solid line) as function of cross-shore position.

The simulated test and depth averaged sediment concentration increases towards the shoreline but is underestimated, especially in deeper water where the modeled sediment concentration is smaller (Figure 6.9 left and right panel). In the proximity of the dune face the simulated mean sediment concentration is within a factor two with the measurements. Further offshore the discrepancy between simulations and measurements is larger. The sharp rise in the near dune sediment concentration compares well with the bore averaged near-bed turbulence intensity (Figure 6.9, lower left panel) that also increases towards the shoreline. This increase in turbulence intensity through the inner surf is explained by more intensive wave breaking (turbulence production at the water surface increases) and by decreasing water depth (generated turbulence at the water surface is more effective in reaching the bed).

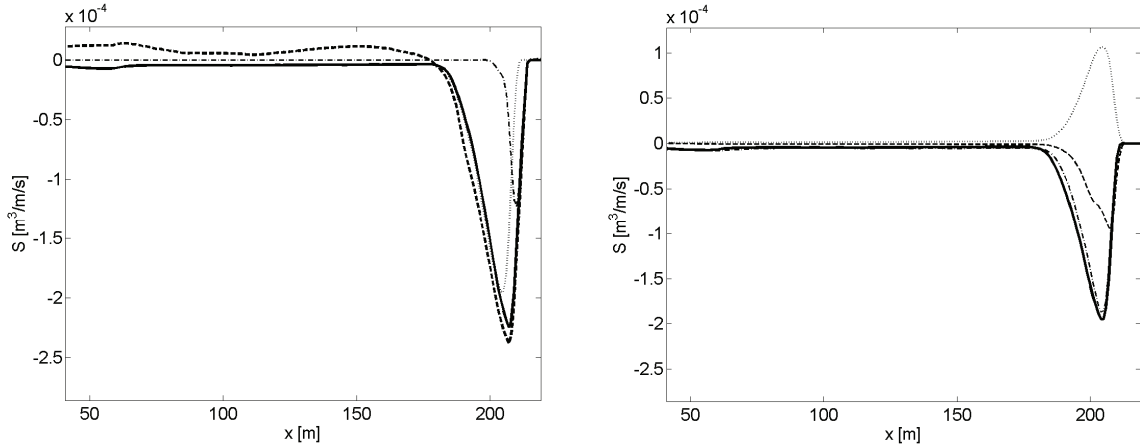


Figure 6.10 Left panel: Measured (thick dashed line) and simulated (thick solid line) test averaged sediment transport from bed level changes. The simulated transport is separated in a transport due to avalanching (dashed-dotted line) and a transport related to the hydrodynamics (dotted line). Right panel: Simulated test averaged sediment transport related to the hydrodynamics (solid line) divided into wave asymmetry related sediment transport (dotted line), long wave related sediment transport (dashed line) and sediment transport associated with the short wave undertow (dashed-dotted line).

The simulated time averaged sediment transport compares well with the measured sediment transport computed from profile changes (Figure 6.10 left panel). Sediment is eroded from the dune face via avalanching (see Appendix A) and as a result the sediment transport associated with avalanching is dominant over the dune face and in the swash zone. From the swash zone seaward, the flow based sediment transport becomes more important. At 205 m from the wave board, in a water depth that varies between 0.1 m and 0.2 m, the flow related sediment transport is dominant.

The simulated flow related sediment transport is separated in sediment transports associated with nonlinear waves (S_W), long waves (S_L) and the short wave driven undertow (S_R) (Figure 6.10 right panel):

$$\begin{aligned}
 S_W &= \overline{u_A ch} \\
 S_L &= \overline{u^L ch} \\
 S_R &= \overline{(u^E - u^L) ch}
 \end{aligned} \tag{6.22}$$

The offshore sediment transport results from the short wave and roller driven undertow (S_R) combined with the transport associated with the long waves (S_L). The transport that follows from the short wave undertow is dominant in the present simulation but the long wave related sediment transport cannot be neglected (about 30% at the location of the maximum offshore transport). The wave related sediment transport (S_W) is onshore and suppresses the offshore sediment transport with some 30%. The effect of long and short waves on dune erosion is examined in more detail in Section 6.5.1.

Profile evolution and dune erosion volumes are favourably predicted with the model during test T01 (Figure 6.11 and Figure 6.12). Between $t = 2.04$ and 6.0 hours (in-

terval E) the dune erosion rate is slightly underestimated. At the offshore edge of the developing foreshore, the model seems not capable to reproduce the steep transition from the original (unaffected) profile towards the newly developed foreshore. A bar type feature is observed at this transition that is hypothesized to be related to (partly) plunging breakers that generate a water jet, which penetrates in the water column and causes additional sediment stirring when it reaches the bed. Though the effect of wave breaking induced turbulence on sediment suspension is included in the simulation, the applied model only considers spilling breakers (see Chapter 5), which are expected to be less efficient than plunging breakers in stirring up sand.

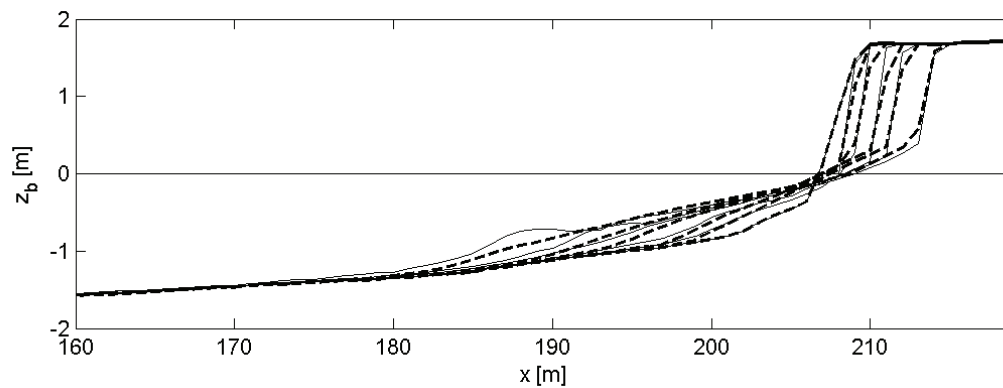


Figure 6.11 Simulated profile evolution (dashed lines) compared with measured profile evolution (solid lines) after $t = 0.0, 0.1, 0.3, 1.0, 2.04$ and 6.0 hours.

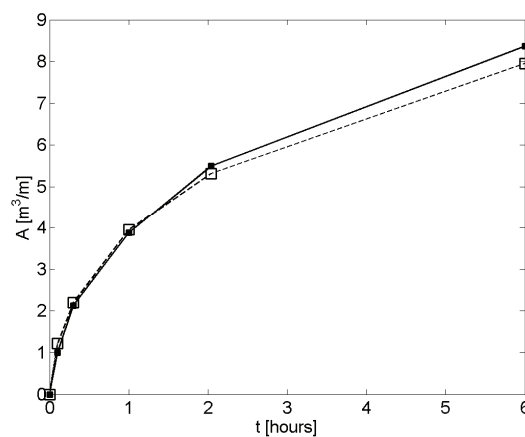


Figure 6.12 Simulated dune erosion volume above still water level (dashed line with open squares) compared with the measured dune erosion volume (solid lines with closed squares) as function of time.

Conclusions and discussion

For the optimal parameter setting as found in Section 6.3 profile evolution and dune erosion during test T01 are favourably simulated. Also simulated wave heights, flows, sediment concentrations and sediment transports compare well with measurements. However, looking at the results in more detail some discrepancies are found:

1. The long wave height and especially associated long wave orbital flows are underestimated.

2. The test and depth averaged flow between $x = 170$ m and $x = 200$ m is underestimated. Close to the shoreline no reliable measurements are available to verify the model results.
3. The simulated sediment concentration compares well with measurements close to the dune face. However, for smaller sediment concentrations in deeper water the simulated concentration is underestimated.
4. The offshore sediment transport is mainly driven by the short wave and roller induced undertow ($O(70\%)$ at the location of the maximum offshore transport) whereas the offshore directed long wave related sediment transport cancels out with the onshore sediment transport due to nonlinear short waves.

It is remarked that shoreward of the maximum offshore sediment transport, the importance of the long wave related transport increases and eventually becomes dominant in relation to the transport associated with short wave and roller driven undertow (Figure 6.13). Considering the mainly long wave associated sediment transport in proximity of the dune face and the importance of long wave run-up for avalanching (see Section 6.5) it is expected that long waves are mainly responsible for the swash zone sediment transport.

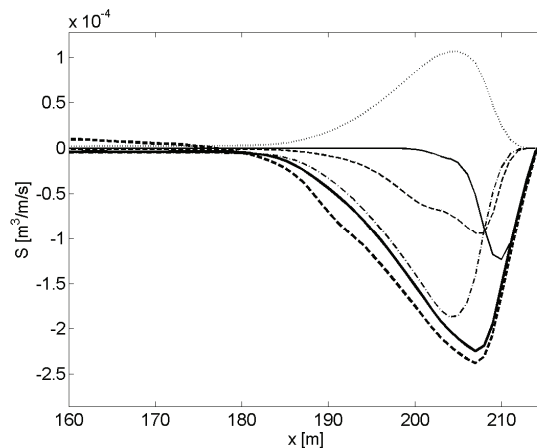


Figure 6.13 Measured test averaged sediment transport from profile evolution (thick dashed line) compared with the test averaged sediment transport from simulated profile evolution (thick solid line). The simulated transport is separated into the avalanching related sediment transport (thin solid line), the wave asymmetry related sediment transport (dotted line), the long wave related sediment transport (dashed line) and the sediment transport associated with the short wave undertow (dashed-dotted line).

Modeling the effect of the wave period on dune erosion

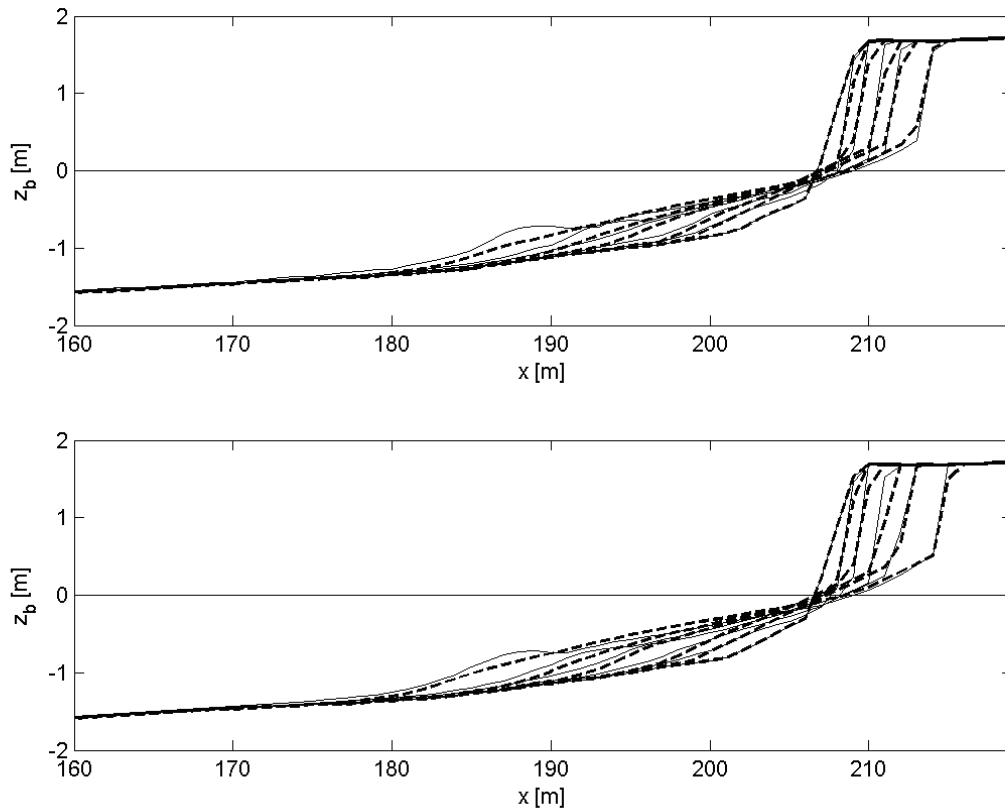
During test T01, T02 and T03 of the Deltaflume experiment the effect of the wave period on dune erosion was examined. It was found that the dune erosion volume increases for a larger wave period, which is caused by a larger flow related sediment transport. In addition, the increase in flow related sediment transport is mainly a result of a higher mean sediment concentration whereas the time and depth averaged flow velocity has the same order of magnitude within the range of wave periods examined.

The aim of this subsection is to examine the processes, which cause the wave period effect in the model and to what extent these processes are in line with the mechanisms observed in the measurements. To this end test T01, T02 and T03 of the Delta-flume experiment are simulated. The model setup is as described in Section 6.3. Settings for the wave energy dissipation model and imposed wave conditions are listed in Table 6.2.

Table 6.2 Wave dissipation parameter settings for test T01, T02 and T03. The imposed wave conditions at the model boundary are obtained from measured wave characteristics at 41 m from the wave board.

Test	H_{rms} [m]	$T_{m-1,0}$ [s]	Spectrum	α [-]	γ [-]	n [-]
T01	1.02	4.57	Pierson-Moskowitz	1.0	0.50	10
T02	1.07	5.54	Pierson-Moskowitz	1.0	0.48	10
T03	1.10	6.36	Pierson-Moskowitz	1.0	0.45	10

In Figure 6.14 simulated profile evolution during the tests compares well with the measured profile evolution. However, the bar type feature at the offshore edge of the developing foreshore is not reproduced in the simulations. Comparing measured and simulated dune erosion volumes in Figure 6.15 it is seen that for test T03 the erosion volume after 1 hour and 2.04 hours of waves is underestimated whereas for test T01 and T02 simulated erosion volumes are reasonably well predicted over all test intervals.



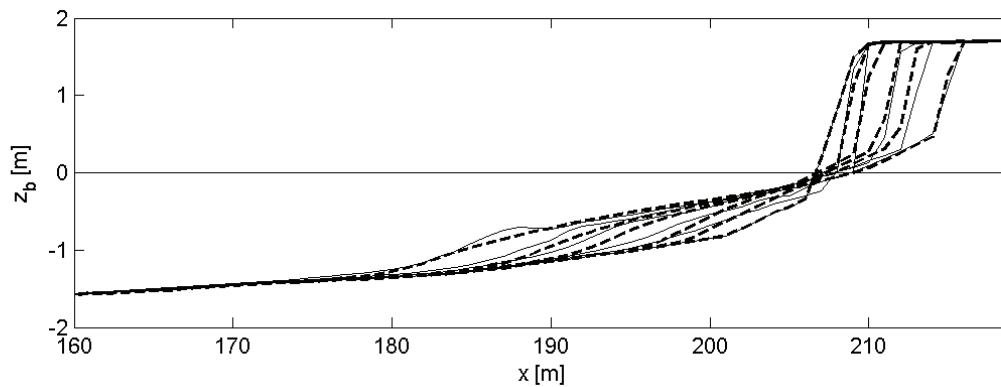


Figure 6.14 Simulated profile evolution (dashed lines) for test T01 (upper panel), test T02 (middle panel) and test T03 (lower panel) compared with measured profile evolution (solid lines) after $t = 0.0, 0.1, 0.3, 1.0, 2.04$ and 6.0 hours.

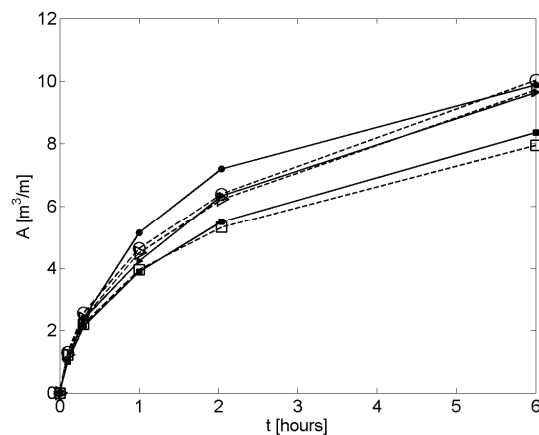


Figure 6.15 Simulated dune erosion volume above still water level (dashed lines) for test T01 (open squares), T02 (open triangles) and T03 (open circles) compared with measured dune erosion volume (solid lines) for test T01 (closed squares), T02 (closed triangles) and T03 (closed circles) as function of time.

Simulated time and depth averaged flows are compared in Figure 6.16, which shows that the mean flow slightly increases with a larger wave period (6% between $x = 170$ m and $x = 205$ m). This tends to be a slightly different trend than observed in the measurements that show a 3% increase in the same cross-shore area. It is remarked though that any firm conclusions cannot be made since the measured time and depth averaged flow velocities are based on limited sensors over depth (and for that reason in Chapter 2 it was concluded that the mean flows for test T01 and T03 are comparable).

The increase in the simulated offshore directed mean flow is caused by an increase of the short wave related mass flux whereas the roller related mass flux is only slightly different. The maximum long wave related mean flow is larger during test T01 than during test T03.

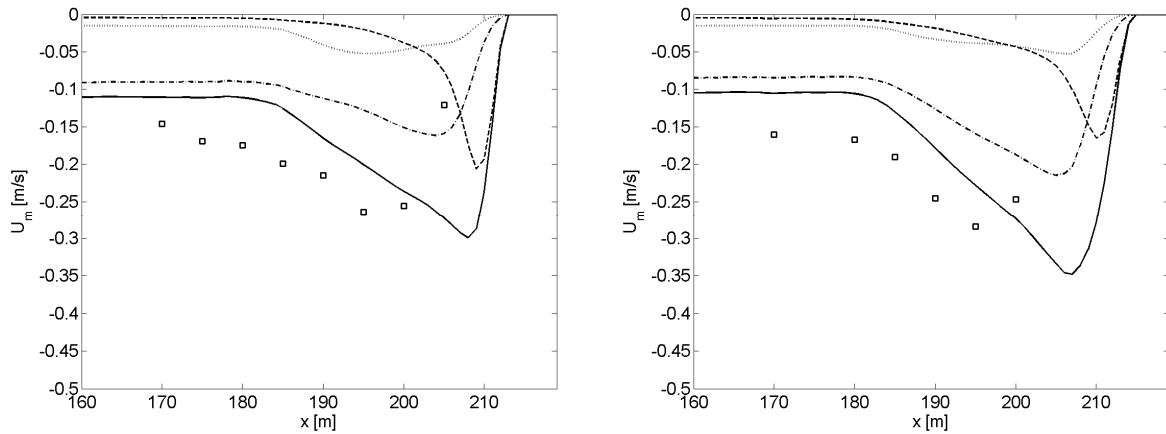


Figure 6.16 Simulated test and depth averaged flow associated with short waves (dashed-dotted line), rollers (dotted line) and long waves (dashed line) for test T01 (left panel) and test T03 (right panel). The simulated total test and depth averaged flow (solid line) is compared with measurements (squares).

Simulated sediment concentrations are compared with measurements in Figure 6.17 and show an $O(60\%)$ increase in the mean sediment concentration for a larger wave period between $x = 170$ m and $x = 205$ m. This increase is comparable as observed in the measurements ($O(60\%)$) for the test and depth averaged sediment concentration). The simulated mean sediment concentration is underestimated with $O(40\%)$ compared to the measurements between $x = 170$ m and $x = 205$ m for both model simulations.

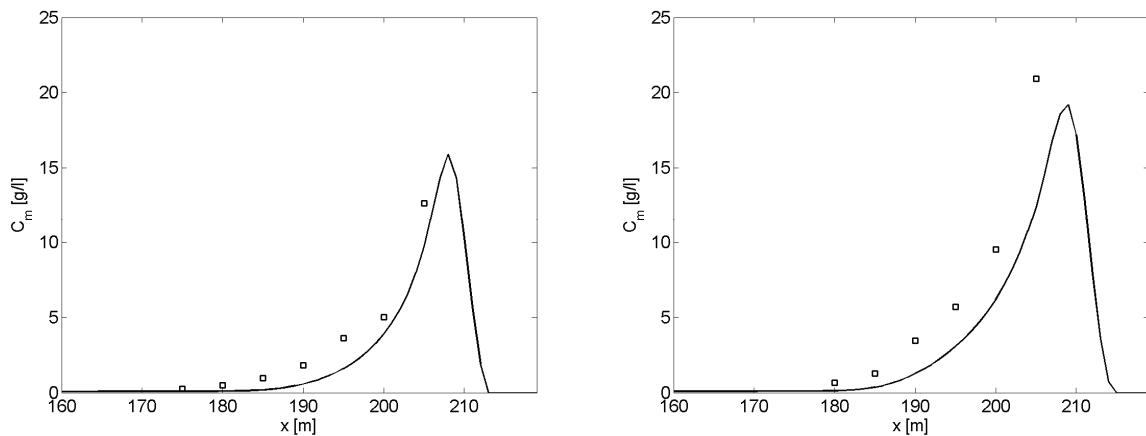


Figure 6.17 Simulated mean sediment concentration (solid line) compared with test and depth averaged sediment concentrations obtained from the suction tubes (squares) for test T01 (left panel) and test T03 (right panel).

Conclusions and discussion

The effect of the wave period on dune erosion and dune face retreat is favourably predicted with the model. The simulated increase in dune erosion with a larger wave period is mainly caused by an increase of the mean sediment concentration of $O(60\%)$, which is comparable to the measurements. The near dune return flow

slightly increases with approximately 6% for a larger wave period. However, the accuracy of measured time and depth averaged flows is insufficient to verify this increase.

Measurements presented in Chapter 2 revealed that 10 to 15 % more wave energy is present in the inner surf area during test T03 with the largest wave period. Given the presence of more near shore wave energy for a larger wave period, the short wave related mass flux also increases, which is likely to result in a stronger offshore directed undertow. However, the latter is not obvious from the measurements (see Figure 2.15). A possible explanation may be found in more short wave reflections for a larger wave period, which (partly) compensates the larger incoming mass flux. These short wave reflections are not accounted for in the XBeach model

Another explanation may be found in a change of the roller energy and associated mass flux. For a larger wave period the maximum surface slope is found to be larger on average (see Section 5.2) and consequently the average roller dissipation is expected to be higher (see Equation A.18). Assuming that the wave dissipation (source in the roller energy balance) is about the same in the near shore for all wave periods (see Figure 5.5, right panel) this will lead to a decline in roller energy and related mass flux.

Comparing model simulations for test T01 and T03 indeed a small decline of roller energy in the near dune area is shown between $x = 180$ m and $x = 200$ m from the wave board (Figure 6.18). However, this decline only partly compensates for the increase in short wave related mass flux and as a result simulated undertow increases with a larger wave period.

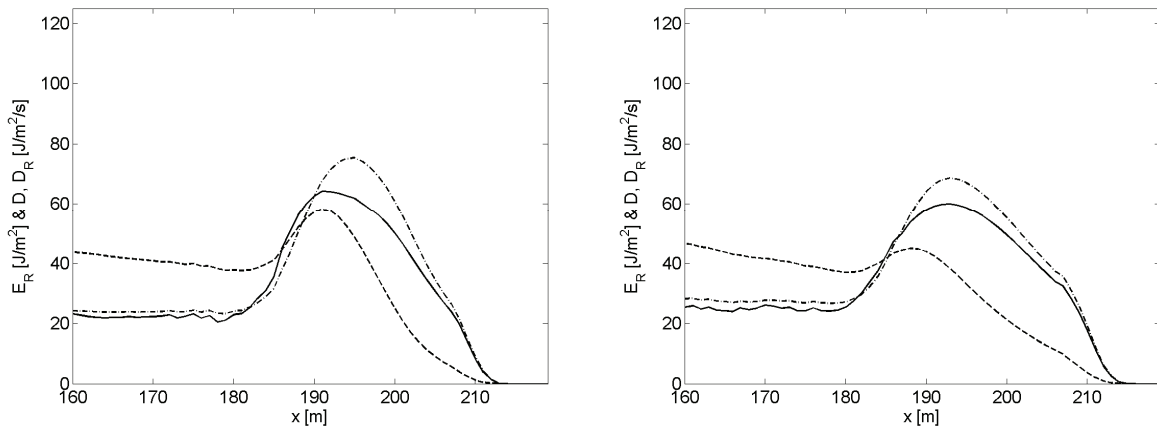


Figure 6.18 Simulated wave energy dissipation (solid line), roller energy (dashed line), and roller energy dissipation (dashed-dotted line) for test T01 (left panel) and test T03 (right panel).

Data analysis of measurements revealed that the $O(100\%)$ increase in the time averaged near-bed sediment concentration for test T03 correlates well with the increase of a measure for the near-bed turbulence intensity (see Figure 5.5 left panel). It is found that (Figure 6.19) the time averaged near-bed turbulence energy between $x = 170$ m and $x = 205$ m also increases with order $O(100\%)$ for test T03, which is in line with data analysis and correlates well to the simulated increase in sediment concentration.

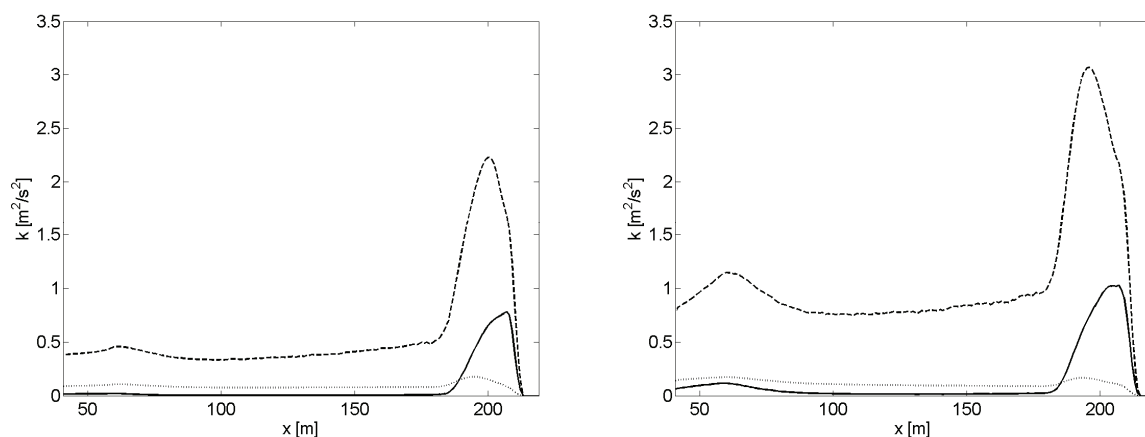


Figure 6.19 Simulated wave averaged turbulence energy at the water surface (dotted line), bore averaged turbulence energy at the water surface (dashed line) and near-bed bore averaged turbulence energy (solid line) for test T01 (left panel) and test T03 (right panel) as function of the cross-shore position.

Modeling the effect of the wave spectral shape on dune erosion

Two tests were conducted with a double-peaked wave spectrum to investigate what (spectral) wave period is best qualified to describe dune erosion (Van Gent et al., 2008). The aim of this sub-section is to obtain further insight in the capability of the model to simulate dune erosion for various wave spectra. The model setup is as described in Section 6.3 and settings for the wave dissipation model are listed in Table 6.3. The short wave group velocity (associated with advection of wave action) is based on the $T_{m-1,0}$ wave period (like in the previous simulations), which is obtained from pressure measurements at $x = 41$ m from the wave board.

Table 6.3 Parameter settings for the wave dissipation model in test DP01 and DP02. The imposed wave conditions at the model boundary are obtained from measured wave characteristics at $x = 41$ m from the wave board.

Test	H_{rms} [m]	$T_{m-1,0}$ [s]	Spectrum	α [-]	γ [-]	n [-]
DP01	1.02	4.57	Double-peaked: $T_{p1} = 6.12$ s and $T_{p2} = 3.06$ s	1.0	0.50	10
DP02	1.07	5.54	Double-peaked: $T_{p1} = 7.35$ s and $T_{p2} = 4.42$ s	1.0	0.48	10

Simulated and measured profile evolution and dune erosion volumes for test DP01 and DP02 are compared in Figure 6.20 and Figure 6.21 respectively. For test DP01 the profile evolution is accurately reproduced and results for test DP02 are reasonable even though the erosion rate during the last interval is overestimated.

The imposed double-peaked wave spectra affect the time scale and amplitude of the simulated wave groups. Consequently, the interaction of simulated long waves with the short wave groups is different and hydrodynamics in front of the dune face are expected to have other characteristics. In Figure 6.22 the simulated wave transformation, flows and sediment concentrations are favourably compared with measurements

obtained during test DP01. It seems the model is capable to take into account the effect of various wave spectra on near dune hydrodynamics and sediment transports.

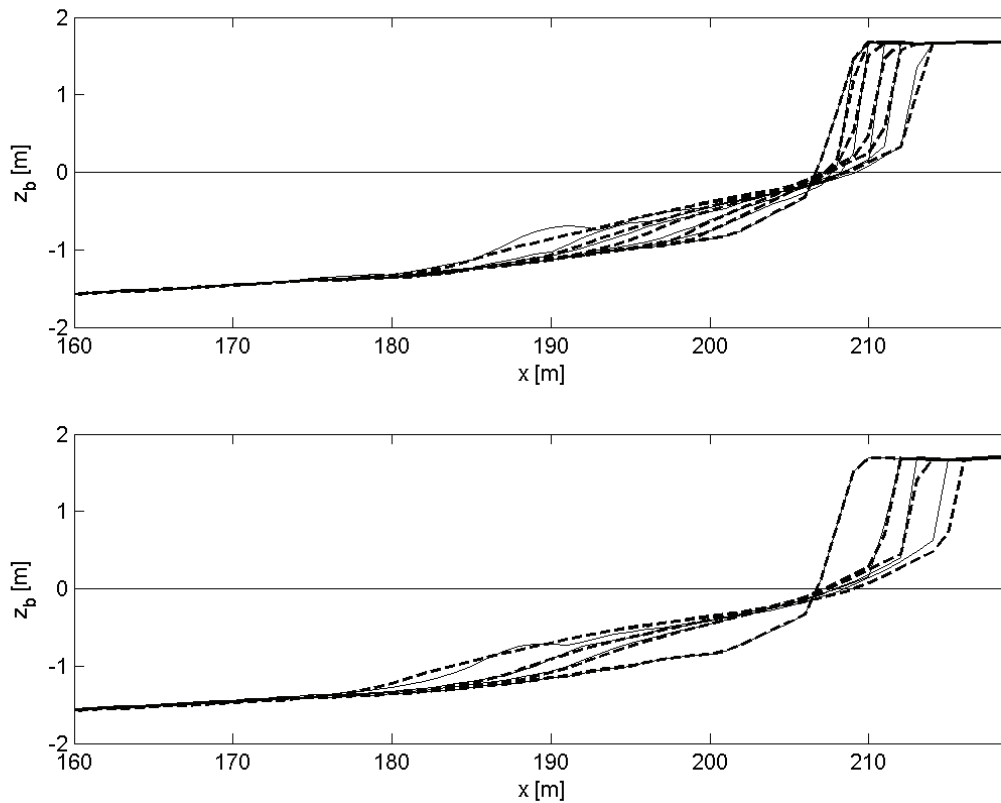


Figure 6.20 Simulated profile evolution (dashed lines) compared with the measured profile evolution (solid lines) for test DP01 (upper panel) and test DP02 (lower panel) after $t = 0.0, 0.1, 0.3, 1.0, 2.04$ and 6.0 hours for test DP01 and $1.0, 2.04$ and 6.0 hours for test DP02.

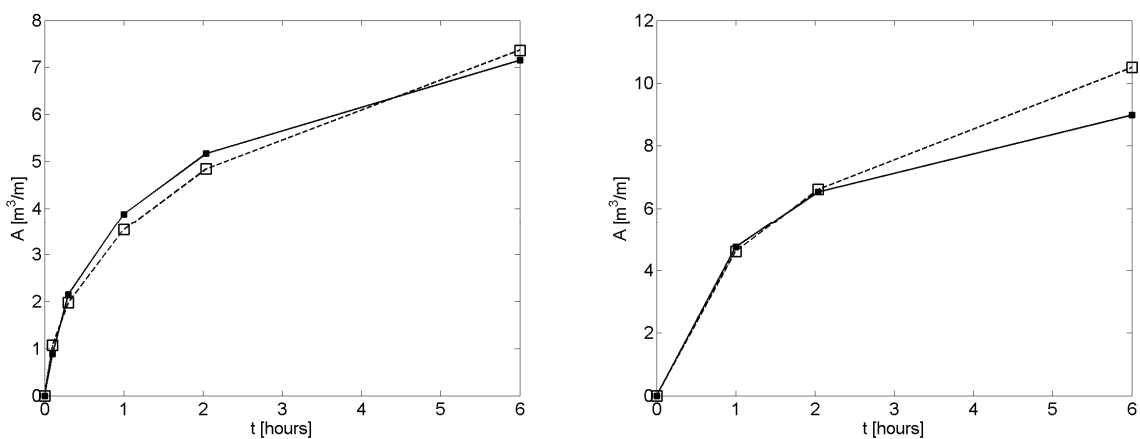


Figure 6.21 Simulated dune erosion volume above still water level (dashed line with open squares) compared with measured dune erosion volume (solid lines with closed squares) as function of time for test DP01 (left panel) and test DP02 (right panel).

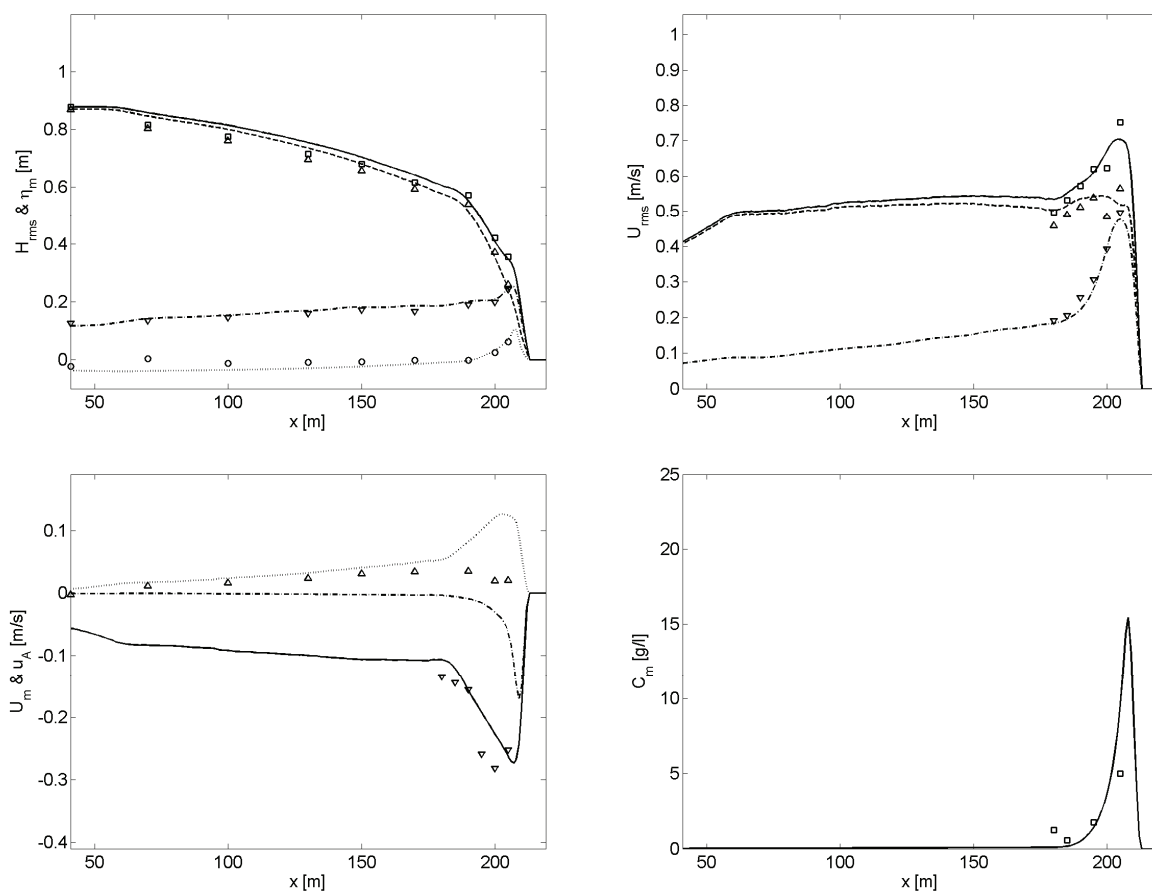


Figure 6.22 Upper left panel: Simulated wave setup (dotted line) and transformation of the total (solid line), short (dashed line) and long (dashed-dotted line) wave height compared with measurements of the setup (circles) and the total (squares), short (upward triangles) and long (downward triangles) wave height. Upper right panel: Transformation of the simulated total (solid line), short (dashed line) and long (dashed-dotted line) wave orbital flow velocity compared with the measured total (squares), short (upward triangles) and long (downward triangles) wave orbital flow velocity as function of the cross-shore position. Lower left panel: Simulated test and depth averaged flow U_m due to short and long waves (solid line) and long waves only (dashed line) as function of the cross-shore position. The dotted line corresponds to the wave averaged sediment advection velocity u_A due to nonlinear waves. Markers correspond to measured undertow flow velocities due to short and long waves (downward triangles) and the measured^{XVI} mean flow due to nonlinear waves (upward triangles). Lower right panel: Simulated mean sediment concentration (solid line) compared with the measured time and depth averaged sediment concentrations (squares) as function of the cross-shore distance.

Conclusions and discussion

The effect of the wave spectral shape on dune erosion and dune face retreat is favourably predicted with the model. The time averaged simulated wave transformation, flow and sediment concentration compare well with the mobile frame measurements obtained during test DP01.

In Van Gent et al. (2008) the spectral mean wave period $T_{m-1,0}$ is argued to be more qualified to describe dune erosion than the peak wave period T_p . The simulations pre-

sented in this subsection are performed with the $T_{m-1,0}$ wave period and show satisfying results suggesting the spectral mean wave period proposed by Van Gent et al. is indeed a good measure to describe dune erosion. It is remarked though that any firm conclusion would require extra simulations in which the peak wave period T_p is applied instead of the $T_{m-1,0}$ wave period. In addition this would demand for a new model optimization and most likely different settings for the wave dissipation model.

Modeling a small dune collapse

Test T04 of the Deltaflume experiment is carried out with a different initial profile containing a small dune in front of a larger volume dune that collapses after approximately one hour of waves (interval C and D). After breaching of the small dune, the foreshore is already very efficient in reducing wave impacts on the dune face resulting in small erosion rates over the remaining test intervals. Here it is examined to what extent the dune breach can be reproduced with the XBeach model and whether the (substantially smaller) erosion rate at the end of a storm is correctly predicted. Parameter settings are the same as described in Section 6.3 and settings for the wave dissipation model are equal as in test T03 (see Table 6.2 for the details).

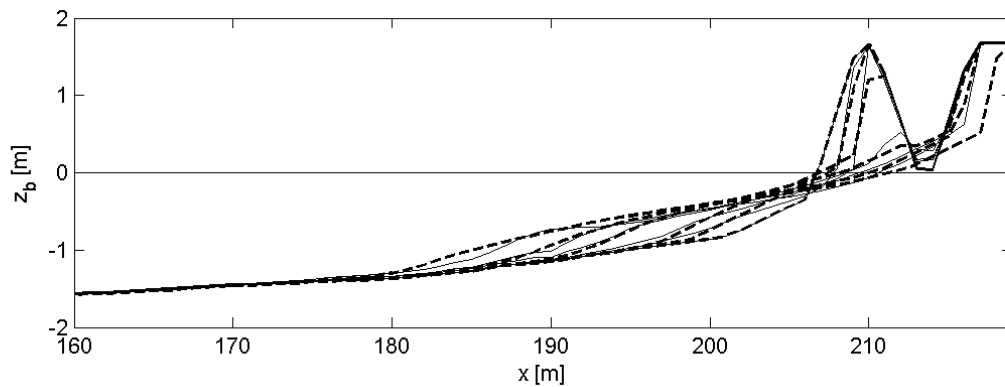


Figure 6.23 Simulated profile evolution (dashed lines) compared with measured profile evolution (solid lines) for test T04 after $t = 0.0, 0.1, 0.3, 1.0, 2.04$ and 6.0 hours.

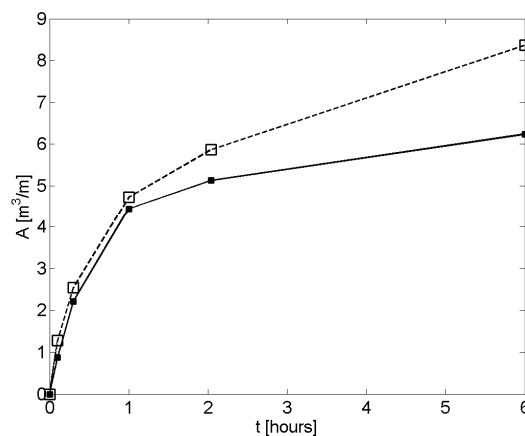


Figure 6.24 Simulated dune erosion volume above still water level (dashed line with open squares) compared with measured dune erosion volume (solid lines with closed squares) as function of time for test T04.

Simulated profile evolution and dune erosion volumes are shown in Figure 6.23 and Figure 6.24 respectively. For the first three intervals (the small dune breaches in interval 3) the dune erosion rate is slightly overestimated but the profile evolution compares favourably with the measured profiles. Considering the last two intervals erosion rates and dune face retreat are too large.

Conclusions and discussion

Breaching of a small dune in front of a larger volume dune causes that suddenly the foreshore is significantly closer to equilibrium with the storm surge conditions. As a result near shore hydrodynamics, near shore sediment transports and wave impacts on the dune face are less severe. It is concluded that the feedback between profile evolution and near dune processes is not sufficiently well included in the model at the end of test T04, which is representative for conditions at the end of a storm. More insight in the model performance at the end of a storm could possibly be obtained by comparing the evolution of simulated driving processes (undertow, sediment concentrations and avalanching) with measurements.

6.4.1 Dune revetment

In situations where the dune width is small or buildings are found close to the beach a revetment can be applied to reduce dune erosion during a storm surge. In the model these constructions can be accounted for by specifying a hard layer (see Section 6.2.4). In this subsection two large scale dune erosion tests with respectively a high and low revetment (test T1 and T3 in Steetzel (1987)) are simulated and the profile evolution is compared with measurements.

The simulations are performed on a uniform grid with $dx = 1$ m to which an additional grid point is added at the cross-shore location of the revetments top (so around this location the grid is non-uniform). Parameter settings are as listed in Appendix B. The imposed wave conditions and settings for the wave energy dissipation model are listed in Table 6.4.

Table 6.4 Parameter settings for the wave dissipation model in test T1 and T3 with a high and low revetment respectively. The applied wave conditions are based on the imposed Pierson-Moskowitz spectrum at the wave board.

Test	H_{rms} [m]	$T_{m-1,0}$ [s]	Spectrum	α [-]	γ [-]	n [-]
T1	1.06	4.90	Pierson-Moskowitz	1.0	0.50	10
T3	1.06	4.90	Pierson-Moskowitz	1.0	0.50	10

Simulation results are shown in Figure 6.25 and reveal that the depth of the scour hole that develops during test T1 (left panel Figure 6.25) is significantly underestimated. The average sediment stirring at the toe of the revetment seems insufficient and it is concluded that at this stage the model lacks the right physics to simulate the development of a scour hole. The missing physics are hypothesized to be related to (short) wave reflections, vertical flow velocities associated with the up and down-

rush of waves and turbulence generation near the bed at the transition of the sand bed to the revetment.

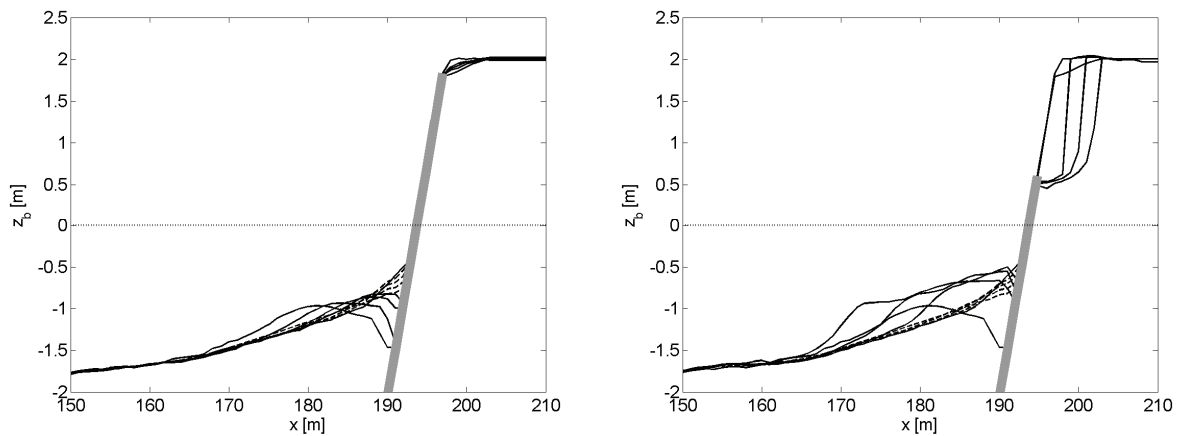


Figure 6.25 Left panel: Simulated profile evolution (dashed line) compared with the measured profile evolution (solid line) for test T1 with a high dune revetment (thick solid line). The maximum storm surge level is indicated with the dotted line as a reference. Right panel: Simulated profile evolution (dashed line) compared with measured profile evolution (solid line) for test T2 with a low dune revetment (thick solid line). The maximum storm surge level is indicated with the dotted line as a reference.

Simulation results for the low revetment are also not satisfying. In the experiment sand is eroded above the low revetment and this sand accumulates in front of the revetment reducing the wave impacts on it. However, in the simulation results no sediment above the structure is delivered to the foreshore. The long wave run-up is too small to reach over the top of the revetment and can consequently not initiate an avalanche that causes the sandy dune face to collapse. It is hypothesized that short wave reflections and run-up should be considered in order to get a better model performance.

Conclusions

The scour hole that can develop near the toe of a dune revetment is underestimated by the model and simulated long wave run-up is not sufficient to erode sand above the top of a low revetment. However, in the model the morphodynamic of the foreshore is influenced by the presence of a structure. In Section 6.6.4 the interaction of a dike with a sandy dune system (2DH simulation) is studied.

6.4.2 Calm and moderate conditions

So far the proposed model has been applied solely for storm conditions in which the coastline retreats. In this section the model is used to simulate less extreme conditions in which the coastline stays roughly in the same place. Two tests (1B and 1C) of the LIP experiment (Arcilla et al., 1994) are considered representing respectively moderate conditions with offshore bar migration and calm conditions with onshore bar migration. Simulations are conducted on a uniform grid with parameter settings as described in Appendix B. Imposed wave conditions and the wave energy dissipation coefficients are listed in Table 6.5.

Table 6.5 Parameter settings for the wave dissipation model in test 1B and 1C of the LIP experiment. The applied wave conditions are based on the imposed Jonswap spectrum at the wave board.

Test	H_{rms} [m]	$T_{m-1,0}$ [s]	Spectrum	α [-]	γ [-]	n [-]
1B	1.00	4.52	Jonswap	1.0	0.40	10
1C	0.41	7.23	Jonswap	1.0	0.35	10

Profile evolution for test 1B and 1C after respectively 18 and 12 hours is shown in Figure 6.26. In both simulations the coastline retreats (approximately 5 m in test 1B and 2 m in test 1C) whereas in the physical model tests the coastline remains roughly at the same location. The bar that is present in both tests diffuses (it is completely washed out for test 1B). Though the model is not capable of reproducing the measured profile evolution (with the parameter settings as described in Appendix B) it is remarked that erosion rates in both tests are small (more than a factor 10 smaller than the dune erosion tests).

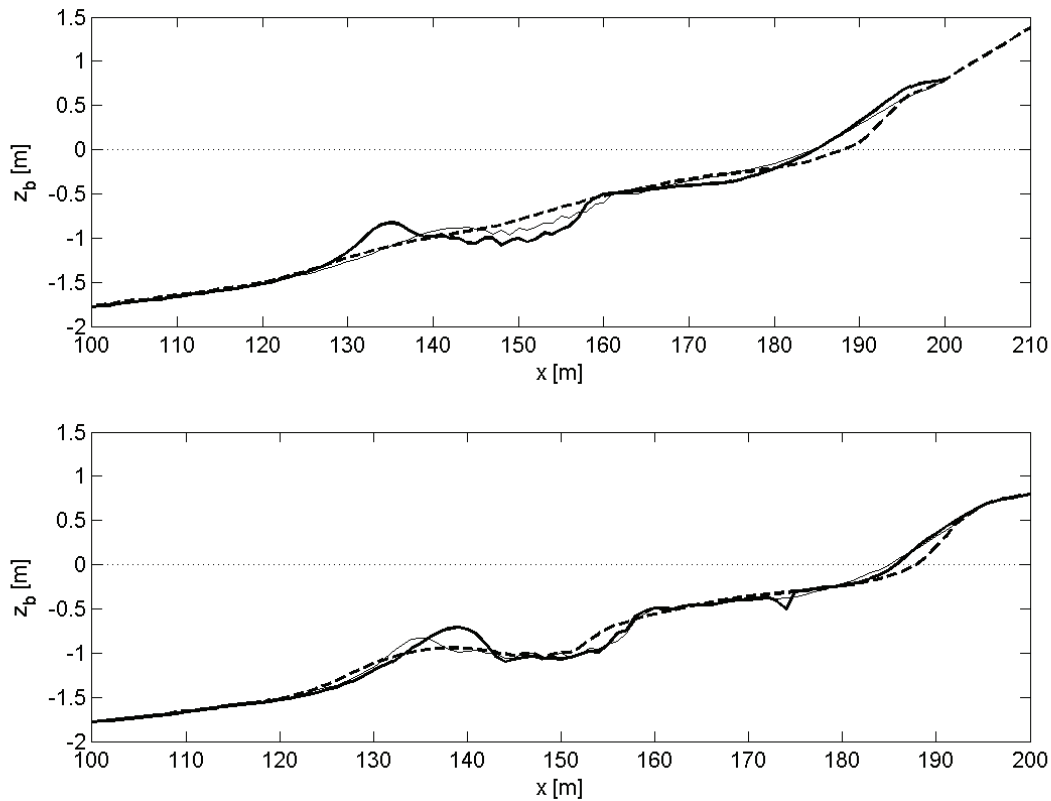


Figure 6.26 Upper panel: Simulated profile evolution for test 1B after 18 hours waves (thick dashed line) compared with the measured profile (thick solid line). The initial profile is indicated with the solid line. Lower panel: Simulated profile evolution for test 1C after 12 hours waves (thick dashed line) compared with the measured profile (thick solid line). The initial profile is indicated with the solid line.

In order to obtain more insight in the processes driving the shoreline erosion, simulation results from test 1B are studied in more detail. Separating the sediment trans-

port in components associated with nonlinear waves (S_W), long waves (S_L), short wave driven undertow (S_R) and avalanching (S_W , S_L and S_R are defined in Equation 22) it is seen (Figure 6.27, left panel) that transports near the waterline are offshore and mainly caused by long waves. The long wave sediment transport is only partly compensated by the onshore sediment transport due to nonlinear short waves.

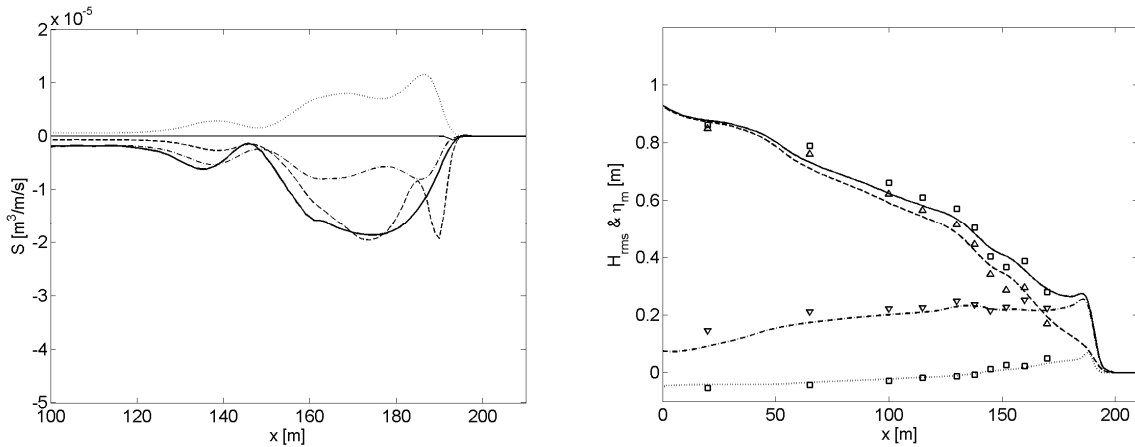


Figure 6.27 Left panel: Simulated sediment transport from bed level changes (thick solid line) separated in components related to nonlinear waves (dotted line), long waves (dashed line), short wave and roller undertow (dashed-dotted line) and avalanching (thin solid line). Right panel: Simulated wave setup and transformation of the total (solid line), short (dashed line) and long (dashed-dotted line) wave height compared with measurements of the total (squares), short (upward triangles) and long (downward triangles) wave height.

Presuming that the long wave height is correctly simulated in the near shore (Figure 6.27, right panel) it is hypothesized that inner surf and swash zone sediment transports associated with long waves are not properly simulated since the model misses some relevant physics. On mildly sloped beaches long waves may break closer to the waterline (Van Dongeren et al., 2007) generating turbulence at the wave fronts, which causes additional sediment stirring and possibly onshore sediment transport. Also short and long wave fronts are expected to merge in shallow water (Sénéchal et al., 2001) meaning that short wave breaking induced turbulence is mainly generated at the long wave fronts. This merging of long wave and short wave fronts is only roughly taken into account in the XBeach model (the correlation between long wave water surface elevations and short wave energy increases towards the shore).

Conclusions

Considering moderate and calm conditions the shoreline retreats (a bit), which is mainly caused by the offshore sediment transport associated with long waves. It is hypothesized that inner surf and swash zone suspension mechanisms at the long wave fronts should be included to obtain a better model performance for calm and moderate conditions.

6.4.3 1953 storm surge

The prototype storm surge conditions simulated during the large scale dune erosion experiment described in Chapter 2 have never been observed in nature since the probability that these conditions manifest is expected to be very small (in the order of once per 100,000 years). As a result it is difficult to verify any dune erosion model for representative storm surge conditions in a prototype situation.

In order to test the behaviour of the proposed model in prototype conditions, this subsection studies the impact of the 1953 storm surge on the Dutch coast at Delfland. The initial profile for the simulation is obtained from test T4 of the M1263-III experiment conducted in the Deltaflume (Vellinga, 1984) and is scaled-up to prototype. The profile is representative for the coast at Delfland. The applied grid is uniform with $dx = 4.56$ m and the applied hydrodynamic conditions vary over the storm (see Figure 6.28). Simulation settings are as found in Appendix B except for the maximum erosion rate A_{max} , which is scaled-up to $0.17 \text{ m}^3/\text{ms}$ applying the scale relation for the erosion volume:

$$n_A = n_l \cdot n_d = n_d^2 \cdot \left(\frac{n_d}{n_w^2} \right)^{0.28} \quad (6.23)$$

where $n_d = 6$ and $n_l = 9.42$ for the Deltaflume experiment.

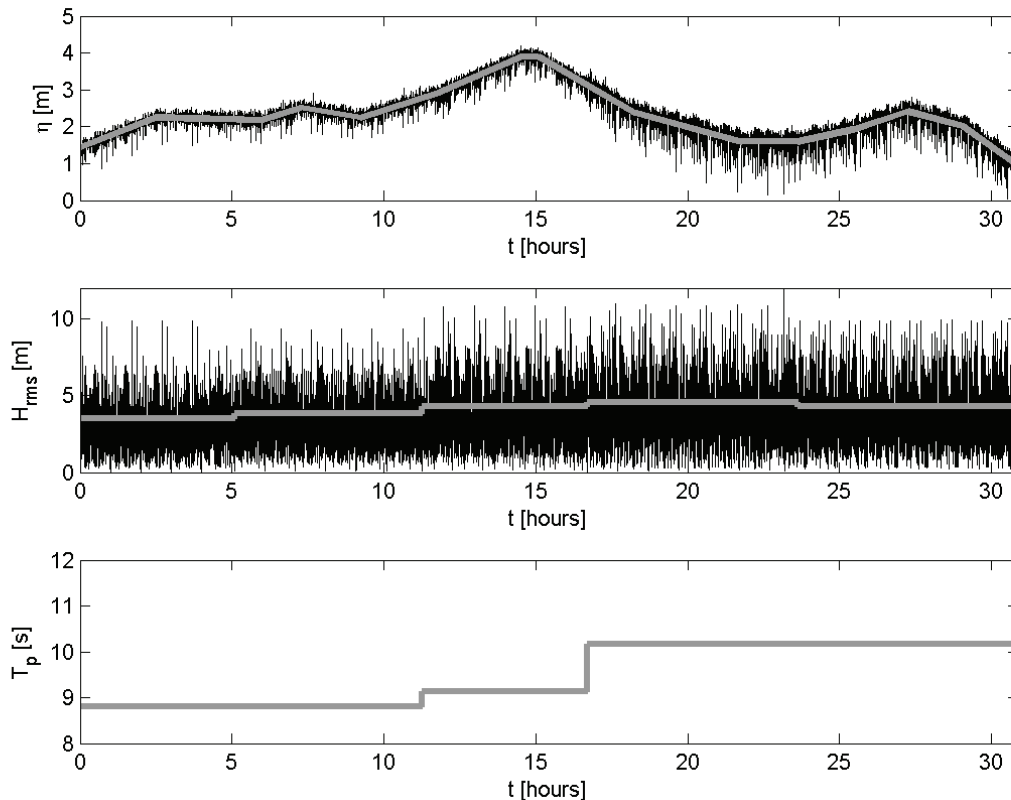


Figure 6.28 Imposed (thick line) and simulated (black line) hydrodynamic conditions at the offshore model boundary. Upper panel: Surge level above mean sea level as function of time. The simulated surge time series include water surface fluctuations due to long waves. Middle panel: Short wave height as function of time. Simulated wave height time series include fluctuations on the wave group time scale. Lower panel: Short wave peak period as function of time.

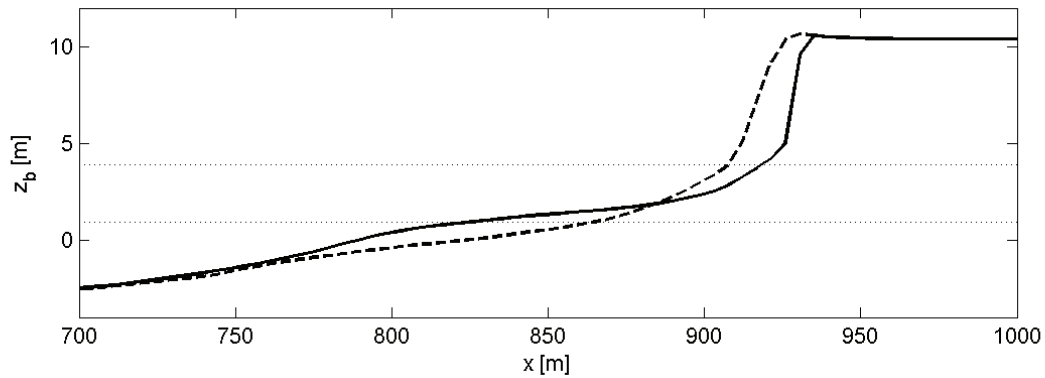


Figure 6.29 Simulated profile evolution during the 1953 storm surge (dashed line is initial profile and solid line is post surge profile). The minimum and maximum surge levels are indicated by the dotted lines.

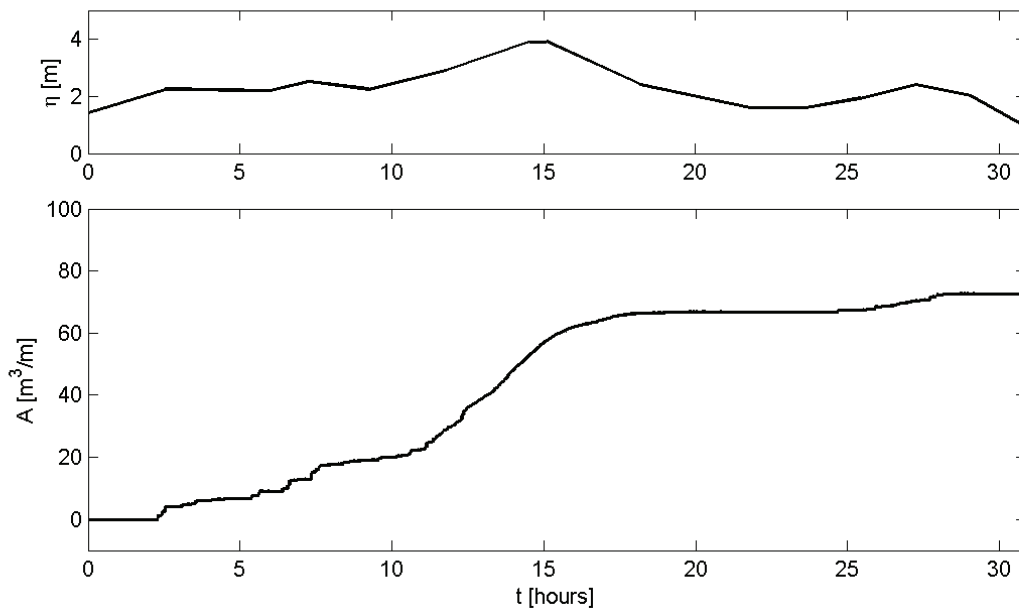


Figure 6.30 Upper panel: Imposed storm surge level as function of time. Lower panel: Simulated dune erosion volume above the maximum storm surge level during the 1953 storm surge as function of time

Simulated profile evolution is shown in Figure 6.29. The erosion volume above maximum storm surge level is $73 \text{ m}^3/\text{m}$ and the total erosion volume^{xvii} is $98 \text{ m}^3/\text{m}$. This is in reasonable agreement with the estimated erosion volumes (above storm surge level) after the 1953 storm surge, which had a mean value of $90 \text{ m}^3/\text{m}$ and a standard deviation of $26 \text{ m}^3/\text{m}$. At the end of the storm surge the dune foot in the simulations is located approximately 1 m above the maximum storm surge level.

Evolution of the simulated dune erosion volume is shown in Figure 6.30 and reveals that most dune erosion occurs in a relatively short time interval between $t = 10$ hours and $t = 15$ hours when the mean water level is increasing towards the maximum storm surge level. After the peak of the storm surge the erosion rates are relatively small.

Conclusions

The 1953 storm surge conditions are favourably reproduced by the model and simulated dune erosion volume is within the range of estimated erosion volumes.

6.5 MODEL SENSITIVITY

6.5.1 Importance of long waves and short waves

In the Deltaflume experiment discussed in Chapter 2 it was observed that in more shallow water a shift in wave variance towards lower wave frequencies takes place. This shift was assumed to be related to wave group generated long waves. In Chapter 4 a surf beat model was applied to solve for the hydrodynamics of wave group generated long waves under short wave group forcing. It was found that for dissipative conditions (including dune erosion) near shore hydrodynamics are accurately reproduced.

Both long and short waves are expected to be important for dune erosion. The long waves initiate avalanches of the dune face and directly influence the sediment supply from the dune to the beach and swash zone. Also, long waves contribute to the offshore flow (e.g. Figure 6.8 left panel) and sediment stirring near the dune. Finally, the positive correlation between short wave groups and long waves in the near dune area (e.g. Figure 6.7 upper right panel) causes that more and higher short waves can reach the dunes.

Short waves contribute to the mean offshore directed flow in the near dune area (e.g. Figure 6.8 left panel) and are important for sediment stirring. In addition, mainly short waves break in the near shore and the generated turbulence is expected to stir-up extra sediment (see Chapter 5). The nonlinearity of short waves can cause onshore sediment transport, which is expected to (partly) balance the offshore sediment transport at the end of a storm.

^{xvii} The total erosion volume per meter is computed as the area where $z_{b,\text{end}} < z_{b,\text{initial}}$ in which $z_{b,\text{initial}}$ is the initial profile and $z_{b,\text{end}}$ is the post storm profile.

Table 6.6 Overview of conducted simulations to obtain more insight in the effect of long waves and short waves on dune erosion.

Simulation	Parameter settings	Remarks
S0: no waves		Still water level increased with 10 cm
S1: stationary waves		No wave groups
S2: no long waves	$F_x = 0 \text{ N/m}^2$ $u_i = 0 \text{ m/s}$	Only short wave groups. Still water level increased with 10 cm.
S3: free long waves	$H_{rms,hf} = 0 \text{ m}$	No interaction between short and long waves (short wave energy is zero). Still water level increased with 10 cm.
S4: no short wave stirring no short wave undertow	$u_{rms,2} = 0 \text{ m/s}$ $k_b = 0 \text{ m}^2/\text{s}$ $u^E = u^L$	As S3 but now including interactions between short and long waves
S5: no short wave stirring	$u_{rms,2} = 0 \text{ m/s}$ $k_b = 0 \text{ m}^2/\text{s}$	No sediment up-stirring due to short waves and wave breaking induced turbulence.
S6: no short wave undertow	$u^E = u^L$	Short wave and roller energy do not contribute to undertow

In this section the effect of long waves and short waves on dune erosion is further examined making seven simulations that are listed in Table 6.6. The simulations are conducted for test T01 of the Deltaflume experiment. The model set-up is as described in Section 6.3 except for the adaptations as listed in Table 6.6. Settings for the wave dissipation model are listed in Table 6.2.

To obtain detailed insight in the mechanisms that drive dune erosion simulation S0 is performed without any wave forcing. For a first order comparison with the other simulations discussed in this section, the effect of wave setup is artificially included in the still water level, which is set 10 cm higher as during the flume experiment. Model results are shown in Figure 6.31 and show that initially significant dune erosion takes place.

It is found that the critical wet slope ($m_{cr,wet}$) near the dune face is exceeded during the start of the simulation, initiating a series of avalanches, which cause computed profile evolution and dune erosion. Initially, the simulated dune erosion rate compares well with the measured rate, suggesting that the erosion rate during the start of test T01 (interval A and B) is determined by the sediment supply from the dune face, which is related to slope stability. During interval B a stable under water slope is reached that approximates the critical wet slope. Over the remaining test intervals the dune erosion rate is zero and the dune foot is now located above the maximum water level.

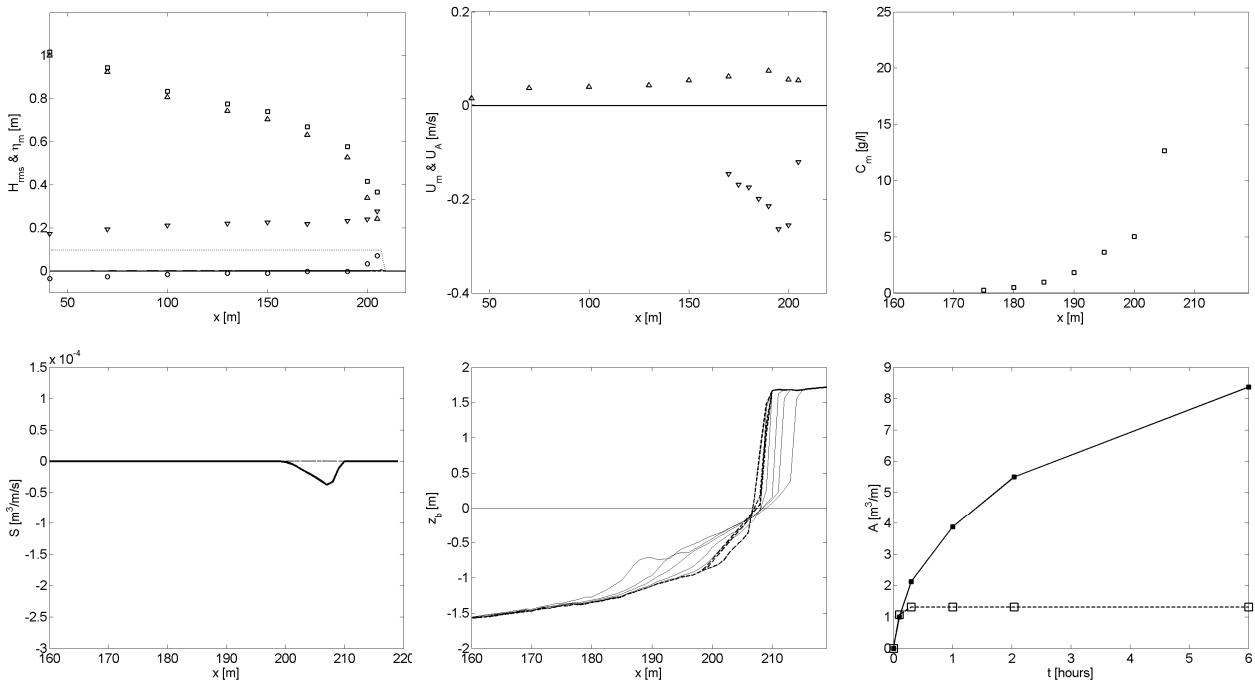


Figure 6.31 Simulation results for test S0 without waves. Upper left panel: Simulated wave setup (dotted line) and transformation of the total (solid line), short (dashed line) and long (dashed-dotted line) wave height compared with measurements of the setup (circles) and the total (squares), short (upward triangles) and long (downward triangles) wave height. Upper middle panel: Simulated test and depth averaged flow U_m due to short waves and long waves (solid line) and long waves only (dashed line) as function of cross-shore position. The dotted line corresponds to the wave averaged sediment advection velocity U_A due to nonlinear waves. Markers are related to the measured undertow flow velocities due to short and long waves (downward triangles) and the measured mean flow due to nonlinear waves (upward triangles). Upper right panel: Simulated test and depth averaged sediment concentration (solid line) compared with measured sediment concentrations from the suction tubes (squares) as function of the cross-shore position. Lower left panel: Simulated test averaged sediment transport from bed level changes (thick solid line) separated in a component due to avalanching (solid line), long waves (S_L ; dashed line), short wave and roller induced mean flow (S_R ; dashed-dotted line) and nonlinear short waves (S_W ; dotted line). S_L , S_R and S_W are defined in Equation 6.22. Lower middle panel: Simulated (thick dashed line) and measured (solid line) profile evolution compared after $t = 0.0, 0.1, 0.3, 1.0, 2.04$ and 6.0 hours. Lower right panel: Simulated (dashed line with open squares) and measured (solid lines with closed squares) dune erosion volume as function of time.

Simulation S1 is performed with stationary wave forcing and the modeled physics are expected to be in line with 1D process-based dune erosion models, in which the physical processes fluctuate on the morphodynamic time scale (Steetzel, 1993). Though not considering wave groups, the wave transformation was computed with the extended dissipation formulation of Roelvink (1993) that is also applied in the other simulations. Simulation results in Figure 6.32 show that not including wave groups and associated long waves, the amount of dune erosion is underestimated with approximately 30%. Considering the first two test intervals the erosion rate is correctly predicted and the effect of not including wave groups and long waves becomes more visible towards the end of the test. The location of the dune foot at the end of

the simulation is a little above the maximum storm surge level but apparently below the mean water level (including wave setup) since sediment supply from the dune face via avalanches can still take place. The sediment transport due to avalanching mainly takes place shoreward of $x = 205$ m. The simulated sediment concentration and undertow velocity are underestimated but still correlate reasonably with measurements (they show the same trend). Excluding the sediment transport associated with nonlinear waves would increase the model performance since this sediment transport (partly) cancels the offshore sediment transport associated with long waves (Figure 6.10 right panel).

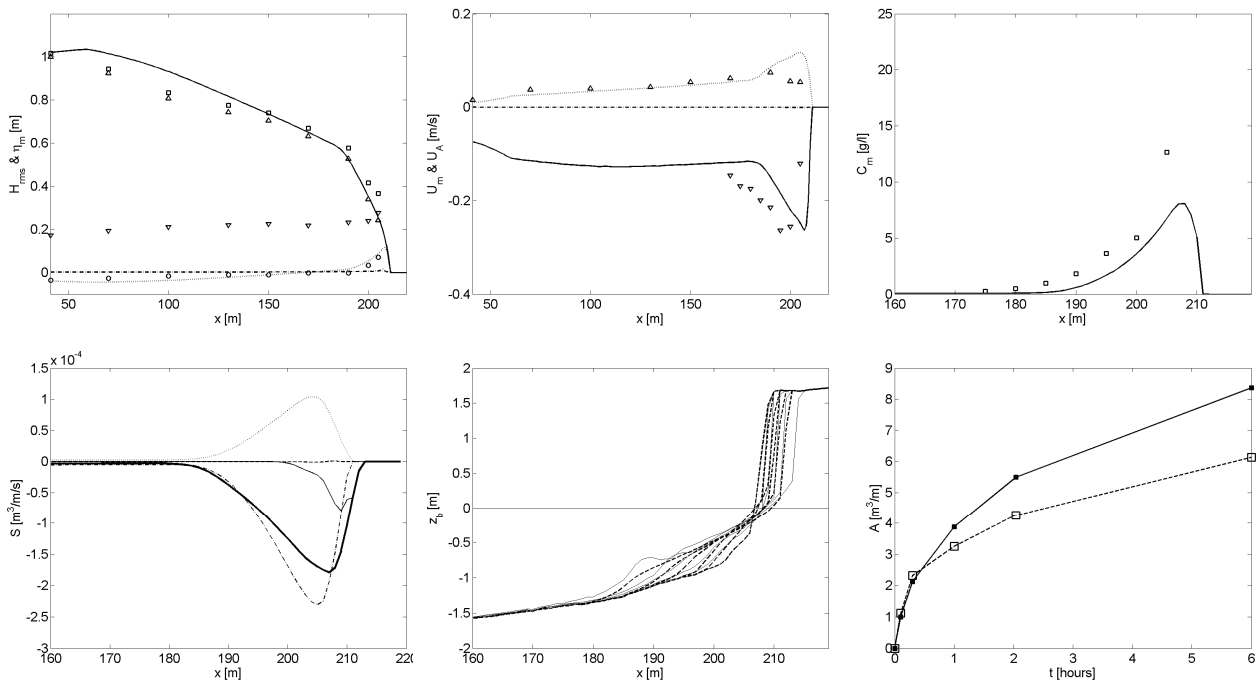


Figure 6.32 Simulation results for test S1 with stationary waves. Panels: See Figure 6.31

In addition to simulation S1 with stationary waves, simulation S2 is conducted with wave group varying energy and the short wave forces (that generate the long waves in the nonlinear shallow water equations) are set to zero. Excluding the wave forces, the wave setup is not simulated and like in simulation S0 this is compensated for by increasing the still water level with 10 cm. Simulation results are shown in Figure 6.33. Like in test S1 the amount of dune erosion after six hours waves is underestimated with order 30%. Computed dune erosion for test S2 is slightly smaller compared to S1, which is caused by the increased sediment transport due to nonlinear waves whereas the sediment transport due to short wave and roller driven undertow is comparable for both tests. The position of the dune foot is located at approximately the same height as the maximum storm surge level, which is lower than in test S1. The foreshore steepness reduces for the simulation with wave groups and apparently wave groups have a diffusive effect on the sediment transport and associated bed level change. Simulated undertow velocity is comparable for both tests whereas the sediment concentration is higher close to the dune face in the simulation with wave groups.

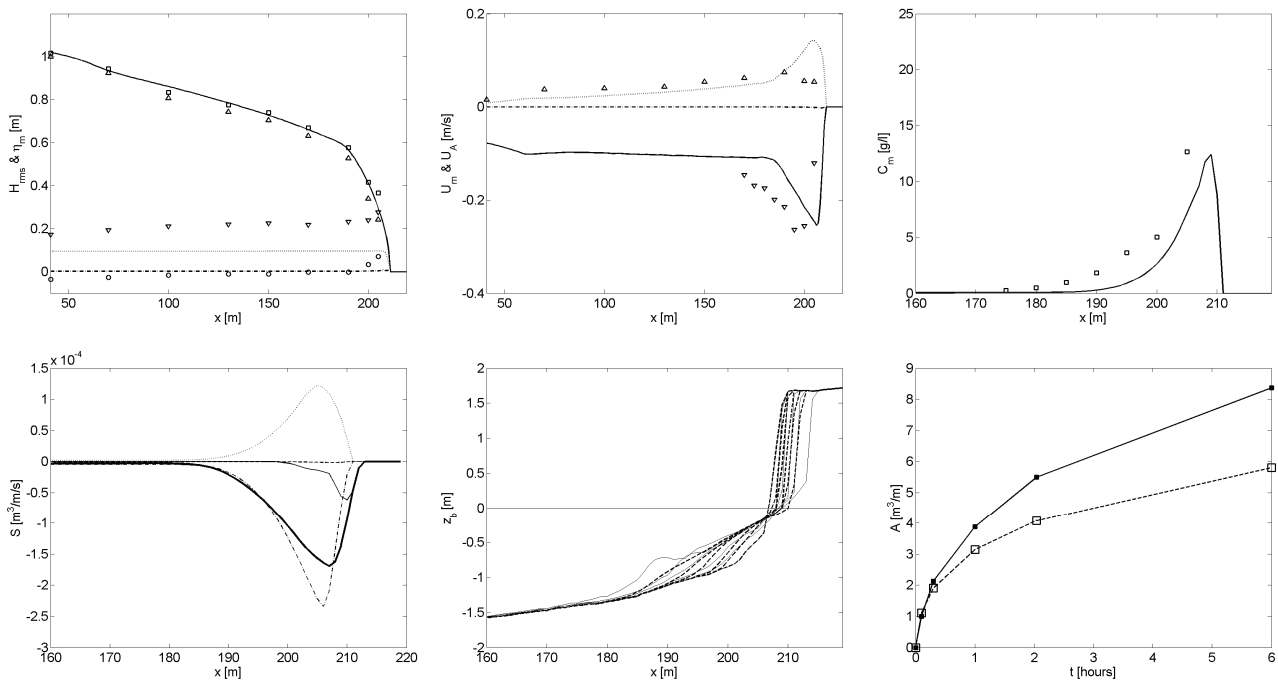


Figure 6.33 Simulation results for test S2 without long waves, but with wave group varying energy. Panels: See Figure 6.31

The effect of long waves on dune erosion is further examined with test S3 and S4. In simulation S3 the incoming wave energy is set to zero and free long waves are considered. Due to the absence of short wave energy the wave setup is not modeled, which again is artificially compensated for by increasing the still water level with 10 cm. Simulation results for test S3 are shown in Figure 6.34. The amount of dune erosion after six hours waves is underestimated with about 70% and most of the sediment transport is related to avalanching. It is remarked though that the avalanched volume is larger than in test S0 (without any waves) and long waves increase the sediment supply from the dune. It is found that during long wave run-up dry points on the dune face become wet and consequently unstable. At the end of the simulation the dune foot is approximately located at the long wave run-up level. Simulated sediment concentration and undertow velocity are significantly underestimated, which explains why the dune erosion rate is underestimated. Finally, it is observed that simulated long wave variance is too small along the whole cross-shore profile, which suggests that the interaction between long waves and short wave groups cannot be neglected (see also simulation results test S4 and Chapter 4).

In simulation S4 the short wave transformation and the interaction between short waves and long waves are included. However, short wave stirring (due to orbital flows and wave breaking induced turbulence) and the short wave and roller related mass flux are set to zero. Simulation results are presented in Figure 6.35 and reveal that the dune erosion volume after six hours waves is underestimated with about 50%. The predicted erosion volume is significantly larger than during test S3, which is explained by more accurate modeling of the long wave height transformation. The dune foot location is positioned further above maximum storm surge level since long wave run-up has increased in relation to test S3. The sediment transport is mainly associ-

ated with avalanching but is larger than in test S3. The long waves are expected to be more efficient in releasing sand from the dune and the offshore transport capacity of the long waves has increased. Simulated sediment concentration and undertow velocity are underestimated but are slightly larger than in test S3.

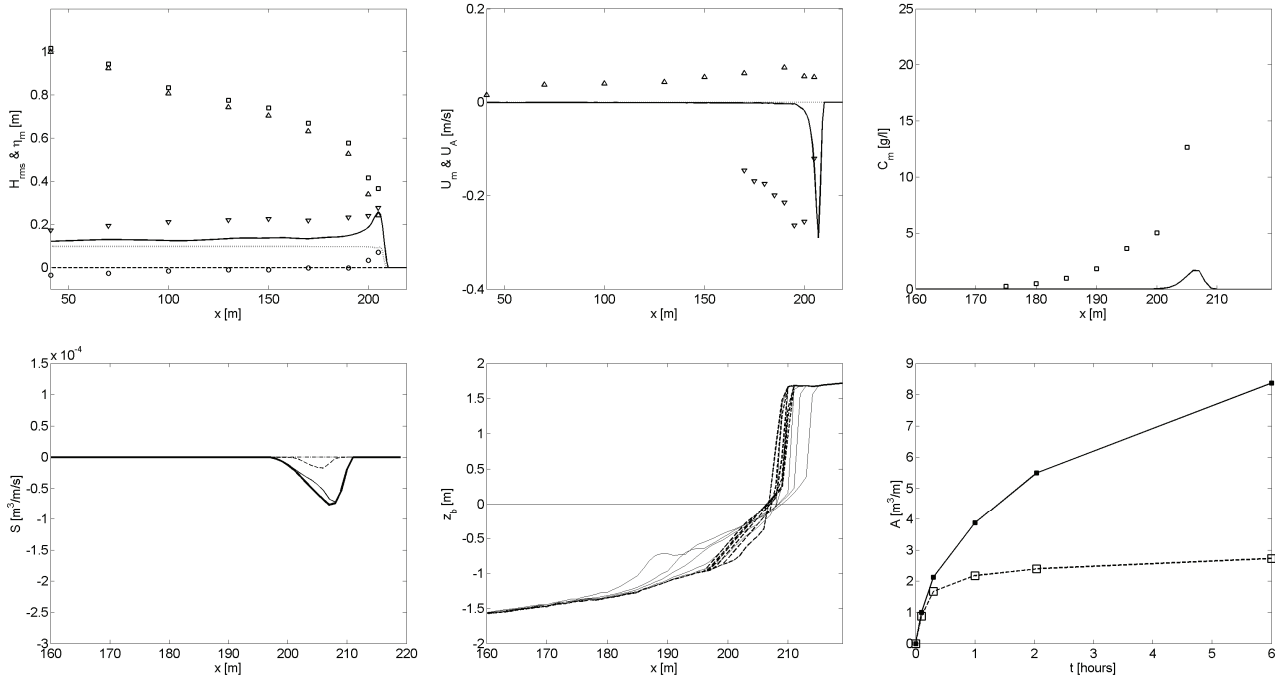


Figure 6.34 Simulation results for test S3 with free long waves and without short wave energy. Panels: See Figure 6.31

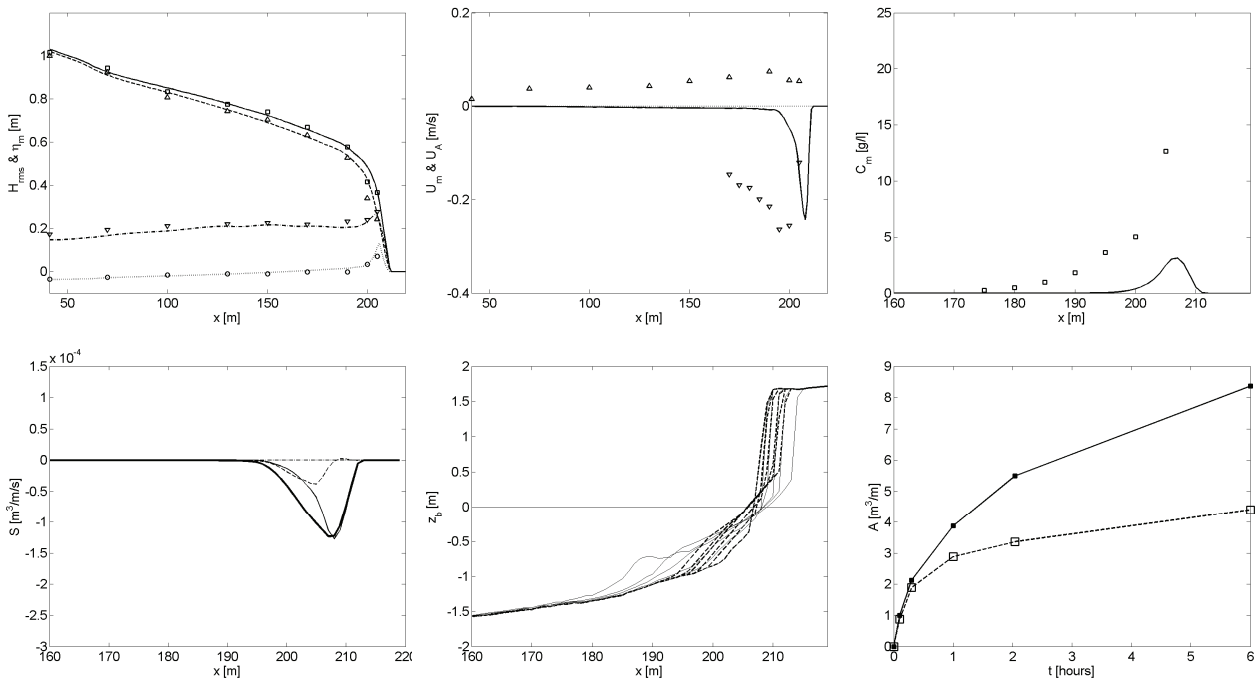


Figure 6.35 Simulation results for test S4 with (bound) long waves, but without short wave stirring and short wave driven undertow. Panels: See Figure 6.31

Simulation results from test S0-S4 show that long wave dynamics influence the morphodynamics in the near dune area. However, the undertow and sediment stirring associated with short waves and rollers is crucial for the correct modeling of dune erosion. In simulations S5 and S6 the importance of respectively the short wave induced undertow and short wave stirring are examined in more detail.

Figure 6.36 shows that excluding the short wave stirring during test S5 results in a 30% underestimation of the dune erosion volume after six hours of waves. The steepness of the upper beach in front of the dune face decreased in relation to test S4, which seems to result from a larger transport capacity of the flow in this area. The dune foot is located at about the same vertical position and the avalanching related sediment transport is important shoreward of $x = 205$ m. The contribution of the undertow to sediment stirring is small and the simulated sediment concentration is comparable to that in S4.

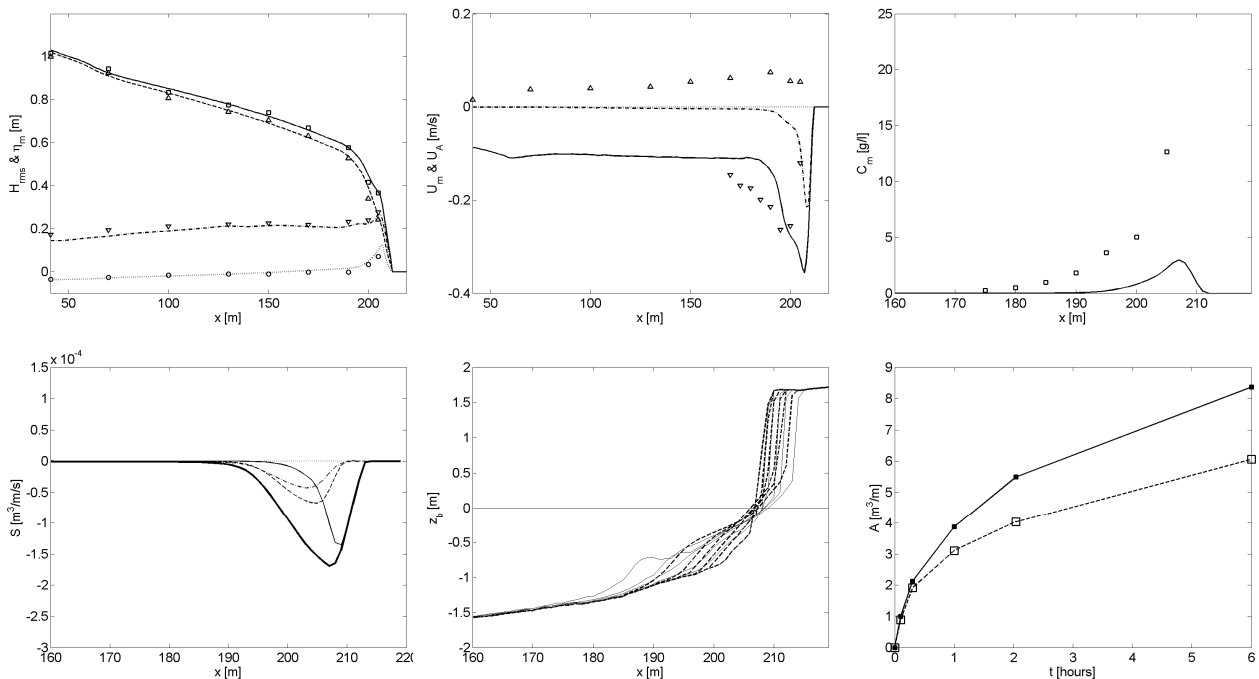


Figure 6.36 Simulation results for test S5 with (bound) long waves, but without short wave stirring. Panels: See Figure 6.31

Excluding the short wave and roller related contribution to the undertow in test S6 results in an underestimation of the simulated dune erosion volume of about 40% after six hours of waves. It is remarkable that the steepness of the foreshore is significantly smaller than in all the previous tests. Close to the dune face the sediment suspension is high whereas sand is hardly transported seaward since the capacity of the undertow is small. As a result it is expected that diffusion related transports are important, which is likely to result in a profile evolution containing less steep slopes. The sediment transport due to avalanching is important shoreward of $x = 205$ m and is (below the water surface) partly compensated by the sediment transport due to nonlinear waves. The sediment suspension in front of the dune face is overestimated due to the absence of a (strong) undertow.

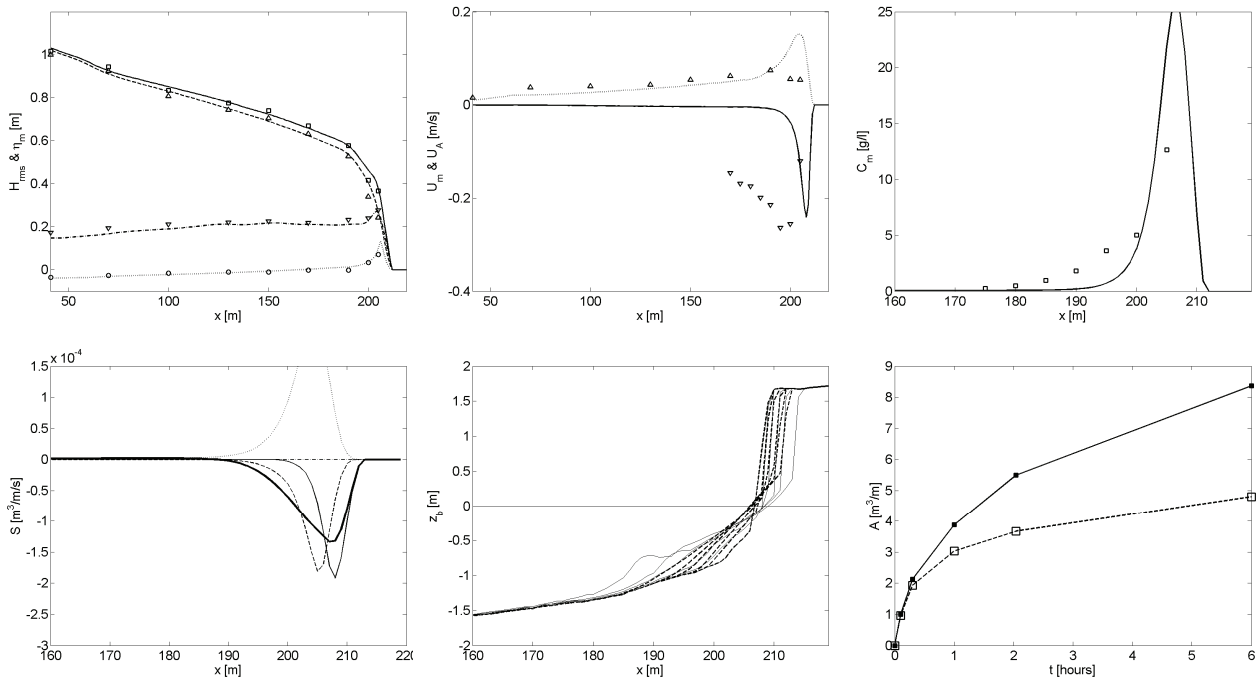


Figure 6.37 Simulation results for test S6 with (bound) long waves, but without short wave driven undertow. Panels: See Figure 6.31

Conclusions and discussion

The discussed simulations show that:

1. The dune erosion rate over approximately the first two intervals is controlled by the sediment supply from the dune face to the wet system (collapsing of the dune face due to avalanching) and the physics-based sediment transport (the product of sediment suspension and flow) is expected to be of minor importance. Instead it is expected that soil properties and the interaction of the dune face with impacting waves will give more insight in the driving processes during these intervals.
2. Using stationary wave conditions and not taking into account the groupiness of waves and related long waves, it seems possible to make a reasonable estimation of the dune erosion volume. The effect of long waves on dune erosion becomes visible after the first two test intervals when the erosion rate is not mainly controlled by the sediment supply from the dune and the foreshore is more developed reducing the short wave energy that reaches the dune face.
3. Long waves contribute to the near dune morphodynamics and are efficient in releasing sand from the dune since they trigger the avalanching algorithm. This triggering is especially important in conditions where the dune foot is located at (or above) mean sea level. In shallow water long waves contribute to the undertow and sediment stirring. However, short waves are required to generate enough offshore transport capacity to transport the long wave released sand from the dune face further seaward.

Finally, it is remarked that in nature the effect of wave groups and long waves might be different since the water level gradually rises during a storm surge and conse-

quently conditions with the dune foot located (significant) below the storm surge level are not likely to occur.

6.5.2 Sediment supply from dunes by avalanching

The interaction of dune face and swash zone, causing that episodically sand is released from the dune by slumping is complex and the processes involved are far from understood. In Chapter 3 a relation as proposed by Fisher et al., (1986) was examined in more detail and it was found that the average wave impact force on the dune face is linearly related to the dune face erosion rate. In addition, it was observed that between successive slumps the dune face steepens until a critical slope is reached and a new collapse of the dune face takes place.

In the XBeach model dune face erosion is mimicked with a simple avalanching algorithm in which the dune face collapses if a critical slope is exceeded. The objective of this paragraph is to test the robustness of the algorithm and to obtain further insight in the sensitivity of simulated dune erosion volume to avalanching settings.

Robustness of avalanching algorithm

In order to test the robustness of the avalanching algorithm a dry bank is considered with a slope of 1:2. The critical dry slope is set at 2:5 meaning the bank is unstable and will start to avalanche as soon as the simulation is started. The maximum avalanche speed A_{max} is set at $0.005 \text{ m}^3/\text{ms}$. Simulations are performed on three different grids including two uniform grids with different dx and one non-uniform grid (see Table 6.7 for more details).

Simulation results are shown in Figure 6.38 and reveal that in all three simulations the avalanche speed of the bank is equal and the bank evolves towards the same stable slope. It is concluded that the avalanche algorithm shows consistent results for various grids.

Table 6.7 Overview of conducted simulations to obtain more insight in the robustness of the avalanching algorithm.

	T01A (Uniform)	T01B (Uniform)	T01C (non-uniform)
Avalanching of dry bank	$dx = 0.1 \text{ m}$	$dx = 0.05 \text{ m}$	$dx_{max} = 0.43 \text{ m}$ and $dx_{min} = 0.06 \text{ m}$
Dune erosion test T01	$dx = 1 \text{ m}$	$dx = 0.5 \text{ m}$	$dx_{max} = 3.7 \text{ m}$ and $dx_{min} = 1 \text{ m}$

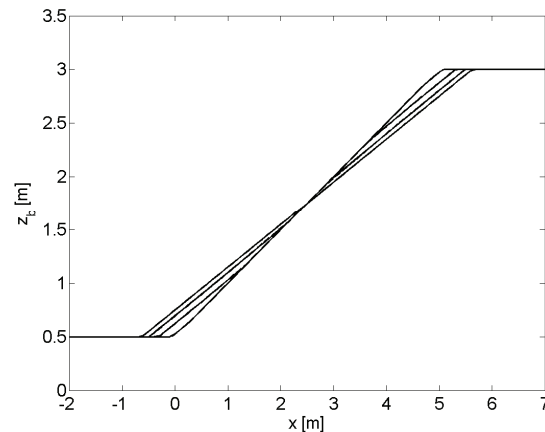


Figure 6.38 Simulated profile evolution during the avalanche of an instable dry bank for three different grids including a uniform grid with $dx = 0.1$ m (solid line), a uniform grid with $dx = 0.05$ m (dashed line) and a non-uniform grid (dotted line). Profiles are shown at $t = 0$ s, $t = 20$ s, $t = 50$ s and $t = 120$ s (simulated profiles for the different grids coincide and cannot be distinguished separately).

In morphodynamic simulations the dune face erosion rate evolves from the interaction of the avalanching algorithm with the near dune hydrodynamics. Long waves initiate avalanches by inundating dry points that become unstable. In order to further investigate this interaction test T01 of the Deltaflume experiment is simulated^{XVIII} on three grids including two uniform grids with different dx and a non-uniform grid (see Table 6.7).

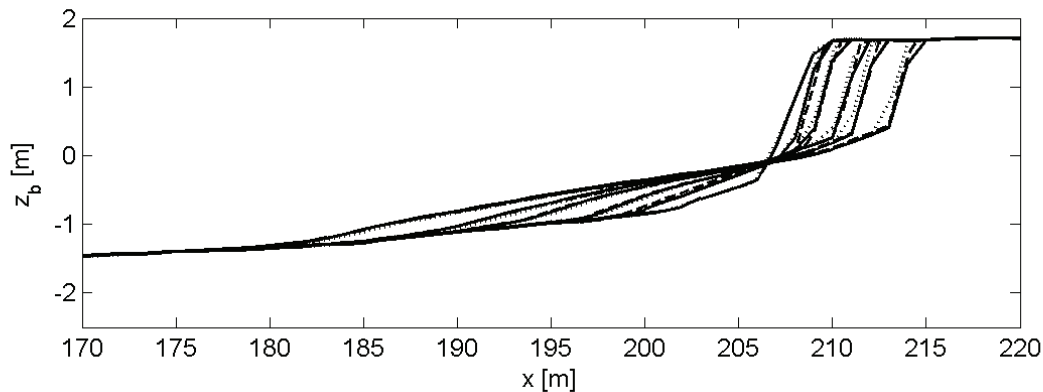


Figure 6.39 Simulated profile evolution during test T01 of the Deltaflume experiment on 3 grids including a uniform grid with $dx = 1$ m (solid line), uniform grid with $dx = 0.5$ m (dashed line) and a non-uniform grid (dotted line). Profiles are shown at $t = 0$ h, $t = 0.1$ h, $t = 0.3$ h, $t = 1.0$ h, $t = 2.04$ h and $t = 6.0$ h.

Simulation results are shown in Figure 6.39 and it is seen that profile evolution for the three simulations is comparable. Occasionally small deviations in profile develop-

^{XVIII} In contrast to earlier simulation settings, in this section a morphological factor of ten was used to speed up the computations. The other settings are equal to those applied in the previous simulations (see Appendix B for more details).

ment are observed, which are related to grid resolution. However, these differences do apparently not affect the dune erosion rate and associated evolution of the foreshore.

Sensitivity to avalanching parameters

The dune erosion rate is determined by the capacity of the near dune hydrodynamics to transport sediment offshore but is also expected to depend on the sediment supply from the dune. The sediment supply from the dune face is simulated with an avalanching algorithm (see Figure 6.40) that considers a critical wet slope ($m_{cr,wet}$) below the water surface and a critical dry slope ($m_{cr,dry}$) in the dry area with dunes and beach. The transition of the critical wet slope to the critical dry slope takes place at a user specified water depth (h_{switch}). In addition, a maximum dune face erosion rate due to avalanching can be specified (A_{max}). The critical wet slope is smaller than the critical dry slope (Verruijt (1994), Chapter 44) and when stable dry points inundate they might become unstable and avalanche. In the model long waves contribute to avalanching since they inundate the upper beach and dune face during run up (see also Section 6.5.1).

The aim of this subsection is to examine how avalanching affects the evolution of the simulated dune erosion volume during a storm surge. Sixteen simulations are performed in which the four variables related to avalanching are varied independently around the optimal parameter settings as found in Section 6.3. The simulations are conducted for test T01 during the Deltaflume experiment. An overview of the simulations is given in Table 6.8.

Table 6.8 Overview of simulations; the bold underlined values refer to the default settings applied in this thesis.

A_{max} , maximum avalanche rate ($m^3/s/m$)	0.001	<u>0.003</u>	0.01	0.05
h_{switch} , water depth at which critical wet slope switches to a critical dry slope (m)	0.01	0.05	<u>0.10</u>	0.20
$m_{cr,wet}$, critical wet slope (-)	<u>0.10</u>	0.15	0.20	0.30
$m_{cr,dry}$, critical dry slope (-)	0.25	0.50	<u>1.00</u>	2.00

Simulation results are shown in Figure 6.41. The dune erosion volumes is sensitive to variations in the parameter settings for avalanching, especially during the initial phase of the experiment. The beach evolution near the dune face is influenced by avalanching and affects the offshore transport capacity of the flow, which should equal the sediment supply from the dunes over a longer period of time. The influence of the critical dry slope (upper left panel) is relatively small and for slopes larger than 0.5, the computed evolution of the dune erosion volume is comparable. The critical wet slope (upper right panel) affects the erosion rate during the whole test except during the first test interval when the erosion rate seems to be consistently limited by the maximum avalanching rate A_{max} . The influence of A_{max} (lower left panel) on the erosion rate vanishes as a test progresses. Finally, the water depth at which the critical

wet slope is switched to the critical dry slope (lower right panel) influences the evolution of the dune erosion volume mainly in the initial phase of the simulation.

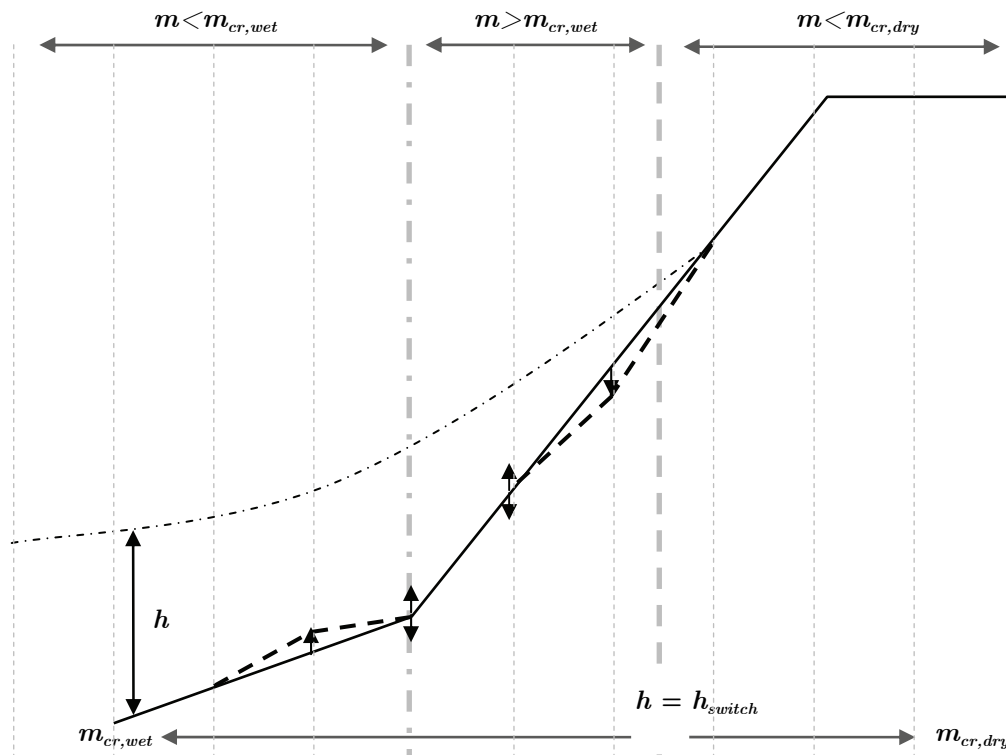


Figure 6.40 Explanation of the avalanching algorithm; the bed is indicated by the black solid line and the water surface by the black dashed-dotted line. The thin gray dashed lines indicate the computational bed level points, which are unstable between the thick gray dashed-dotted line and the thick gray dashed line that show the transition towards a steeper bed slope ($m > m_{cr,wet}$) and to dry points ($h < h_{switch}$) respectively. The post avalanche profile is indicated with the black dashed line. In the present example three bed level points are located in the avalanching zone. In the algorithm first the most seaward point will avalanche, followed by the second and third point respectively. The effect of the avalanches on the bed evolution is indicated by the black dashed line. Note that the new bed is not necessarily stable and new avalanches may take place in the following time step. Also it is seen that the first dry point steepens and might become unstable in the next time step since the local bed slope m might be larger than $m_{cr,dry}$.

Conclusions and discussion

The avalanching algorithm is a relative simple tool to describe the complex process of dune face erosion under wave impacts. The algorithm performs consistent on different grids and sediment supply from the dunes is found to influence the offshore transport capacity of the near dune flows.

It is remarked that instantaneously the dune face erosion rate can be different than the offshore transport capacity of the flow. As a result the beach elevation is allowed to change in time (breathing), which introduces a feedback in the system and cause that over a longer period of time the offshore sediment transport capacity and the sediment supply from the dunes are in equilibrium. In addition, it is hypothesized that the time averaged dune face erosion rate and associated offshore transport capacity of the flow are related to the soil properties of the dune face.

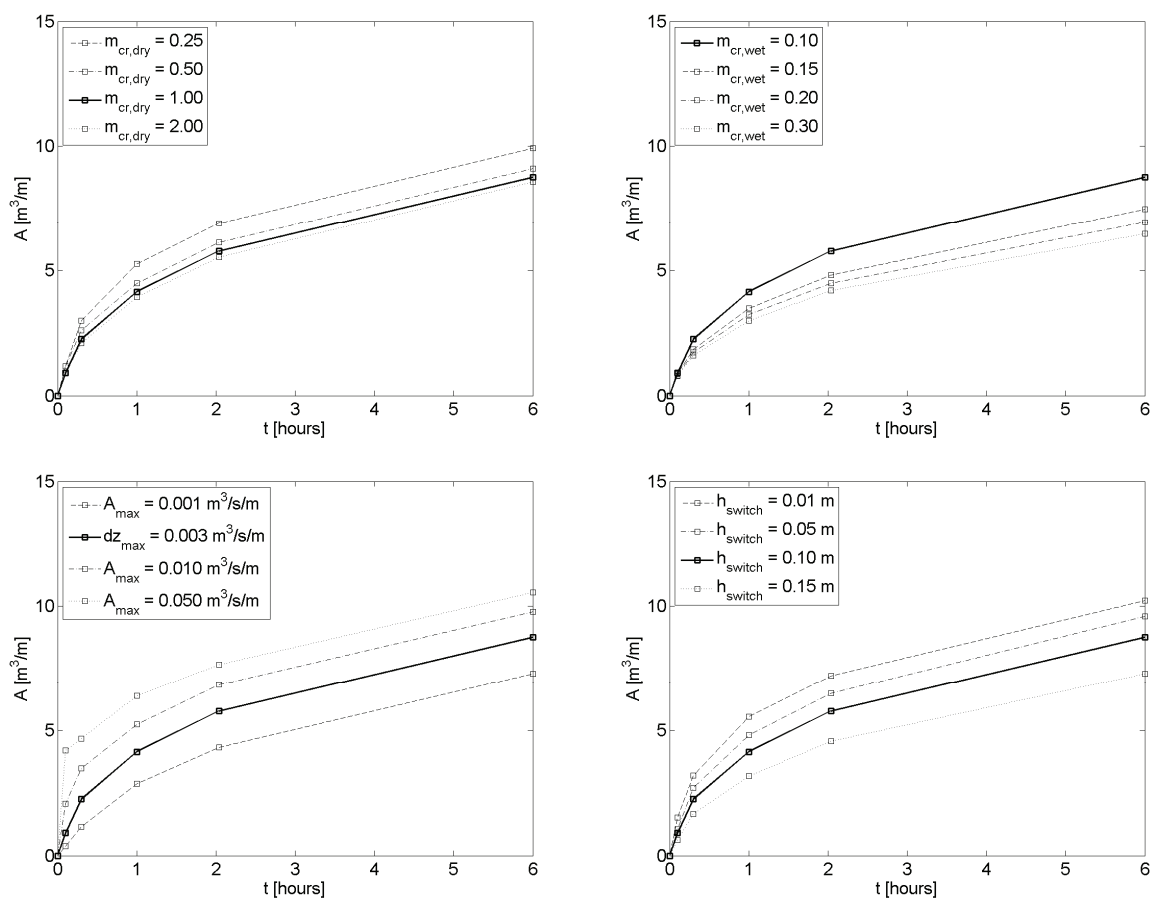


Figure 6.41 Simulated dune erosion volume during test T01 as function of time for different settings of the critical dry slope (upper left panel), the critical wet slope (upper right panel), the maximum dune face erosion rate (lower left panel) and the water depth at which is switched from a critical wet slope to a critical dry slope (lower right panel).

6.6 2DH MORPHODYNAMIC SIMULATIONS

The Dutch government assesses the strength of dunes against normative storm surge conditions every five years. The assessment is performed with an empirical guideline that is based on (large scale) dune erosion experiments in a flume. The number of experiments that is utilized is limited and for that reason the applied guideline is not generic. In addition, the possible non-uniformity of the coastline is not considered.

The model presented in this chapter is physics-based and consequently expected to be more generic. Also the model has the possibility to include the longshore dimension and is capable of dealing with alongshore variability in hydrodynamics, bathymetry and topography.

The aim of this section is to make a qualitative study on the effect of longshore variability on dune erosion. First in Section 6.6.1 2DH model results for a uniform coast are compared with results from a 1D model. In addition, three situations are investigated including a longshore uniform foreshore and varying dune height (Section

6.6.2), a non-uniform foreshore containing shoals and rips with a constant dune height (Section 6.6.3) and the interaction of a dike (hard structure) with a sandy dune system (Section 6.6.4).

6.6.1 Uniform coast

The understanding and modeling of dune erosion is mainly based on (large) scale flume experiments whereas field observations and experiments that include the longshore direction are rare. In the experiments usually a constant maximum storm surge level (Vellinga, 1986) is applied and waves are assumed to come in shore normal. In nature however the surge level varies during a storm and waves are directionally spread. As a result in nature dune erosion mechanisms and the associated retreat of the dune face might be different than found in a flume. For example near shore wave conditions are hypothesized to be less severe in case of directionally spread short waves. The short waves will refract, reducing the energy over a wave crest and the energy transfer from short waves to long waves is also expected to be less (Reniers et al., 2002).

The aim of this subsection is to examine the effect of a storm varying surge and a directionally spread wave field on dune erosion. To this end three simulations are conducted including a 2DH simulation for a longshore uniform coast (S1) and two 1D simulations with a constant (S2) and varying (S3) storm surge level respectively.

The 2DH model covers an area of 800 m alongshore and 3565 m cross-shore. The applied grid is uniform in longshore direction with $dy = 10$ m and non-uniform in cross-shore direction with $dx_{max} = 25$ m (at the offshore boundary) and $dx_{min} = 5$ m (in shallow water and the dune area). The bathymetry (Figure 6.43) is based on the Dutch characteristic profile (see Figure 2.1).

Imposed hydrodynamic conditions are representative for the Dutch coast (Steetzel, 1993) and vary during the simulation (Figure 6.42). The duration of the storm surge considered is 45 hours however only 32 hours are simulated (16 hours before and after the peak of the storm). At the start of the simulation the mean water level is about 0.9 m above mean sea level. The wave conditions are based on a Jonswap spectrum with a directional spreading (Kuik et al., 1990) of about 12 degrees and the mean direction is shore normal. At the lateral boundaries the longshore gradients in water surface elevation and cross-shore flow are set to zero (Neumann boundary) and to save computational time all simulations are performed with a morphological factor of ten. The other simulation settings are described in Appendix B.

The 1D-simulations consider the same cross-shore profile and grid as the 2DH model. Incoming waves are shore normal and without directional spreading. Simulation S2 is performed for a duration of five hours (Vellinga, 1986) and the still water level equals the maximum storm surge level in the time varying surge applied in test S1 and S3.

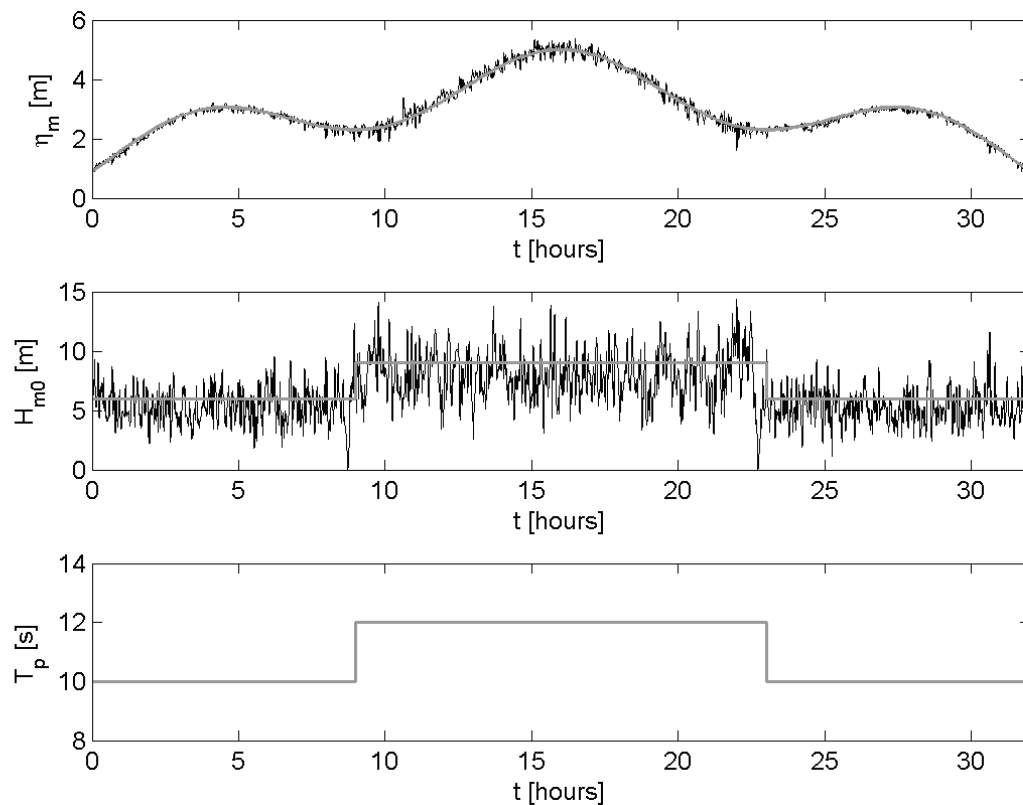


Figure 6.42 Imposed hydrodynamic conditions. Upper panel: Imposed (thick line) and simulated (black line) mean water level. The simulated water level includes long wave water surface fluctuations. Middle panel: Imposed (thick line) and simulated (black line) wave heights. Lower panel: Imposed wave period.

The 2DH simulation results for test S1 are shown in Figure 6.43. It is seen that the mean flow and sediment concentration are reasonably uniform in longshore direction. However, upon closer inspection it is found that the mean flow and sediment concentration vary in magnitude in alongshore direction. These variations can be associated with irregularities in the simulated bed and evolve in the drying and flooding area. It is not clear what causes the irregularities but the retreat of the dune face seems not to be affected by it. Bed level changes and retreat of the dune face are favourably uniform in the alongshore direction and disturbances created at the lateral boundaries on dune face retreat and foreshore evolution seem to be small.

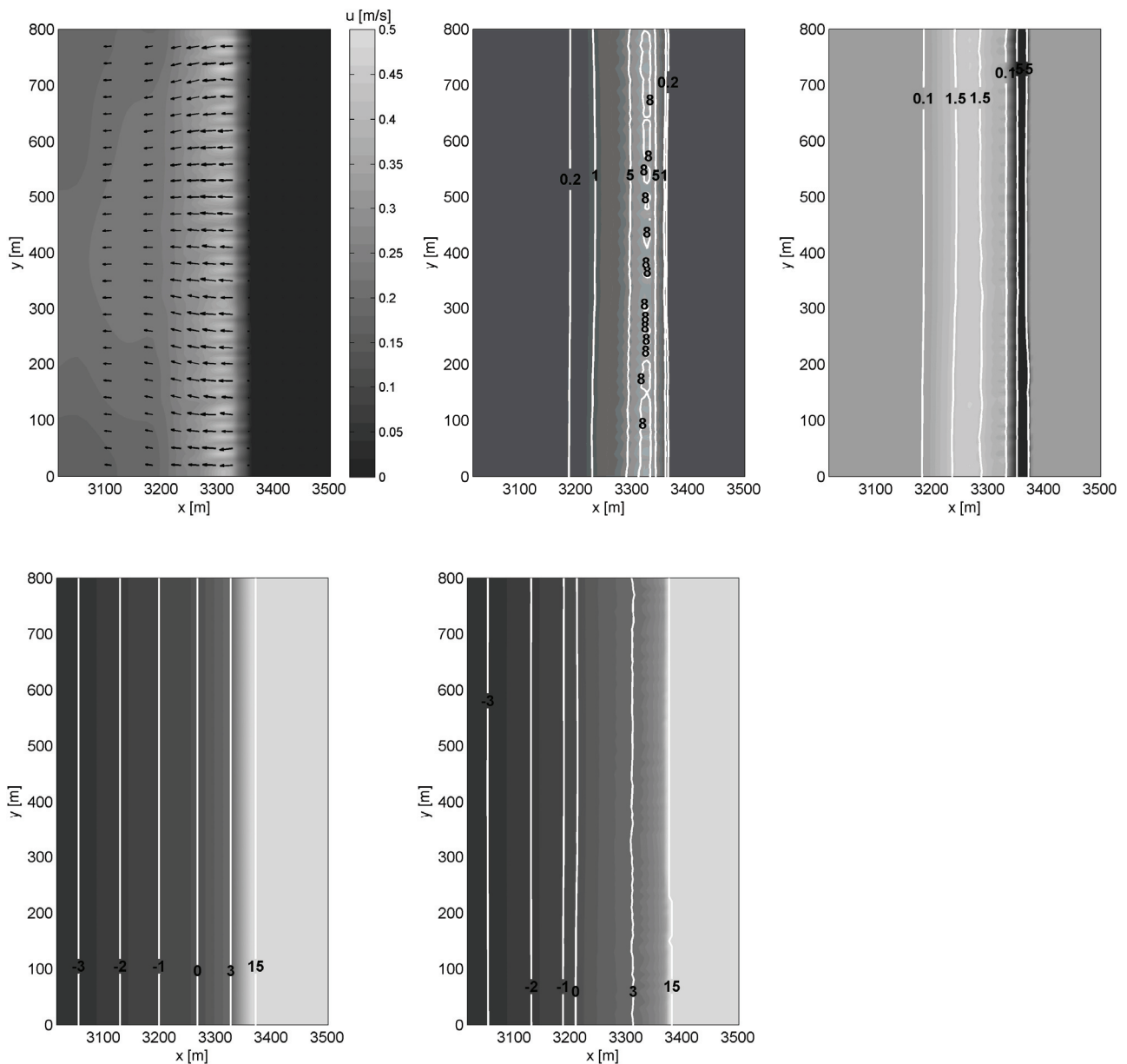


Figure 6.43 Simulation results for test S1 with a longshore uniform coast. Upper left panel: Simulated mean flow field (m/s). Upper middle panel: Mean sediment concentration (g/l). Upper right panel: Bed level change (m). Lower left panel: Initial bathymetry with respect to mean sea level (m). Lower right panel: Final profile with respect to mean sea level (m).

Profile evolution and erosion volume above maximum storm surge level for test S1, S2 and S3 are compared in Figure 6.44. It is seen that dune face retreat for all simulations is comparable but is slightly smaller for the 1D simulation that considers the maximum storm surge level for 5 hours. Also the shape of the foreshore that develops is significantly different for this test. The eroded sand from the dunes is deposited closer to the shore and the post surge beach ends up at a higher elevation. Profile evolution for test S1 and S3, which both include the time varying surge are comparable and look very similar. It seems that the (relatively small) directional spreading in the 2DH simulation has little influence on the post storm longshore averaged profile.

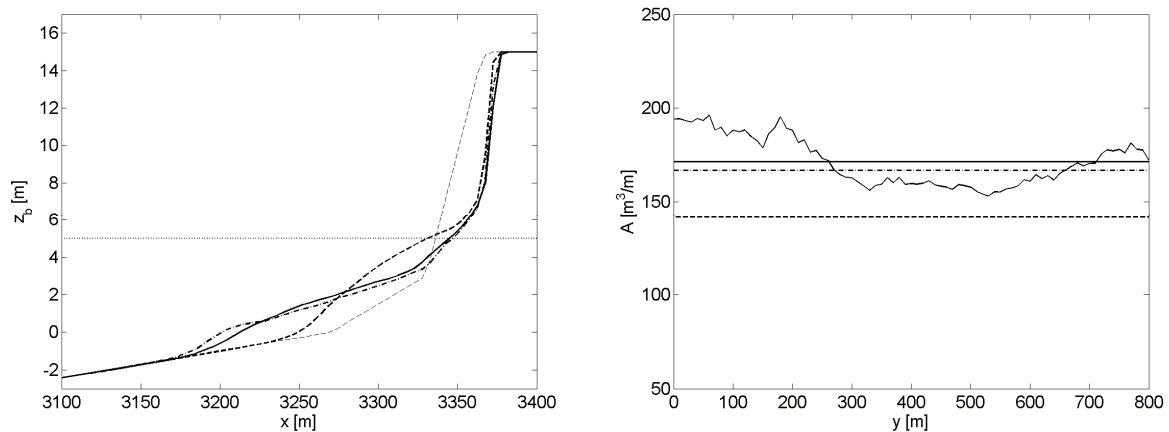


Figure 6.44 Left panel: Alongshore averaged profile evolution for test S1 (solid line), test S2 (dashed line) and test S3 (dashed-dotted line). Right panel: Simulated erosion volume above maximum storm surge level for test S1 (thin solid line) as function of the alongshore position. The alongshore averaged erosion volume for test S1 (thick solid line), S2 (dashed line) and test S3 (dashed-dotted line) are also shown.

The erosion volume above the maximum storm surge level varies in longshore direction (about $\pm 10\%$ in relation to the longshore averaged erosion) and increases towards the lateral boundaries (see Figure 6.44, right panel). Looking at the total erosion volume (not shown) variations in longshore direction are smaller ($\pm 5\%$ in relation to the longshore mean). Alongshore averaged erosion volumes for test S1 and S3 are comparable but are slightly larger for simulation S1 with directionally spread waves. An explanation can be found in lateral boundary effects causing larger erosion volumes in this area, which partly mask the (relatively) small effect of directionally spread waves in the simulation. In the middle of the computational domain between approximately $x = 250$ m and $x = 650$ m the erosion volume in simulation S1 is smaller than in simulation S2, which is in line with the expectations. Erosion volumes in test S2 are order 15% smaller compared to test S1 and S3.

Conclusions and discussion

2DH model results for a uniform coast are compared with results from a 1D model and show that dune face retreat and erosion volumes are comparable. Dune face retreat and foreshore evolution for a 1D simulation with a constant maximum storm surge level are a little smaller with respect to model results with a varying surge. However, the model tends to overestimate dune and beach erosion at the end of a storm and during calm and moderate conditions (see Section 6.4.1, the case of small dune collapse and Section 6.4.2, the case with calm and moderate conditions). As a result any firm conclusion about applying a constant maximum storm surge level as substitute for a varying surge cannot be made at this stage with the present model.

The hydrodynamic conditions (surge level and wave conditions) are comparable to those applied in test T01 of the Deltaflume experiment (see Chapter 2). Using scale relations (Equation 6.23) a prototype erosion volume of about 330 m³/m is found for a profile that is a factor 1.27 steeper than the Dutch reference profile considered here. However, the up-scaled volume is difficult to compare with the erosion volumes found for the simulations presented in this section. It is expected that for a less steep pro-

file, the erosion rates is smaller since the foreshore is more effective in dissipating incoming waves (the profile is expected to be closer to equilibrium with the extreme hydrodynamic conditions).

6.6.2 Alongshore variability in dune height

Several observations show that after a storm surge the cross-shore position of the dune face hardly varies alongshore. Considering a situation with varying dune height alongshore suggests that areas with higher dunes deliver more sand to build up a new foreshore with respect to areas with a smaller dune height. In addition, longshore varying processes should be present that transport eroded sand from higher dunes to the foreshore in areas with lower dunes.

The aim of this section is to examine the effect of alongshore variability of dune height on foreshore evolution during a storm surge. To this end a 2DH simulation is conducted with shore normal incoming waves that are directionally spread.

An area of 800 m alongshore and 3565 m cross-shore is considered and the computational grid is as described in Section 6.6.1. The bathymetry is based on the Dutch characteristic profile (see Figure 2.1) and is uniform in longshore direction below the dune foot. Above the dune foot bed levels locally deviate from the reference profile and are non-uniform alongshore. The vertical elevation of the dune crest varies between 15 m and 10 m above mean water level. Two areas with a dune crest elevation smaller than 15 m are observed in Figure 6.45, lower left panel. The first area ($x = 75$ m to $x = 325$ m) has a length of 250 m and the second area ($x = 375$ to $x = 725$ m) has a length of 350 m. Applied hydrodynamic boundary conditions vary with time and are similar to those applied in Section 6.6.1. Other simulation settings are found in Appendix B.

Model results in Figure 6.45 show that despite alongshore variability in the dune height its crest retreats more or less uniformly (the contour at 10 m above mean sea level shows small variation in longshore direction. However, the variability is comparable to that in the initial profile). Also the evolution of the foreshore looks quite uniform in alongshore direction (except for some small disturbances near the lateral boundaries).

Simulated flow and sediment concentration field show variations in longshore direction. The sediment concentration is higher in front of areas with higher dunes and the near dune flow field shows a time averaged longshore flow component such that sand from higher dunes is transported to areas with smaller dunes. Looking at the bed level change it is clearly seen that the largest volume of sand is eroded in the areas with the highest dunes (about $170 \text{ m}^3/\text{m}$ is eroded from the high dunes and approximately $110 \text{ m}^3/\text{m}$ for the low dunes. The alongshore averaged erosion is $145 \text{ m}^3/\text{m}$, which is 15% smaller as found for the uniform coast). Sand from these areas is transported to cross-shore transects with a smaller dune height such that the foreshore develops more or less uniform in longshore direction.

It seems that weaker areas with a smaller dune height are less exposed to storm surge impact in the presence of higher volume dunes in the neighbourhood. In addition, it

is expected that storm surge impact in areas with higher dunes will be larger in case smaller volume dunes are nearby.

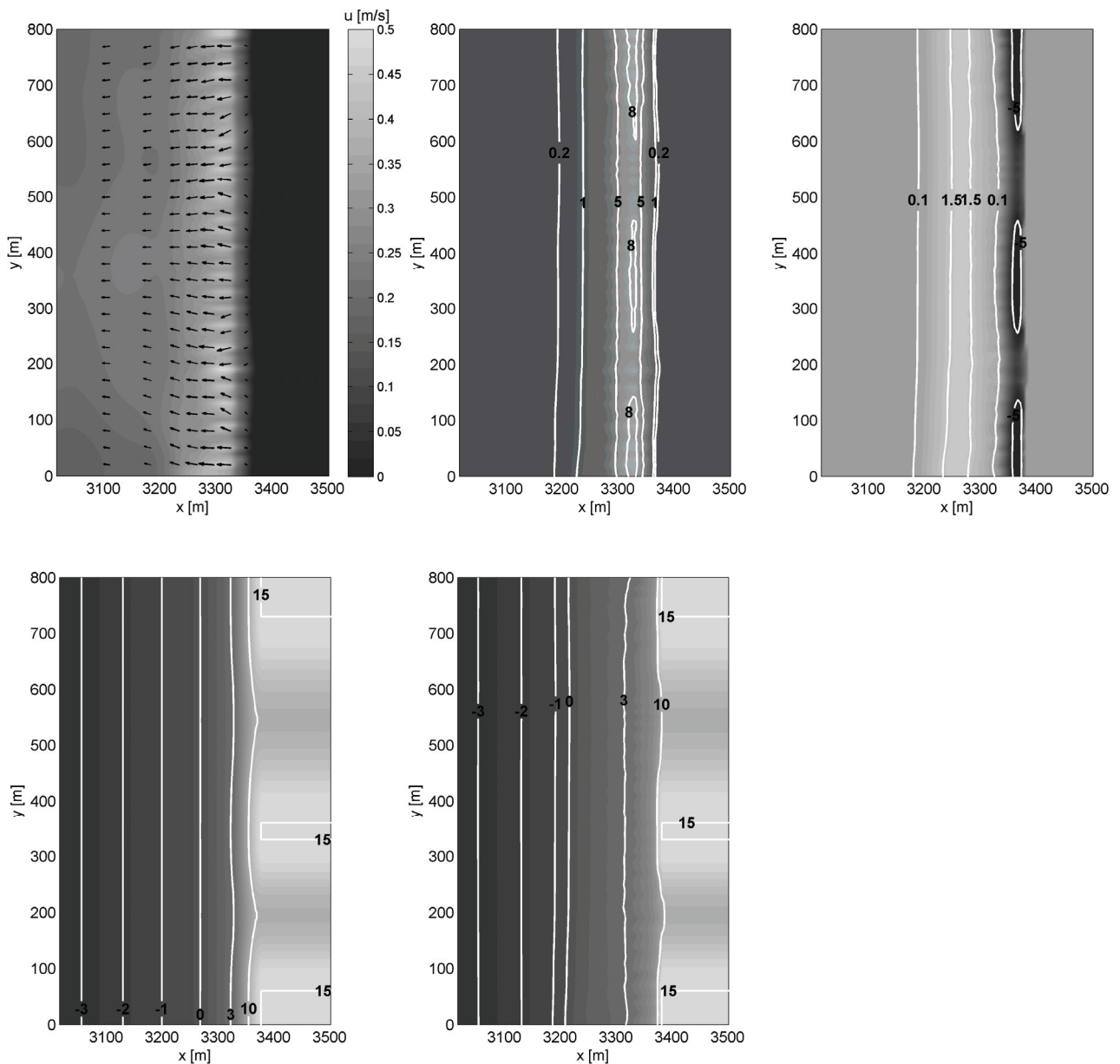


Figure 6.45 Simulation results for a longshore varying dune height. Upper left panel: Simulated mean flow field (m/s). Upper middle panel: Mean sediment concentration (g/l). Upper right panel: Bed level change (m). Lower left panel: Initial bathymetry with respect to mean sea level (m). Lower right panel: Final profile with respect to mean sea level (m).

Conclusions and discussion

Considering a uniform bathymetry and varying dune height alongshore the foreshore is expected to develop uniformly during a storm surge. In addition, the dune crest retreats also quite uniformly and sand from higher dune areas is transported to transects with lower dunes.

6.6.3 Alongshore variability in bathymetry

At several locations along the Dutch coast the bathymetry contains alongshore non-uniform features as bars intersected by rips and beach cusps. Depending on the cross-shore location of these features and their magnitude they can affect near shore wave transformation and hydrodynamics during a storm surge. This could locally affect the dune erosion rate and may lead to a non-uniform retreat of the dune crest.

The aim of this section is therefore to examine the effect of an alongshore non-uniform bathymetry on dune erosion. To this end a 2DH simulation is conducted with shore normal directionally spread incoming waves.

An area of 800 m alongshore and 3565 m cross-shore is considered and the computational grid is as described in Section 6.6.1. Starting point for the bathymetry is the Dutch characteristic profile (see Figure 2.1) to which an offshore bar, an intertidal bar intersected by rips and beach cusps are added (see Figure 6.46). The magnitude of the features is roughly in line with the situation at Egmond beach in The Netherlands. Applied hydrodynamic boundary conditions vary with time and are similar to those applied in Section 6.6.1. Other simulation settings are given in Appendix B.

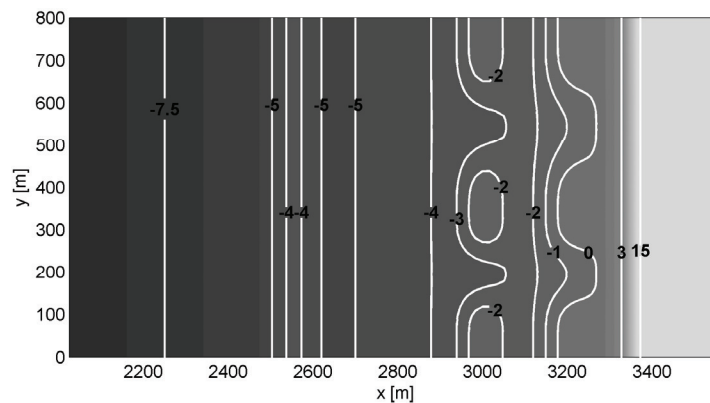


Figure 6.46 Initial profile with an offshore bar (at -4 m with respect to mean sea level), an intertidal bar (at -2 m with respect to mean sea level) intersected by rips and beach cusps (at 0 m in relation to mean sea level). Contours are with respect to mean sea level.

Model results are presented in Figure 6.47 and show that the simulated flow and sediment concentration field are non-uniform in both cross-shore and longshore direction. However, despite that the system is highly 2DH, the foreshore evolution and dune crest retreat is quite uniform. Apparently near dune hydrodynamics and sediment suspensions result in a system that creates a uniform foreshore and uniform retreat of the dune face. The alongshore averaged erosion volume is $155 \text{ m}^3/\text{m}$, which is about 9% smaller as for the uniform coast and 7% larger as for the simulation with alongshore varying dune height.

The intertidal bars move a little shoreward during the simulation and the offshore bar remains more or less in the same position but diffuses (not shown). The beach cusps partly disappear since the area in between the cusps is filled up with sand from the dunes.

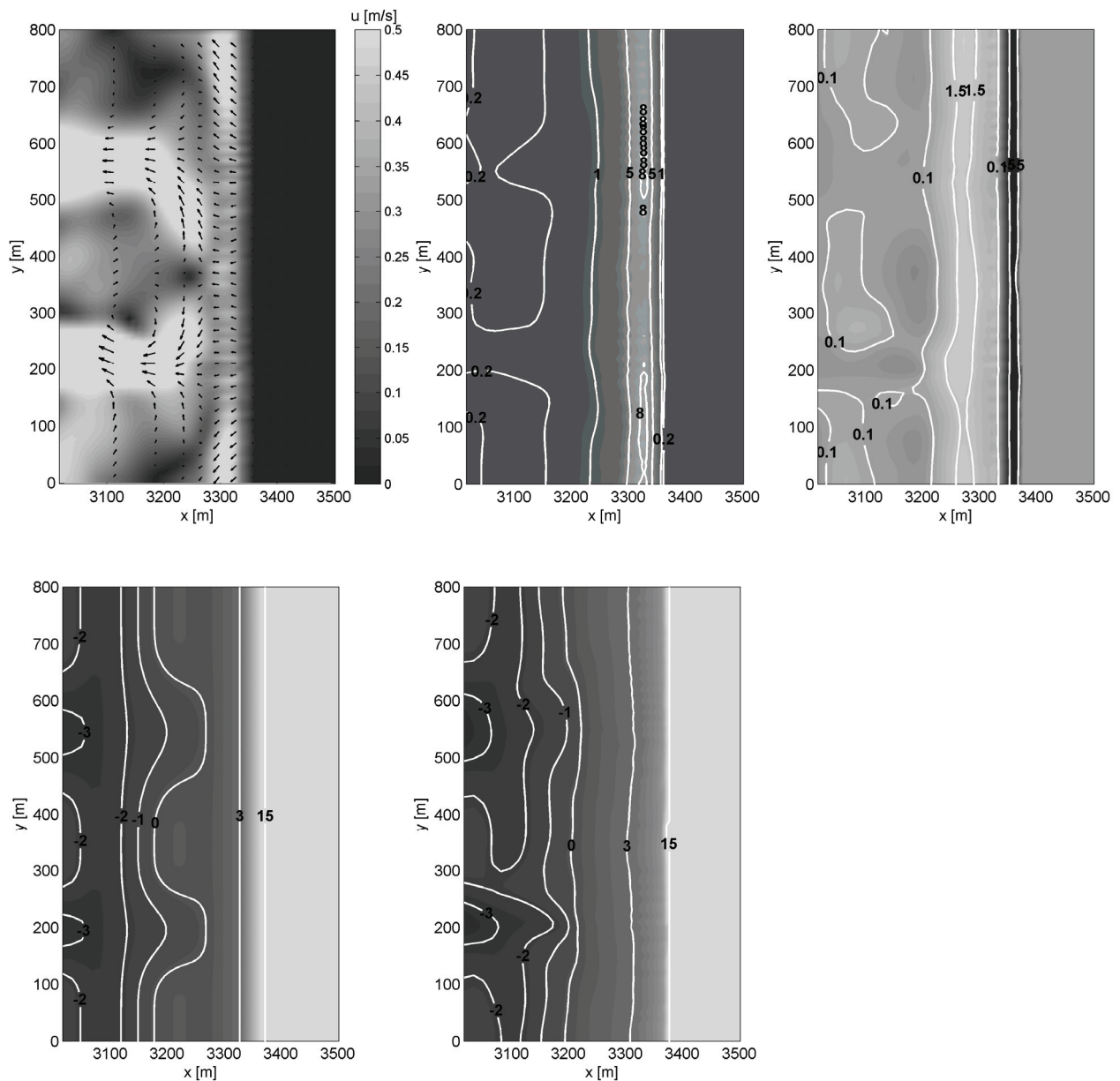


Figure 6.47 Simulation results for a longshore varying bathymetry. Upper left panel: Simulated mean flow field (m/s). Upper middle panel: Mean sediment concentration (g/l). Upper right panel: Bed level change (m). Lower left panel: Initial bathymetry with respect to mean sea level (m). Lower right panel: Final profile with respect to mean sea level (m).

Conclusions and discussion

Considering a non-uniform bathymetry and a constant dune height, the dune crest retreats uniformly in alongshore shore direction. In addition, the foreshore develops quite uniformly even though the near shore flow and sediment concentration field are highly non-uniform in both cross-shore and alongshore direction.

6.6.4 Interaction between a dike and dunes

At several locations along the Dutch coast, the dune system is intersected by hard elements like dune foot revetments, seawalls, groins, breakwaters, dikes and buildings. The alongshore interaction of these non-erodible elements with a sandy dune system during storm surges is far from understood but it is expected that hard structures can locally affect the amount of dune erosion.

The aim of this section is to study the possible effect of the presence of a dike in a sandy dune system (e.g. as found at the Hondsbossche sea defence in The Netherlands). To this end a 2DH simulation is conducted with directionally spread oblique incoming waves (incoming waves have an average angle of 30 degrees with the shore normal).

An area of 800 m alongshore and 3565 m cross-shore is considered and the computational grid is as described in Section 6.6.1. Starting point of the bathymetry is the Dutch characteristic profile (see Figure 2.1) to which a dike is added between $y = 400$ m and $y = 800$ m. The dike has a crest height equal to that of the dunes (is 15 m above the still water level) but protrudes about 50 m seaward with respect to the dune crest (see Figure 6.48). The dike is presumed to be non-erodible and has a sea side slope of one to five.

Simulation results are shown in Figure 6.48 and reveal that dune crest retreat and associated foreshore evolution are affected by the presence of the dike. The strong longshore current (partly) transports the eroded sand from the dunes downstream of the dike out of the cross-shore sections where the sand was first eroded. Due to the presence of the dike this sand is not (or only partly) filled up by upstream sand and consequently the foreshore in front of the downstream dunes develops less fast, which results in a larger average erosion rate over the storm.

The mean erosion between $y = 0$ m and $y = 400$ m is about $190 \text{ m}^3/\text{m}$, which is comparable to a uniform case with oblique waves (not shown). However, near the transition from the dike to the dune system, the erosion volume is significantly larger (about $250 \text{ m}^3/\text{m}$) than further downstream (about $165 \text{ m}^3/\text{m}$ near the lateral boundary). The influence zone of the dike extends over a length of 200 to 400 m downstream of the dike (see Figure 6.48).

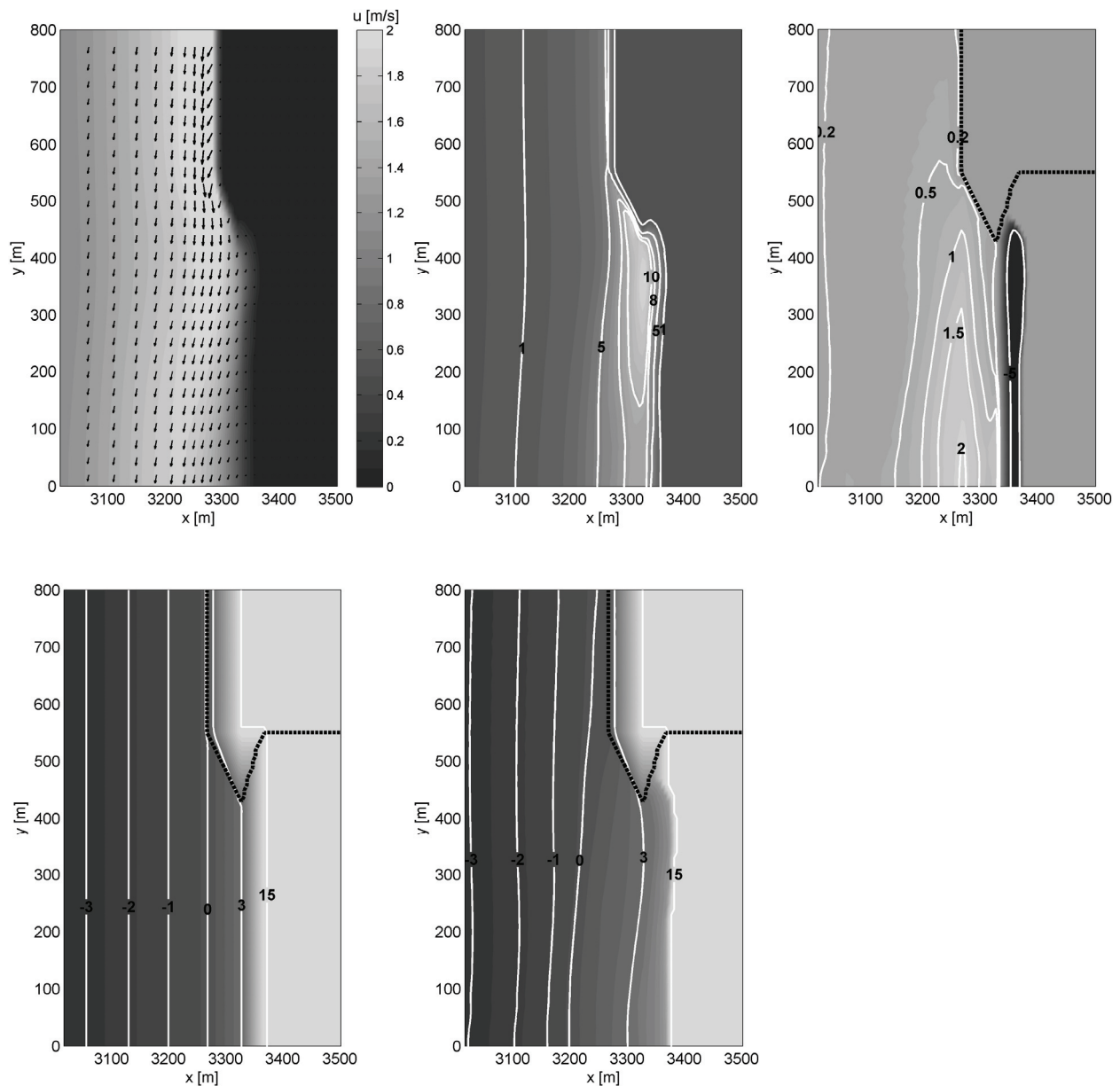


Figure 6.48 Simulation results for the transition of a dike to a sandy dune system. Upper left panel: Simulated mean flow field (m/s). Upper middle panel: Mean sediment concentration (g/l). Upper right panel: Bed level change (m); the thick dotted contour line shows the area where the dike is not covered with sand and consequently no erosion takes place (upper right corner of plot area). Lower left panel: Initial bathymetry with respect to mean sea level (m). Lower right panel: Final profile with respect to mean sea level (m).

Conclusions and discussion

The presence of a dike in the neighbourhood of a sandy dune system is expected to affect the amount of dune erosion during a storm surge with oblique incoming waves. Downstream of the dike, eroded dune sand in the developing foreshore is (partly) picked up by the longshore flow and transported further downstream. In addition this sand is not filled up by upstream sand, since the dike (partly) blocks the sand supply from upstream dunes. This means just downstream of the dike a longshore transport

gradient is present, which results in a less fast developing foreshore and consequently a larger dune erosion rate in this area.

6.7 SUMMARY AND CONCLUSIONS

The morphodynamic model XBeach is extended and optimized. The results of several 1D morphodynamic simulations are compared with measurements and it is shown that:

- The simulated physics over the developing foreshore (e.g. wave height transformation, flow, sediment suspension, sediment transport etc) compare well with detailed measurements obtained during the large scale dune erosion experiment described in Chapter 2.
- The effect of the wave period on dune erosion can favourably be reproduced with the model. The simulated wave period effect is mainly caused by O(60%) increase of the time and depth averaged sediment concentration, which is in line with the measurements.
- The model can accurately reproduce profile evolution and inner surf physics for situations with double-peaked wave spectra.
- The breaching of a small dune can successfully be modeled, but the erosion rate at the end of a storm is overestimated in the model.
- The depth of the scour hole in front of a dune revetment is underestimated by the model and the simulated long wave run-up is insufficient to erode sand above low revetments.
- During calm and moderate conditions the coastline tends to erode a bit, which is caused by a small offshore sediment transport associated with long waves. Bars that are present in the initial profile diffuse.
- Predicted dune erosion volume during the 1953 storm surge at the Delflandse coast is within the range of (prototype) estimated erosion volumes.

Further insight in the modeled dune erosion physics is obtained by studying the effect of long and short waves on dune erosion. In addition, the model sensitivity to different settings for avalanching (the sediment supply from the dune face) is examined. It is found that:

- In the initial phase of the simulations of the large scale dune erosion tests in the Deltaflume (Chapter 2) the erosion rate is controlled by the sediment supply from the dune face (avalanching). At this stage of the test inner surf hydrodynamics and related sediment transport have little influence on the initial profile evolution.
- Imposing only short waves at the model boundary about 70% of the measured dune erosion volume is simulated. A model that considers only long waves simulates about 50% of the measured dune erosion volume.

- Long waves influence the near dune morphodynamics. They are efficient in releasing sand from the dune face and in shallow water long waves contribute to the undertow and sediment stirring.

The XBeach model considers the longshore direction and a 2DH simulation for a uniform coast is compared to results from a 1D model. In addition, three more 2DH simulations are conducted to qualitatively study the effect of longshore variability on dune erosion. It is found that:

- Dune face retreat for 1D-simulations with a constant maximum surge level or a varying surge are comparable to the dune face retreat in a 2DH simulation with a varying surge and directionally spread waves (12°).
- In a situation with a longshore varying dune height and a uniform bathymetry, areas with high dunes are subject to more dune erosion than areas with lower dunes. The dune crest retreats reasonably uniform.
- In a situation with a non-uniform bathymetry and a constant dune height in longshore direction a non-uniform near shore flow and sediment suspension field is simulated. However, at the end of the simulation, foreshore evolution and dune face retreat are quite uniform in longshore direction.
- In a situation with oblique incoming waves and a dike (hard element) that protrudes about 50 m in front of a sandy dune system, dunes just downstream of the dike are subject to more dune erosion.

Chapter 7

CONCLUSIONS AND RECOMMENDATIONS

7.1 CONCLUSIONS

Dune erosion physics

The measured sediment transport during large scale dune erosion tests in a flume increases towards the shoreline and is dominated by the offshore time and depth averaged sediment transport below the wave trough that is associated with the mean flow and mean sediment concentrations (see also Steetzel (1993)). The mean flow velocity gradually increases and the mean sediment concentration rises sharply towards the shoreline. The shoreward wave related sediment transport and transport above the wave trough partly compensate for the mean offshore transport.

In more shallow water a shift in variance towards lower frequencies takes place that is associated with wave group generated long waves (surf beat). Close to the dune face they dominate the hydrodynamics and it is mainly long waves that reach the dune face and impact it. Near dune hydrodynamics can reasonably well be simulated with a depth averaged surf beat model in which the time varying wave forces computed from a wave energy balance and roller energy balance are input to the nonlinear shallow water equations. Time series of measured flows and water surface elevations have been favorably compared with simulation results for large scale dune erosion tests and dissipative conditions in the field. In addition, it was shown that long waves contribute to the mean flow. This contribution becomes more important towards the shoreline.

The measured sediment concentration over the developing foreshore correlates much better with the maximum wave surface slope than with the flow drag. The maximum wave surface slope is associated with (mainly short) wave breaking induced turbulence that is injected in the water column over a relatively short period (the bore interval) and reaches the bed as a pulse. Simulations with a 1DV suspension model revealed that the sediment entrainment is nonlinearly related to the near-bed turbulence intensity and the sediment suspension is substantially higher in conditions with wave varying near-bed turbulence energy instead of wave constant near-bed turbulence energy. Finally, a (depth and short wave averaged) equilibrium sediment con-

centration formulation based on the bore averaged turbulence energy is found to have larger predicting capability than an equilibrium concentration formulation that is based on the wave averaged turbulence energy.

A linear relation between the average wave impact force and the erosion rate as proposed by (Fisher et al., 1986) has been confirmed by measurements. Also it is found that the initial erosion rate is larger than the erosion rate under wave impacts. Initially, waves run over the dune face and steepen it by flow drag based erosion till a transitional slope is reached and waves start to impact the dune face. Due to the wave impacts, the dune face further steepens till a critical slope is reached and a volume of sand slumps from the dunes. The slump volume is more or less constant over a storm surge, however the time interval between successive slumps increases as a surge progresses.

Wave period effect on dune erosion

A 50% increase in the incident short wave period results in 24% more dune erosion after 2 h test duration, which corresponds to the normative storm surge duration for the Dutch coast. The extra dune erosion was explained by a higher offshore directed mean sediment transport that is only partly compensated by an increase of the wave related sediment transport and sediment transport above the wave trough. The higher offshore directed mean sediment transport is mainly caused by higher mean sediment concentrations ($O(100\%)$ near the bed) whereas the mean flows are comparable.

The higher sediment concentrations for a larger wave period correlate well with an increase in the wave maximum surface slope that was associated with the intensity of wave breaking. In addition, it is found that the wave averaged energy dissipation is comparable for tests with different wave periods. However, for a larger wave period this energy is dissipated by fewer waves, which suggests steeper wave fronts and more intensive breaking waves.

Modeling

A generic depth averaged morphodynamic model that solves the physics on the wave group time scale and includes the alongshore direction has been further developed and applied to simulate dune erosion in several conditions. The model includes a surf beat model to accurately reproduce the near dune hydrodynamics. Also the model is extended with an equilibrium sediment concentration formulation that, in addition to flow drag, also depends on the bore averaged near-bed turbulence energy. In order to estimate the bore interval a wave shape parameterization has been developed, which is also applied to compute the roller energy dissipation rate and the intra wave sediment transport associated with skewed and asymmetric waves. An optimal parameter set has been obtained and applied in the simulations.

Detailed comparison of simulated wave transformation, flow, sediment concentration, sediment transport and profile evolution with the measurements from a large scale dune erosion experiment show that modeled physics correspond well to the observations. The effect of the wave period on dune erosion is successfully modeled and is mainly caused by an ($O(60\%)$) increase in the time and depth averaged sediment concentration, which is in line with the measured increase in the sediment concentra-

tion. Model tests with double-peaked wave spectra are favorably simulated and compared to (detailed) measurements. Also the breach of a small dune in front of a larger volume dune and a prototype simulation of the 1953 storm surge at the Delflandse coast are reasonably well modeled.

The model performance is less good for calm and moderate conditions and for situations with a dune foot revetment. For calm and moderate conditions the shoreline tends to erode a bit and bars diffuse. Also the scour hole depth in front of a dune foot revetment is insufficient and the simulated erosion volume above a revetment is generally underestimated.

The importance of short and long waves for dune erosion is studied in more detail and it is found that:

- Initially, the erosion rate is controlled by the sediment supply from the dune face. At this stage inner surf hydrodynamics and related sediment transport have little influence on the profile evolution.
- Long waves influence the near dune morphodynamics and are efficient in releasing sand from the dune face. In shallow water long waves contribute to the undertow and sediment stirring. A model driven by only long waves predicts about 50% of the measured dune erosion volume.
- A model driven by only short waves explains about 70% of the measured dune erosion volume. Neglecting the intra wave sediment transport associated with skewed and asymmetric waves it is expected that a model driven by short waves only can make a reasonable prediction of the amount of dune erosion.

Results from a 2DH simulation with directionally spread waves and a varying surge on a longshore uniform coast are compared with 1D simulation results on the same cross-shore profile with a constant maximum surge level and a varying surge level respectively. It is found that in all simulations the retreat of the dune face is comparable whereas the final profile in the 1D simulation with a constant maximum storm surge level is different with respect to the other model results.

Finally, three exploring simulations that include the longshore direction have been conducted. These simulations reveal that:

- Considering a longshore varying dune height and a uniform bathymetry, areas with high dunes are subject to more dune erosion than areas with lower dunes. The dune crest retreats reasonably uniform.
- Considering a non-uniform bathymetry and a longshore constant dune height a non-uniform near shore flow and sediment suspension field is simulated. However, foreshore evolution and dune face retreat are quite uniform in longshore direction.
- Considering oblique incoming waves and a dike (hard element) that protrudes about 50 m in front of a sandy dune system, a larger dune erosion volume is simulated for dunes just downstream of the dike.

7.2 RECOMMENDATIONS

Interaction of dune face and swash zone

- The sediment supply from the dune face to the beach remains poorly understood and is modeled with a simple avalanching model. Also analysis of the simulation results reveals that in the initial phase of a storm (when the coastal profile is far out of equilibrium with the hydrodynamic forcing) this sediment supply is determinative for the dune erosion rate. As a result more research on the interaction between the swash and the soil mechanics in the dune face seems crucial for a better understanding of dune erosion during storm surges.
- An algorithm to make 3D reconstructions of the dune face and swash zone is discussed to analyse dune face slumping in more detail. However, the amount of bathymetric data obtained from stereo video images is limited, which is partly caused by changing light conditions during the experiment. At this stage the algorithm is not capable to deal with these changing conditions and its robustness is recommended to be improved. Also it is desirable to reduce the computational time required for a reconstruction (De Vries et al., 2009) for faster processing of video data. Finally, it is recommended to further explore different applications for the stereo reconstruction technique in the coastal engineering field (see Clarke et al. (in preparation) and De Vries (2007) for i.e wave shape evolution and the reconstruction of ship hull generated waves).

Near dune hydrodynamics

- Near dune hydrodynamics are solved for quite accurately with a surf beat model getting closer to the dune face. However, in the inner surf zone also short waves are present, which are less detailed resolved (wave action balance and roller energy balance, so no phase information). Models that indeed solve for the short wave water surface elevations and flow velocities are usually expensive in computational effort. However, an interesting model approach, that takes into account the non-hydrostatic pressure under the incident waves is presented by (Stelling and Zijlema, 2003) and (Zijlema and Stelling, 2008). This model is substantially faster than Boussinesque type models (Peregrine, 1967) and consequently might be interesting to be applied on the (short) storm time scale.

Sediment suspensions

- Taking into account intra wave variations in turbulence energy at the bed, the time and depth averaged sediment concentration can reasonably well be predicted. However, in the analysis presented in this thesis a holistic approach is followed and several assumptions and simplifications are made that are worthwhile to be studied in order to further improve the understanding of sediment entrainment and sediment suspension. The dune erosion experiment discussed in this thesis lacks turbulence measurements over depth, which seem crucial additional data to the instantaneous sediment concentration measurements in order to make a more detailed analysis of the proposed suspension mechanism by wave breaking induced turbulence. Additional detailed measurements can give insight in near-bed variations in turbulence energy, turbulence advection

and diffusion in time and space and the different behaviour of turbulence generated by spilling and plunging breaking waves respectively. Without additional data it seems not useful to extend the present analysis with i.e. more complex turbulence models.

Comparing process-based models with empirical models

- In the safety assessment of the Dutch dune coast against normative storm surge conditions it seems logical to apply an empirical dune erosion model in conditions that are comparable to those studied during the large scale flume experiments and to apply a generic model in more complex situations. However, this approach requires that an empirical model and a generic model predict the same amount of dune erosion for i.e. the Dutch reference profile (Figure 2.1), which is not the case at this stage. The amount of dune erosion simulated with the XBeach model in Section 6.1 (erosion volume in the order of $170 \text{ m}^3/\text{m}$) and with other generic models (Steetzel (1993) about $200 \text{ m}^3/\text{m}$ and Van Rijn (2009) about $190 \text{ m}^3/\text{m}$) is substantially smaller than the erosion volume obtained with the empirical model that is currently applied in the guideline (about $330 \text{ m}^3/\text{m}$). It is recommended to further study these differences, which could be attributed to the wrong up-scaling of the flume profiles to prototype conditions or by scale effects in the implemented physics in generic models.

Uncertainties

- In order to apply a generic model for the safety assessment of dunes against normative storm surges requires that uncertainties in the representative storm surge conditions are investigated and taken into account. Several combinations of surge level, and wave characteristics may lead to a storm with a normative frequency of exceedance of 1/100,000 years, each causing a different amount of dune erosion (Den Heijer et al., 2008). Also uncertainties in the initial bathymetry and hydrodynamic boundary conditions cause nonlinear effects in the modeled bed evolution during a storm surge. It is desirable to obtain more insight in these effects in order to estimate the normative storm surge conditions and to make an inventory of desirable model improvements for the future.

2DH validation

- In this thesis exploring 2DH simulations are presented. However, to make quantitative predictions of storm surge impact on a longshore non-uniform coast requires a validation of the 2DH processes in a model (i.e. longshore flow, rips, large eddies). To make this validation requires a different approach in setting up a physical model, which should not be carried out solely in a flume but also in facilities in which the longshore dimension can be included (see i.e. the tests recently conducted at Deltares (2009)). It is remarked though that given the limited dimensions of these facilities scale effects are expected to increase and considering several new observations techniques measurements in the field might be an interesting alternative.

REFERENCES

- Aarninkhof, S.G.J., 2003. Nearshore bathymetry derived from video imagery. PhD Thesis, Delft University of Technology, Delft, 175 pp.
- Abdelrahman, S.M. and Thornton, E.B., 1987. Changes in the short wave amplitude and wavenumber due to presence of infragravity waves, Proceedings of Specialty Conference on Coastal Hydrodynamics, pp. 458-478.
- Arcilla, A.S., Roelvink, J.A., O' Connor, B.A., Reniers, A.J.H.M. and Jiminez, J.A., 1994. The Deltaflume '93 experiment, Coastal Dynamics, Barcelona, pp. 488-502.
- Bailard, J.A., 1981. An energetics total load sediment transport model for a plane sloping beach. *Journal of Geophysical Research*, 86(C11): 10938-10954.
- Battjes, J.A., 1974. Surf similarity, 14th International Conference on Coastal Engineering, Copenhagen, pp. 466-477.
- Battjes, J.A., 1975. Modelling of turbulence in the surfzone, Symposium on Modelling Techniques, San Francisco, pp. 1050-1061.
- Battjes, J.A., Bakkenes, H.J., Janssen, T.T. and Van Dongeren, A.R., 2004. Shoaling of subharmonic gravity waves. *Journal of Geophysical Research*, 109(C02009): doi:10.1029/2003JC001863.
- Bosman, J.J., Van der Velden, E.T.J.M. and Hulsbergen, C.H., 1987. Sediment concentration measurements by transverse suction. *Coastal Engineering*, 11(4): 353-370.
- Bowen, A.J., 1980. Simple models of nearshore sedimentation: Beach profiles and longshore bars. *The Coastline of Canada*, edited by S.B. McCann pp. 1-11, Geological Survey of Canada, Ottawa, 1980.
- Clarke, L.B., Van Thiel de Vries, J.S.M. and Holman, R.A., in preparation. High resolution morphology from stereo video cameras. Planned to be submitted to *Journal of Geophysical Research*.

- Coeveld, E.M., Den Heijer, C., Van de Graaff, J., De Vroeg, J.H. and Steetzel, H.J., 2005. The effect of the wave period on dune erosion, Coastal Dynamics, Barcelona, pp. 11.
- De Ronde, J.G., Van Marle, J.G.A., Roskam, A.P. and Andorka Gal, J.H., 1995. Wave boundary conditions along the Dutch coast in relatively deep water (in Dutch), National Institute for Coastal and Marine Management (RIKZ), The Hague, The Netherlands.
- De Vries, S., 2007. On the generation of surfable ship waves in a circular pool, part II: The application of stereo photo technique measuring water surface elevation and surface flow velocities. MSc Thesis, Delft University of Technology, Delft, 67 pp.
- De Vries, S., Hill, D., De Schipper, M.A. and Stive, M.J.F., 2009. Using stereo photogrammetry to measure coastal waves, 10th International Coastal Symposium, Lisbon, Portugal, pp. 5.
- Deigaard, R. and Fredsøe, J., 1989. Shear stress distribution in dissipative water waves. Coastal Engineering, 13(4): 357-378.
- Deigaard, R., 1993. A note on the three dimensional shear stress distribution in a surf zone. Coastal Engineering, 20(1-2): 157-171.
- Delft Hydraulics, 1984. Scaling series dune erosion, large scale tests in the Delta flume (in Dutch), Report M1263-III, Delft, The Netherlands.
- Delft Hydraulics, 1996. Scale relations; further analysis scale relations of cross-shore transport through pragmatic transport model (in Dutch), Report H2167.
- Delft Hydraulics, 2006. Dune erosion: measurement report large scale model tests, Report H3457, Delft, The Netherlands.
- Deltares, 2009. Dunes and dikes: Lab experiments in the Vinjé Wave Basin, Report H5019.50, Delft, The Netherlands.
- Den Heijer, C., Reniers, A.J.H.M., Van de Graaff, J. and Van Gelder, P.H.A.J.M., 2008. Reducing uncertainty in prediction of dune erosion during extreme conditions, 31th International Conference on Coastal Engineering Hamburg, Germany, pp. 13.
- Deng, G. and Cahill, L.W., 1994. Image enhancement using the log ratio approach, 28th Asilomar Conference on Signals, Systems and Computers. IEEE computer society press, Los Alamitos, California, pp. 198-202.

- Doucette, J.S., Harvey, E.A. and Shortis, M.R., 2002. Stereo-video observation of nearshore bedforms on a low energy beach. *Marine Geology*, 189(3-4): 289-305.
- Drake, T.G. and Calantoni, J., 2001. Discrete particle model for sheet flow sediment transport in the nearshore. *Journal of Geophysical Research*, 106(C9): 19859-19868.
- Duncan, J.H., 1981. An experimental investigation of breaking waves produced by a towed hydrofil. *Proceedings of the Royal Society of London, A* 377: 331-348.
- Fisher, J.S. and Overton, M.F., 1984. Numerical model for dune erosion due to wave uprush, 19th International Conference on Coastal Engineering, Houston, pp. 1553-1558.
- Fisher, J.S., Overton, M.F. and Chisholm, T., 1986. Field Measurements of dune erosion, 20th International Conference on Coastal Engineering, Taipei, Taiwan, pp. 1107-1115.
- Fredsøe, J. and Deigaard, R., 1992. *Mechanics of coastal sediment transport*. Advanced Series on Ocean Engineering, 3, 392 pp.
- Galapatti, R., 1983. A depth-integrated model for suspended transports, Report 83-7. 83-7, Faculty of Civil Engineering, Delft University of Technology, Delft, The Netherlands.
- Guza, R.T., Thornton, E.B. and Holman, R.A., 1984. Swash on steep and shallow beaches., 19th International Conference on Coastal Engineering, Houston, pp. 708-723.
- Hartley, R. and Zisserman, A., 2003. *Multiple view geometry in computer vision*. Cambridge University Press.
- Hoefel, F. and Elgar, S., 2003. Wave-induced sediment transport and sandbar migration. *Science*, 299: 1885-1887.
- Holland, K.T. and Holman, R.A., 1997. Video estimation of foreshore topography using trinocular stereo. *Journal of Coastal Research*, 13(1): 81-87.
- Holman, R.A. and Stanley, J., 2007. The history and technical capabilities of Argus. *Coastal Engineering*, 54(6-7): 477-491.
- Holthuijsen, L.H., Booij, N. and Herbers, T.H.C., 1989. A prediction model for stationary short-crested waves in shallow water with ambient currents. *Coastal Engineering*, 13(1): 23-54.

- Janssen, C.M., Hassan, W.N., Van de Wal, R. and Ribberink, J.S., 1998. Grain-size influence on sand-transport mechanisms, Coastal Dynamics, Plymouth, pp. 58-67.
- Janssen, T.T. and Battjes, J.A., 2007. A note on wave energy dissipation over steep beaches. Coastal Engineering, 54(9): 711-716.
- Komar, P.D. and Miller, M.C., 1975. On the comparison between the threshold of sediment motion under waves and unidirectional currents with a discussion of the practical evaluation of the threshold. Journal of Sedimentary Petrology, 45: 362-367.
- Kuik, A.J., Van Vledder, G.P. and Holthuijsen, L.H., 1990. A method for the routine analysis of pitch-and-roll buoy data. Journal of Physical Oceanography, 18: 1020-1034.
- Larson, M., Kraus, N.C. and Byrnes, M.R., 1989. SBeach: Numerical model for simulating storm-induced beach change. Report 1: Empirical foundation and model development, U.S. Army Engineer Waterways Experiment Station, Coastal Engineering Research Center, Vicksburg, MS.
- Larson, M., Erikson, L. and Hanson, H., 2004a. An analytical model to predict dune erosion due to wave impact. Coastal Engineering, 51(8-9): 675-696.
- Larson, M., Kubota, S. and Erikson, L., 2004b. Swash-zone sediment transport and foreshore evolution: field experiments and mathematical modeling. Marine Geology, 212(1-4): 61-79.
- Law on Water Defenses, 1996. (in Dutch). Government Gazette of the Dutch Kingdom, 8.
- Le Méhauté, B., 1962. On non-saturated breakers and the wave run-up, 8th International Coastal Engineering Conference, Mexico City, pp. 77-92.
- Lewis, J., 1995. Fast normalized cross-correlation. Vision Interface: 120-123.
- Lippmann, T.C. and Holman, R.A., 1989. Quantification of sand bar morphology: A video technique based on wave dissipation. Journal of Geophysical Research, 94(C1): 995-1011.
- Longuet-Higgins, M.S. and Stewart, R.W., 1961. Changes in the form of short gravity waves on long waves and tidal currents. Journal of Fluid Mechanics, 8: 565-583.
- Longuet-Higgins, M.S. and Turner, J.S., 1974. An 'entrainment plume' model of a spilling breaker. Journal of Fluid Mechanics, 63(1): 1-20.

- Madsen, O.S., 1974. Stability of a sand bed under the action of breaking waves, Ralph M. Parsons laboratory for water resources and hydrodynamics.
- Munk, W.H., 1949. Surf beat. *EOS Transactions American Geophysical Union*, 30: 849-854.
- Nairn, R.B., Roelvink, J.A. and Southgate, N.H., 1990. Transition zone width and implications for modelling surf zone hydrodynamics, 22th International Conference on Coastal Engineering, Delft, The Netherlands, pp. 68-81.
- Nielsen, P., 1992. Coastal bottom boundary layers and sediment transport. *Advanced series on Coastal Engineering*, 4, 340 pp.
- Nishi, R. and Kraus, N.C., 1996. Mechanism and calculation of sand dune erosion of storms, 25th International Conference on Coastal Engineering, Orlando, Florida, USA, pp. 3034-3047.
- Overton, M.F. and Fisher, J.S., 1988a. Laboratory investigation of dune erosion. *Journal of Waterway, Port, Coastal and Ocean Engineering*, 114(3): 367-373.
- Overton, M.F. and Fisher, J.S., 1988b. Simulation modeling of dune erosion, 21th International Conference on Coastal Engineering, Malaga, Spain, pp. 1857-1867.
- Overton, M.F., Pratikto, W.A., Lu, J.C. and Fisher, J.S., 1994a. Laboratory investigation of dune erosion as function of sand grain size and dune density. *Coastal Engineering*, 23(1-2): 151-165.
- Overton, M.F., Fisher, J.S. and Hwang, K., 1994b. Development of a dune erosion model using supertank data, 24th International Conference on Coastal Engineering, Kobe, Japan, pp. 2488-2502.
- Peregrine, D.H., 1967. Long waves on a beach. *Journal of Fluid Mechanics*, 27(4): 815-827.
- Phillips, O.M., 1977. *The dynamics of the upper ocean*. Cambridge University Press, New York, 336 pp.
- Plant, N.G. and Holman, R.A., 1997. Intertidal beach profile estimation using video images. *Marine Geology*, 140(1-2): 1-24.
- Puleo, J.A., Beach, R.A., Holman, R.A. and Allen, J.S., 2000. Swash zone sediment suspension and transport and the importance of bore-generated turbulence. *Journal of Geophysical Research*, 105(C7): 17,021-17,044.
- Raubenheimer, B., 2002. Observations and predictions of fluid velocities in the surf and swash zones. *Journal of Geophysical Research*, 107(C11): doi: 10.1029/2001JC001264.

- Reniers, A.J.H.M. and Battjes, J.A., 1997. A laboratory study of longshore currents over barred and non-barred beaches. *Coastal Engineering*, 30(1-2): 1-21.
- Reniers, A.J.H.M., Van Dongeren, A.R., Battjes, J.A. and Thornton, E.B., 2002. Linear modelling of infragravity waves during Delilah. *Journal of Geophysical Research*, 107(C10): doi:10.1029/2001JC001083.
- Reniers, A.J.H.M., Roelvink, J.A. and Thornton, E., 2004a. Morphodynamic modeling of an embayed beach under wave group forcing. *Journal of Geophysical Research*, 109(C01030): doi: 10.1029/2002JC001586.
- Reniers, A.J.H.M., Thornton, E.B., Stanton, T.P. and Roelvink, J.A., 2004b. Vertical flow structure during Sandy Duck: observations and modeling. *Coastal Engineering*, 51(3): 237-260.
- Ribberink, J.S. and Chen, Z., 1993. Sediment transport of fine sand in asymmetric oscillatory flow, Delft Hydraulics, Delft, The Netherlands.
- Rienecker, M.M. and Fenton, J.D., 1981. A Fourier approximation method for steady water waves. *Journal of Fluid Mechanics*, 104: 119-137.
- Roelvink, J.A. and Stive, M.J.F., 1989. Bar-generating cross-shore flow mechanisms on a beach. *Journal of Geophysical Research*, 94(C4): 4785-4800.
- Roelvink, J.A., 1993. Surf beat and its effect on cross-shore profiles. PhD Thesis, Delft University of Technology, Delft, The Netherlands.
- Roelvink, J.A., Meijer, T.J.G.P., Houwman, K., Bakker, R. and Spanhoff, R., 1995. Field validation and application of coastal profile model, Coastal Dynamics, Gdansk, Poland, pp. 818-828.
- Roelvink, J.A., Reniers, A.J.H.M., Van Dongeren, A.R., Van Thiel de Vries, J.S.M. and Lescinski, J., 2006. XBeach annual report and model description, UNESCO-IHE, WL | Delft Hydraulic and Delft University of Technology, Delft, The Netherlands.
- Roelvink, J.A., Reniers, A.J.H.M., Van Dongeren, A.R., Van Thiel de Vries, J.S.M., Lescinski, J. and Walstra, D.J.R., 2007. Modeling hurricane impact on beaches, dunes and barrier islands. , International workshop on wave hindcasting and forecasting, Hawaii, USA.
- Roskam, A.P. and Hoekema, J., 1996. Boundary conditions for wave periods along the Dutch coast (in Dutch), National Institute for Coastal and Marine Management (RIKZ), The Hague, The Netherlands.

- Ruessink, B.G., Miles, J.R., Feddersen, F., Guza, R.T. and Elgar, S., 2001. Modeling the alongshore current on barred beaches. *Journal of Geophysical Research*, 106(C10): 22451-22463.
- Ruessink, B.G. and Van Rijn, L.C., manuscript in preparation. Observations and empirical modelling of near-bed wave skewness and asymmetry.
- Santel, F., Heipke, C., Konnecke, S. and Wegmann, H., 2002. Image sequence matching for the determination of three dimensional wave surfaces. *International Archives of Photogrammetry, Remote Sensing and Spatial Information Sciences*, XXXIV(5): 596-600.
- Sénéchal, N., Dupuis, H., Bonneton, P., Howa, H. and Pedreros, R., 2001. Observations of irregular wave transformation in the surf zone over a gently sloping beach on the French Atlantic coastline. *Oceanologica Acta*, 24(6): 545-556.
- Soulsby, R.L., Hamm, L., Klopman, G., Myrhaug, D., Simons, R.R. and Thomas, G.P., 1993. Wave-current interaction within and outside the bottom boundary layer. *Coastal Engineering*, 21(1-3): 41-69.
- Steetzel, H.J., 1987. Systematic reserach on the effectiveness of dune toe revetments, Large scale model investigation (in Dutch), Report H298-I, Delft Hydraulics, Delft, The Netherlands.
- Steetzel, H.J., 1993. Cross-shore transport during storm surges. PhD Thesis, Delft University of Technology, Delft, The Netherlands.
- Steetzel, H.J., 1994. Closer refinement DUROSTA-model (in Dutch), Report H1865, Delft Hydraulics, Marknesse, The Netherlands.
- Stelling, G.S. and Duijnmeijer, S.P.A., 2003. A staggered conservative scheme for every Froude number in rapidly varied shallow water flows. *International Journal for Numerical Methods in Fluids*, 43: 1329-1354.
- Stelling, G.S. and Zijlema, M., 2003. An accurate and efficient finite-difference algorithm for non-hydrostatic free-surface flow with application to wave propagation. *International Journal for Numerical Methods in Fluids*, 43(1): 1-23.
- Stive, M.J.F. and Dingemans, M.W., 1984. Calibration and verification of a one-dimensional wave energy decay model. Report on investigation, Delft Hydraulics, Delft, The Netherlands.
- Stive, M.J.F. and De Vriend, H.J., 1994. Shear stresses and mean flow in shoaling and breaking waves, 24th International Conference on Coastal Engineering, Kobe, Japan, pp. 594-608.

- Sun, C., 2002. Fast stereo matching using rectangular subregioning and 3d maximum surface techniques. *International Journal of Computer Vision*, 47(1-3): 99-117.
- Svendsen, I.A., 1984. Wave heights and set-up in a surf zone. *Coastal Engineering*, 8(4): 303-329.
- Symonds, G., Huntley, D.A. and Bowen, A.J., 1982. Two dimensional surf-beat: Long wave generation by a time varying breakpoint. *Journal of Geophysical Research*, 87(C1): 492-498.
- Van Dongeren, A.R. and Svendsen, I.A., 1997. Absorbing-generating boundary condition for shallow water models. *Journal of Waterway, Port, Coastal and Ocean Engineering*: 303-313.
- Van Dongeren, A.R., Battjes, J.A., Janssen, T.T., Van Noorloos, J., Steenhauer, K. and Reniers, A.J.H.M., 2007. Shoaling and shoreline dissipation of low-frequency waves. *Journal of Geophysical Research*, 112(C02011): doi: 10.1029/2006JC003701.
- Van Gent, M.R.A., Van Thiel de Vries, J.S.M., Coeveld, E.M., De Vroeg, J.H. and Van de Graaff, J., 2008. Large-scale dune erosion tests to study the influence of wave periods. *Coastal Engineering*, 55(12): 1041-1051.
- Van Rijn, L.C., 1984. Sediment transport, Part II: suspended load transport. *Journal of Hydraulic Engineering*, 110(11): 1613-1641.
- Van Rijn, L.C., 1993. Principles of sediment transport in rivers, estuaries and coastal seas. Aqua Publications, Amsterdam, The Netherlands.
- Van Rijn, L.C., 2007. Unified view of sediment transport by currents and waves, part I, II, III and IV. *Journal of Hydraulic Engineering*, 133(6,7): 649-689 (part I & II), 761-793 (part III & IV).
- Van Rijn, L.C., 2009. Prediction of dune erosion due to storms. *Coastal Engineering*, 56(4): 441-457.
- Van Thiel de Vries, J.S.M., Van de Graaff, J., Raubenheimer, B., Reniers, A.J.H.M. and Stive, M.J.F., 2006. Modeling inner surf hydrodynamics during storm surges, 30th International Conference on Coastal Engineering, San Diego, USA, pp. 896-908.
- Van Thiel de Vries, J.S.M., Clarke, L.B., Aarninkhof, S.G.J., Coeveld, E.M., Holman, R.A., Palmsten, M.L., Reniers, A.J.H.M., Stive, M.J.F. and Uijtewaal, W.S.J., 2007. Interaction of dune face and swash zone, *Coastal Sediments*, New Orleans, pp. 1975-1987.

- Van Thiel de Vries, J.S.M., Van Gent, M.R.A., Walstra, D.J.R. and Reniers, A.J.H.M., 2008. Analysis of dune erosion processes in large-scale flume experiments. *Coastal Engineering*, 55(12): 1028-1040.
- Van Thiel de Vries, J.S.M. and Reniers, A.J.H.M., 2009. Modeling inner surf sediment concentrations during storm surges. Manuscript for *Coastal Engineering*, in preparation.
- Vellinga, P., 1984. Scale series dune erosion: Large scale tests in the Deltaflume (in Dutch), Delft Hydraulics, Delft.
- Vellinga, P., 1986. Beach and dune erosion during storm surges. PhD Thesis, Delft University of Technology, Delft, The Netherlands, 169 pp.
- Verruijt, A., 1994. Soil Mechanics (in Dutch). VSSD, Delft.
- Walstra, D.J.R., Roelvink, J.A. and Groeneweg, J., 2000. Calculation of wave-driven currents in a 3D mean flow model, 27th International Conference on Coastal Engineering, Sydney, pp. 1050-1063.
- Weng, J., Cohen, P. and Herniou, M., 1992. Camera calibration with distortion models and accuracy evaluation. *IEEE Transactions on pattern analysis and machine intelligence*, 14(10): 965-980.
- Wolf, P.R., 1983. *Elements of Photogrammetry*. McGraw-Hill, Inc., New York.
- Zhang, Z., 2000. A flexible new technique for camera calibration. *IEEE Transactions on pattern analysis and machine intelligence*, 22(11): 1330-1334.
- Zijlema, M. and Stelling, G.S., 2008. Efficient computation of surf zone waves using the nonlinear shallow water equations with non-hydrostatic pressure. *Coastal Engineering*, 55(10): 780-790.

LIST OF SYMBOLS

ROMAN SYMBOLS

A	(dune) erosion volume
A_{env}	short wave envelope
A_i	amplitude of i th short wave harmonic
A_{max}	maximum dune face erosion rate
A_r	roller area
A_{sb}	bed load coefficient
A_{ss}	suspended load coefficient
A_w	wave action
C_d	drag coefficient
C	actual depth averaged sediment concentration
C_E	empirical dune face erosion coefficient
C_m	time and depth averaged sediment concentration
D	wave energy dissipation
D_b	expected dissipation rate in a breaking wave
D_h	horizontal diffusion coefficient for sediment
D_r	roller energy dissipation
D_v	vertical diffusion coefficient for sediment
D_{50}	median grain diameter
D_*	dimensionless particle size
E_r	roller energy
E_w	wave energy
F	wave impact force on dune face
F_i	wave forcing in i -direction
H_{rms}	root mean square wave height
H_{mo}	spectral wave height ($\sqrt{2}H_{rms}$)
H_0	dimensionless wave height
I	incoming momentum flux
L	short wavelength
L_{mix}	mixing length
P_b	fraction of breaking waves
Q	discharge (uh)
R	reflection coefficient
S_f	shape function for intra-wave turbulence
$S_{m-1,0}$	wave steepness associated with the spectral mean wave period ($T_{m-1,0}$)
S_p	wave steepness associated with the peak wave period (T_p)

S_w	wave energy per directional bin
S_r	roller energy per directional bin
S_i	sediment transport in i -direction
S_{ij}	short wave contribution to radiation stress
$S_{ij,r}$	roller contribution to radiation stress
$S_{\eta\eta}$	water surface variance per Hertz
T	wave period
T_{bore}	bore interval period
T_{long}	long wave period
T_s	adaptation time scale for sediment
T_m	mean intrinsic wave period
$T_{m-1,0}$	spectral mean wave period
T_0	dimensionless wave period
U_m	time and depth averaged flow velocity
a	flow acceleration
c_g	wave group velocity
c	actual sediment concentration
c_m	time averaged sediment concentration
c_{eq}	equilibrium sediment concentration
c_f	demeaned sediment concentration
c_{stir}	actual sediment entrainment concentration
c_w	wave celerity
c_θ	wave celerity in θ -space
c_0	actual near bed sediment concentration
f_m	mean intrinsic wave frequency
f_{split}	split frequency between low frequency and high frequency waves
g	gravitational acceleration
h	water depth
h_{min}	threshold water depth considered in computing undertow
h_{switch}	water depth at which is switched from a critical wet bed slope to a critical dry bed slope
k	turbulence energy
k_b	turbulence energy near the bed
k_s	turbulence energy at the water surface
k_w	wave number
m_{cr}	critical bed slope
$m_{cr,dry}$	critical bed slope in dry points
$m_{cr,wet}$	critical bed slope in wet points
n	wave breaking parameter
p	sediment porosity
p_{bed}	near-bed water pressure due to waves
s	relative density (ρ_s/ρ_w)
t	time
u	flow velocity in x-direction
u_A	mean flow component due to nonlinear waves

u_{bed}	intra wave near-bed flow velocity
u_{cr}	critical flow velocity for sediment entrainment
$u_{cr,c}$	critical flow velocity for sediment entrainment due to currents only
$u_{cr,w}$	critical flow velocity for sediment entrainment due to waves only
u^E	Eulerian flow velocity in x -direction
u_f	demeaned flow velocity
u_m	time averaged flow velocity
u^L	Lagrangian flow velocity in x -direction
u^S	Stokes drift velocity in x -direction
v	flow velocity in y -direction
v^E	Eulerian flow velocity in y -direction
v^L	Lagrangian flow velocity in y -direction
v^S	Stokes drift velocity in y -direction
w	wave shape parameter ($0 < w < 1$)
w_s	sediment fall velocity
x	horizontal cross-shore coordinate
y	horizontal alongshore coordinate
z	vertical coordinate
z_b	bed elevation

GREEK SYMBOLS

α	wave breaking parameter
α_u	coefficient for time averaged flow due to nonlinear waves, related to the phase shift between intra wave sediment suspension and flow
α_0	orientation of computational coordinate system in relation to the real world
β	mean angle of wave front
γ	wave breaking parameter
γ_{cbed}	calibration coefficient for near-bed sediment concentration
γ_{flow}	flow calibration factor in equilibrium sediment concentration
γ_{morf}	bed level multiplication factor
γ_{Tbore}	calibration factor for bore interval period
γ_{turb}	turbulence calibration factor in equilibrium sediment concentration
γ_{visch}	calibration factor for horizontal sediment diffusion coefficient
γ_{viscv}	calibration factor for vertical sediment diffusion coefficient
γ_{wave}	wave calibration factor in equilibrium sediment concentration
ΔW	weight of slumped dune erosion volume
ΔV	slumped dune erosion volume
ΔT	time interval between successive slumps
η	water surface elevation
η_m	setup / setdown of mean water level
η_r	characteristic wave surface elevation
η_{tr}	wave trough elevation
θ	wave angle
θ_m	mean wave angle
ν_h	horizontal viscosity
$\nu_{h,back}$	horizontal background viscosity

ν_v	vertical viscosity
$\nu_{v,back}$	vertical background viscosity
ρ	correlation coefficient
ρ_s	mass density of sand
ρ_w	mass density of water
τ_{bi}	bottom shear stress in i -direction
τ_r	wave averaged shear stress between roller and water surface
τ_{si}	wind shear stress in i -direction
ϕ	wave phase
ω	radian wave frequency

SUBSCRIPTS

i,j	indices being x or y
x,y	indices corresponding to the cross-shore and alongshore direction

Appendix A

DESCRIPTION OF THE MORPHODYNAMIC MODEL XBEACH^{XIX}

MODEL DESCRIPTION

In the coordinate system the computational x -axis is always oriented towards the coast, and the y -axis is directed alongshore (see Figure A.1). The coordinate system is defined relative to world coordinates (x_w, y_w) through the origin (x_{ori}, y_{ori}) and the orientation α_0 , defined counter-clockwise with relation to the x_w -axis (East).

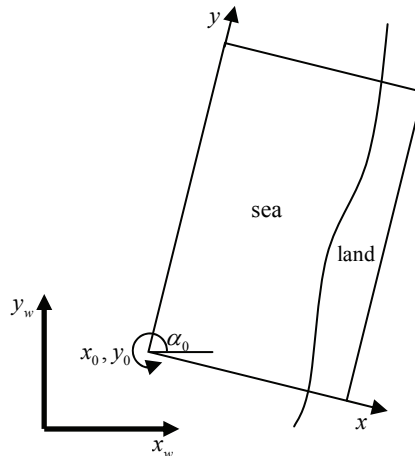


Figure A.1 Coordinate system

The grid applied is a rectilinear, non-equidistant, staggered grid, where the bed levels, water levels, water depths and concentrations are defined in cell centers, and velocities and sediment transports are defined in u - and v -points, located at the cell interfaces. In the wave model, wave action, roller energy and radiation stresses are defined in cell centers, whereas radiation stress gradients are defined at u - and v -points.

^{XIX} The model description in this Appendix is derived from: Roelvink, J.A., Reniers, A.J.H.M., Van Dongeren, A.R., Van Thiel de Vries, J.S.M., Lescinski, J. and Walstra, D.J.R., 2007. Modeling hurricane impact on beaches, dunes and barrier islands. , International workshop on wave hindcasting and forecasting, Hawaii, USA.

Short waves

Short wave transformation is obtained from a time dependent version of the wave action balance equation. Using a similar approach as in Delft University's HISWA model (Holthuijsen et al., 1989), the directional distribution of the wave action is taken into account whereas the frequency spectrum is represented by a single characteristic mean frequency. The wave action balance is then given by:

$$\frac{\partial A_w}{\partial t} + \frac{\partial c_{g,x} A_w}{\partial x} + \frac{\partial c_{g,y} A_w}{\partial y} + \frac{\partial c_\theta A_w}{\partial \theta} = -\frac{D}{\omega} \quad (\text{A.1})$$

in which A_w is wave action that is expressed as:

$$A_w = \frac{S_w}{\omega} \quad (\text{A.2})$$

where S_w is the wave energy in each directional bin and ω is the mean intrinsic radian wave frequency. The wave action propagation speeds in x - and y -direction are given by:

$$\begin{aligned} c_{g,x} &= c_g \cos(\theta) \\ c_{g,y} &= c_g \sin(\theta) \end{aligned} \quad (\text{A.3})$$

where θ represents the angle of incidence with respect to the x -axis and c_g is the wave group velocity. The propagation speed in θ -space is computed as:

$$c_\theta = \frac{\omega}{\sinh 2k_w h} \left(\frac{\partial h}{\partial x} \sin \theta - \frac{\partial h}{\partial y} \cos \theta \right) \quad (\text{A.4})$$

and counts for bottom refraction^{xx}. The wave number k_w is obtained from the linear dispersion relation:

$$\omega = \sqrt{gk_w \tanh k_w h} \quad (\text{A.5})$$

and also is the wave group velocity in Equation A.3:

$$c_g = nc_w = \left(\frac{1}{2} + \frac{k_w h}{\sinh 2k_w h} \right) \frac{\omega}{k_w} \quad (\text{A.6})$$

The wave energy dissipation due to breaking is modeled with an adapted formulation of Roelvink (1993) following a comparable approach as Janssen and Battjes (2007):

$$\bar{D} = 0.25 \alpha \rho_w g P_b f_m \frac{H_{rms}^3}{h} \quad (\text{A.7})$$

^{xx} XBeach also includes the possibility to take into account wave current interaction and possible refraction on flows. However in this thesis wave current interaction is not modeled and the equations are therefore not written.

where α is calibration factor of $O(1)$. Physical parameters are the water density ρ_w , the gravitational acceleration g , the mean intrinsic frequency f_m , the water depth h , the wave height H_{rms} and the fraction of breaking waves P_b :

$$P_b = 1 - \exp\left(-\left(\frac{H_{rms}}{\gamma h}\right)^n\right) \quad (\text{A.8})$$

in which γ (between 0 and 1) and n (about 10) are calibration factors. The root mean square wave height is computed from the short wave energy E_w as:

$$H_{rms} = \sqrt{\frac{8E_w}{\rho_w g}} \quad \text{where} \quad E_w = \int_0^{2\pi} S_w d\theta \quad (\text{A.9})$$

Next the total wave dissipation, \bar{D} is distributed proportionally over the wave directions:

$$D = \frac{S_w}{E_w} \bar{D} \quad (\text{A.10})$$

From the spatial distribution of wave energy radiation stresses can be evaluated:

$$\begin{aligned} S_{xx} &= \int \left(\frac{c_g}{c_w} (1 + \cos^2 \theta) - \frac{1}{2} \right) S_w d\theta \\ S_{xy} = S_{yx} &= \int \sin \theta \cos \theta \left(\frac{c_g}{c_w} S_w \right) d\theta \\ S_{yy} &= \int \left(\frac{c_g}{c_w} (1 + \sin^2 \theta) - \frac{1}{2} \right) S_w d\theta \end{aligned} \quad (\text{A.11})$$

Surface rollers

Short wave energy dissipation serves as a source term to a roller energy balance. Similar to the wave action balance the directional distribution of roller energy is taken into account whereas the frequency spectrum is represented by a single mean characteristic frequency. The roller energy balance is given by:

$$\frac{\partial S_r}{\partial t} + \frac{\partial c_{w,x} S_r}{\partial x} + \frac{\partial c_{w,y} S_r}{\partial y} + \frac{\partial c_\theta S_r}{\partial \theta} = -D_r + D \quad (\text{A.12})$$

in which S_r is the roller energy in each directional bin. The roller energy propagation speeds in x - and y -direction are given by:

$$\begin{aligned} c_{w,x} &= c_w \cos(\theta) \\ c_{w,y} &= c_w \sin(\theta) \end{aligned} \quad (\text{A.13})$$

where c_w is the short wave celerity obtained from linear wave theory:

$$c_w = \frac{\omega}{k_w} \quad (\text{A.14})$$

The roller energy dissipation is computed from the work done by shear between roller and wave (Deigaard, 1993):

$$\bar{D}_r = c_w \tau_r \quad (\text{A.15})$$

In which τ_r represents the wave averaged shear stress between the roller and water surface that is given by (Duncan, 1981):

$$\tau_r = \frac{\rho_w g A_r \sin(\beta)}{L} \quad (\text{A.16})$$

where β is the slope of the wave front, L is the wavelength corresponding to the mean intrinsic frequency and A_r is the roller area, which is related to the roller energy as proposed by Svendsen (1984):

$$E_r = \frac{1}{2} \frac{\rho_w A_r c_w^2}{L} \quad \text{where} \quad E_r = \int_0^{2\pi} S_r d\theta \quad (\text{A.17})$$

Substituting Equation A.17 in Equation A.16 gives Reniers and Battjes (1997):

$$\bar{D}_r = \frac{2g \sin(\beta) E_r}{c_w} \quad (\text{A.18})$$

in which the surface slope of the wave front (β) is computed with the wave shape model described in Section 6.2.3. Like the short wave energy dissipation also the total roller dissipation \bar{D}_r is distributed proportionally over the wave directions:

$$D_r = \frac{S_r}{E_r} \bar{D}_r \quad (\text{A.19})$$

Finally, the roller contribution to radiation stresses is computed and added to the wave-induced radiation stresses:

$$\begin{aligned} S_{xx,r} &= \int \cos^2 \theta S_r d\theta \\ S_{xy,r} &= S_{yx,r} = \int \sin \theta \cos \theta S_r d\theta \\ S_{yy,r} &= \int \sin^2 \theta S_r d\theta \end{aligned} \quad (\text{A.20})$$

The total radiation stress tensor is utilized to calculate the wave forcing:

$$\begin{aligned} F_x &= - \left(\frac{\partial S_{xx}}{\partial x} + \frac{\partial S_{xy}}{\partial y} \right) \\ F_y &= - \left(\frac{\partial S_{xy}}{\partial x} + \frac{\partial S_{yy}}{\partial y} \right) \end{aligned} \quad (\text{A.21})$$

Long wave hydrodynamics and time averaged flow

For the low-frequency and mean flow the shallow water equations are applied. To account for wave induced mass-flux and subsequent return flow the shallow water equations are cast into a depth-averaged Generalized Lagrangian Mean (GLM) formulation (Walstra et al., 2000). To that end the Eulerian shallow water velocities u^E and v^E (in x -direction and y -direction respectively) are replaced with the Lagrangian equivalent, u^L and v^L :

$$u^L = u^E + u^S \quad \text{and} \quad v^L = v^E + v^S \quad (\text{A.22})$$

in which u^S , v^S represent the Stokes drift in x - and y -direction respectively (Phillips, 1977):

$$u^S = \frac{(E_w + 2E_r)\cos\theta}{\rho_w h c_w} \quad \text{and} \quad v^S = \frac{(E_w + 2E_r)\sin\theta}{\rho_w h c_w} \quad (\text{A.23})$$

The resulting GLM-shallow water equations are given by:

$$\frac{\partial u^L}{\partial t} + u^L \frac{\partial u^L}{\partial x} + v^L \frac{\partial u^L}{\partial y} - f v^L - \nu_h \left(\frac{\partial^2 u^L}{\partial x^2} + \frac{\partial^2 u^L}{\partial y^2} \right) = \frac{\tau_{sx}}{\rho_w h} - \frac{\tau_{bx}^E}{\rho_w h} - g \frac{\partial \eta}{\partial x} + \frac{F_x}{\rho_w h} \quad (\text{A.24})$$

$$\frac{\partial v^L}{\partial t} + u^L \frac{\partial v^L}{\partial x} + v^L \frac{\partial v^L}{\partial y} + f u^L - \nu_h \left(\frac{\partial^2 v^L}{\partial x^2} + \frac{\partial^2 v^L}{\partial y^2} \right) = \frac{\tau_{sy}}{\rho_w h} - \frac{\tau_{by}^E}{\rho_w h} - g \frac{\partial \eta}{\partial y} + \frac{F_y}{\rho_w h} \quad (\text{A.25})$$

$$\frac{\partial \eta}{\partial t} + \frac{\partial h u^L}{\partial x} + \frac{\partial h v^L}{\partial y} = 0 \quad (\text{A.26})$$

where τ_{sx} , τ_{sy} are wind shear stresses, τ_{bx} , τ_{by} are bed shear stresses, g is the acceleration of gravity, η is the water level, F_x , F_y are the wave-forces, ν_h is the horizontal viscosity and f is the Coriolis coefficient. It is remarked that the bottom shear stresses are computed following Ruessink et al. (2001) and are based on the Eulerian flow velocity instead of the Lagrangian flow velocity. The horizontal viscosity associated with lateral mixing is related to wave breaking induced eddies (Battjes, 1975) and a user specified background viscosity, $\nu_{h,back}$ (default 0.1 m²/s):

$$\nu_h = h \left(\frac{\bar{D}_r}{\rho_w} \right)^{\frac{1}{3}} + \nu_{h,back} \quad (\text{A.27})$$

Sediment transport

The sediment transport is modeled with a depth-averaged advection diffusion equation (Galapatti, 1983):

$$\begin{aligned} \frac{\partial hC}{\partial t} + \frac{\partial hC(u^E + u_A \sin \theta_m)}{\partial x} + \frac{\partial hC(v^E + u_A \cos \theta_m)}{\partial y} \\ + \frac{\partial}{\partial x} \left[D_h h \frac{\partial C}{\partial x} \right] + \frac{\partial}{\partial y} \left[D_h h \frac{\partial C}{\partial y} \right] = \frac{hc_{eq} - hC}{T_s} \end{aligned} \quad (\text{A.28})$$

where C represents the depth-averaged sediment concentration, which varies on the wave-group time scale, u_A is a flow velocity related to wave nonlinearity (see Section 6.2.3) and θ_m is the mean wave direction of incoming waves. The sediment concentration adapts gradually to changing hydraulic conditions using an adaptation time scale T_s for sediment entrainment that is given by a simple expression based on the local water depth, h , and the sediment fall velocity w_s :

$$T_s = \max \left(0.05 \frac{h}{w_s}, T_{s,\min} \right) \quad (\text{A.29})$$

In this expression $T_{s,\min}$ is a user specified minimum adaptation time (default set at 1.0 second). In shallow water T_s becomes small ($T_s \approx T_{s,\min}$) and the sediment concentration responds nearly instantaneously to changing hydrodynamics. The entrainment or deposition of sediment is determined by the mismatch between the actual sediment concentration C and the equilibrium concentration c_{eq} thus representing the source term in the sediment transport equation.

The equilibrium sediment concentration c_{eq} is calculated with an extended transport formulation of Van Rijn (2007):

$$c_{eq} = \frac{A_{sb}}{h} \left(\sqrt{(u^E)^2 + 0.64u_{rms,2}^2} - u_{cr} \right)^{1.5} + \frac{A_{ss}}{h} \left(\sqrt{(u^E)^2 + 0.64u_{rms,2}^2} - u_{cr} \right)^{2.4} \quad (\text{A.30})$$

where A_{sb} and A_{ss} are a bed load and suspended load coefficient respectively. Sediment is stirred by the Eulerian flow velocity and the near-bed short wave orbital velocity. The effect of wave breaking induced turbulence is included in the near-bed orbital velocity u_{rms} following Reniers et al., (2004a):

$$u_{rms,2} = \sqrt{u_{rms}^2 + 1.45k_b} \quad (\text{A.31})$$

in which k_b is the bore averaged near-bed turbulence energy (see Chapter 5 and Section 6.2.2 for more details). The near-bed orbital peak velocity is obtained from the wave-group varying wave energy using linear wave theory:

$$u_{rms} = \frac{\pi H_{rms}}{\sqrt{2} T_m \sinh(k_w h)} \quad (\text{A.32})$$

In order to entrain sediment a critical flow velocity u_{cr} has to be exceeded, which is constructed from a critical flow due to currents only $u_{cr,c}$ based on Shields and a critical flow for waves $u_{cr,w}$ based on (Komar and Miller, 1975):

$$u_{cr} = \alpha u_{cr,c} + (1 - \alpha) u_{cr,w} \quad \text{where } \alpha = u^E / (u^E + u_{rms,2}) \quad (\text{A.33})$$

Bed level change

Bed level changes in the wet area are (mainly) based on gradients in the sediment transport according to:

$$\frac{\partial z_b}{\partial t} = \frac{1}{1-p} \left(\frac{\partial S_x}{\partial x} + \frac{\partial S_y}{\partial y} \right) \gamma_{morf} \quad (\text{A.34})$$

where p is porosity, γ_{morf} is a multiplication factor for the bed level changes (default set to one) and S_x and S_y are computed sediment transports in x -direction and y -direction respectively, given by:

$$\begin{aligned} S_x &= hC(u^E + u_A \sin \theta_m) + \frac{\partial}{\partial x} \left(D_h h \frac{\partial C}{\partial x} \right) \\ S_y &= hC(v^E + u_A \cos \theta_m) + \frac{\partial}{\partial y} \left(D_h h \frac{\partial C}{\partial y} \right) \end{aligned} \quad (\text{A.35})$$

in which D_h is a sediment diffusion coefficient expressed by:

$$D_h = \gamma_{visc} \nu_h \quad (\text{A.36})$$

In this expression γ_{visc} is a calibration factor (default value 1.0) and ν_h is the horizontal viscosity as expressed in Equation A.27.

To account for slumping of the dune face and associated sediment supply from the dry dune to the beach an avalanching algorithm is applied. An avalanche is introduced if locally the critical bed-slope is exceeded:

$$\left| \frac{\partial z_b}{\partial x} \right| > m_{cr} \quad (\text{A.37})$$

with a similar expression for the y -direction. It is presumed that inundated areas are much more prone to slumping and therefore separate critical slopes for dry and wet points are applied (see Section 6.5.2 for more details).

BOUNDARY CONDITIONS

Short wave energy at the offshore boundary is prescribed as a function of the alongshore location, direction and time. Time series of wave group varying energy are generated from (directional) spectra prescribed by the user. At the lateral boundaries, the alongshore short wave energy gradient is set to zero (Neumann boundary), effectively eliminating shadow zones.

At the seaward boundary and landward (in case of a bay) boundary, a radiating condition is prescribed for the flow, which also takes into account the incoming bound long waves (see Van Dongeren and Svendsen (1997) for more details). For the lateral boundaries the longshore water level gradient is prescribed and is default set to zero (Neumann boundary). In addition, the longshore gradient in the cross-shore flow velocity (u) is assumed to be zero. The boundary conditions work quite well for (quasi) stationary situations, where the coast is assumed to be uniform alongshore outside

the model domain. Considering obliquely incident wave groups, the boundary conditions give reasonable results, though rigorous testing still has to be done.

The longshore sediment concentration gradient is set to zero at both lateral boundaries (Neumann boundary). However, the longshore transport gradient is not necessarily zero since the longshore flow velocity v is computed at the lateral boundaries. Bed level gradients at the lateral boundaries are assumed to be zero (Neumann boundary).

NUMERICAL IMPLEMENTATION

The propagation of short wave action and roller energy can be computed with two schemes including an explicit upwind scheme (default) or an explicit (central) Lax-Wendroff scheme (used in this thesis). Hydrodynamics are computed explicitly and the momentum advection terms are computed with a first-order momentum conservative scheme according to Stelling and Duijnmeijer (2003) whereas the pressure gradient and horizontal viscosity are computed with an upwind scheme. Finally, the advection diffusion equation for sediment and the bed update are also explicitly solved for with an upwind scheme. More details about the numerical implementation can be found in (Roelvink et al., 2006).

Appendix B MODEL INPUT FILES

Parameter settings for test T01 of the Deltaflume experiment with a morphological factor $T_{morf} = 1$.

General input

<code>nx = 178</code>	[-] number of grid cells in x -direction
<code>ny = 2</code>	[-] number of grid cells in y -direction
<code>depfile = h_T06x_41.dep</code>	[-] file that contains bathymetry
<code>posdwn = -1</code>	[-] vertical elevations defined positive downwards (= 1) or upwards (= -1)
<code>vardx = 0</code>	[-] 0 = equidistant grid; 1 = non-equidistant grid
<code>dx = 1</code>	[m] discretization in x -direction
<code>dy = 5.0</code>	[m] discretization in y -direction
<code>xori = 41.0</code>	[m] x -coordinate of computational grid origin in relation to the world
<code>yori = 0.0</code>	[m] y -coordinate of computational grid origin in relation to the world
<code>alfa = 0.0</code>	[°] grid orientation in relation to the world
<code>tstop = 21700</code>	[s] stop time simulation (is duration simulation)
<code>CFL = 0.9</code>	[-] maximum courant number
<code>tstart = 100</code>	[s] start time of simulation output
<code>tint = 2</code>	[s] time interval output
<code>rho = 1000</code>	[kg/m ³] mass density of water
<code>g = 9.81</code>	[m/s ²] gravitational acceleration
<code>scheme = 2</code>	[-] Numerical scheme for wave and roller energy: 1 = upwind, 2 = Lax-Wendroff

Wave input

<code>instat = 3</code>	[-] option time-varying wave boundary condition.
<code>Hrms = 1.02</code>	[m] root mean square wave height
<code>Trep = 4.57</code>	[s] representative wave period
<code>m = 1024</code>	[-] power in cos ^m directional distribution
<code>dir0 = 270</code>	[°] mean wave direction (Nautical convention)
<code>thetamin = -1.</code>	[°] lower directional limit (angle with respect to computational x -axis)
<code>thetamax = 1.</code>	[°] upper directional limit (angle with respect to computational x -axis)
<code>dtheta = 2.</code>	[°] directional resolution

break = 3	[-] option breaker model
gamma = 0.50	[-] wave breaking dissipation coefficient
alpha = 1.	[-] wave breaking dissipation coefficient
n = 10.	[-] wave breaking dissipation coefficient
roller = 1	[-] roller model, 0 = off, 1 = on
beta = 0.1	[-] coefficient in roller dissipation model related to the wave surface slope ($\beta = \sin(\beta)$)
swtable = RF_table.txt	[-] table with stream function theory amplitudes to describe non-linear waves
rfb = 1	[-] 1 = beta is computed from parameterized wave shape, 0 = rfb is equal to beta defined above

Flow input

tideloc = 0	[-] number of model corners where tidal or surge input time series are defined
zs0 = -0.035	[m] initial water level
C = 65	[m ^{1/2} /s] Chezy value
nuh = 0.1	[m ² /s] horizontal background viscosity
nuhfac = 1.0	[-] coefficient for roller induced horizontal viscosity
eps = 0.0001	[m] threshold depth
umin = 0.0	[m/s] threshold velocity upwind scheme
hmin = 0.20	[m] threshold water depth for undertow

Sed input

morstart = 100	[s] start time morphology
morfac = 1	[-] morphological acceleration factor
form = 3	[-] option for equilibrium sediment concentration formulation
D50 = 0.0002	[m] D50 grain diameter
D90 = 0.0003	[m] D90 grain diameter
rhos = 2650	[kg/m ³] mass density of sand
dryslp = 1.0	[-] critical dry bed slope
wetslp = 0.10	[-] critical wet bed slope
dzmax = 0.003	[m ³ /ms] maximum dune face erosion rate
hswitch = 0.10	[m] water depth at which is switched from a critical wet slope to a critical dry bed slope
facua = 0.10	[-] coefficient for time averaged flow due to wave

asymmetry, which is related to the phase shift between intra wave sediment suspension and flow.

turb = 2

[-] contribution wave breaking induced turbulence on equilibrium sediment concentration. 0 = no turbulence, 1 = wave averaged turbulence, 2 = bore averaged turbulence

Tsmin = 1

[s] Minimum adaptation time scale for the sediment suspension

Parameter settings for test T01 of the Deltaflume experiment with a morphological factor $T_{morf} = 10$.

General input

$nx = 178$	[-] number of grid cells in x -direction
$ny = 2$	[-] number of grid cells in y -direction
$depfile = h_T06x_41.dep$	[-] file that contains bathymetry
$posdwn = -1$	[-] vertical elevations defined positive downwards (= 1) or upwards (= -1)
$vardx = 0$	[-] 0 = equidistant grid; 1 = non-equidistant grid
$dx = 1$	[m] discretization in x -direction
$dy = 5.0$	[m] discretization in y -direction
$xori = 41.0$	[m] x -coordinate of computational grid origin in relation to the world
$yori = 0.0$	[m] y -coordinate of computational grid origin in relation to the world
$alfa = 0.0$	[°] grid orientation in relation to the world
$tstop = 2260$	[s] stop time simulation (is duration simulation)
$CFL = 0.9$	[-] maximum courant number
$tstart = 100$	[s] start time of simulation output
$tint = 1$	[s] time interval output
$\rho = 1000$	[kg/m ³] mass density of water
$g = 9.81$	[m/s ²] gravitational acceleration
$scheme = 2$	[-] Numerical scheme for wave and roller energy: 1 = upwind, 2 = Lax-Wendroff

Wave input

$instat = 3$	[-] option time-varying wave boundary condition
$Hrms = 1.02$	[m] root mean square wave height
$Trep = 4.57$	[s] representative wave period
$m = 1024$	[-] power in \cos^m directional distribution
$dir0 = 270$	[°] mean wave direction (Nautical convention)
$thetamin = -1.$	[°] lower directional limit (angle with respect to computational x -axis)
$thetamax = 1.$	[°] upper directional limit (angle with respect to computational x -axis)
$dtheta = 2.$	[°] directional resolution

break = 3	[-] option breaker model
gamma = 0.50	[-] wave breaking dissipation coefficient
alpha = 1.	[-] wave breaking dissipation coefficient
n = 10.	[-] wave breaking dissipation coefficient
roller = 1	[-] roller model, 0 = off, 1 = on
beta = 0.1	[-] coefficient in roller dissipation model related to the wave surface slope ($\beta = \sin(\beta)$)
swtable = RF_table.txt	[-] table with stream function theory amplitudes to describe non-linear waves
rfb = 1	[-] 1 = beta is computed from parameterized wave shape, 0 = rfb is equal to beta defined above

Flow input

tideloc = 0	[-] number of model corners where tidal or surge input time series are defined
zs0 = -0.035	[m] initial water level
C = 65	[m ^{1/2} /s] Chezy value
nuh = 0.1	[m ² /s] horizontal background viscosity
nuhfac = 1.0	[-] coefficient for roller induced horizontal viscosity
eps = 0.0001	[m] threshold depth
umin = 0.0	[m/s] threshold velocity upwind scheme
hmin = 0.20	[m] threshold water depth for undertow

Sed input

morstart = 100	[s] start time morphology
morfac = 10	[-] morphological acceleration factor
form = 3	[-] option for equilibrium sediment concentration formulation
D50 = 0.0002	[m] D50 grain diameter
D90 = 0.0003	[m] D90 grain diameter
rhos = 2650	[kg/m ³] mass density of sand
dryslp = 1.0	[-] critical dry bed slope
wetslp = 0.10	[-] critical wet bed slope
dzmax = 0.003	[m ³ /ms] maximum dune face erosion rate
hswitch = 0.10	[m] water depth at which is switched from a critical wet slope to a critical dry bed slope
facua = 0.10	[-] coefficient for time averaged flow due to wave

asymmetry, which is related to the phase shift between intra wave sediment suspension and flow.

turb = 2

[-] contribution wave breaking induced turbulence on equilibrium sediment concentration. 0 = no turbulence, 1 = wave averaged turbulence, 2 = bore averaged turbulence

Tsmin = 1

[s] Minimum adaptation time scale for the sediment suspension

Parameter settings for 2DH simulation with an alongshore uniform coastline and a morphological factor $T_{morf} = 10$.

General input

<code>nx = 210</code>	[-] number of grid cells in x -direction
<code>ny = 80</code>	[-] number of grid cells in y -direction
<code>depfile = bed.dep</code>	[-] file that contains bathymetry
<code>posdwn = -1</code>	[-] vertical elevations defined positive downwards (= 1) or upwards (= -1)
<code>vardx = 1</code>	[-] 0 = equidistant grid; 1 = non-equidistant grid
<code>xfile = x.grd</code>	[-] discretization in x -direction
<code>yfile = y.grd</code>	[-] discretization in y -direction
<code>xori = 0.0</code>	[m] x -coordinate of computational grid origin in relation to the world
<code>yori = 0.0</code>	[m] y -coordinate of computational grid origin in relation to the world
<code>alfa = 0.0</code>	[°] grid orientation in relation to the world
<code>tstop = 12024</code>	[s] stop time simulation (is duration simulation)
<code>CFL = 0.6</code>	[-] maximum courant number
<code>tstart = 0</code>	[s] start time of simulation output
<code>tint = 1</code>	[s] time interval output
<code>rho = 1000</code>	[kg/m ³] mass density of water
<code>g = 9.81</code>	[m/s ²] gravitational acceleration
<code>scheme = 2</code>	[-] Numerical scheme for wave and roller energy: 1 = upwind, 2 = Lax-Wendroff

Wave input

<code>instat = 4</code>	[-] option time-varying wave b.c.
<code>bcfile = boundarylst.dat</code>	[-] file in which the wave boundary conditions are listed.
<code>thetamin = -67.5</code>	[°] lower directional limit (angle w.r.t computational x -axis)
<code>thetamax = 67.5</code>	[°] upper directional limit (angle w.r.t computational x -axis)
<code>dtheta = 15.0</code>	[°] directional resolution
<code>break = 3</code>	[-] option breaker model
<code>gamma = 0.50</code>	[-] wave breaking dissipation coefficient

alpha = 1.	[-] wave breaking dissipation coefficient
n = 10.	[-] wave breaking dissipation coefficient
roller = 1	[-] roller model, 0 = off, 1 = on
beta = 0.1	[-] coefficient in roller dissipation model related to the wave surface slope ($\beta = \sin(\beta)$)
swtable = RF_table.txt	[-] table with stream function theory amplitudes to describe non-linear waves
rfb = 1	[-] 1 = beta is computed from parameterized wave shape, 0 = rfb is equal to beta defined above

Flow input

tideloc = 2	[-] number of model corners where tidal or surge input time series are defined
tidelen = 335	[-] length of tide/surge time series
zs0file = surge.dat	[-] file that contains tide/surge time series for tideloc locations and with length tidelen
paulrevere = 0	[-] if tideloc => 2 this indicates at which model corners the tide/surge time series are to be applied.
C = 65	[m ^{1/2} /s] Chezy value
nuh = 0.1	[m ² /s] horizontal background viscosity
nuhfac = 1.0	[-] coefficient for roller induced horizontal viscosity
eps = 0.01	[m] threshold depth
umin = 0.0	[m/s] threshold velocity upwind scheme
hmin = 0.20	[m] threshold water depth for undertow

Sed input

morstart = 0	[s] start time morphology
morfac = 10	[-] morphological acceleration factor
form = 3	[-] option for equilibrium sediment concentration formulation
D50 = 0.00025	[m] D50 grain diameter
D90 = 0.000375	[m] D90 grain diameter
rhos = 2650	[kg/m ³] mass density of sand
dryslp = 1.0	[-] critical dry bed slope
wetslp = 0.10	[-] critical wet bed slope
dzmax = 0.17	[m ³ /ms] maximum dune face erosion rate

hswitch = 0.10	[m] water depth at which is switched from critical wet to critical dry bed slope
facua = 0.10	[-] coefficient for time averaged flow due to wave asymmetry, which is related to the phase shift between intra wave sediment suspension and flow.
turb = 2	[-] contribution wave breaking induced turbulence on equilibrium sediment concentration. 0 = no turbulence, 1 = wave averaged turbulence, 2 = bore averaged turbulence
Tsmin = 1	[s] Minimum adaptation time scale for the sediment suspension

ACKNOWLEDGEMENTS

The Dr.Ir. Cornelis Lely Foundation and the Delft Cluster II joint research program are gratefully acknowledged for the financial support to this PhD-project.

Concluding my PhD gives the possibility to look back and thank the people that guided me towards the end of this thesis:

First I would like to thank Ad Reniers who was involved in my research from the start and as a supervisor inspired me with new ideas and approaches. Especially in the first years of my research we daily had open discussions, which were very helpful to direct the research. Also I'm thankful for the opportunity to spend two months at Miami University to finalize the research and writing of this thesis. It was an intensive period and I want to thank Ad and Stella for a great stay despite the hard working.

Next, I'm grateful to Jan van de Graaff for his thorough reviews on my work over the last years. We had several detailed discussions, which helped to test and validate new ideas. Also I'm thankful for his effort and constructive comments to improve the readability of this thesis.

I want thank Marcel Stive for giving me the freedom and possibility to find my way in the research field of hydraulic engineering.

Finally, I want to express my sincere gratitude to the committee, prof.dr. R.A. Holman, prof.dr.ir. L.C. van Rijn, prof.dr.ir J.A. Roelvink and dr. B.G. Ruessink for reviewing my manuscript and the constructive discussions we had over the last years.

Much of the work presented in this thesis was carried out in cooperation with others. Regarding the dune erosion experiment I want to thank the technical staff of the Deltaflume for helping to get useful data. I appreciate the fruitful teamwork with Martijn Coeveld and I enjoined the beers in the evening when we were "analyzing" the new measurements of the day. Also I appreciate the help of Stefan Aarninkhof and Irv Elshoff to set up a stereo video system. I feel that the experiment in the Deltaflume forms the fundament of this thesis and was the start point for new imagination and developments.

Next, I want to want to express my gratitude to Rob Holman for giving me the possibility to spend three months at the Coastal Imaging Laboratory (CIL) of Oregon State University. I had a great time and learned a lot. Also I would like to thank Linden Clarke for explaining the concepts of stereo photography and the fruitful col-

laboration, which in the end resulted in a working algorithm. I thank my fellow PhD students in CIL (Meg, Greg, Kristen, Joe and Jason) for a good time and the constructive discussions we had to accomplish our nearshore class home work.

Back from Oregon, Dano Roelvink started developing a new nearshore model XBeach to simulate coastal impacts of storms. I'm thankful for the opportunity to get involved in the development of this model, which gave me the possibility to implement new physics related to dune erosion and to learn a lot about how models (should) work. I still enjoy working on the development of XBeach with Dano, Ad, Ap, Jamie and Robert and I feel that many more people should get the opportunity to improve their understanding of nature by building new models.

Returning to the Hydraulic engineering section of TU Delft, I want to express gratitude to all my colleagues for a great time with interesting discussions, too long cycle tours with good BBQ's, a perfect sailing trip on the Wadden Sea, the excellent performance in the Company hockey competition, their nice company on conferences and work trips and for all the other good things we did together! In special I would like to thank my Fellow PhD students (Ruben, Marije, Jasper, Martijn, Wim, Bianca, Kees and Fedor) and Dirk Jan Walstra, Tjerk Zitman and Wim Uijttewaal who also contributed to this thesis.

Finally, I want to thank my family and friends for their support. Especially I want to thank Floor, who unconditionally supported me to finish this thesis and who convinced me to go back to work when the research did not made headway.

CURRICULUM VITAE

Jacob Simon Marie (Jaap) van Thiel de Vries was born in 's-Hertogenbosch on June 30th 1978. He grew up in Boxtel where he graduated from secondary school, Brabant HAVO, 1995 and Jacob Roeland Lyceum (VWO), 1997. Inspired by a family tradition in Civil Engineering he started his academic education at Delft University of Technology. He graduated at the section of Fluid Mechanics in 2003 under supervision of prof.dr.ir. J.A. Battjes on an MSc project entitled “Wave fields in transitional water depth” that was carried out at Witteveen+Bos.

In 2004 he started his PhD research at Delft University of Technology on dune erosion during storm surges, which resulted in the present dissertation. As part of the research he was involved in conducting a large scale flume experiment. He spent three months at Oregon State University at the Coastal Imaging Lab to work on a stereo video reconstruction algorithm and was involved in the development of the morphodynamic nearshore model XBeach.

From October 2006 Jaap was working as a part-time researcher at WL|Delft Hydraulics, which later was merged into a new research institute Deltares. Currently he is working four days a week at Deltares as a researcher/advisor and one day a week at Delft University.

